A Model for the Structural Integrity of Composite Laminates in Fire

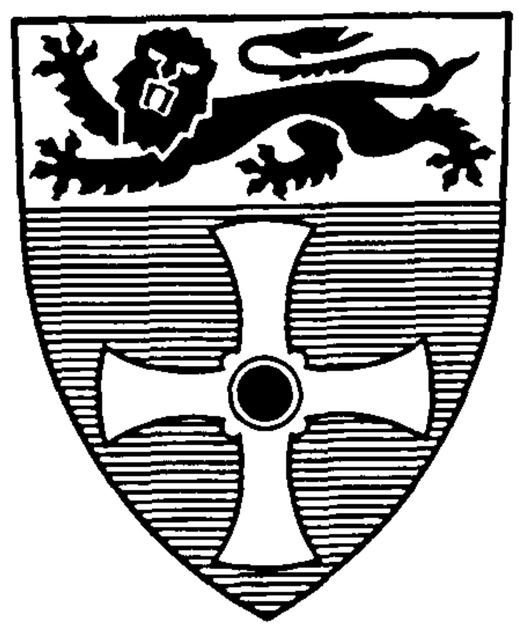

Thesis submitted in accordance with the requirements of the University of Newcastle upon Tyne for the degree of Doctor of Philosophy.

T. N. A. Browne

Centre for Composite Materials Engineering,
School of Mechanical and Systems Engineering,
University of Newcastle upon Tyne.

August 2006

Acknowledgements

I would like to acknowledge the guidance, enthusiasm and support of Professor A.G. Gibson who acted as my Ph.D supervisor. I also acknowledge the financial support offered by the EPSRC for the duration of the project, and materials supplied by the Composites Technology Centre at Vosper Thornycroft, Portchester.

I would like to thank my friends and colleagues at the University of Newcastle upon Tyne for their advice and dedication, in particular Dr Yongshu Wu and Mr Ron Jenson.

Finally, I would like to thank Miss Freya Copping and my family for their overwhelming support, encouragement and patience over the last three years.

Chapter 1 Introduction

Composite materials offer ideal properties for many structural applications; they exhibit excellent strength and stiffness to weight ratio, good corrosion resistance and are easily repaired. Hence, composites are often the preferred choice for many applications in the marine and offshore industries. However in such extreme environments, the risk posed by fire is greatly increased.

Current fire resistance tests, used to qualify such materials, are normally conducted on large scale samples or finished products. Innovation is often inhibited at initial design and material selection stages because of the high cost of these test procedures. A small scale resistance test, supported by thermal and mechanical modelling techniques, could be used to characterise the structural response of composite laminates in fire. The development of such a technique formed the basis of the research presented here.

1.1 Glass Fibre Reinforced Plastic (GFRP) Composites

Composites consist of two or more physically different materials which, when mixed, provide superior properties than each individual component [1]. In recent years there has been a steady increase in the use of polymer composites in the transport, construction, marine and piping industries [2].

1.1.1 Reinforcement

Glass fibres have relatively high strength and modulus but are usually very brittle and prone to chemical attack and aging. A list of E-glass properties is displayed in Table 1.1. When glass fibres are combined with resin, a bulk material is produced with excellent stiffness and strength properties. The 'composite action' between the resin and glass ensures that any loads are distributed evenly through the whole material. All of the fibres, which bear most of the load, are subjected to the same strain levels, despite waviness or misalignment. The addition of plastic resin also improves energy absorption, resistance to crack propagation and chemical resistance [1].

Table 1.1 Properties of E-glass at 20°C [1].

Property	Value
Diameter	8-14 μm
Density	2560 kgm^{-3}
Young's Modulus	76 GPa
Tensile Strength	1.4 - 2.5 GPa
Thermal conductivity – parallel to fibres	1.04 W/m°C

Continuous fibres are available in roving form either in spools for use in pultrusion, shown in Figure 1.1(i), or woven mat, Figure 1.1(ii). Other forms of continuous fibre mat include multi-axial fabrics, Figure 1.1(iii).

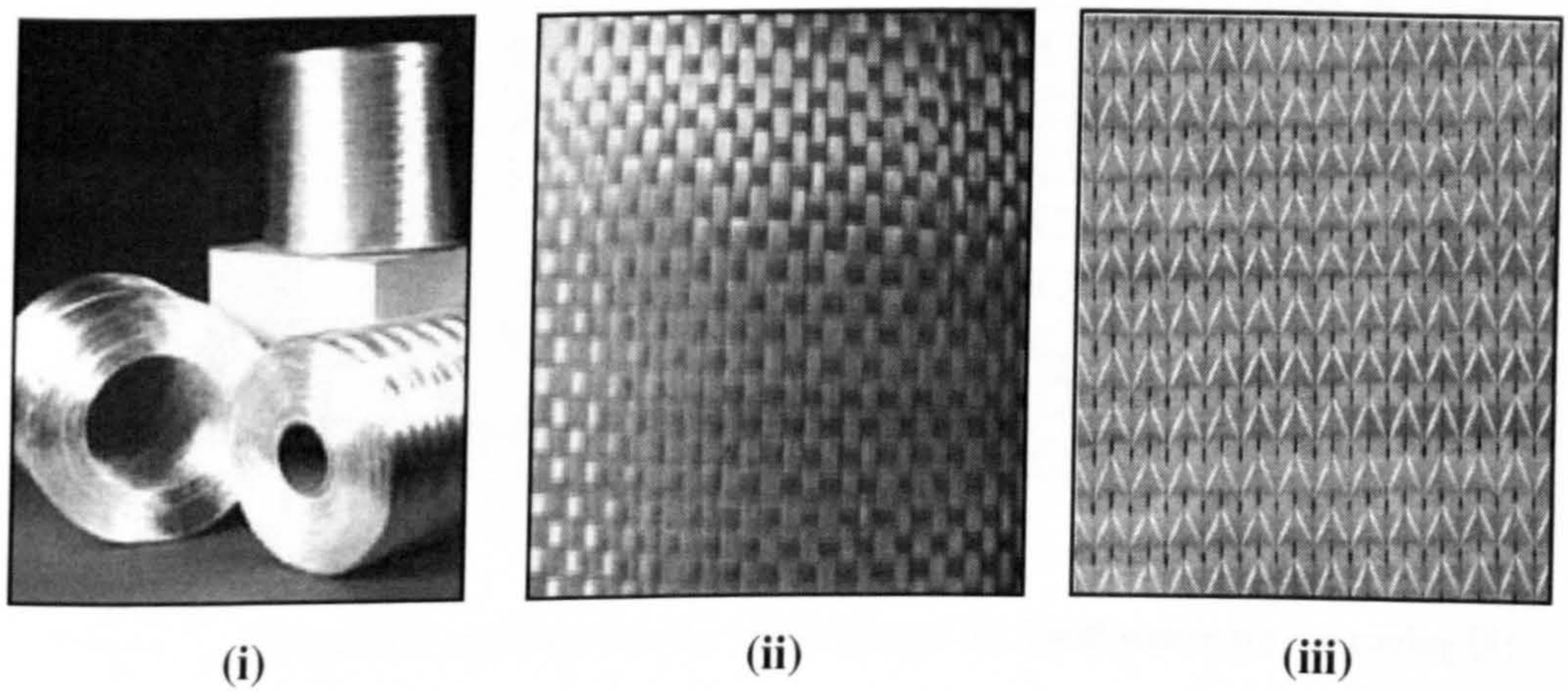

(i) (ii) (iii)

Figure 1.1 Common forms of glass fibre. (i) Roving [3], (ii) Woven Roving [4] and (iii) 0°/90° stitched multi-axis cross-ply [5].

1.1.2 Woven Fabrics

Woven fabrics are produced by weaving fibres in the 0° and 90° directions. Fibres in the 0° direction are referred to as warp fibres and pass alternately over and under the 90° (weft) fibres. There are a number of different styles of woven roving fabrics which provide certain advantages and disadvantages.

The most common style is plain woven roving, shown in Figure 1.2(i). This fabric is the simplest form of weave, producing a symmetrical pattern with good stability. The dense nature of the weave, and therefore high level of fibre crimp, means that the fabric is harder to drape and exhibits poorer mechanical properties than other weave styles [6, 7].

Twill weave, Figure 1.2(ii), is a modification of plain woven roving that provides better wet out and drape characteristics. The pattern is produced by weaving one or more warp fibres alternately over and under two or more weft fibres in a regular manner. A characteristic pattern of diagonal lines is produced on the surface of the fabric [6, 7]. This style of fabric has reduced crimp which, when compared to plain woven roving, gives the finished laminate a smoother surface finish and improved mechanical properties.

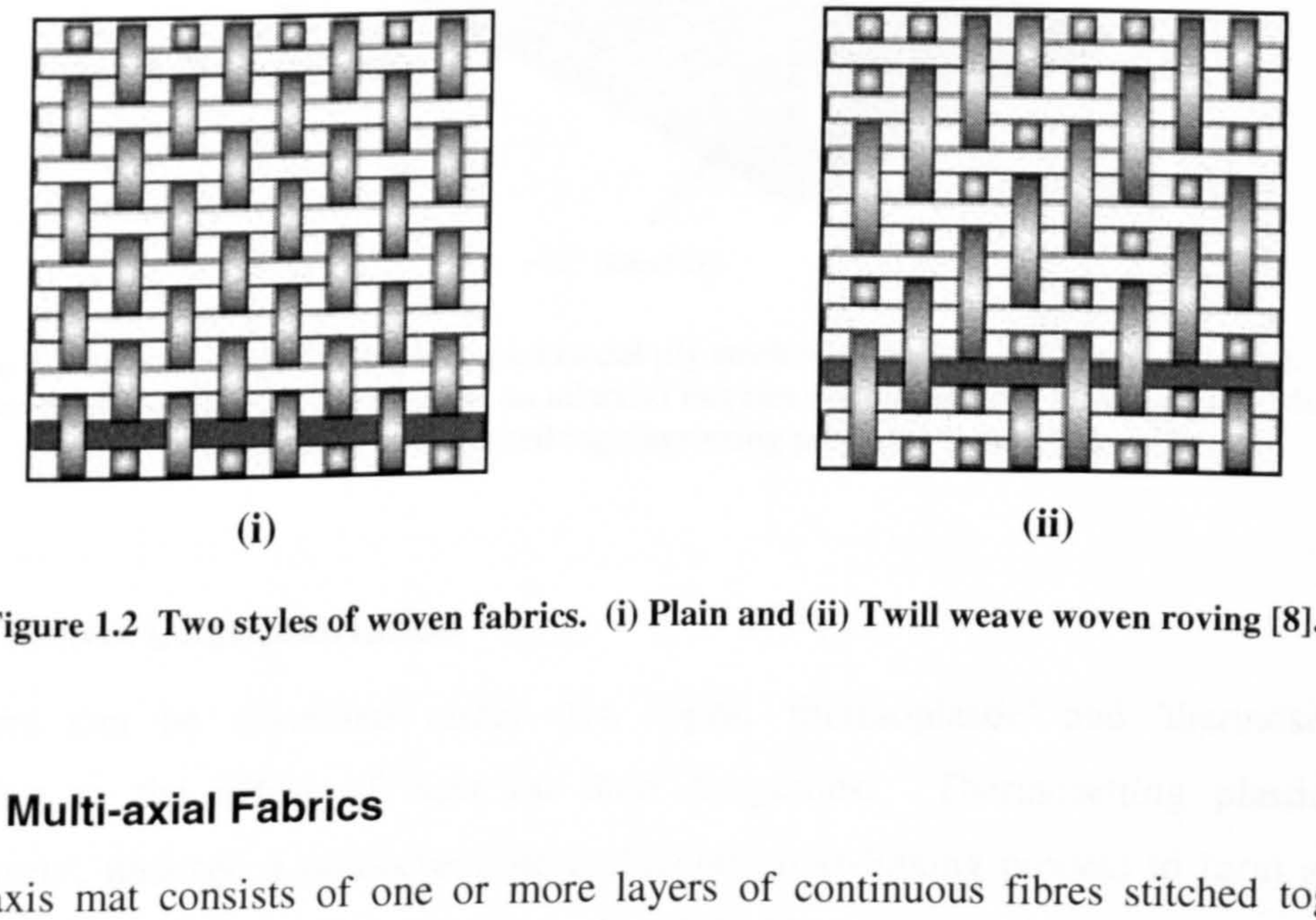

(i) (ii)

Figure 1.2 Two styles of woven fabrics. (i) Plain and (ii) Twill weave woven roving [8].

1.1.3 Multi-axial Fabrics

Multi-axis mat consists of one or more layers of continuous fibres stitched together using polyester thread [7]. An example of the stitching process is shown in Figure 1.3. Polyester is usually used as the stitching thread as it has the necessary properties which allow it to be formed into fibres and is also very cheap. Multi-axis fabric can be made using a variety of fibre orientations, unlike woven fabrics which are only produced in the 0°/90° directions.

Multi-axis fabrics have superior mechanical properties to woven materials because the fibres are straight rather than crimped. The possibility of multiple fibre orientations means that multi-axis mat can also provide strength and stiffness in more directions than woven mat. However, multi-axis mat requires more expensive, low tex (finer) fibres and more sophisticated manufacturing techniques than woven mat, leading to higher production costs.

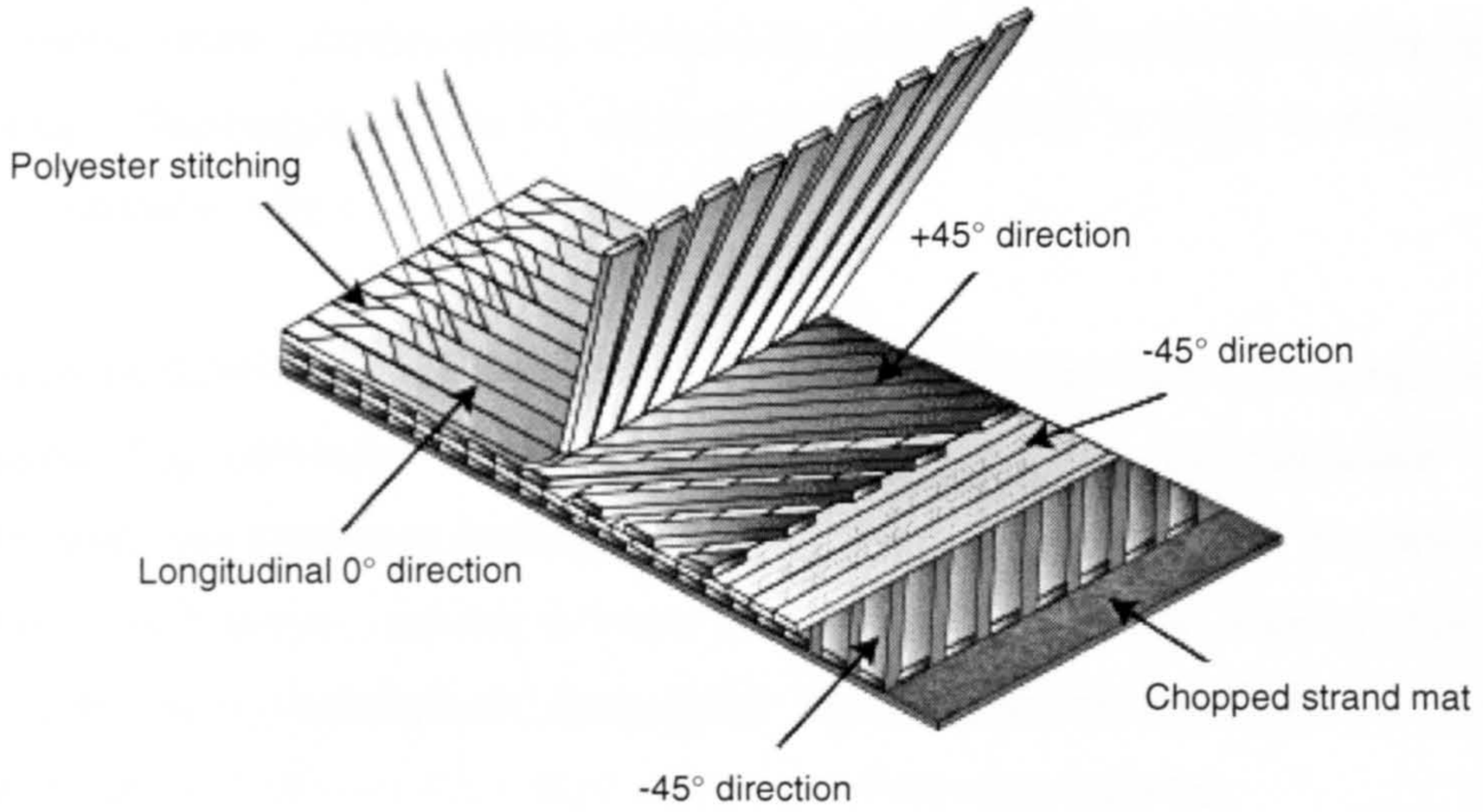

Figure 1.3 Manufacture of a typical quadraxial ply stack with 0°, 90°, +45°, and –45° plies. They are often made balanced (equal weight on all axes) but can also be tailored to suit a particular load case. Plies are stitched together using polyester thread [9].

1.1.4 Matrix Characteristics

Polymers can be classified under two types, 'thermoplastic' and 'thermosetting', according to the effect of heat on their properties. Thermosetting plastics, or 'thermosets', undergo a non-reversible molecular cross-linking process to form a rigid product when resin is mixed with a catalyst [7]. They generally exhibit good thermal stability, rigidity and hardness properties.

Once cured, thermosets do not melt if heated, although in some cases liquid droplets can be formed when certain thermosets are burned. Above a certain temperature their mechanical properties will change significantly. This temperature is known as the glass

transition temperature (T_g), and varies according to the particular resin system used. Above T_g, the molecular structure of the thermoset changes from that of a rigid crystalline polymer to a more flexible, amorphous polymer. At these temperatures, properties such as flexural modulus, compressive strength, tensile strength and shear strength drop significantly. This change is reversed when the material is cooled back below T_g.

In contrast, thermoplastics soften with heating and eventually melt, hardening again with cooling. Thermoplastics can be softened and re-solidified as often as desired without any appreciable effect on the material properties.

Reinforced thermoplastic composites are not as common as thermoset composites. The compounding operation tends to be more expensive for thermoplastics than for thermosets, and thermoset laminates normally offer better mechanical properties [7]. In recent years however, interest in more environmentally friendly materials has led to a rise in the use of thermoplastic composites. Not only are thermoplastics recyclable, but they do not give off harmful styrene emissions when manufactured.

1.1.5 Polyester Resin

Unsaturated polyester resins cover a wide range of materials with varying degrees of mechanical properties [6, 7]. Polyesters are the most commonly used resin system due to their good mechanical, electrical and chemical resistance properties and low cost. Polyesters are generally classified by which materials are used in their manufacture; the most common being orthophthalic or isophthalic. Orthophthalic polyester is the standard low cost resin used by many industries but can be prone to certain forms of chemical attack. Isophthalic polyester resin has superior water resistance properties and is therefore used more frequently in the marine industry [7].

1.1.6 Vinyl ester Resin

Vinyl ester resins are similar in their molecular structure to polyesters, but tend to be tougher and more resilient. The vinyl ester molecule features fewer ester groups than polyester. These ester groups are susceptible to water degradation by hydrolysis, meaning vinyl esters exhibit better resistance to water and other chemicals than polyesters [7]. These properties mean vinyl esters are frequently used in applications such as pipelines and chemical storage tanks. Although vinyl ester resins demonstrate superior mechanical and chemical resistance properties, they are much more expensive than polyester resins.

1.1.7 Polypropylene

Polypropylene is the second most common reinforced thermoplastic after nylon. It is a tough, semi-rigid plastic with good fatigue, heat and chemical resistance. Polypropylene is commonly used in injection moulded products with short fibre reinforcement, suitable for automotive and appliance products [7]. Recently, long-fibre and continuous fibre developments have facilitated the use of glass reinforced polypropylene in structural components, most notably in the marine industry where pre-preg mat has been used for the production of small boat hulls [10]. One of the main reasons behind the increased use of polypropylene in marine applications is the fact that it is a recyclable material. Glass reinforced polypropylene was included in this research to compare the material's structural performance in fire with the more traditional marine materials; glass reinforced polyester and vinyl ester.

Table 1.2 Relevant properties of polyester, vinyl ester and polypropylene plastics [1, 7, 11].

Property	Polyester	Vinyl ester	Polypropylene
Density	1.1-1.5 Mgm^{-3}	1.2-1.5 Mgm^{-3}	0.9 Mgm^{-3}
Young's Modulus	2-4.5 GPa	7.8-8.7 GPa	0.3 GPa
Poisson's ratio	0.37-0.39	0.38-0.4	0.3
Tensile yield strength	40-90 MPa	115-124 MPa	25-38 MPa
Thermal conductivity	0.2 $Wm^{-1}°C$	0.2 $Wm^{-1}°C$	0.2 $Wm^{-1}°C$
Melting point	-	-	165 °C

1.2 Fire Standards

Polymer composites' excellent structural and corrosion resistant properties have led to their use in areas where the risk of fire is a major hazard, such as offshore environments and the transport and construction industries. Fire regulations are constantly evolving, but many existing regulations are now considered conservative. It is thought that a more performance based design strategy is required to assess and qualify fire engineering approaches [12-14].

Existing legislation in fire standards covers a broad range of areas and materials, and is produced by a number of international organisations. This large scope of standards and tests often disqualifies the use of composites in many applications, hence there is a need for global regulations [13]. Certain standards organisations are making progress in this area, the European Union enforces railway and construction fire safety standards [15-17], and the International Maritime Organisation have created fire safety guidelines for the United Nations member states [18-20].

These standards describe test procedure and fire protection measures. They also define which test methods are required to qualify a material for a particular application. Current tests involve the use of small scale fire reaction tests along with large scale fire resistance tests in order to fully characterise a material's response.

1.3 Fire Reaction

Fire reaction involves the response of a material to fire, especially in the early stages, and its interaction with the environment [21]. There are many reaction tests which can analyse a wide range of material characteristics including heat release rate, surface spread of flame, time-to-ignition, oxygen index, combustibility and smoke and gas toxicity. The most significant and popular tests are detailed below.

1.3.1 Cone Calorimeter Test (ISO 5660-1)

The cone calorimeter test provides a large amount of useful information from a relatively small sample (100mm x 100mm x sample thickness) [22]. The specimen is subjected to a constant heat flux provided by a conical electrical heating element. An electric spark igniter is used to ignite gases produced at the surface of the sample. The sample is then allowed to burn until the surface flame extinguishes naturally. A small hood above the sample collects combustion products and the concentrations of oxygen, carbon monoxide and carbon dioxide are measured. The cone is capable of providing heat fluxes from 10-100kW/m^2 and can be used in either a vertical or, more commonly, a horizontal configuration. The cone calorimeter is illustrated in Figure 1.4.

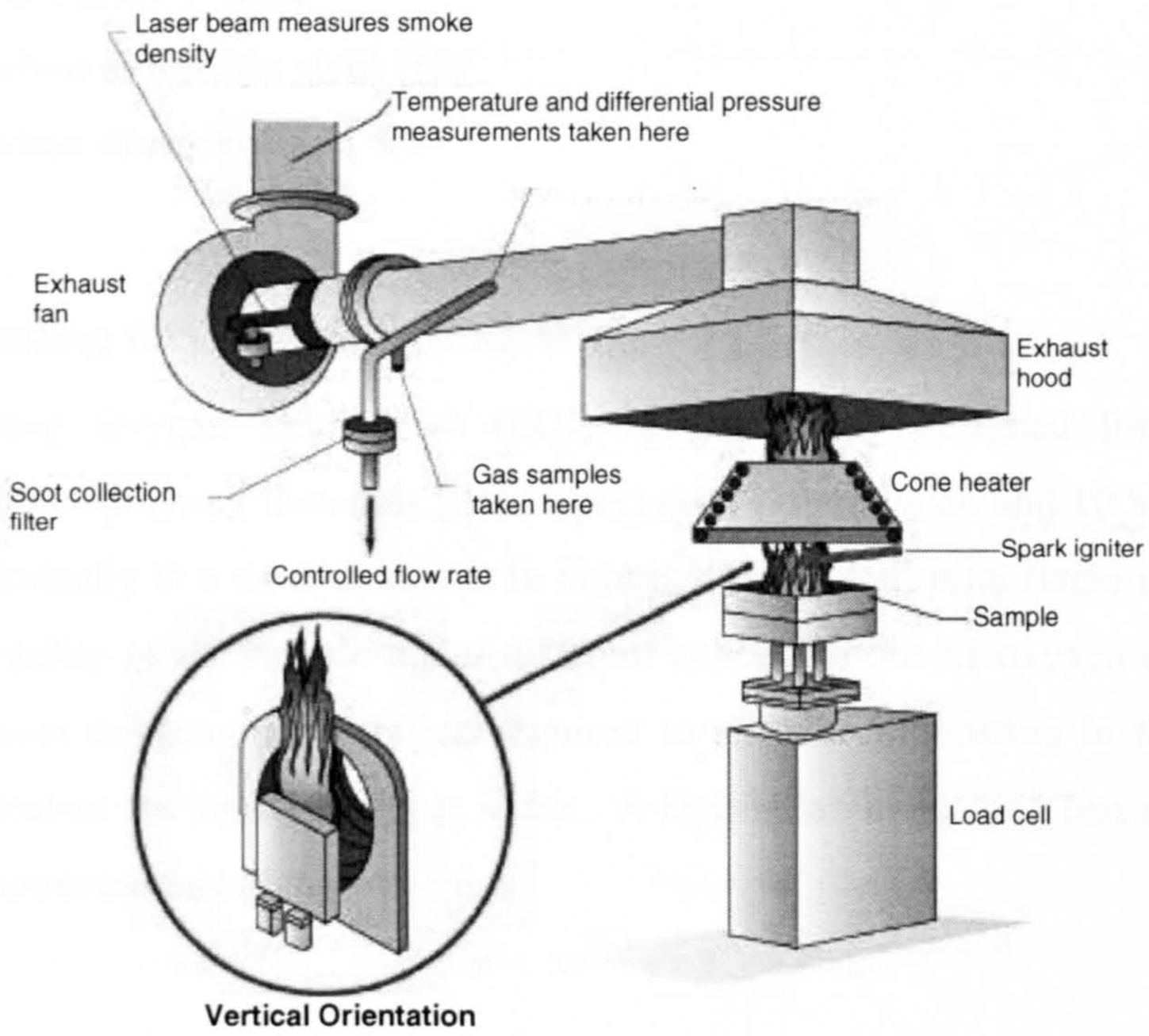

Figure 1.4 Diagram of the cone calorimeter used in the horizontal orientation (Inset: vertical orientation) [23].

The cone calorimeter accurately measures the heat release rate of a burning sample using the oxygen consumption principle [22]. In addition to the peak and average heat release rates (HRR), the apparatus can measure:

- **Time to ignition, TTI (s):** determined visually as the period required for the entire surface of the sample to burn with a sustained luminous flame.
- **Fire performance index (m^2.s/kW):** the ratio of TTI to peak HRR
- **Mass loss (g):** measured using a load cell underneath the sample.
- **Specific extinction area, SEA (m^2/kg):** a measure of smoke obscuration averaged over the entire test period.
- **Smoke parameter (MW/kg):** SEA x Peak HRR. Indicative of the amount of smoke generated in a full-scale fire scenario.
- **Total smoke release**
- **Carbon monoxide yield (%)**
- **Carbon dioxide yield (%)**

1.3.2 Limiting Oxygen Index (ISO 4589)

The Limiting Oxygen Index Test (LOI) is specifically designed for testing the flammability of polymer materials [24]. Specimens (10mm wide and 100mm long) are clamped vertically in a tube, as shown in Figure 1.5. A small pilot flame is used to test the flammability of the sample under different concentrations of oxygen and nitrogen. The minimum oxygen concentration required to sustain combustion in the sample is used to calculate the limiting oxygen index. A high index indicates a less easily ignited and less flammable material.

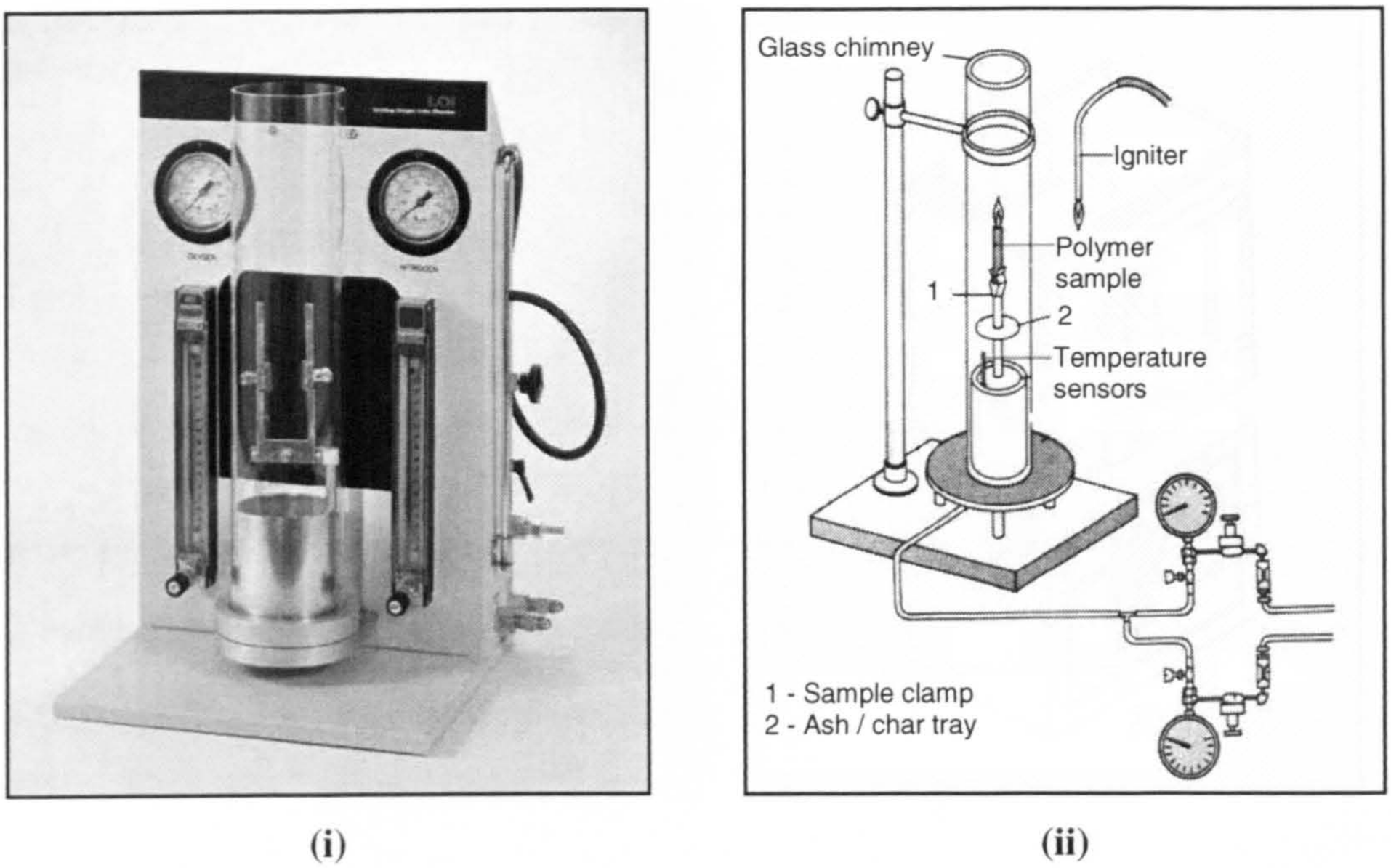

(i) (ii)

Figure 1.5 (i) Photograph [25], and (ii) schematic diagram [26] of the Limiting Oxygen Index test equipment.

1.3.3 NBS Smoke Density Chamber Test (ISO 5659-2)

The National Bureau of Standards (NBS) Smoke Density Chamber, also known as the Smoke Box Test, is one of the most widely used techniques for quantifying smoke generation [27]. Figure 1.6 shows a photograph and schematic diagram of the test. Small scale specimens, 76mm x 76mm and up to 25mm thick, are tested either alight or smouldering, allowing the resulting smoke to accumulate within the test box. The sample is normally held in the vertical orientation and a 25 kW/m^2 heat flux provided by an electrical heater. However the test does allow the option of testing in the horizontal orientation and heat fluxes of 10-50 kW/m^2 are possible. The optical density of the smoke is measured over time using lasers, and the sample mass loss is also monitored throughout the test.

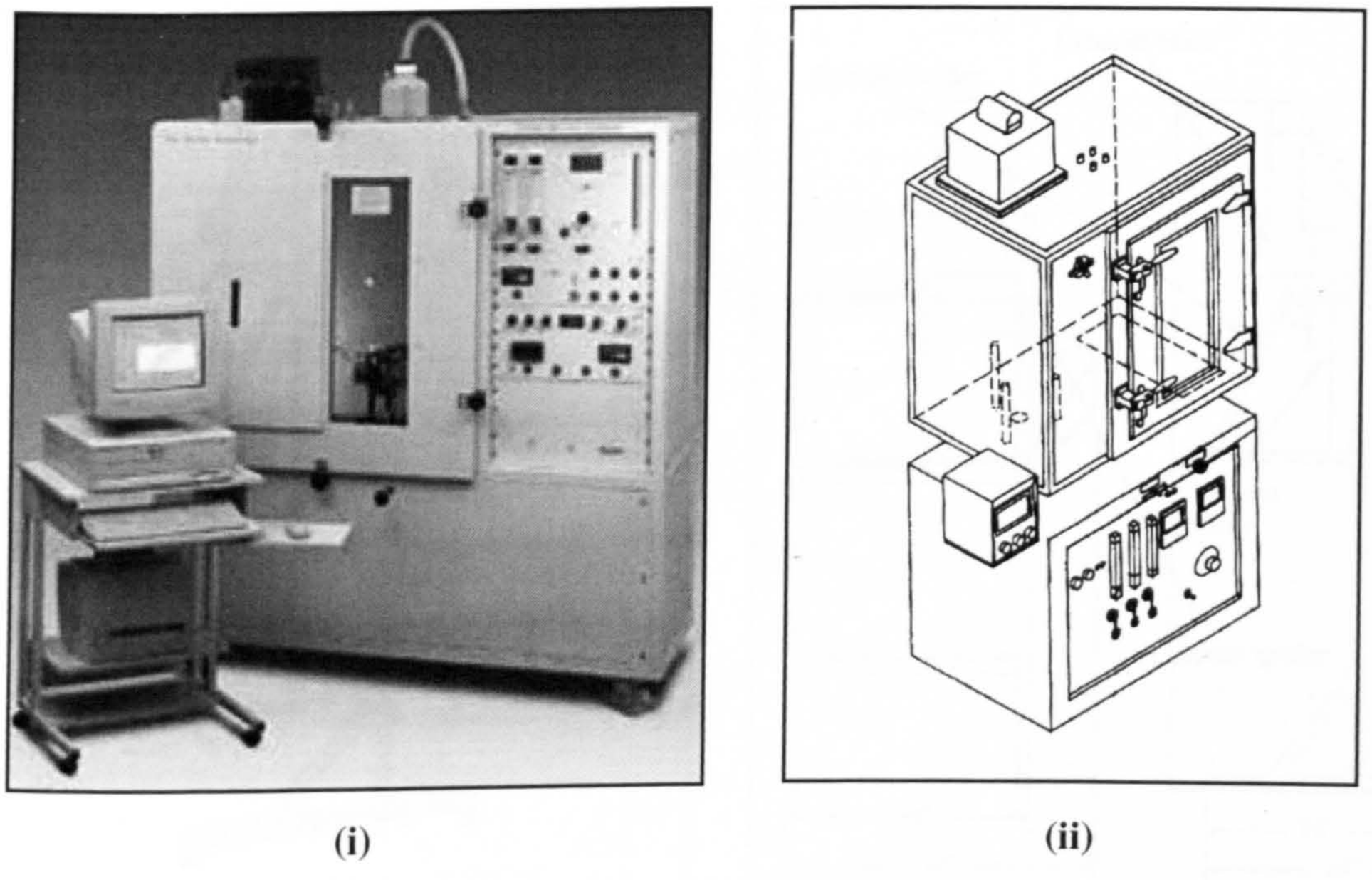

(i) (ii)

Figure 1.6 (i) Photograph [26] and (ii) schematic diagram [28] of the NBS smoke density chamber.

1.3.4 Radiant Panel Test (ASTM E 162)

The radiant panel test is used to qualify the flammability of a material by measuring the surface flame spread and heat evolution [29]. A 6" x 18" specimen, inclined at 45°, is subjected to a heat flux generated by a 12" x 8" gas-fuelled panel heater. A small pilot burner is used to ignite the surface of the sample nearest the heater. The time taken for a flame front to travel down the sample's surface, and the temperature rise in the exhaust stack are monitored during the test. A Flame Spread Index is calculated from this information in order to qualify the test material. Figure 1.7 shows a photograph and schematic diagram of the test equipment.

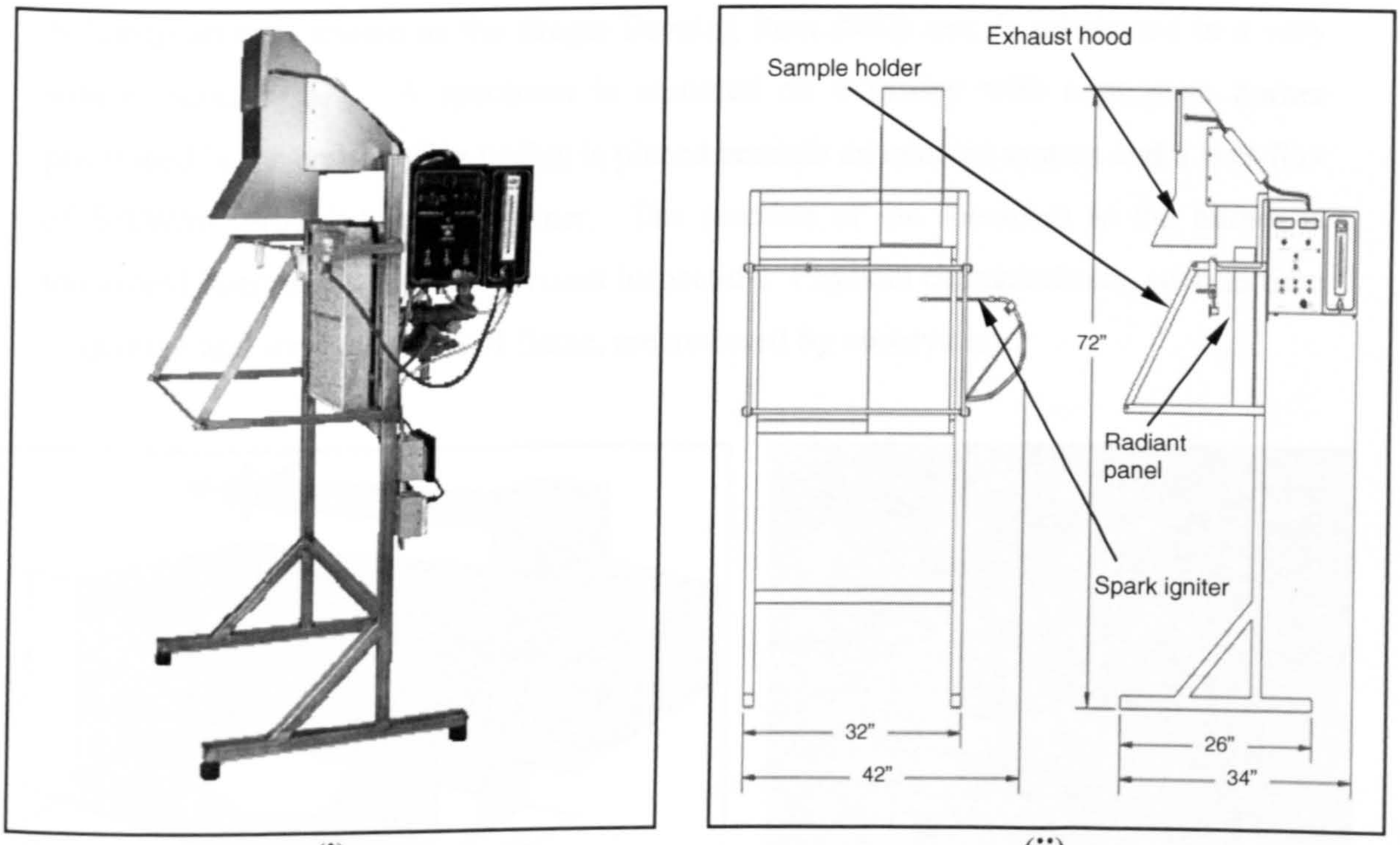

Figure 1.7 (i) Photograph and (ii) schematic diagram of the radiant panel test equipment [30].

1.3.5 Room Calorimeter Test (ISO 9705) / SBI Test (BS EN 13823)

Many fire reaction tests suffer from certain limitations. Due to the small scale nature of some tests, the effect of fire growth cannot be accurately measured. These tests do not represent a realistic fire scenario with respect to ignition, heating and atmospheric conditions. The room calorimeter test, pictured in Figure 1.8, was designed to investigate these effects on a larger scale [31]. The test sample is mounted on three walls and the ceiling of a small room, with a gas burner placed in one of the corners. A doorway, 2.0m high x 0.8m wide is situated at the other end of the room from the burner, and an extraction hood placed above the doorway. The burner provides a heat flux of 100kW/m^2 for the first ten minutes of the test, and is then increased to 300kW/m^2 for another ten minutes. The test is designed to represent one of the major fire hazards in room or office environments; a waste paper bin fire. The HRR is calculated by measuring the volume flow rate and oxygen concentration in the exhaust duct. Smoke production rate is measured by testing the opacity of the smoke using lasers.

A European test, known as the Single Burning Item (SBI) test, is conducted in a very similar manner [32]. A specimen is mounted on a trolley with a propane burner positioned in the corner. The trolley is placed beneath an exhaust system and a heat flux of 50kW/m^2 provided by the burner. The reaction of the specimen to the burner is monitored instrumentally and by visual inspection. Physical characteristics, such as time to ignition and surface spread of flame, are assessed by observation.

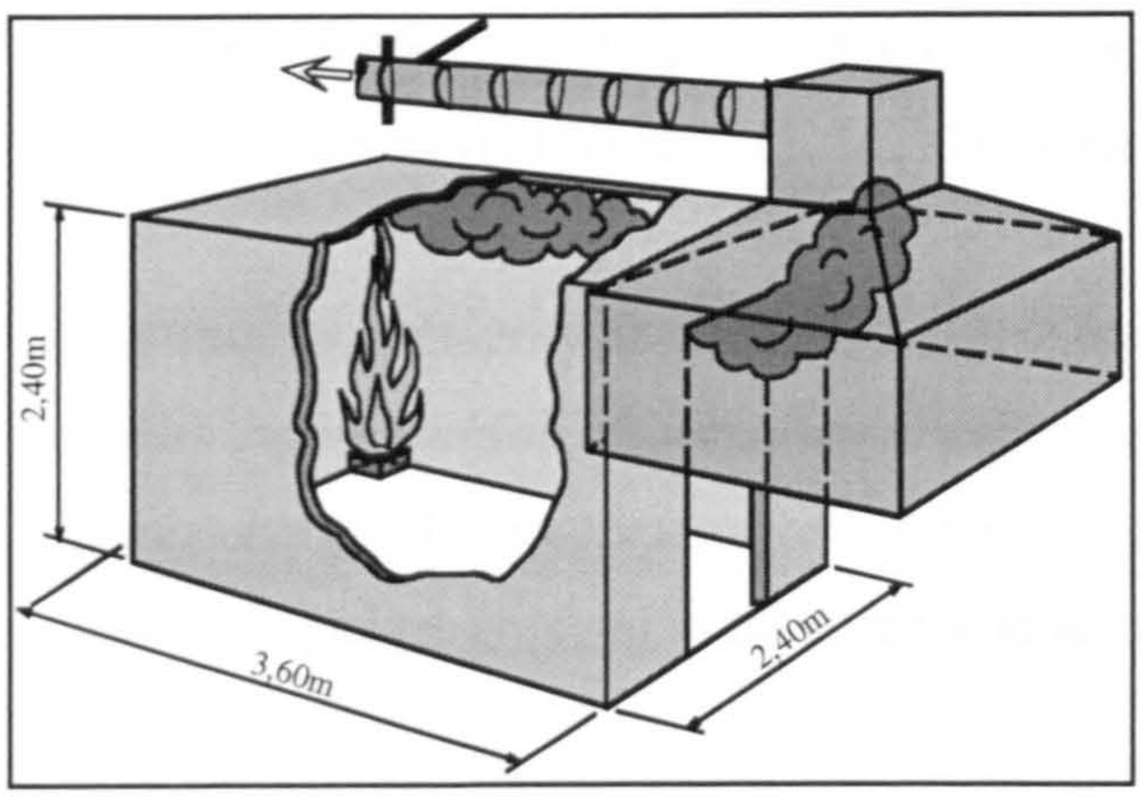

Figure 1.8 (i) The Room Calorimeter Test showing dimensions of the test area [33]. (ii) Photograph of a fully developed fire test [33].

1.4 Fire Resistance

Fire resistance is defined by a material's ability to retain structural integrity and limit heat transmission to other remote objects when exposed to fire [21]. Fire resistance tests are often on a larger scale than fire reaction tests because the test samples are representative of structural items, such as floors, ceilings, beams, columns, doors and walls, rather than individual materials. Tests normally involve the use of a furnace, jet fire or pool fire.

1.4.1 Furnace test

The most commonly used resistance test is the furnace test [34]. A test sample is normally mounted on the open face of the furnace, and thermocouples attached to various points on the rear face of the sample. A sample is deemed to have failed when

the cold face reaches 140°C above ambient temperature, or if a 'hot spot' on the cold face of the sample reaches 180°C above ambient [21]. Samples are normally tested in their end-use condition and, depending on the furnace size, can range from $1m^2$ to $10m^2$ in size.

Standard fire curves, shown in Figure 1.9, are used to represent a fire scenario by increasing temperature within the furnace at a pre-defined rate. The hydrocarbon curve, described in BS 476-20/21, is used to represent the severity of a fuel fire [21, 35], whilst the cellulosic curve, ISO 834 [21, 36, 37], is used to replicate a wood or fabric fire.

The structural integrity of materials can also be measured by placing samples under load whilst exposed to fire. Special large scale furnaces have been designed to subject $3m^2$ composite panels to compressive and bending loads in fire. Displacement transducers and strain gauges are used to monitor the structural response of the panel for the duration of the test.

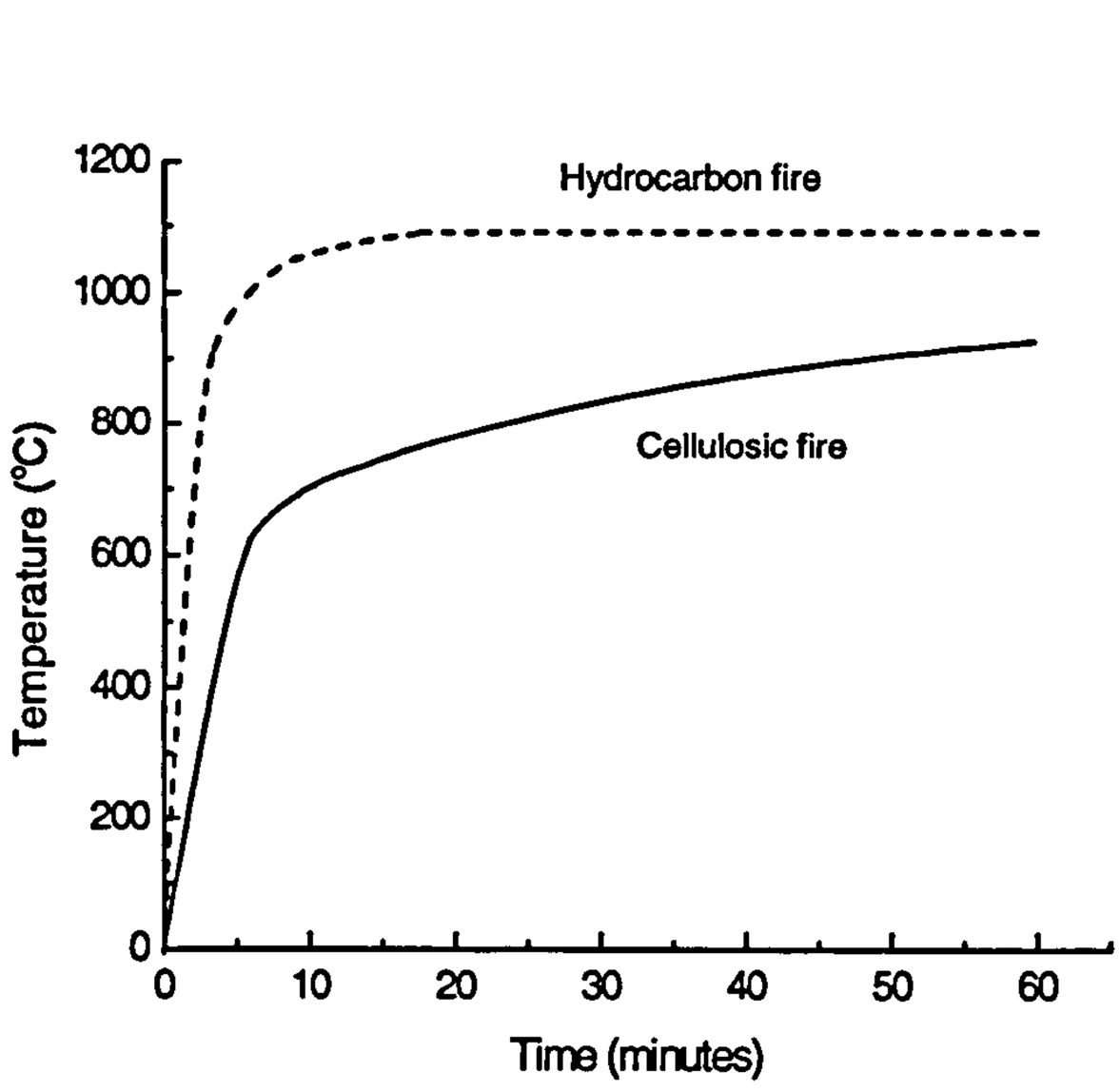

Figure 1.9 The cellulosic and hydrocarbon fire curves used for furnace fire resistance testing.

Furnace tests have been known to suffer problems in reproducibility [38]. Although the test is based on standard fire curves, substantial discrepancies can occur due to variability in the emissivity of furnace liner materials [39]. The control of the furnace temperature profile can also be difficult, especially in the case of samples which burn generating heat release.

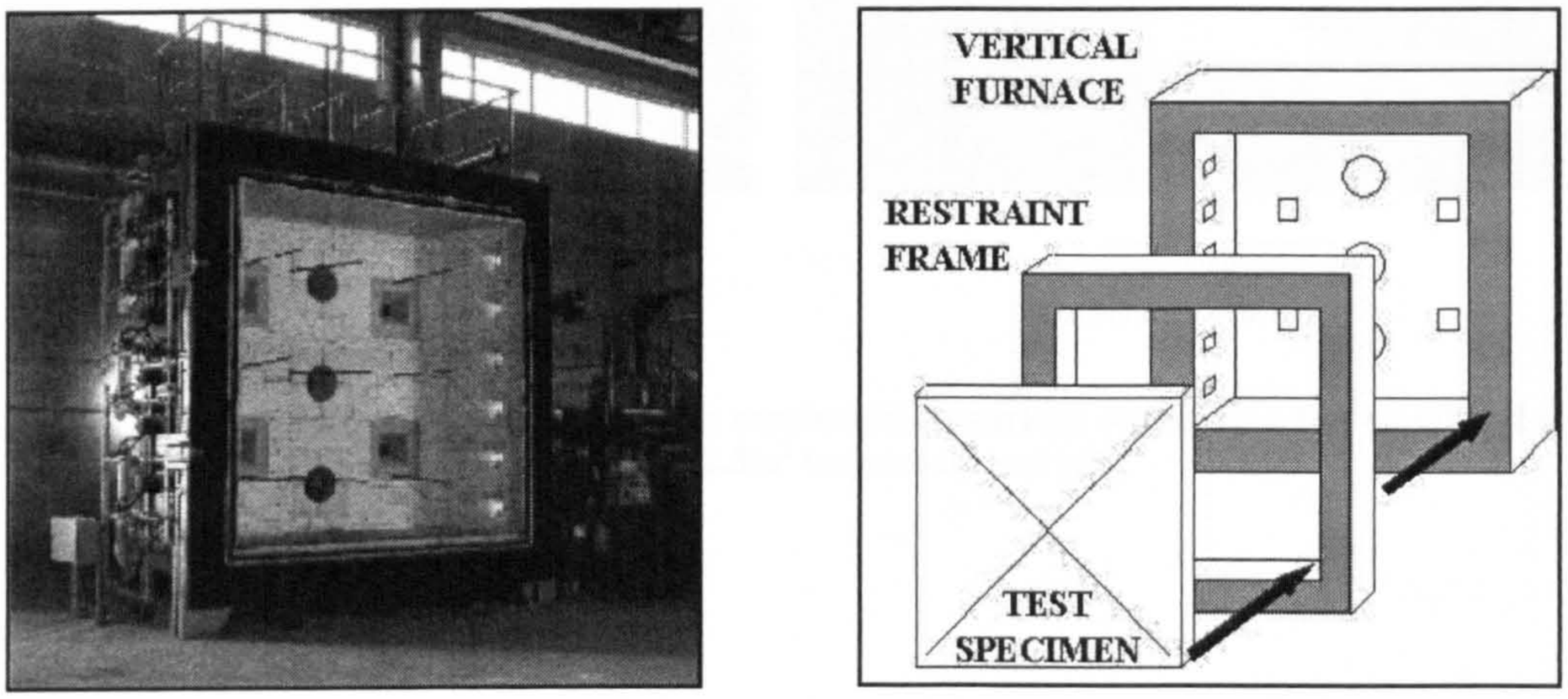

Figure 1.10 (i) Photograph of a vertical furnace test facility, and (ii) diagram of the specimen orientation [40].

1.4.2 Pool fire test

A pool fire is defined as the natural combustion of a horizontal fuel surface. Such a fire may occur as a result of the accidental ignition of spilled liquids or open tanks. Pool fires have both fundamental and practical interest because they are one of the most basic forms of fuel combustion often present in accidental fires. The unpredictable nature of a pool fire means that when testing, it is difficult to maintain a steady heat flow from the fire. For this reason, pool fires tend to be used as indicative tests [41].

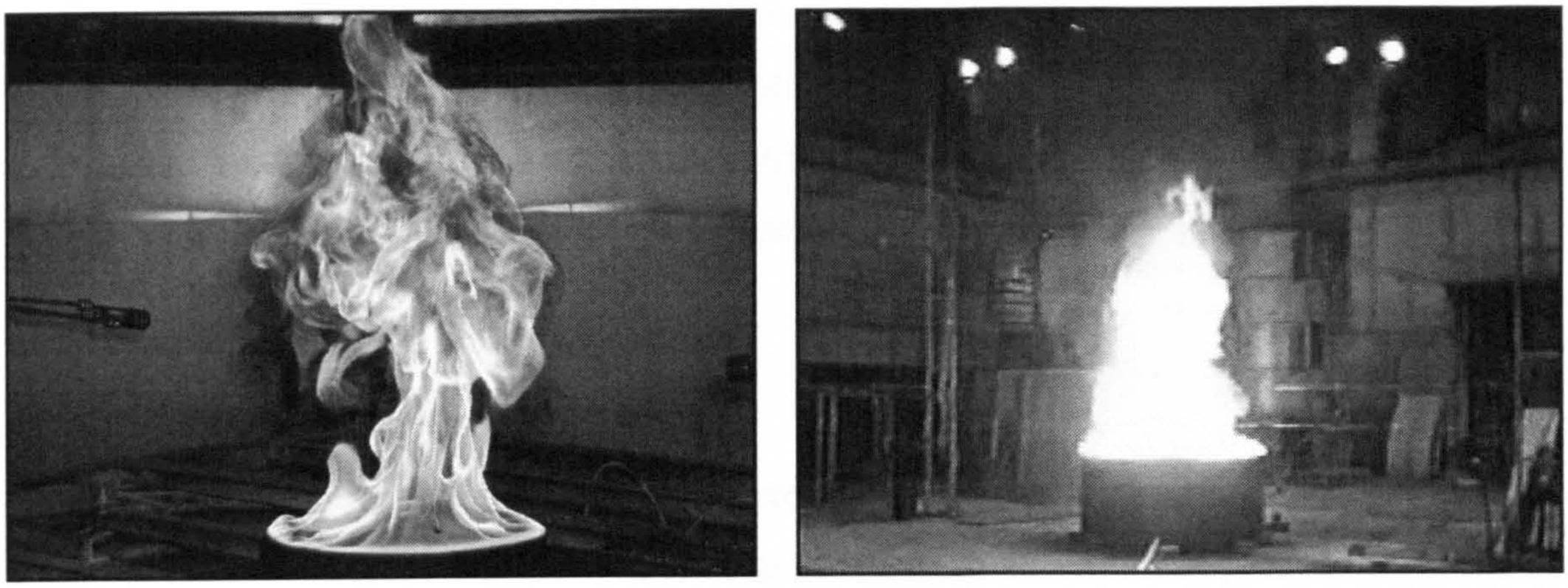

(i) (ii)

Figure 1.11 The pool fire test. The test can be conducted on various scales; (i) a $1m^2$ small scale test [41], and (ii) a $12.5m^2$ large scale test [42].

1.4.3 Jet Fire Test

Jet fire tests are mainly used to simulate accidents which may occur in environments where fuel is kept under pressure, for example a gas line rupture on an offshore rig. The combined effects of very high temperatures and the erosion caused by a high velocity jet are more damaging than a simple pool fire, and may have critical consequences to the ability of a structure to retain load. A large scale jet fire test is shown in Figure 1.12.

Figure 1.12 Large scale jet fire test at RAF Spadeadam test site, Northumberland. Liquid hydrocarbons and oils can be released under pressure to form jet fires either alone or mixed with other gases [43].

The jet fire test offers a more realistic fire scenario than the hydrocarbon furnace for structures at risk of jet fire impingement. Most tests measure the resistance of a material by either burn-through time or the loss of structural integrity. The procedure is designed as a complimentary test to furnace testing, and not as a replacement [44-47].

1.5 Objectives

The principal objectives of this research were:

- The development of a low cost, reproducible small scale test procedure for fire resistance testing of composite laminates.
- Characterisation of the variation in material properties with temperature for three laminate materials; glass reinforced polyester, glass reinforced vinyl ester and glass reinforced polypropylene.
- The design of a laminate model to predict the structural integrity of composite laminates in fire.
- Validation of the laminate model by testing small scale test samples under load in fire.

Chapter 2 Literature Review

2.1 Composite Fire Characteristics

A major disadvantage of many composite materials is fire performance. When thermosets are exposed to fire, the organic matrix decomposes at temperatures around 300°C releasing heat, smoke and toxic volatiles. Moderate temperatures, over 100°C, will cause composites to soften, creep and distort, resulting in the buckling and failure of load-bearing structures [48]. These effects are often the main reasons for industries, such as infrastructure and public transportation, to refrain from using composites.

Although polymer composite materials are inherently combustible, it has been shown that under certain circumstances such materials possess relatively good resistance to fire [12]. This is due to the slow burn-through properties of these materials.

Four main factors which contribute to the slow burn-through effect include [49]:

- The low thermal conductivity and diffusivity of composites.
- The low thermal conductivity of the residual glass, depleted of resin, which remains on the surface of the material in fire.
- The endothermic process of resin decomposition and vaporisation.
- The cooling effect created by the convection of volatile gases diffusing through the material towards the hot face.

The most significant factor in relation to the fire integrity of polymer composites is the endothermic process of resin decomposition [49]. Most polymer decomposition processes are endothermic, irrespective of whether the polymer is a thermoset or thermoplastic. Although the thermal conductivity of crystalline thermoplastics may significantly decrease as the material melts, this has little influence on the slow burn through effect when compared to the endothermic decomposition process.

2.2 Thermal Modelling

The use of GRP laminates in hazardous environments and applications has highlighted a need for models to predict their resistance to high temperatures and fire. Accurate thermal models are an essential tool in the design process of composite structures, reducing the need for expensive fire testing and assisting in the development of new materials. The development of mathematical thermal models for composite materials has been largely based on work on the fire behaviour of wood [50-54]. These thermal models consider the processes of heat conduction, endothermic decomposition reactions of wood, convection flow of volatile gases, and the combustion of volatiles at the surface. More recently, mathematical models for composites [49, 55-70] have successfully described one, two and three dimensional heat transfer processes and reactions with respect to all four of these factors.

2.2.1 Heat Conduction Modelling

The most basic thermal model considers the effect of heat conduction, ignoring external convection and material radiation, under the condition of one-sided heating, as shown in Figure 2.1 [71]. The one dimensional model is expressed as:

$$\rho C_p \frac{\partial T}{\partial t} = \frac{\partial}{\partial x}\left[k_x \frac{\partial T}{\partial x}\right] \tag{2.1}$$

where: T is temperature (K),

t is time (s),

x is the distance below the hot surface in the through-thickness direction (m),

ρ is the density of the composite (kg/m^3),

C_p is the specific heat of the composite (J/kg.K),

k_x is the thermal conductivity of the composite in the through-thickness direction (W/m.K).

The left hand side of the equation corresponds to the change in thermal energy per unit volume, and the right hand side is the energy flux due to conduction. The model assumes that the thermal conductivity, specific heat and density of the composite are not affected by temperature.

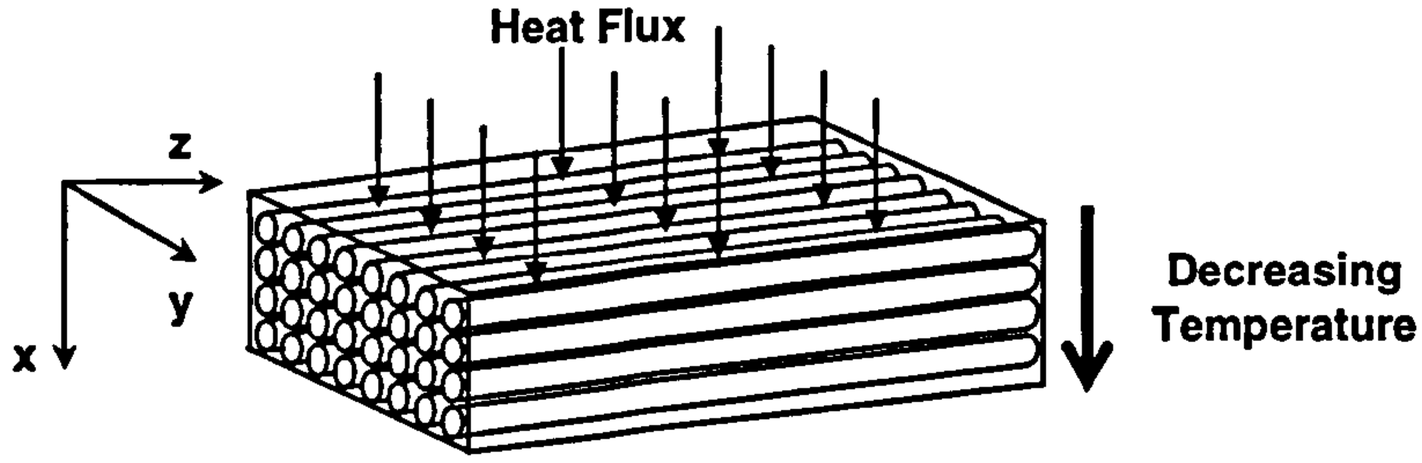

Figure 2.1 One dimensional heat conduction through a composite plate exposed to a one sided, uniformly distributed heat flux [72].

One-dimensional heat conduction analysis has formed the basis for many other more complicated models. Two and three dimensional models have been designed to analyse the effects of a uniformly distributed heat flux [73-75] and localised heating on composite materials [76]. The 1-D heat conduction model was expanded for orthotropic laminates by Asaro et al. [73], Charles and Wilson [74], and Milke and Vizzini [75] to give a three dimensional model:

$$\rho C_p \frac{\partial T}{\partial t} = \frac{\partial}{\partial x}\left[k_x(T)\frac{\partial T}{\partial x}\right] + \frac{\partial}{\partial y}\left[k_y(T)\frac{\partial T}{\partial y}\right] + \frac{\partial}{\partial z}\left[k_z(T)\frac{\partial T}{\partial z}\right] \qquad (2.2)$$

where: x is the through thickness direction and y and z are the planar directions,
$k_x(T)$, $k_y(T)$ and $k_z(T)$ are the thermal conductivities in the x, y and z directions.

Again, the model assumes that the thermal conductivity, specific heat and density of the material do not vary with temperature. The 3-D model has made very accurate predictions of the thermal response of laminates exposed to low levels of heat flux (10-20 kW/m^2). Figure 2.2 shows theoretical and measured temperature profiles for the case

of a glass/vinyl ester laminate which was exposed to a low heat flux for over an hour [73]. In this case, the heat flux level was too low for resin decomposition to initiate and hence heat conduction was the main thermal process.

Although the theoretical curves appear to have three or four stages, this was unlikely to be the case in practice. If the process was purely conductive, there should not be separable stages. The incident heat flux used here was so low that, after one hour, temperatures at the front face were only around 100°C. At these temperatures, resin decomposition would not have initiated and it is unlikely that flashover would have occurred until the front face reached temperatures of around 250 - 300°C. The variations in the theoretical curve may therefore have arisen due to inaccuracies in the computational procedure adopted for modelling.

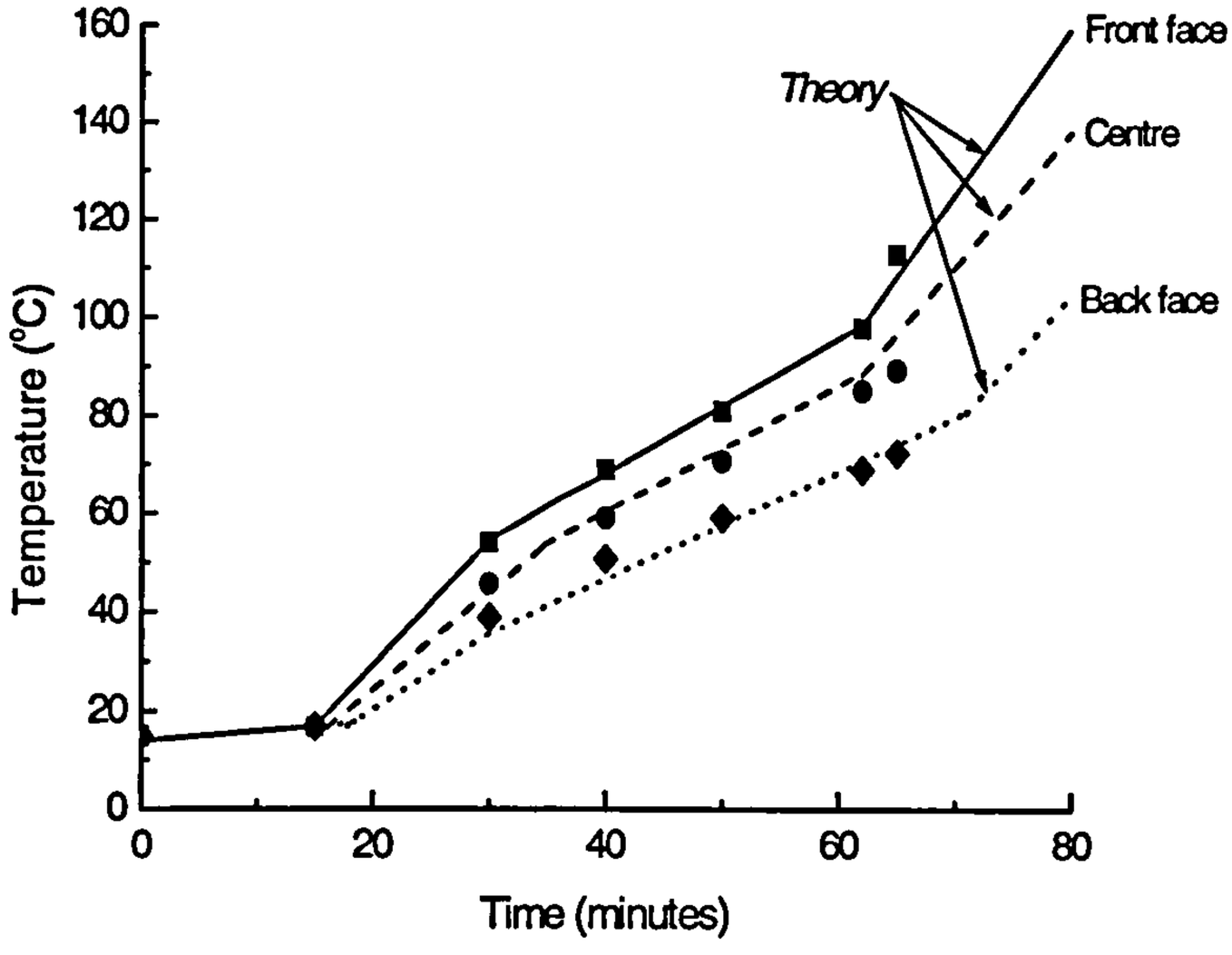

Figure 2.2 Temperature profiles for a glass/vinyl ester laminate exposed to a low level heat flux [73]. Theoretical curves were constructed using a 3-D heat conduction model (Equation 2.2).

2.2.2 Thermal Decomposition Modelling

An accurate thermal model will not only consider heat conduction through the laminate, but also the resin decomposition process and the convective flow of reaction volatiles. The first thermal model to include the effects of resin decomposition was developed by Pering, Farrell and Springer [65]. The model is based on the 1-D heat transfer equation but also includes a term for the heat of pyrolysis, which is determined experimentally from the material's mass loss rate:

$$\rho C_p \frac{\partial T}{\partial t} = \frac{\partial}{\partial x}\left[k_x(T)\frac{\partial T}{\partial x}\right] + \frac{\partial m}{\partial t} Q \qquad (2.3)$$

where: $\frac{\partial m}{\partial t}$ is the mass rate of vapour generated per unit volume (kg/s),

Q is the heat of pyrolysis (J).

Pering et al. had some success with the estimation of the mass loss of composites in fire. Figure 2.3 shows the results for a carbon/epoxy laminate exposed to a gas flame with a temperature of around 540°C.

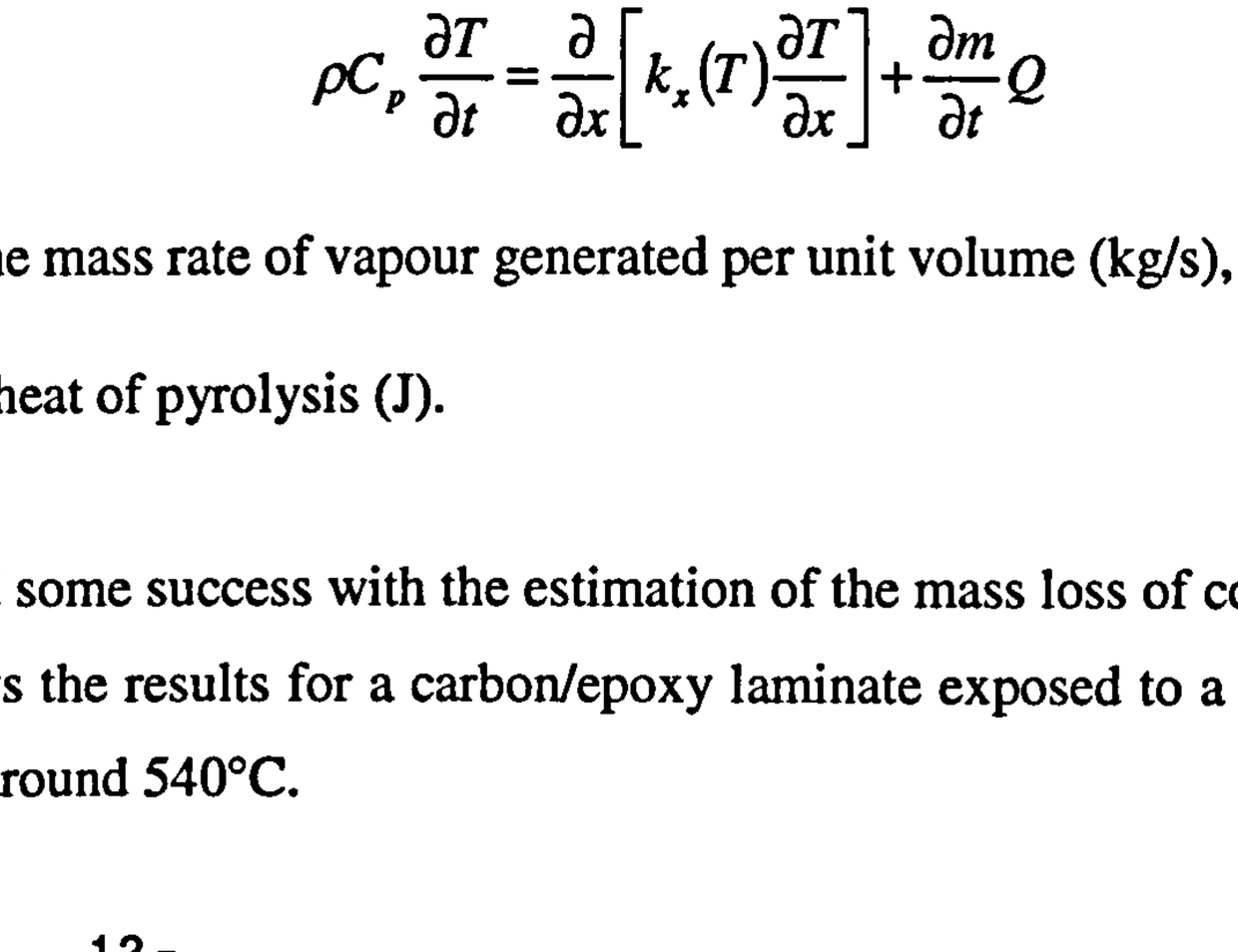

Figure 2.3 Normalised matrix mass loss results for a carbon/epoxy laminate exposed to a 540°C flame [65]. The theoretical curve was calculated using Equation 2.3.

The data points are normalised mass loss values. They were calculated by dividing the measured mass loss of the polymer matrix by the original mass of the matrix. The theoretical mass loss curve, calculated using Equation 2.3, shows excellent agreement with the experimental results. However, the presented data must be analysed with care.

The normalised data points displayed occasionally exceed the maximum value of 1. This would indicate that a number of tests were conducted on samples of various mass. It is possible that many of the samples did not fully decompose because of the presence of carbon fibres. The samples should have been exposed for several hours before full decomposition of the matrix could be assumed.

Equally, the normalised mass loss results would have been calculated using a theoretical fibre volume fraction value. The actual fibre volume fraction of each sample may have varied significantly from this theoretical value. This would introduce an error sufficient enough to distort the calculated mass loss value.

By defining full decomposition from a scatter of experimental points, the researchers then effectively made a "best fit" for the model curve. If the normalised full decomposition points were calculated exactly, the theoretical curve may not have provided such an accurate fit in the early stages of the test.

2.2.3 The Henderson Model

The Henderson model [55, 59] is an extension to the one dimensional model which not only considers heat conduction but also the effects of pyrolysis and decomposition gases. The model was based on work which was conducted by Kung [52] and Kansa et al. [51] into the decomposition and fire response of wood. The one dimensional governing equation is applicable to GRP laminates and is expressed as:

$$\rho C_p \frac{\partial T}{\partial t} = k \frac{\partial^2 T}{\partial x^2} + \frac{\partial k}{\partial x}\frac{\partial T}{\partial x} - \dot{M}_G C_{pG} \frac{\partial T}{\partial k} - \frac{\partial \rho}{\partial t}(Q + h_C - h_G) \qquad (2.4)$$

where: ρ, C_p and k are the density (kg/m^3), the specific heat (J/kgK) and the thermal conductivity (W/mK) of the material in the through thickness direction (x),

T is temperature (K),

t is time (s),

$\dot{M}_G$ and C_{pG} are the mass flux (kg/m^{2}s) and the specific heat (J/kgK) of the volatile gas respectively,

Q, h_C and h_G are the heat of decomposition (J/kg), enthalpy of the solid phase (J/kg), and enthalpy of the volatile gas (J/kg), respectively.

1-D heat transfer theory is used to model the process of heat conduction, represented by the first two terms on the equation's right hand side. In contrast to Equations 2.2 and 2.3, the Henderson equation considers the change in thermal conductivity of the laminate with increasing temperature. The third term considers the effect of decomposition reaction gases diffusing through the laminate thickness. This process provides a cooling effect, hence the term being negative, and is modelled using convective mass transfer theory. Finally, the rate of heat generation or consumption is modelled by the fourth term on the right hand side.

The subscript i refers to either resin decomposition or carbon-silica reactions, both of which are considered by the model [55]. Decomposition reaction rates are calculated from the mass loss rate of the material. Thermo-gravimetric analysis is used to determine the mass loss rate under controlled heating conditions, and the relevant material parameters may be evaluated using the Arrhenius rate equation:

$$\frac{\partial m}{\partial t} = -A_i m_o \left[\frac{m - m_f}{m_o}\right]^{ni} \cdot \exp\left(E_i / RT\right) \qquad (2.5)$$

where: m, m_o and m_f are the mass, the initial mass and the final mass (kg),

A_i is the pre-exponential rate factor (s^{-1}),

n_i is the order of the reaction,

E_i is the activation energy (J/mol),

R is the universal gas constant (8.314 J/mol.K)

T is the temperature (K).

The Henderson model was validated by comparing theoretical temperatures values against measured temperature profiles for a 3mm thick glass/phenolic laminate exposed to a 279.9 kW/m^2 heat flux, as shown in Figure 2.4. A high level of heat flux was selected to create sufficiently high temperatures for resin decomposition and glass/char reactions. Temperature values were monitored at various depths through the laminate thickness throughout the test, and good agreement was observed between these and the theoretical profiles.

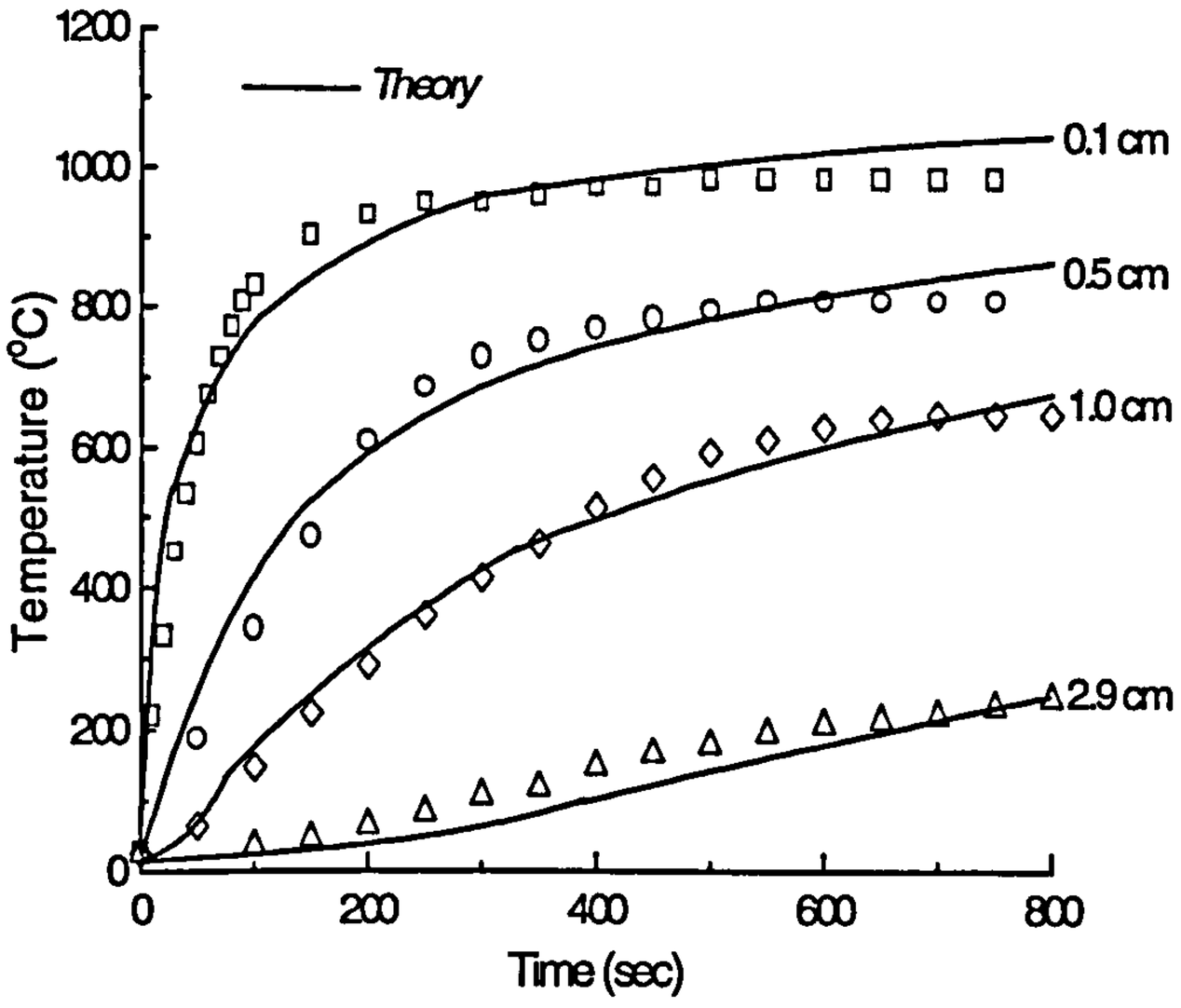

Figure 2.4 Comparison of experimental and theoretical temperature profiles for a 3mm thick glass/phenolic laminate exposed to a 279.9kW/m^2 heat flux [55]. Theoretical values were calculated using Equation 2.4.

More recently, the Henderson equation has been adapted by Gibson et al. [49] and Dodds [70] to predict the fire performance of glass reinforced plastic laminates at lower levels of heat flux (25-100kW/m^2).

$$\rho C_p \frac{\partial T}{\partial t} = \frac{\partial}{\partial x}\left(k\frac{\partial T}{\partial x}\right) - \dot{M}_G \frac{\partial}{\partial x} h_G - \rho A\left[\frac{m-m_f}{m_o}\right]^n e^{\frac{-E}{RT}}\left(Q + h_C - h_G\right) \qquad (2.6)$$

Heat conduction | Mass flow of volatile products | Endothermic reaction of resin decomposition

Equation 2.6 shows the adapted model, which has been simplified in a number of ways. The thermal conductivity and specific heat properties are assumed to remain constant with the increase in temperature, and thermal and gas transport properties are assumed to be constant during the decomposition process. The carbon-silica reactions are not described by the updated model. The model predicts lower levels of heat flux and these reactions would therefore not occur. The Arrhenius rate equation, shown in Equation 2.5, is still used to model the decomposition reaction.

The three main processes involved in energy transfer are highlighted in Equation 2.6; heat conduction through the material, the convective mass flow of volatile products and the endothermic reaction of resin decomposition. The model can be used to predict temperature and residual resin content evolution with time using finite difference techniques, but can also be solved using finite element analysis [48, 77]. Accurate predictions, such as those shown in Figure 2.5, have been made for many types of glass reinforced thermoset laminates [48, 49, 70, 77], but successful modelling of thermoplastic composites, although possible, has not yet been fully demonstrated.

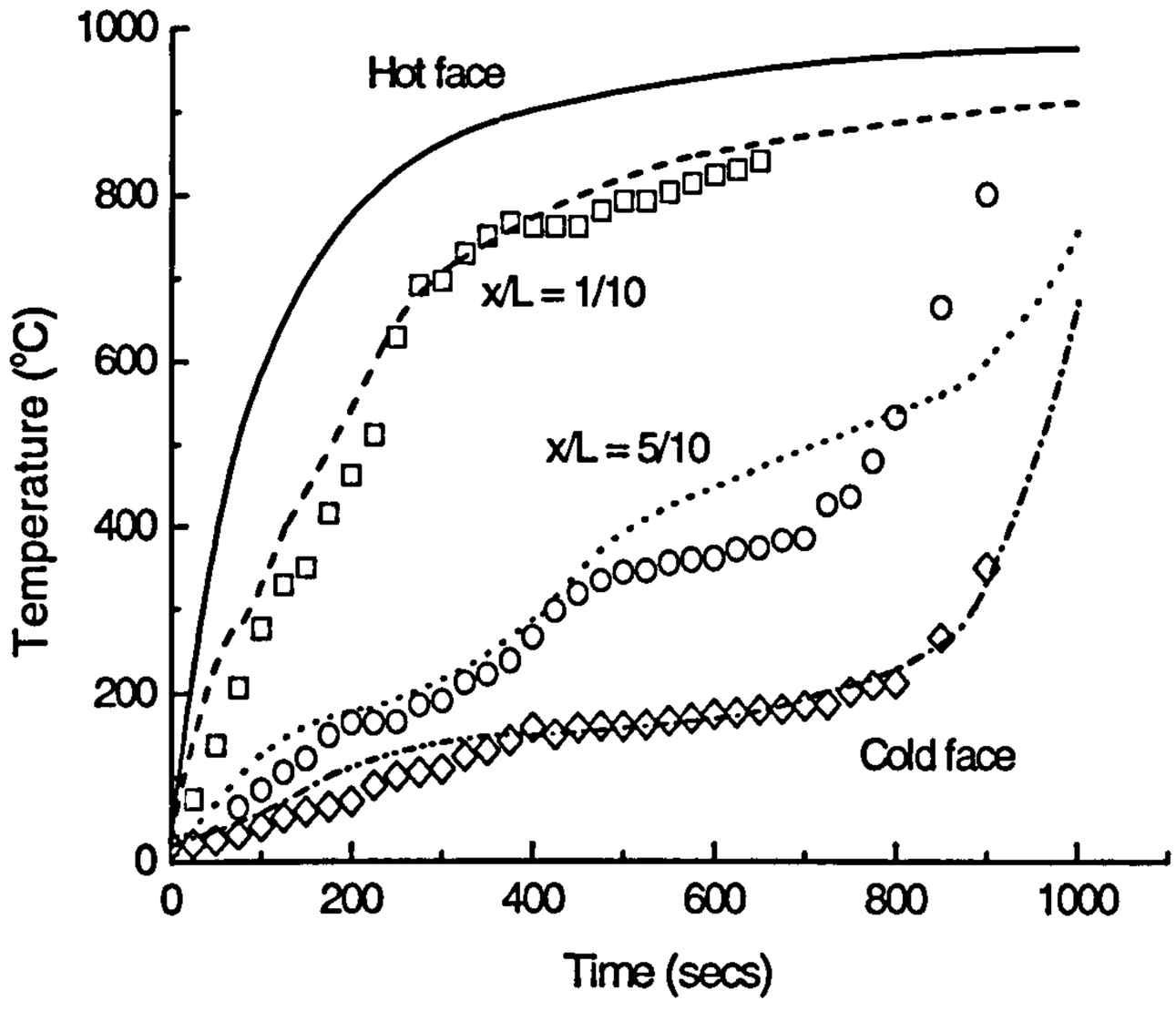

Figure 2.5 Measured and predicted temperature profiles for a 10.9mm thick glass/polyester laminate exposed to a one-sided hydrocarbon fire [72]. The term *x/L* represents the distance below the hot surface (*x*) divided by the specimen thickness (*L*). The temperatures were determined at the hot face, a distance 1/10th through the composite, half-way (*x/L* = 5/10), and at the cold face.

2.3 Fire Response of Composites under Load

In recent years a number of mechanical models have been developed to characterise the response of composites in fire under load [78-88]. The models are based on a variety of analysis methods including, the rule of mixtures [80-82, 86], finite element techniques [79, 88], laminate analysis [83] and creep based analysis [84].

2.3.1 The Two Layer Model

A two layer model has been developed to calculate the mechanical properties of a composite material after it has been exposed to a one sided heat flux [80-82, 85, 86]. The model assumes that the damaged laminate consists of two distinct layers; a damaged (char) region and an undamaged (virgin) region. The char region is assumed to have negligible mechanical properties in comparison to the virgin material, whilst the undamaged material has properties equal to those of the original material at room temperature.

The model can be used to estimate the tensile properties of the laminate after fire exposure. The tensile strength of the virgin layer is assumed to be constant and has the value of the material at room temperature. In reality this is not the case; the strength of the undamaged region will be lowest at the char/virgin boundary and will increase towards the rear face of the sample. The strength of the char region is also assumed to be constant. Figure 2.6 shows a schematic diagram of the assumed state of a laminate exposed to fire.

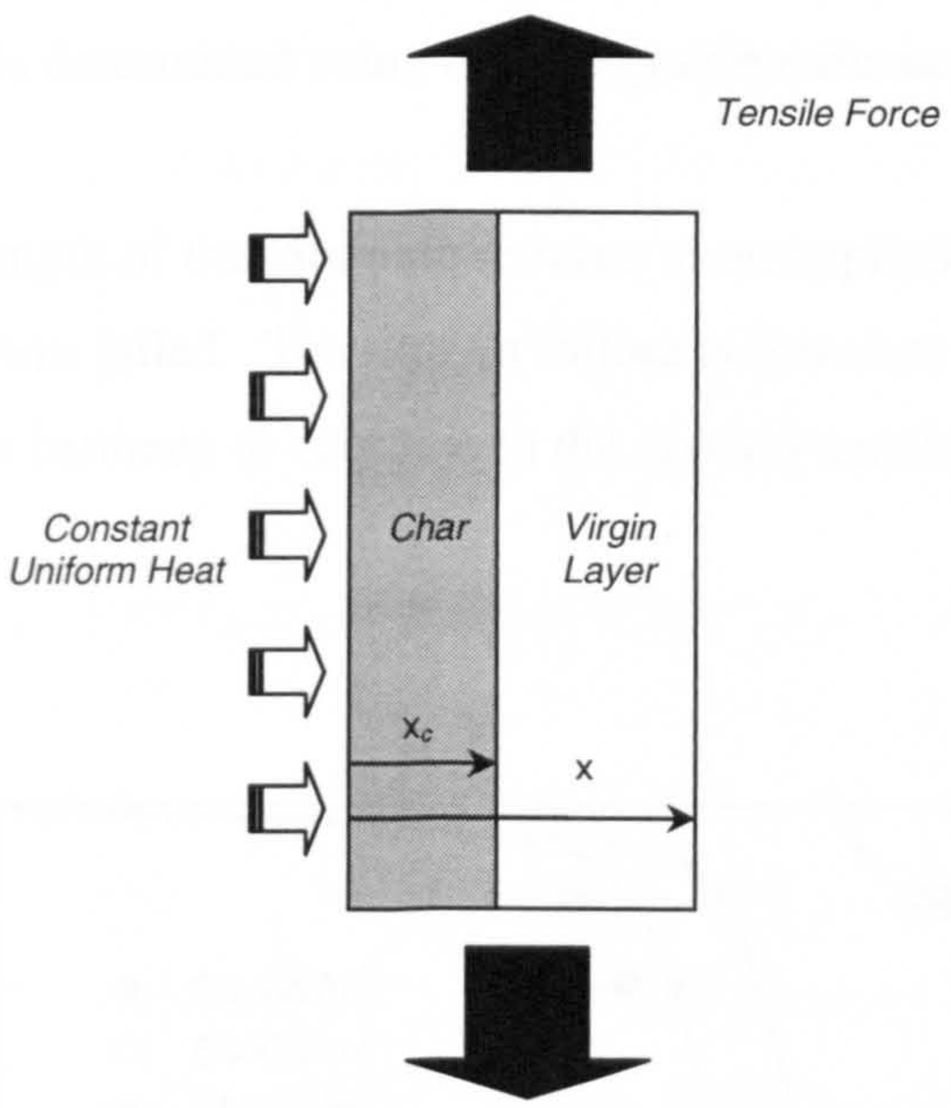

Figure 2.6 Schematic diagram of a laminate under one-sided heating and tensile loading. The laminate is represented in the two layer case. x is the thickness of the original material and x_c is the depth of char [72].

Simple mechanics expressions have been used with this approach to provide successful estimations of the residual properties of composites after fire. Residual tensile strength (σ_T) is calculated using Equation 2.7:

$$\sigma_T = \left(\frac{x_o - x_c}{x_o}\right) \cdot \sigma_{T(o)} + \left(\frac{x_c}{x_o}\right) \cdot \sigma_{T(c)} \qquad \textbf{(2.7)}$$

where: $\sigma_{T(o)}$ is the original tensile strength of the material at room temperature (MPa),

$\sigma_{T(c)}$ is the tensile strength of the char layer which, based on experimental data , is assumed to be negligible in this case,

x_o is the total thickness of the laminate (m),

x_c is the thickness of char (m).

The char thickness (x_c) is a depth in the through thickness direction at which point the temperature is still high enough for the polymer matrix to decompose to char. x_c is calculated using Equation 2.6 and the temperature at which the matrix begins to char. The char temperature is determined using thermo-gravimetric analysis.

When the residual strength of the laminate reduces to an applied tensile stress value, the sample is deemed to have failed. The time to failure is therefore the time it takes for the residual strength of the laminate to decrease to the applied tensile stress value.

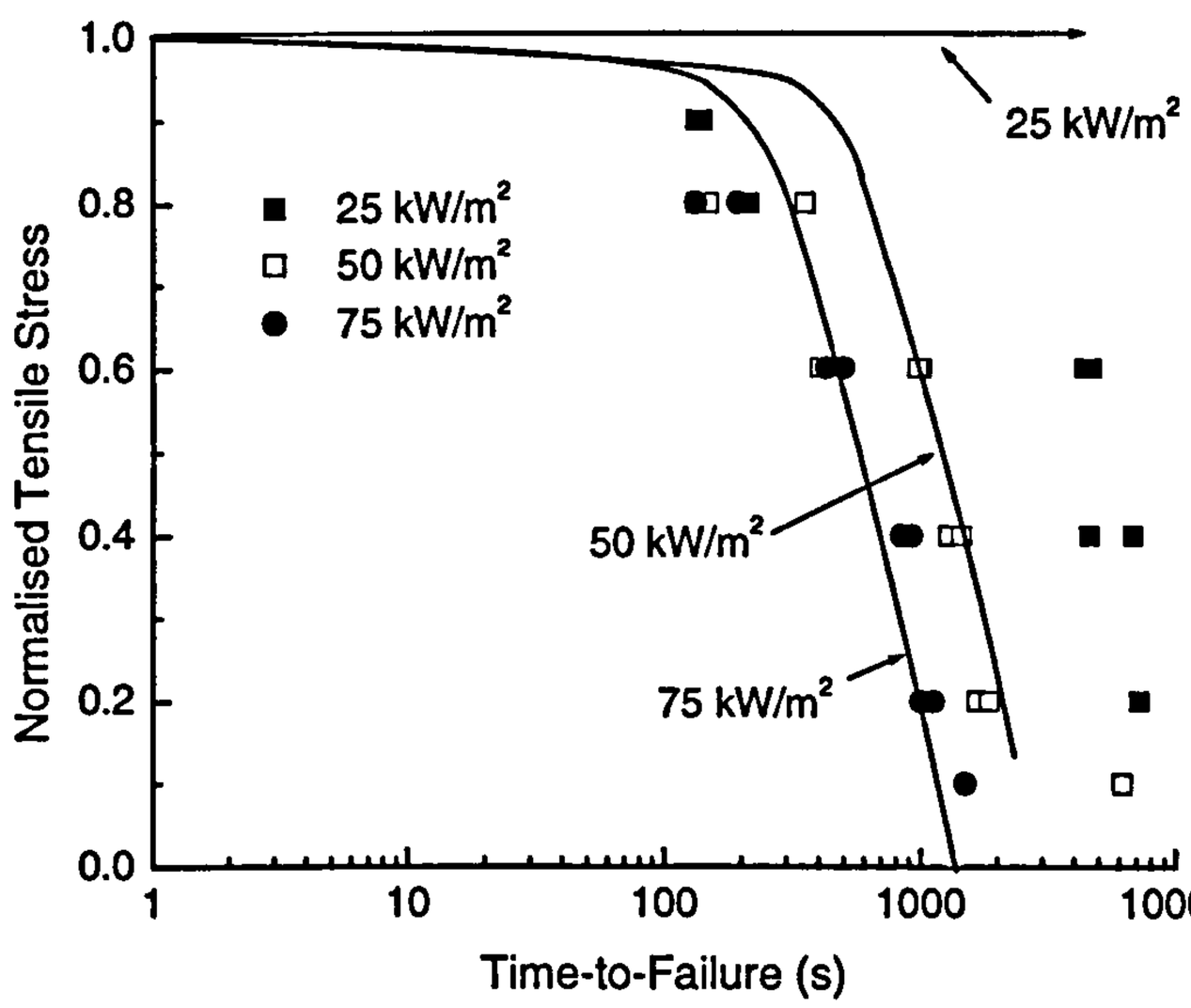

Figure 2.7 Calculated and measured times to failure for a woven glass/vinyl ester laminate under tensile loading at heat fluxes of 25, 50 and 75 kW/m^2 [72]. The theoretical curves were calculated using the two layer model.

Figure 2.7 shows calculated and measured failure times for a glass/vinyl ester laminate exposed to various heat fluxes. The theoretical curves, constructed using the two layer model, show very good correlation to the failure times for heat fluxes of 50 and 75kW/m^2. However, the 25kW/m^2 prediction shows the laminate retaining its original strength for almost 3 hours whilst there is a clear reduction in the measured strength values. This is because the temperature at which the polymer matrix decomposes to char is at around 440°C. At 25kW/m^2 the laminate does not reach this temperature and hence, according to the two layer model, no char is formed and therefore there is no reduction in strength. The measured times to failure for the 25kW/m^2 case were attributed to creep induced rupture of the hot fibres [72]. The two layer model does not consider fibre creep and therefore cannot be used in cases where long term creep effects are important.

2.4 Test Methods

Currently, most fire resistance tests are conducted on a large scale with the sample in its end use condition. These large scale tests are normally very expensive and it is often difficult to control the heating conditions. A number of small scale resistance tests have been proposed recently that are equivalent to stress rupture tests [65, 78, 80-82, 84-86, 89, 90]. Stress rupture tests involve the testing of a sample under certain loading conditions until failure. In the case of a fire stress rupture test, a sample would be loaded whilst exposed to fire and the time-to-failure recorded. Small scale resistance tests, used in conjunction with failure models, would be a useful tool in product design stages, giving early indications of failure modes and time-to-failure. In recent years, gas burners [85, 86, 89] and electrical radiant heaters [80-82, 84-86, 90], similar to those used on a cone calorimeter, have been used for this purpose.

Chapter 3 The Small Scale Propane Burner Test

There is a need for low cost, small scale test procedures for fire resistance testing of composite materials. Fire reaction tests, such as the cone calorimeter, normally involve the use of small samples, approximately 100mm x 100mm. In contrast, fire resistance tests are much larger and hence more expensive. Ideally, a small scale resistance test supported by modelling techniques could be used to characterise the fire behaviour of composite systems at initial design and material development stages. This chapter will describe the work which has been conducted on the calibration and validation of a technique based on a simple burner.

3.1 The Propane Burner Test

A propane burner was used to produce a constant heat flux for resistance testing of composite laminates. Small scale samples, of similar size to those used in a cone calorimeter test, were held vertically in a steel picture frame as shown in Figure 3.1. The frame allowed a 100mm x 100mm square region to be exposed to the propane flame. The edges of the sample were insulated from the frame by a 5mm layer of kaowool, shown in Figure 3.2. This minimised the effect of heat conduction through the frame and prevented gases escaping and burning at the edge of the sample.

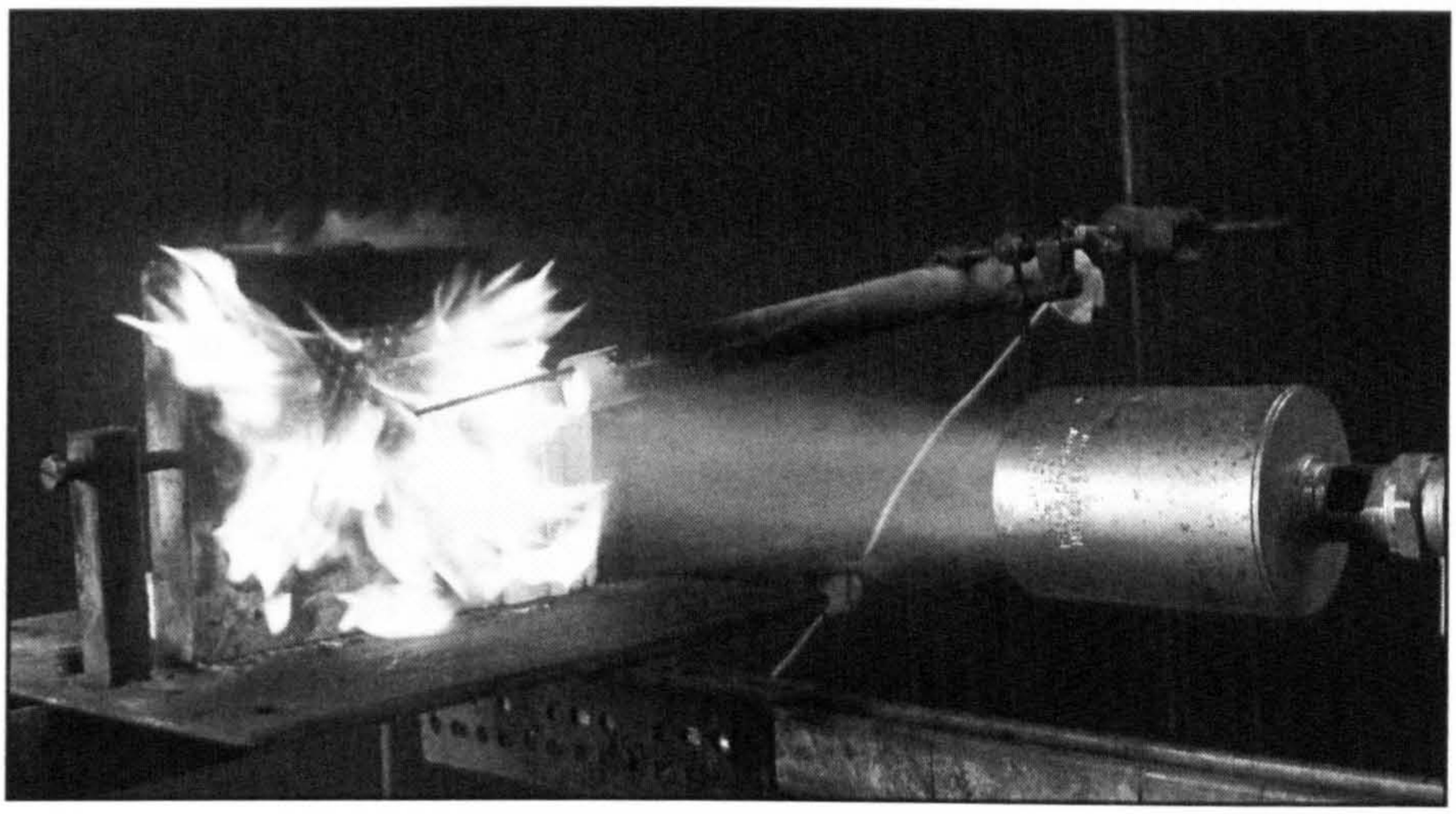

(i)

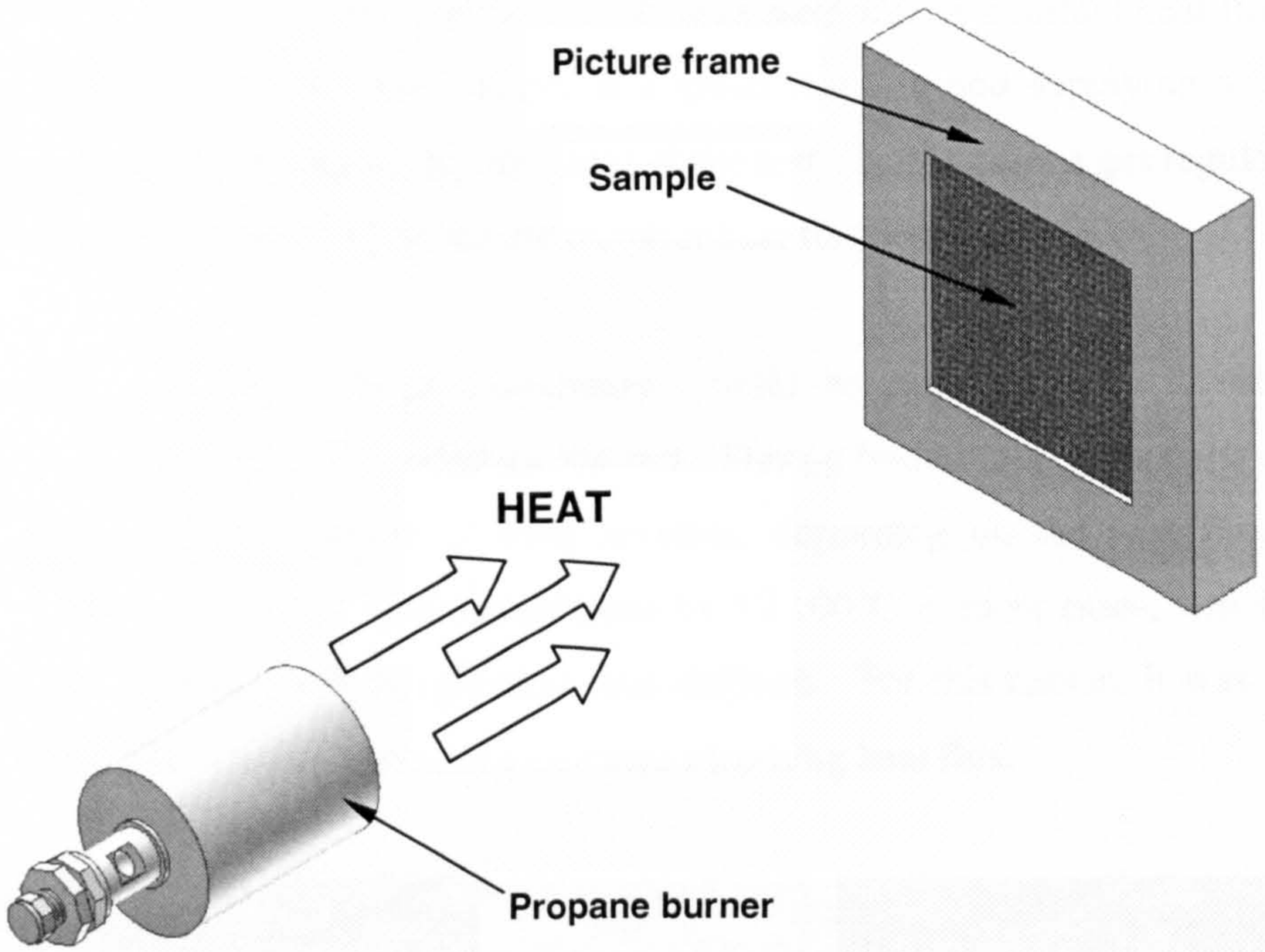

(ii)

Figure 3.1 (i) Photograph and (ii) schematic diagram of the small scale propane burner test. The sample is held in a 150mm x 150mm steel picture frame with a 100mm x 100mm exposed surface.

Three k-type thermocouples were attached to the rear face of the sample to monitor the cold face temperature. An epoxy based resin was used to affix the thermocouples to the sample. Once a test was completed, the cold face data were compared to the profile produced by thermal modelling techniques. The thermal model [49, 70], was used to predict temperature profiles and residual resin content profiles for a composite laminate in fire. If the temperature profiles matched, it could be assumed that the material constants used in the thermal modelling process were of sufficient accuracy. The modelled thermal and residual resin content (RRC) profiles could then be used for structural modelling. A thermocouple was used to monitor an indicative field temperature (T_s) 10mm in front of the sample. This field temperature was used to estimate the emissivity of the heat source and was a useful indication of the severity of the fire.

Test conditions could be controlled by one of three methods. A constant heat flux could be provided by placing the test sample at a given distance and supplying a constant pressure of gas to the burner for the duration of the test. In this case, a gas regulator was used to keep the pressure, and hence the incident heat flux, constant.

Alternatively, a constant "field temperature" could be maintained by adjusting the pressure of gas accordingly throughout the test. During burner tests composite samples tend to ignite within a period of sixty seconds, depending on the heat flux. This flashover increased the test field temperature by 50-100°C in most cases, which meant maintaining a constant field temperature was difficult. For this reason, it was decided that fire tests would be conducted at a constant incoming heat flux.

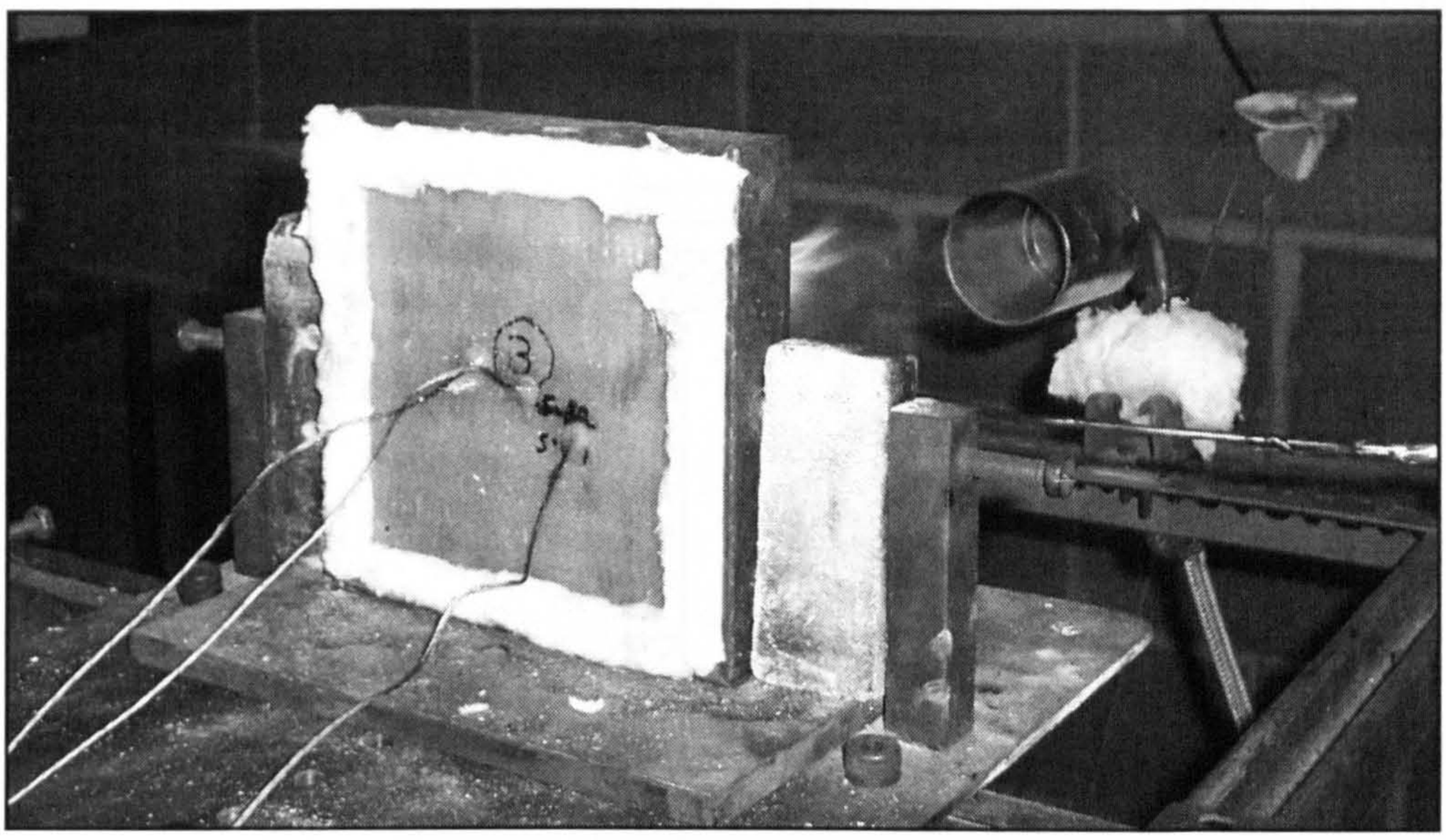

Figure 3.2 The propane burner test. Three thermocouples are used to monitor the thermal response of the rear face. Kaowool insulation holds the sample in place and reduces heat conduction through the steel frame.

It would also be possible to follow standard fire curves by adjusting gas pressure to vary the front face temperature. Again, flashover problems meant that this method of testing was disregarded in favour of constant heat flux tests.

3.2 Heat Flux Calibration

The heat flux provided by the burner at different gas pressures had to be calibrated before fire testing. A Schmidt-Boelter type [91] heat flux meter, fitted as standard to the cone calorimeter, would have been an ideal way of doing this. However this type of meter contains sensitive measurement equipment which relies on a delicate sensing surface. If used to directly calibrate the burner, it would have been damaged by the jet flame. Hence, a more robust meter was designed and built to calibrate the test.

3.2.1 The Copper Block Heat Flux Meter

The heat flux meter consisted of a copper block with thermocouples positioned at various points within the block, as shown in Figure 3.3. The exterior of the block was completely insulated using calcium silicate board and kaowool except for a small exposed circular surface at the front of the meter.

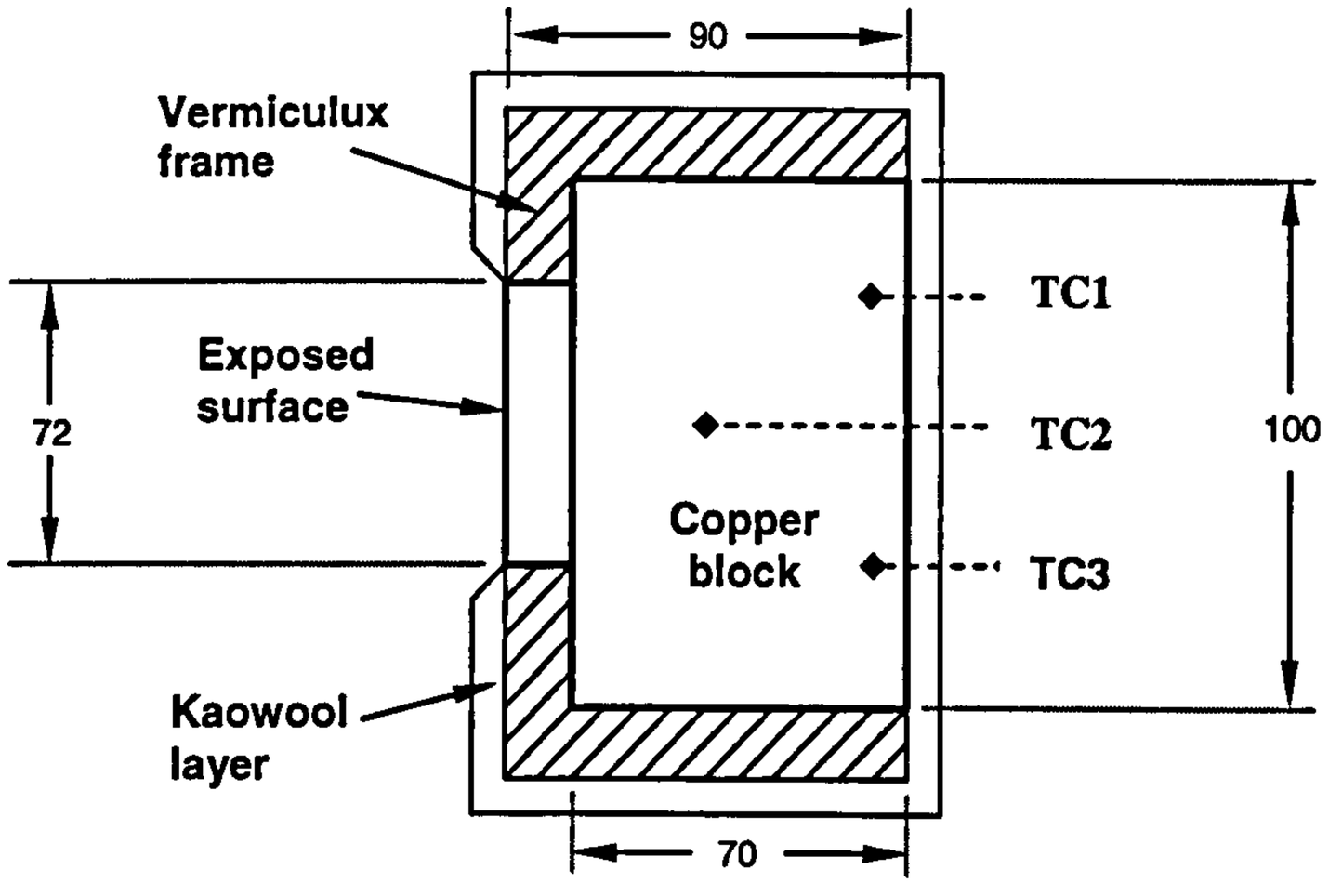

Figure 3.3 Schematic diagram of the heat flux meter (all dimensions in millimetres).

For calibration, the heat flux meter replaced the test sample at a set distance from the propane burner and a constant pressure test conducted as normal, as shown in Figure 3.4. The heat flux provided by the burner could be determined by measuring the rate of change of temperature within the copper block. A number of calibration tests were conducted for different gas pressures and a calibration chart plotted from the results (Figure 3.9).

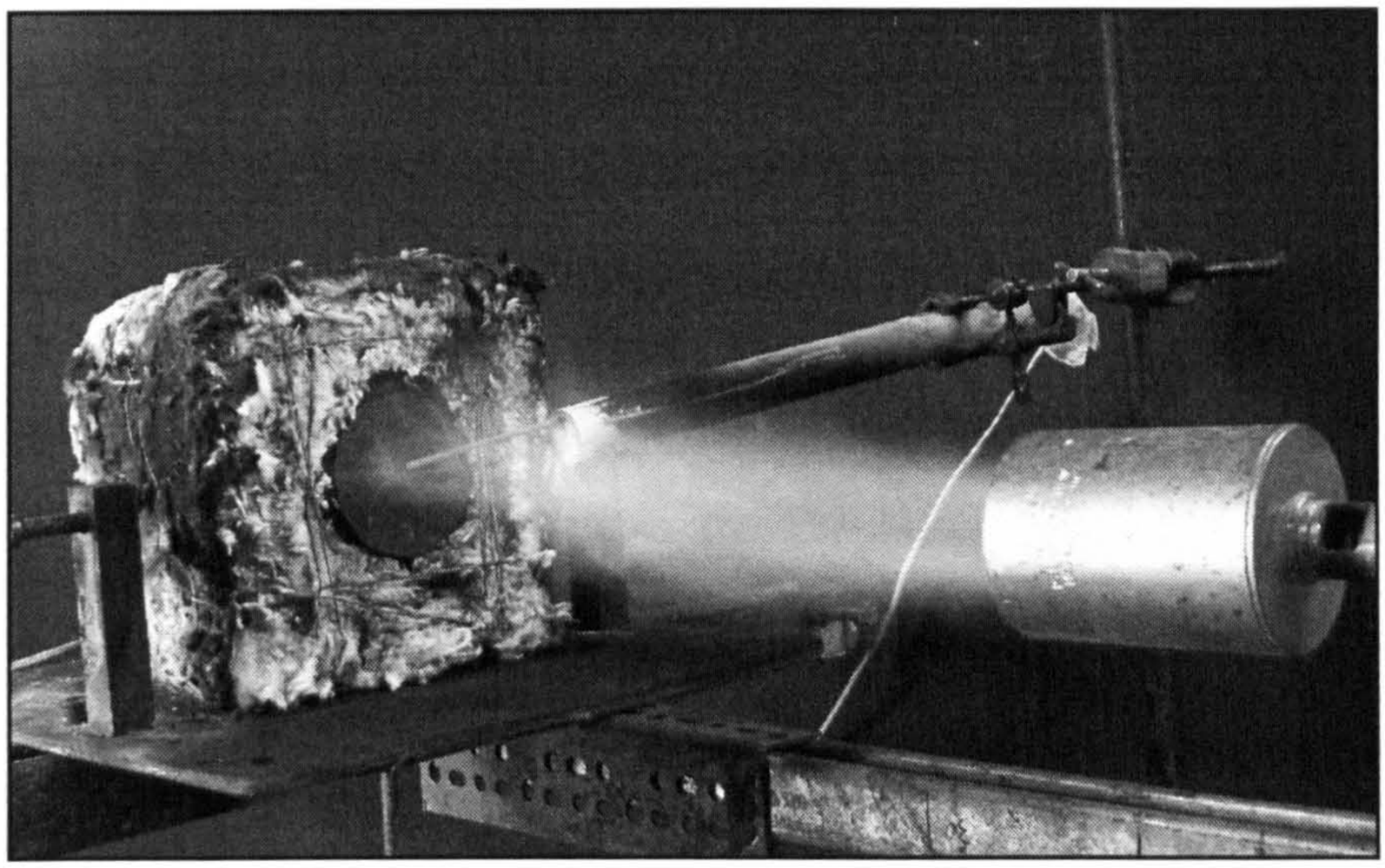

Figure 3.4 Propane burner calibration test. The heat flux meter is positioned 350mm away from the burner and a constant pressure of gas supplied. The heat flux is calculated using the linear temperature response (measured by in-built thermocouples) and the absorptivity of the meter.

3.2.2 The Stefan Botlzmann Law for Radiation

A material which absorbs all radiant energy incident upon it is known as a black body [92-94]. The absorptivity (α) of a body is the ratio of absorbed to total incident energy. The Stefan-Boltzmann law states that the total energy emitted per unit time by a unit area of a black body is:

$$q_b = \sigma \cdot T^4 \tag{3.1}$$

where: q_b is the energy emitted per unit time by a unit area of a black surface (W/m^2),

σ is the Stefan-Boltzmann constant (5.67×10^{-8} W/m^2K^4),

T is the temperature of the black surface (K).

It was assumed the copper block acts as a grey body; an 'ideal' body to which many materials can approximate in practice. Grey bodies do not absorb all the radiant energy incident upon them, but the laws of radiation for grey bodies involve simple

modifications to black-body laws [92-94]. The Stefan-Boltzmann law can be amended for grey body radiation by the inclusion of an emissivity value (ε):

$$q_b = \varepsilon \cdot \sigma \cdot T^4 \tag{3.2}$$

The emissivity of a body is the ratio of the energy emitted by the body to the energy emitted by a black body at the same temperature [92-94]:

$$\varepsilon = \left(\frac{q}{q_b} \right) \tag{3.3}$$

Kirchoff's law relates the absorptivity and emissivity of a body. For a grey body, the values of emissivity and absorptivity are always equal [92-94]. The copper block's absorptivity was required before the meter could be used to measure heat flux.

The measured thermal response within the copper block was affected by several factors. Figure 3.5 shows the energy input and losses during a typical calibration test.

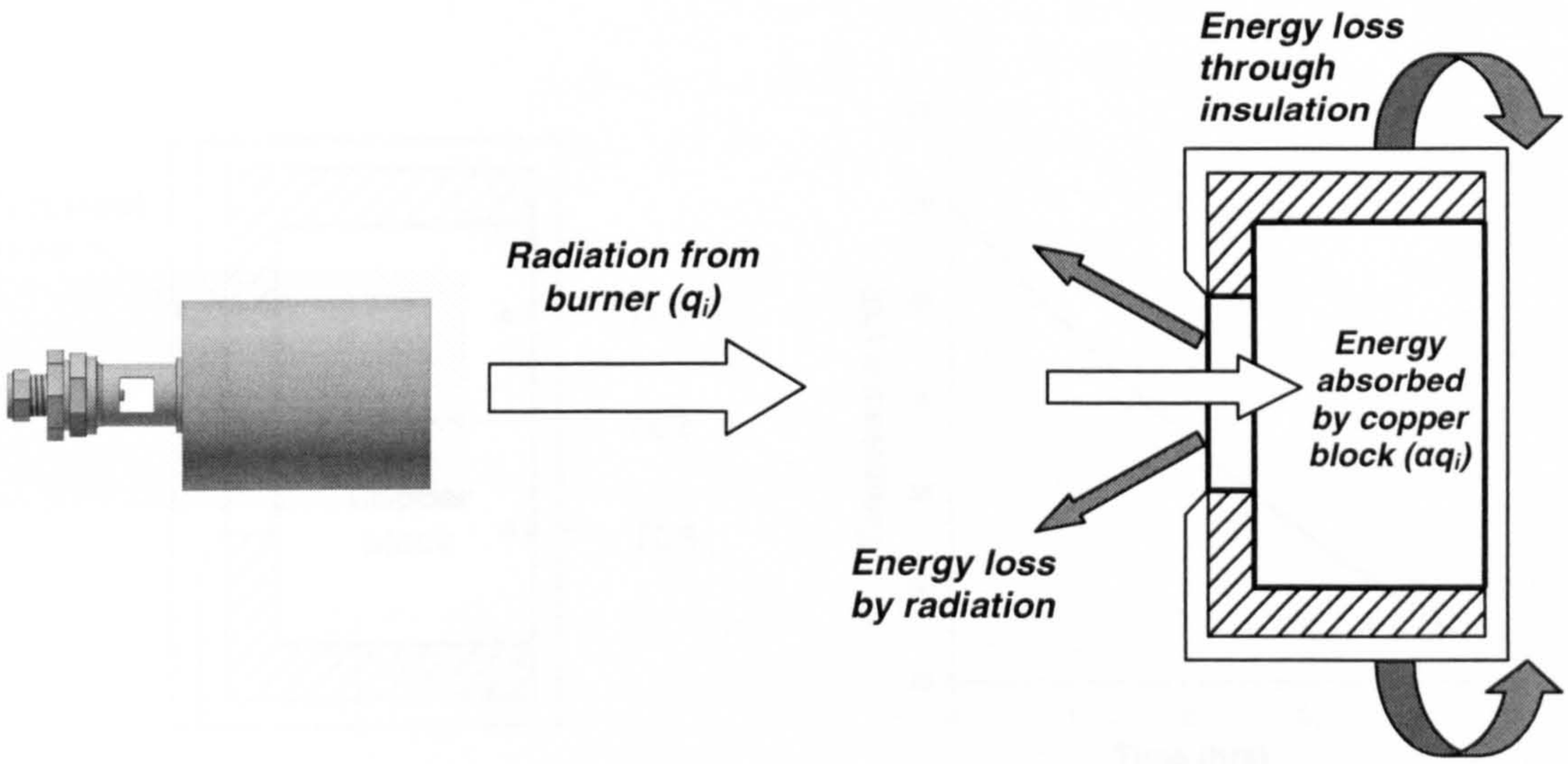

Figure 3.5 Heat transfer processes in a typical calibration test. Heat transfer into the block is by radiation from the burner flame. Energy losses are shown as darker arrows and include heat lost by convection through the insulation layers and by radiation from the exposed surface.

3.2.3 Energy Losses by Convection

A cooling test was conducted to determine the energy losses by convection through the insulation. The meter was heated to an internal temperature of over 70°C, covered as shown in Figure 3.6 (i), and allowed to cool for approximately four hours. The rate of change of temperature within the block (*dT/dt*) was then monitored using the in-built thermocouples.

According to Newton's law of cooling, the total energy transferred through the insulation to the surroundings (Q_C) was equal to the energy loss of the copper block:

$$Q_C = m \cdot C_p \cdot \left(\frac{dT}{dt}\right) = h \cdot A_{co} \cdot [T_b - T_{amb}] \qquad (3.4)$$

where: m is the mass of the copper block (kg),

C_p is the specific heat capacity of copper (J/kg.K),

h is the heat transfer coefficient for convection (W/m^2.K),

A_{co} is the total surface area of the covered meter (m^2),

T_b is the instantaneous temperature of the copper block (K),

T_{amb} is the ambient temperature (K).

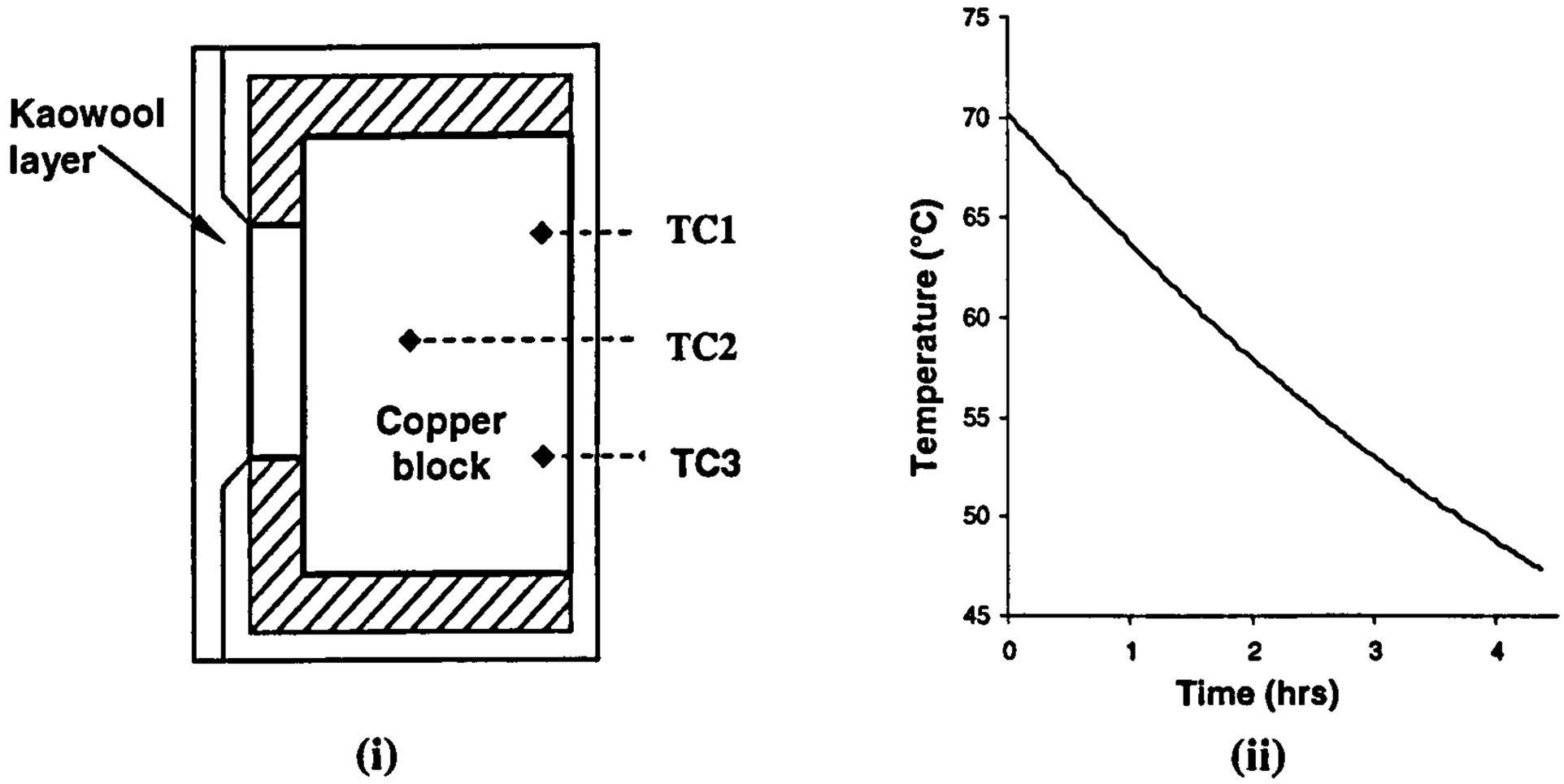

Figure 3.6 (i) Schematic diagram of the covered heat flux meter used to determine the convection heat transfer coefficient. (ii) The measured thermal response of the covered cooling condition.

An average value of 2.1W/m^2.K was calculated for the heat transfer coefficient over the given temperature range shown by the cooling curve in Figure 3.6 (ii).

3.2.4 Energy Losses by Radiation

The Stefan-Botlzmann law was used to calculate the energy lost by radiation (Q_R) through the exposed surface of the heat flux meter:

$$Q_R = A_{ex} \cdot \sigma \cdot \varepsilon_b \cdot \left(T_b^4 - T_{amb}^4\right) \tag{3.5}$$

where: A_{ex} is the exposed area of the meter (m^2),

ε_b is the emissivity of the meter.

The emissivity of the copper block was required before the radiation energy losses could be calculated. Another cooling test was conducted to measure the emissivity of the copper block. The meter was again heated to an internal temperature of over 70°C and then allowed to cool naturally in air with the front surface exposed, as in Figure 3.3. The thermal response was recorded by the in-built thermocouples. In this case, Equation 3.6 described the energy lost by the copper block through radiation from the front surface and convection through the insulation layers:

$$Q = m \cdot C_p \cdot \left(\frac{dT}{dt}\right) = A_{ex} \cdot \sigma \cdot \varepsilon_{Cu} \cdot \left(T_b^4 - T_{amb}^4\right) + h \cdot A_{un} \cdot \left[T_b - T_{amb}\right] \tag{3.6}$$

where: A_{un} is the area of the unexposed surface of the meter (m^2),

Using the value of h calculated previously, an average emissivity value of 0.65 was determined from the cooling curve shown in Figure 3.7

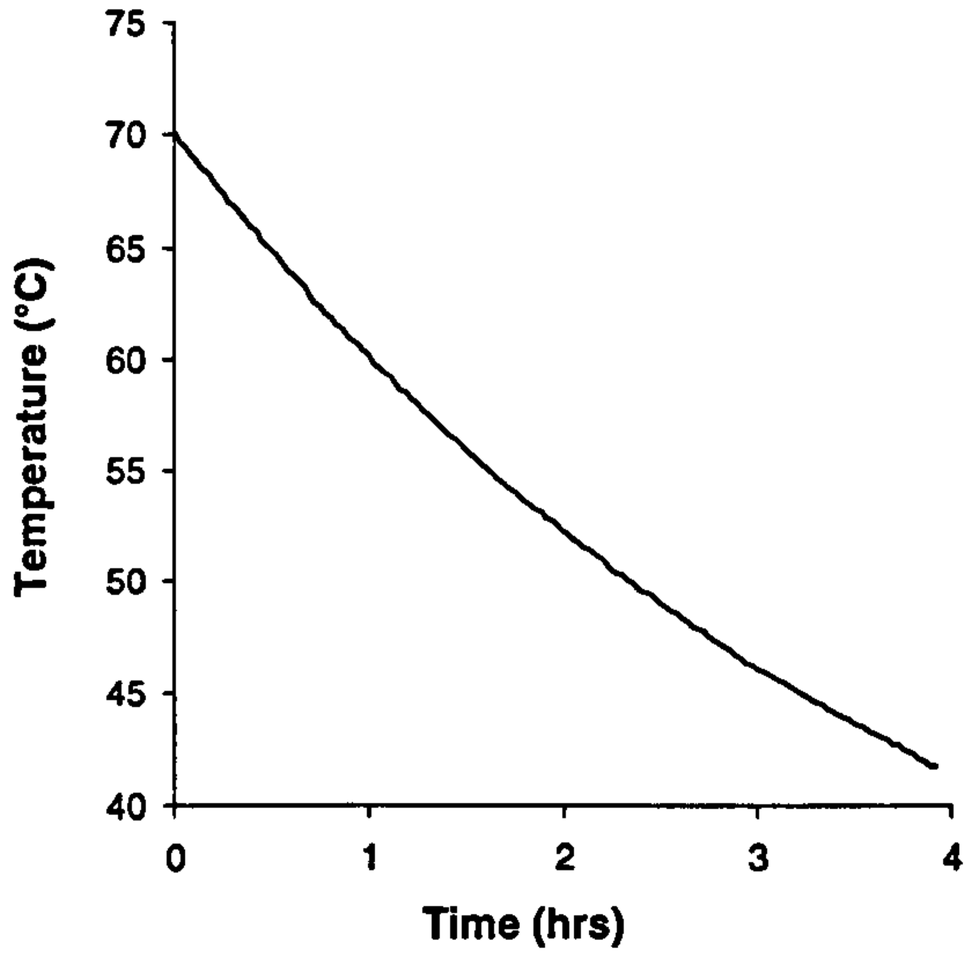

Figure 3.7 The measured thermal response of the uncovered cooling condition. An average emissivity value of 0.65 was calculated from the curve.

3.2.5 Calculation of the absorptivity of copper using a Cone Calorimeter

When a thermal-capacitance type calorimeter, such as the copper heat flux meter, is exposed to a steady-state heating source a linear temperature response is expected [95]. By considering thermal energy balance, the heat flux absorbed by the copper block (αq_i) can be determined by the linear portion of the measured time-temperature curve and the physical properties of the meter. Equation 3.7 describes the energy transfer and losses illustrated in Figure 3.5:

$$\alpha \cdot A_{ex} \cdot q_i = \underbrace{m \cdot C_p \left(\frac{dT}{dt} \right)}_{\text{Thermal response of meter}} + \underbrace{A_{ex} \cdot \varepsilon_b \cdot \sigma \cdot \left(T_b^4 - T_{amb}^4 \right)}_{\text{Energy lost through radiation}} + \underbrace{A_{un} \cdot h \left(T_b - T_{amb} \right)}_{\text{Energy lost through insulation layers}} \quad (3.7)$$

If the temperature within the heat flux meter is low enough (under 100°C) the energy losses due to convection and radiation are small enough to be neglected. Table 3.1 shows calculated values of the thermal response of the meter, the energy lost through radiation and the energy lost through the insulation layers when the meter was exposed

to a heat flux of 50kW/m^2. The relatively small values of the energy losses meant these losses could be neglected.

Table 3.1 Quantification of the energy transfer processes within the heat flux meter when subjected to a 50kW/m^2 heat source. The energy rates displayed are the average rate for the test.

	Average energy transfer rate (J/s)	Fraction of total energy transfer (%)
Thermal response of meter $[m.C_p.(dT/dt)]$	123.6983	99.9974
Energy lost by radiation $[A_{ex}.\varepsilon_b.\sigma.(T_b^4 - T_{amb}^4)]$	0.0014	0.0011
Energy lost through insulation $[A_{un}.h.(T_b - T_{amb})]$	0.0018	0.0015

Equation 3.7 can therefore be simplified to give:

$$\alpha = \frac{m \cdot C_p}{A_{ex} \cdot q_i}\left(\frac{dT}{dt}\right) \tag{3.8}$$

A cone calorimeter was used to provide a pre-calibrated heat flux of 50kW/m^2 to the copper heat flux meter (q_i). Using Equation 3.8, an average value of 0.6 was found for the absorptivity of the flux meter. The test was repeated for other heat fluxes including 25kW/m^2, 75kW/m^2 and 100kW/m^2. The derived values of absorptivity for these heat flux levels ranged from 0.6 to 0.68.

The emissivity value calculated using the uncovered cooling test is very similar to the calculated absorptivity values for this range of heat fluxes. This further reinforces the assumption that the copper heat flux meter acts like a grey body.

3.2.6 Calibration of the Propane Burner Test

Equation 3.7 was amended to calculate the heat flux provided by the burner (q_i):

$$q_i = \left[m \cdot C_p \left(\frac{dT}{dt} \right) + A_{ex} \cdot \varepsilon_b \cdot \sigma \cdot \left(T_b^4 - T_{amb}^4 \right) + A_{un} \cdot h \left(T_b - T_{amb} \right) \right] \Big/ \alpha A_{ex} \qquad (3.9)$$

With all material constants and heat transfer constants defined, the heat flux provided by the burner was calculated using the linear thermal response of the copper meter. The measured surrounding temperature field (T_s) and response profiles at TC1, TC2 and TC3 (defined in Figure 3.3) are shown in Figure 3.8.

After an initial response period (t= 0 to $t = t_o$) the surrounding field temperature becomes reasonably constant. The temperature responses at TC1, TC2 and TC3, are apparently linear. However, when the average rate of change of temperature (dT/dt) was plotted against time, dT/dt was only linear after the initial response period (from $t >$ 190s).

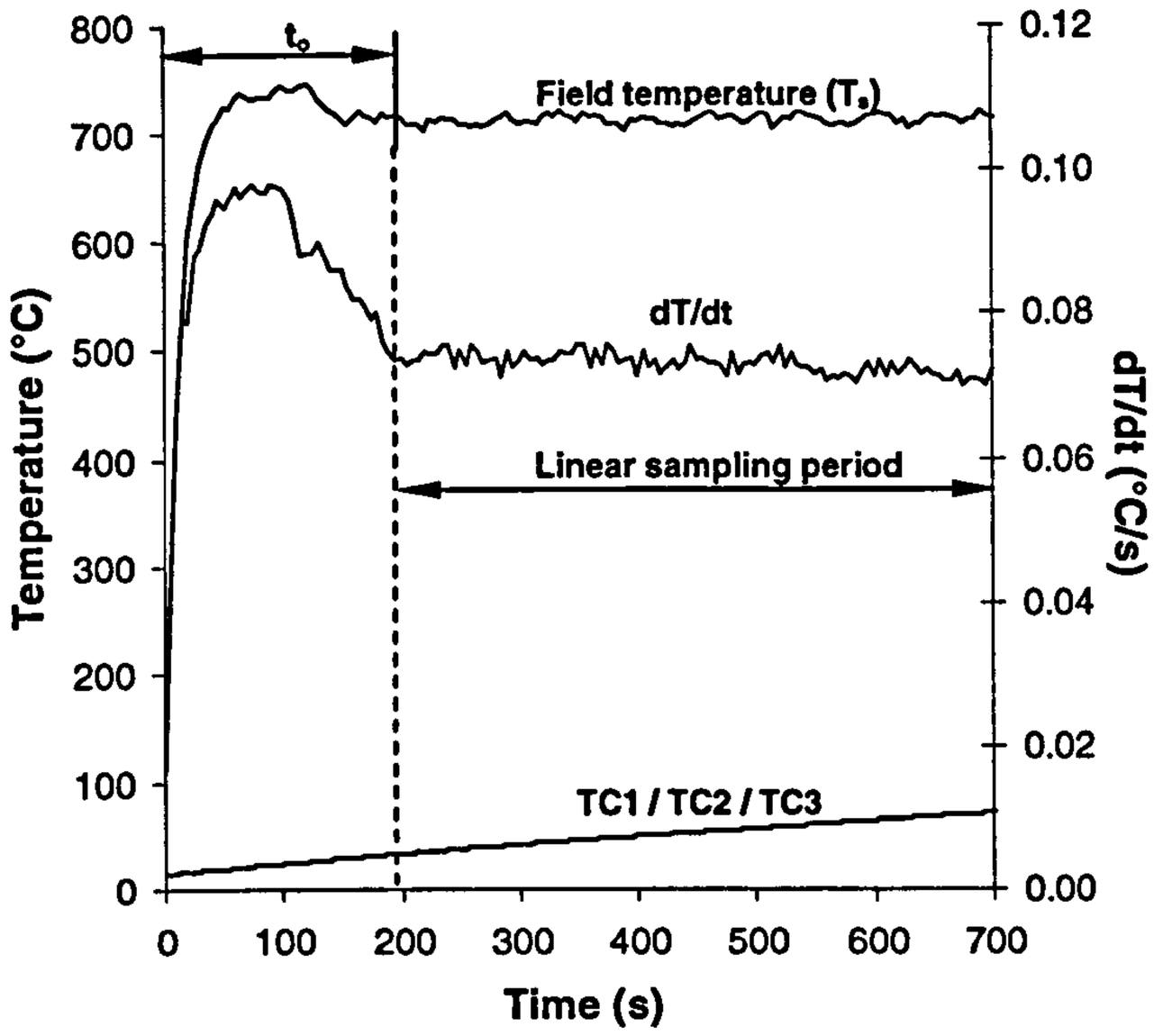

Figure 3.8 The measured surrounding field temperature (T_s) and internal thermal response at TC1, TC2 and TC3. Derived values of (dT/dt) for a typical calibration test are also shown (gas pressure = 0.2 bar). Note that the only linear section of the curve is when $t >$ 190s.

Therefore, only the linear period, from $t = t_o$ to $t = 700$s in this case, should be used to calculate the incident heat flux. In order to make effective use of the calibration results, a standard procedure was adopted for analysis.

- Based on temperature response curves, the initial response time period ($t = 0$ to $t = t_o$) was identified and discarded.
- A relevant linear sampling period was highlighted for the rate of change of meter temperature (dT/dt).
- A value of $\eta = (T_b/T_s)$ was calculated for the sampling period. If $\eta > 0.1$, the sampling period was reduced accordingly until $\eta < 0.1$ for each time step. This ensured that the meter temperature was not large enough to affect the calculated value of heat flux.

A number of calibration tests were conducted at different gas pressures to ascertain the full range of possible heat flux levels. Figure 3.9 shows a calibration curve for the propane burner at a distance of 350mm from the meter. The fire tests conducted for this research were for a heat flux of 50kW/m^2; this corresponded to a gas pressure of 0.21 bar.

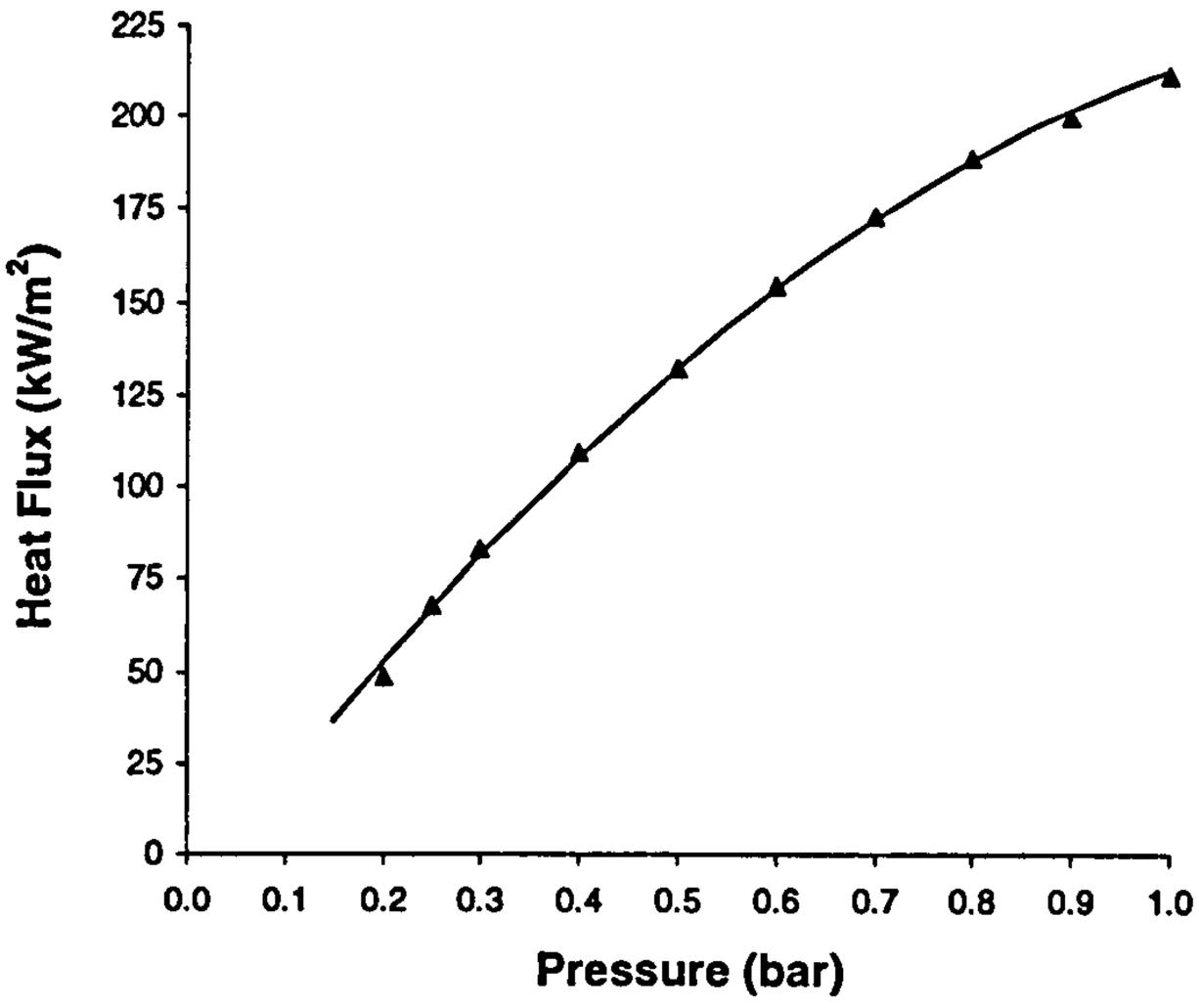

Figure 3.9 The propane burner calibration curve for a burner-sample distance of 350mm. The curve shows the pressure of gas required for any heat flux between 25 and 225kW/m^2 to be determined.

3.3 Thermal Model Temperature and RRC Profiles

The propane burner test was used to validate predictions made by the thermal model detailed in Chapter 2, Equation 2.6. Figure 3.10 shows a comparison of the measured rear face temperature profile and the modelled rear face temperature profile for each laminate system.

If, during the first 300 seconds of the test, the predicted rear face response was constantly within 10°C of the measured temperature profile, the prediction was assumed to be of sufficient accuracy to be used for mechanical modelling. Under this proviso, all three materials were modelled well. The rear face tests were conducted a number of times in order to investigate the reproducibility of the test. With careful sample preparation, the required experimental accuracy was achieved on every test.

During a fire test, it was not necessary to measure the change in residual resin content in order to validate the accuracy of the thermal model. If the modelled temperature profiles and the modelled TGA curves (Chapter 4.2.2) were of sufficient accuracy, it was reasonable to assume the RRC predictions would also be accurate. In theory, the accuracy of the model's RRC predictions could be validated by visual inspection after a given exposure time, as demonstrated by Mouritz and Mathys [80, 81].

The measured rear face responses for the polyester and vinyl ester laminates were very similar. This observation was expected. Both materials have similar glass content and physical structure. Differences in the two profiles are only apparent after approximately eight minutes of testing. At this stage of the test, resin decomposition has developed throughout the laminate cross section and the measured temperature response may become distorted due to thermocouple detachment. The rise in temperature at the rear face of the polypropylene laminate was much slower than that of the polyester and vinyl ester samples. This can be explained by the comparatively higher resin content of the material, which therefore lowers its overall thermal conductivity, and the fact that the sample had a marginally thicker cross-section.

The full temperature and residual resin content profiles were used to provide the necessary input for modelling the structural response of laminates in fire. Figures 3.11, 3.12 and 3.13 show the modelled temperature and RRC profiles for glass/polyester, glass/vinyl ester and glass/polypropylene laminates in a 50kW/m^2 fire.

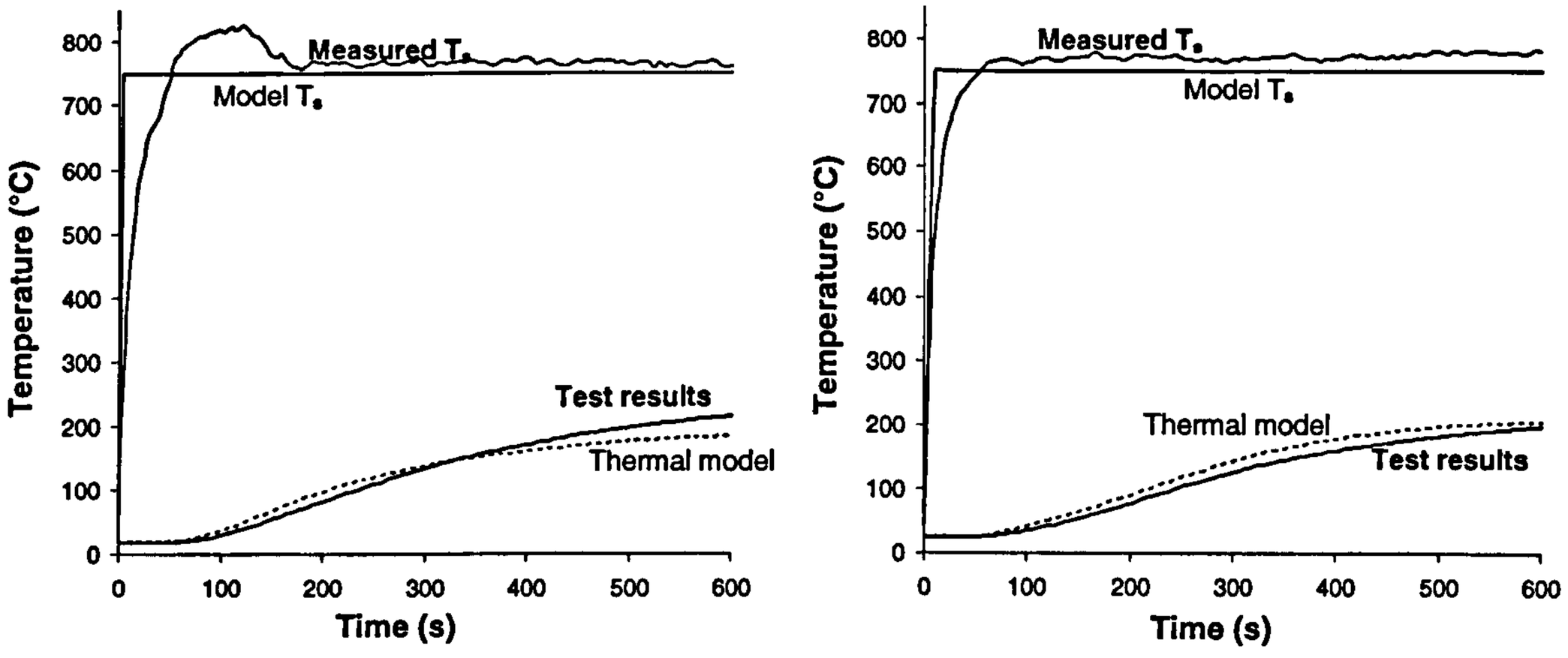

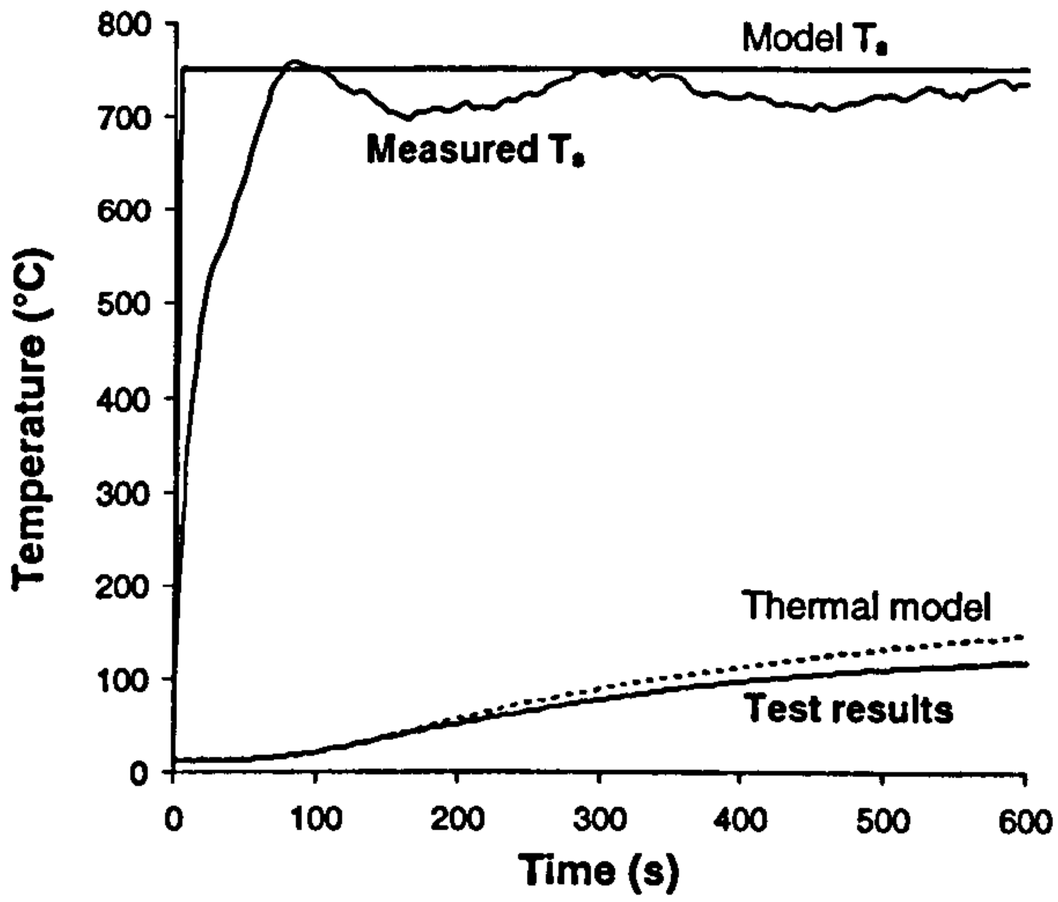

Figure 3.10 Modelled and measured rear face temperature profiles for (i) an 11.3mm glass/polyester laminate, (ii) an 11.6mm glass/vinyl ester laminate, and (iii) a 12.1mm glass/polypropylene laminate, in a 50kW/m^2 fire. The measured field temperature (T_s) and the modelled 'ideal' field temperature which correspond to a 50kW/m^2 heat flux are also shown.

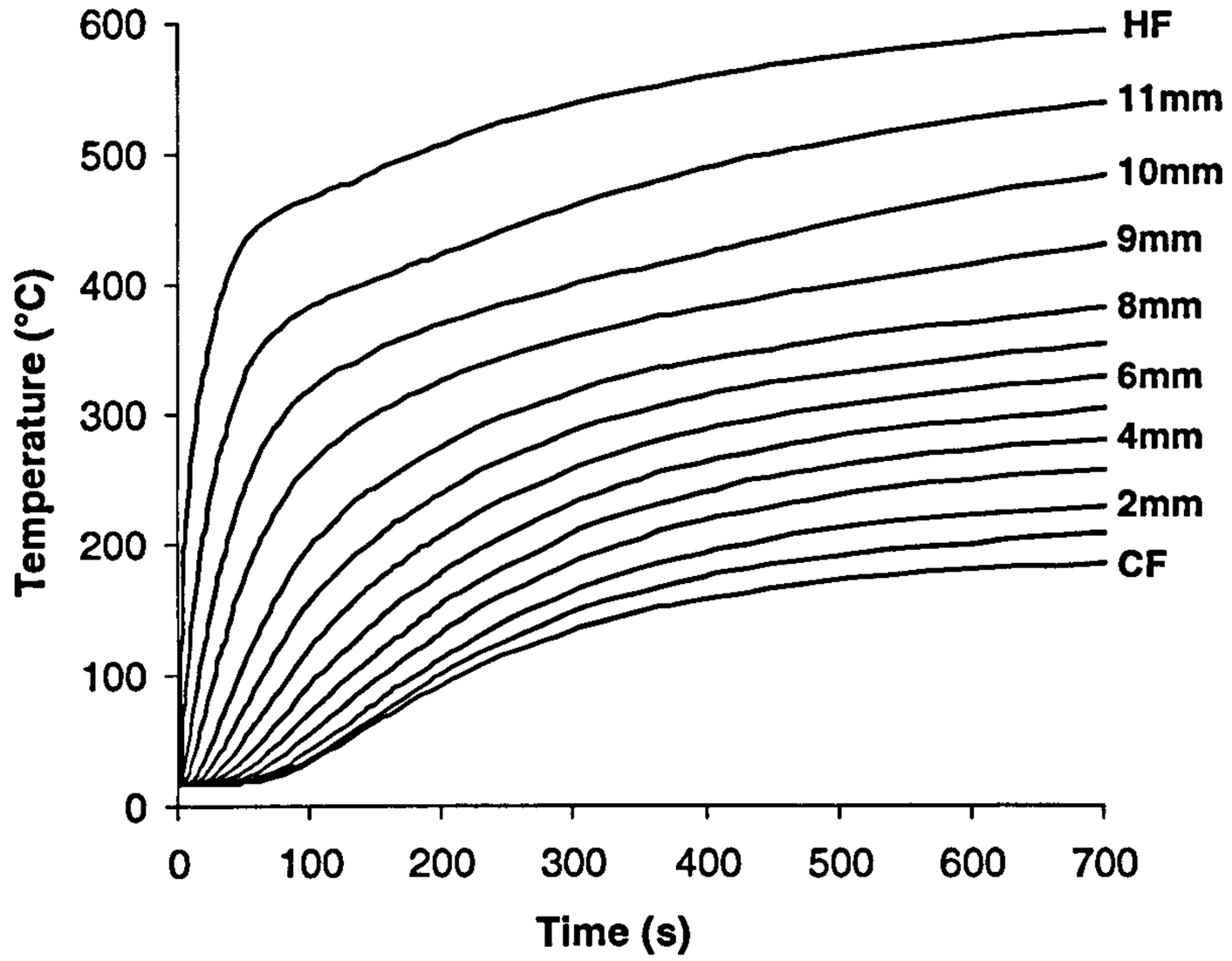

(i)

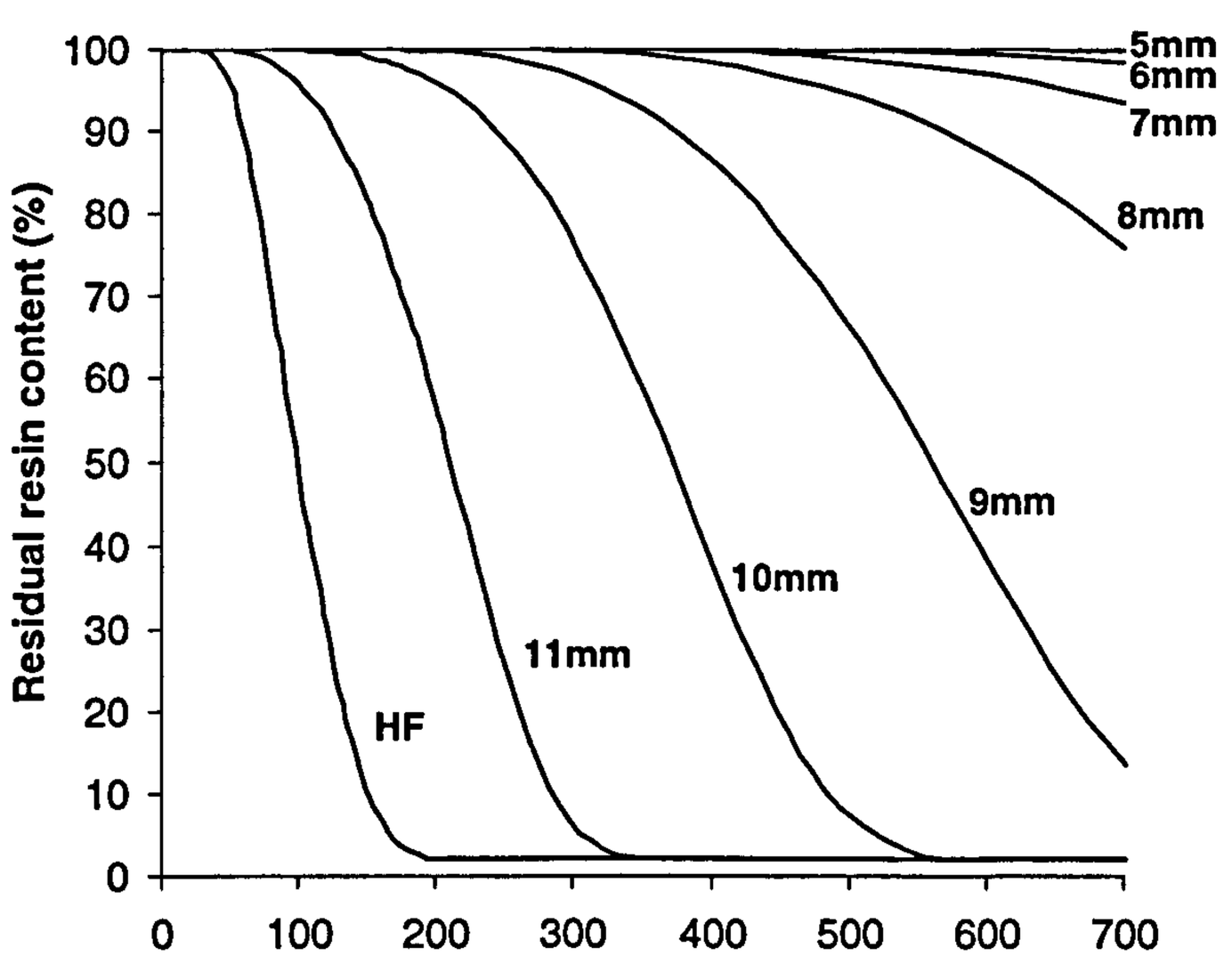

(ii)

Figure 3.11 (i) Predicted temperature profiles and, (ii) residual resin content profiles for a 12mm polyester laminate exposed to a 50kW/m^2 heat flux. The CF profile corresponds to the cold face of the laminate. Each profile corresponds to a depth through the thickness of the laminate, measured from the cold face through to the hot face (HF).

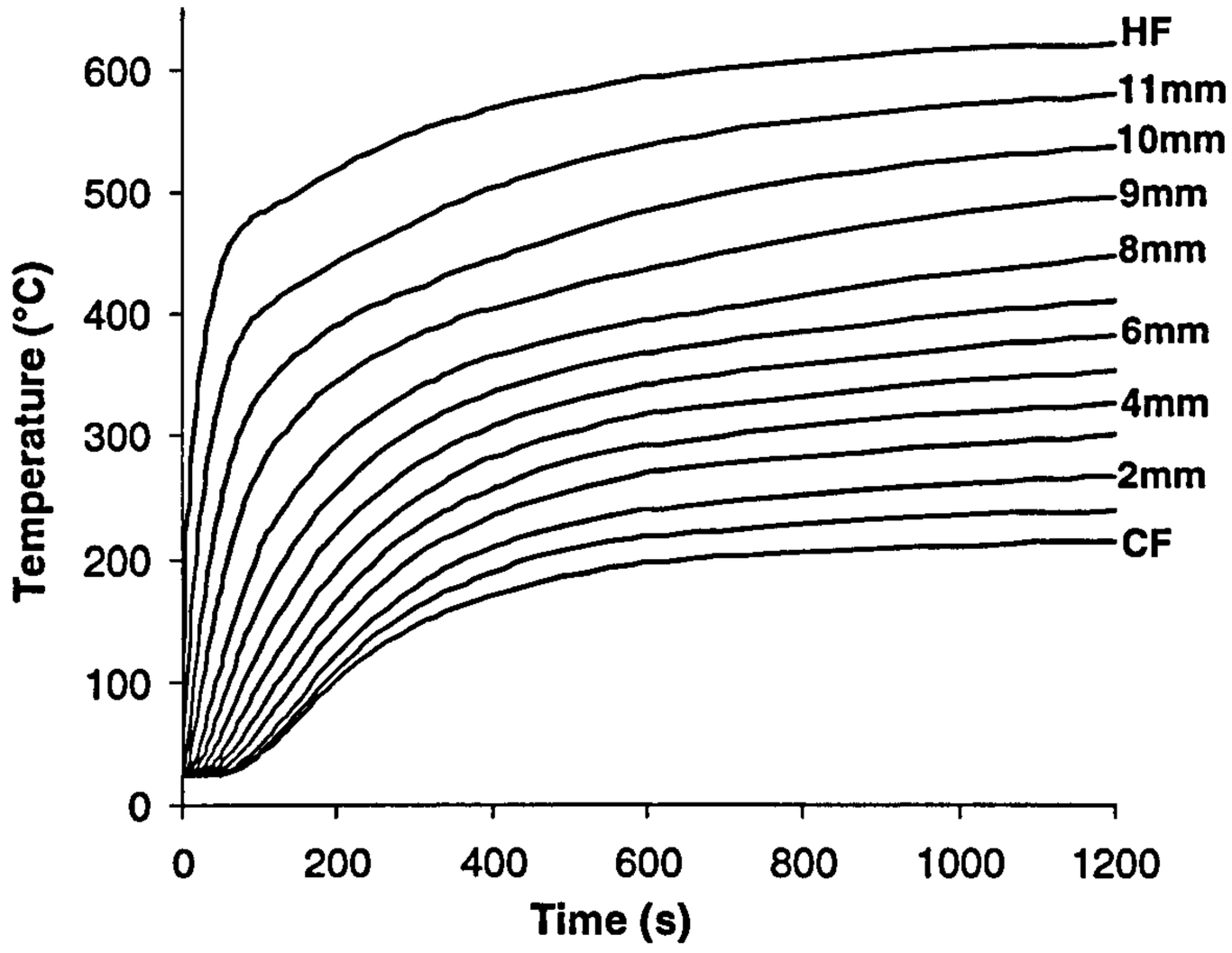

(i)

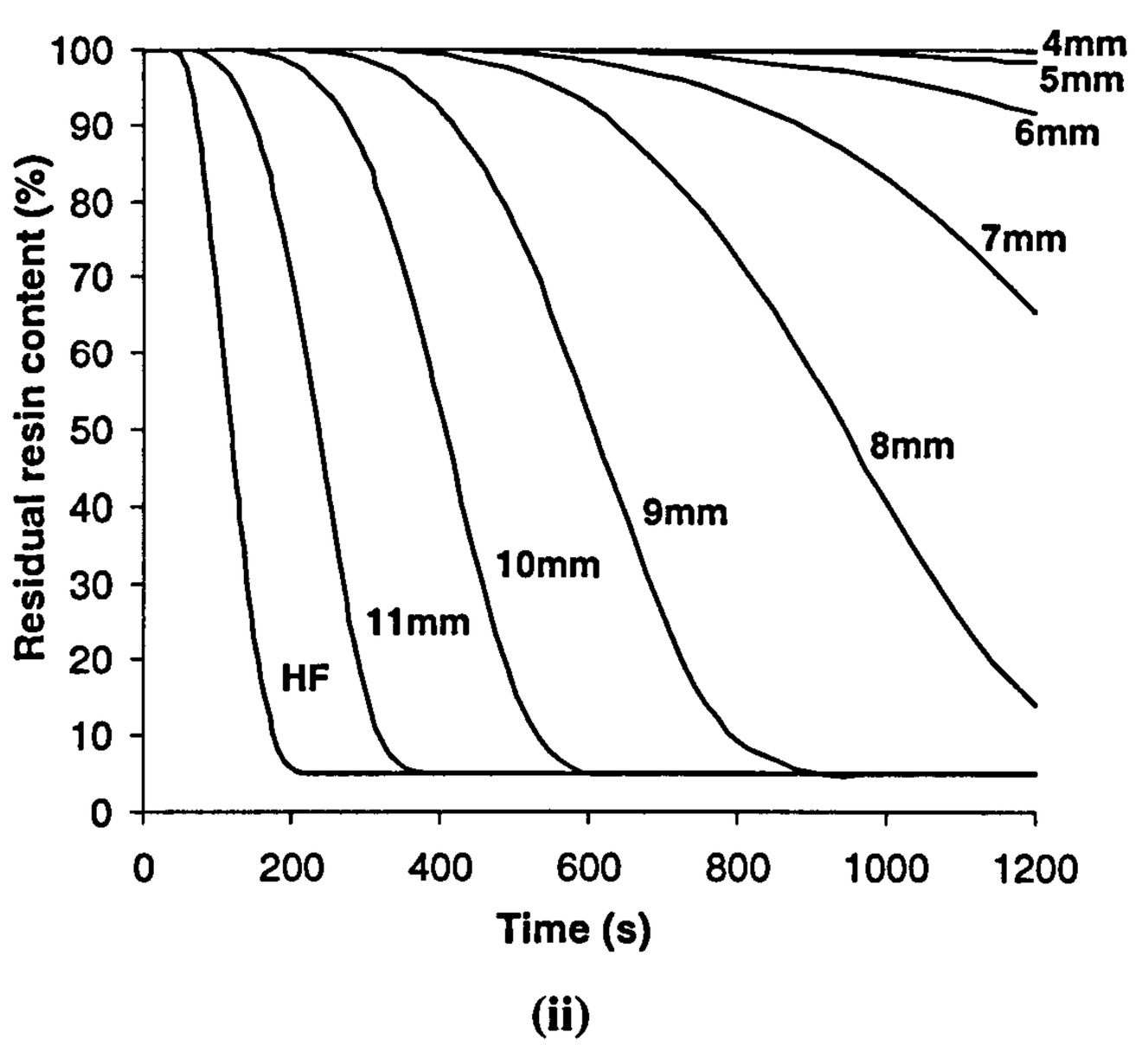

(ii)

Figure 3.12 (i) Predicted temperature profiles and, (ii) residual resin content profiles for a 12mm vinyl ester laminate exposed to a 50kW/m^2 heat flux. The CF profile corresponds to the cold face of the laminate. Each profile corresponds to a depth through the thickness of the laminate, measured from the cold face through to the hot face (HF).

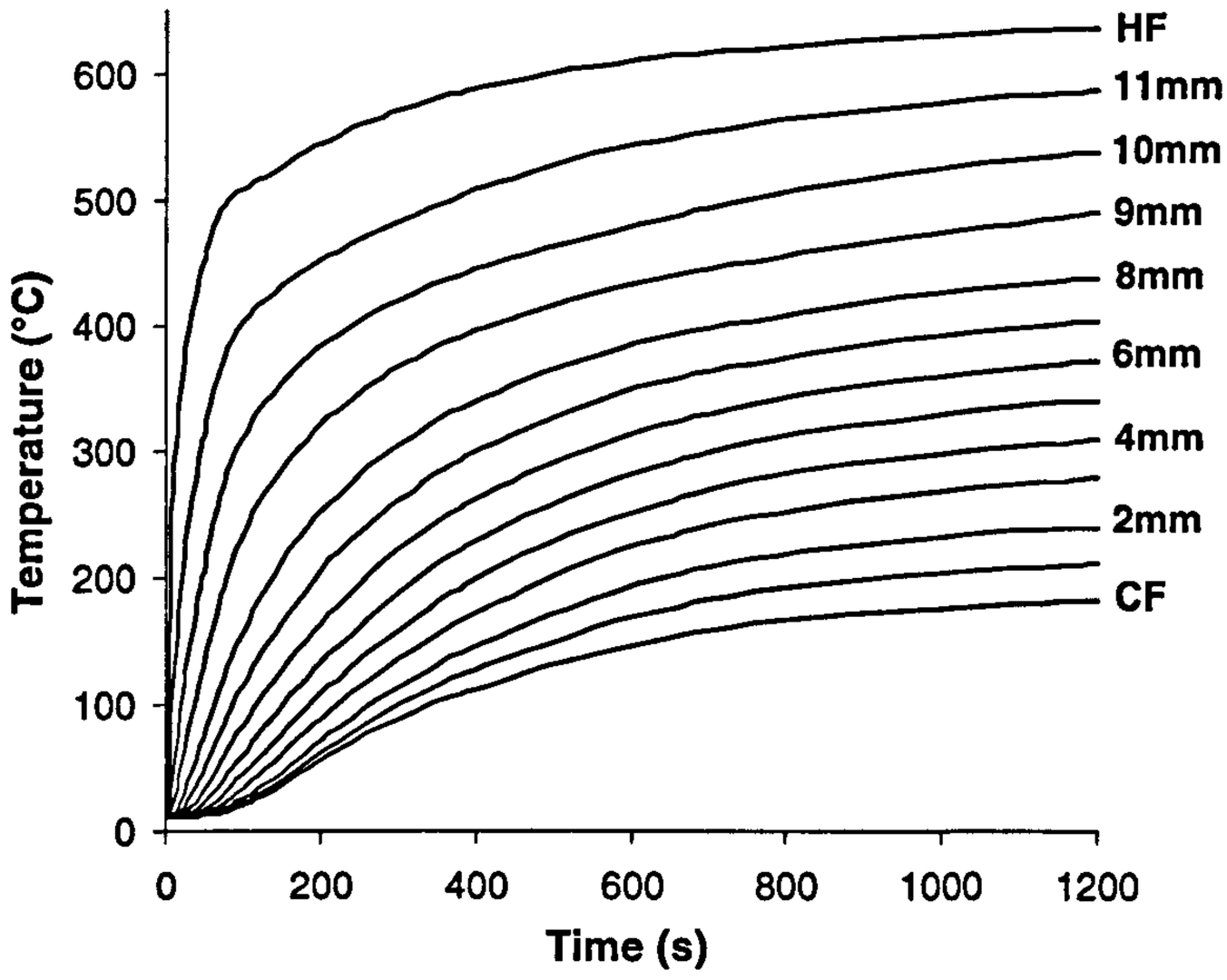

(i)

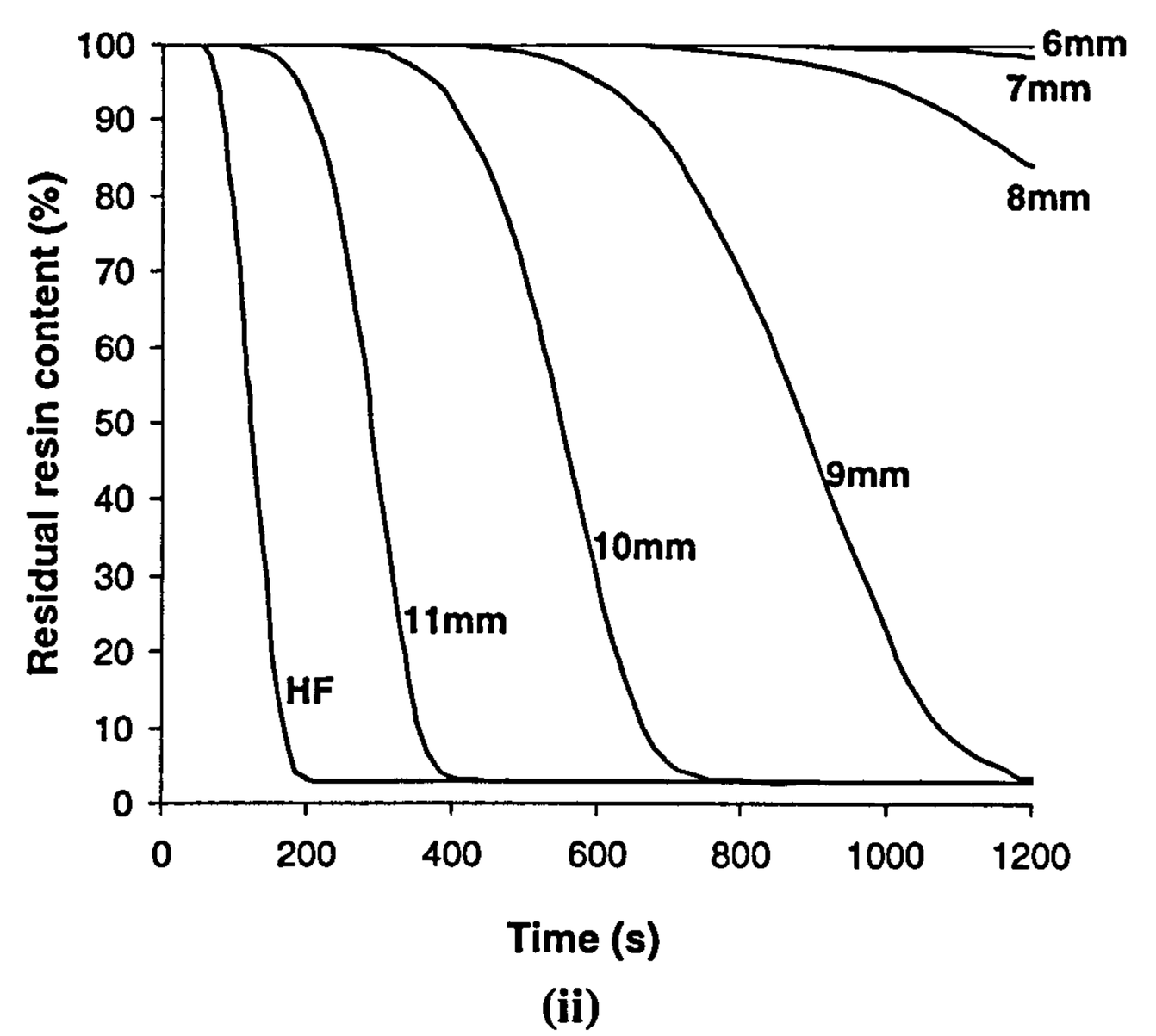

(ii)

Figure 3.13 (i) Predicted temperature profiles and, (ii) residual resin content profiles for a 12mm polypropylene laminate exposed to a 50kW/m^2 heat flux. The CF profile corresponds to the cold face of the laminate. Each profile corresponds to a depth through the thickness of the laminate, measured from the cold face through to the hot face (HF).

Chapter 4 Material Property Classification

Modelling the structural response of composite laminates in fire required knowledge of the thermal and physical material properties over the temperature range of interest. This chapter provides descriptions of the experimental work conducted in order to characterise these properties.

4.1 Materials Specification

The three materials used in this study were 12mm thick glass reinforced polyester, vinyl ester and polypropylene laminates. The polyester and vinyl ester laminates were manufactured by hand lay-up. The polypropylene laminates were manufactured by vacuum bag moulding. Full details of the types of resin and reinforcement used in each laminate are listed in Table 4.1.

Table 4.1 A summary of the materials used. Materials were provided by the Composites Technology Centre (CTC) Vosper Thornycroft, Portchester.

Composite	Reinforcement	Resin	Manufacture
Glass reinforced polyester	Multi-axis E-Glass Fabric (0°/90°).	Crystic 489: Isophthalic Polyester resin (Scott Bader)	Hand lay-up
Glass reinforced vinyl ester	Multi-axis E-Glass Fabric (0°/90°).	Dow 411-45 Vinyl ester resin	Hand lay-up
Glass reinforced polypropylene	Woven E-Glass Fabric 2x2 Balanced twill weave (0°/90°).	Polypropylene (TR PP 60 B 1870)	Vacuum bag moulding

4.2 Properties required for Thermal Modelling

The thermal model required the glass volume fraction of the composite and the kinetic thermal degradation constants for the resin system to predict the thermal response and residual resin content (RRC) of a laminate in fire.

4.2.1 Volume Fraction Calculation

The glass volume fraction was calculated for the three laminate systems. The experimental method followed guidelines set by ASTM D 792-00 Method A [96]. Small samples of each laminate (100mg approx.) were weighed in air and water. The sample resin was then burnt off in an oven and the weight of the remaining fibres measured. Values of glass weight fraction and volume faction were deduced. The test method also provided an estimation of the laminate void content. Table 4.2 summarises these results.

Table 4.2 Glass volume fraction (V_f), weight fraction (W_f) and void content expressed as percentages for the laminate systems.

Composite	V_f (%)	W_f(%)	Void content (%)
Polyester / E-glass	43.7	62.3	2.6
Vinyl ester / E-glass	45.6	64.2	4.6
Polypropylene / E-glass	34.9	60.4	2.3

4.2.2 Thermo-gravimetric Analysis (TGA)

The thermal model required certain kinetic parameters in order to calculate the rate of decomposition of the composite resin. Temperatures within a composite laminate in a 50kW/m^2 fire typically reach values of up to 750°C, resulting in the complete decomposition of the resin.

The resin decomposition reaction can be assumed to follow the Arrhenius rate equation [49, 55, 97]:

$$\frac{\partial M}{\partial t} = -A \cdot M_o \left[\frac{M - M_f}{M_o}\right]^n e^{\left(\frac{-E}{RT}\right)} \qquad (4.1)$$

where: $\frac{\partial M}{\partial t}$ is the rate of change of mass (kg/s),l

A is the rate constant (1/s),

M_o, M and M_f are the original, instantaneous and final mass of the polymer during the decomposition process (kg),

E is the activation energy (J/mol),

R is the universal gas constant (8.314 J/mol.K)

T is the temperature (K),

n is the order of the reaction.

TGA tests were conducted on small samples of each laminate weighing approximately 50mg. The samples were placed in a small furnace, shown in Figure 4.1, and a constant heating rate applied. The tests were conducted in an inert atmosphere to prevent sample ignition and the rate of change of mass loss was recorded up to 900°C.

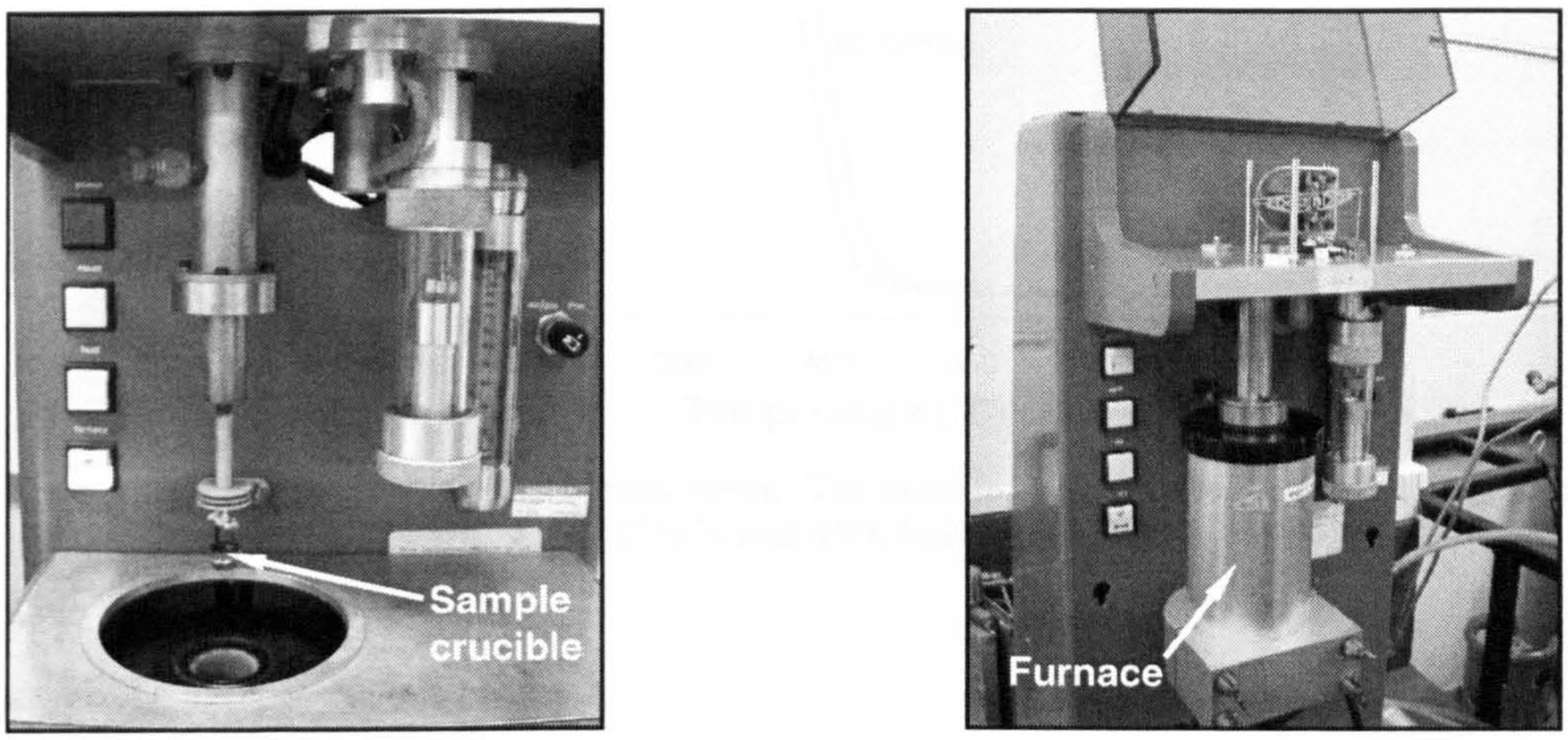

Figure 4.1 Photograph of the TGA equipment with (i) the furnace retracted, and (ii) the furnace in place, ready for testing. The samples were placed in a nitrogen atmosphere, and a constant heating rate applied. A load cell measured the rate of change of mass with increasing temperature.

The tests were conducted at two different heating rates for accurate prediction of the degradation parameters; one at 25°C/min and one at 40°C/min. Analysis and comparison of the TGA curves allowed the calculation of the reaction's rate factor (A) and activation energy (E) for each material. The weight of the fibres was subtracted from the raw data to give a mass loss curve for resin alone. However, because of the presence of fibres a small amount of residual resin, approximately 2% by weight, was not burnt off.

4.2.3 Analysis

Figure 4.2 shows the normalised mass loss results for polyester. The decomposition region starts at around 370°C for the 25°C/min heating rate and at a slightly higher temperature for the 40°C/min heating rate. Both mass loss curves have the same shape, but the different heating rates produced an effective shift in the temperature around which most of the decomposition occurs.

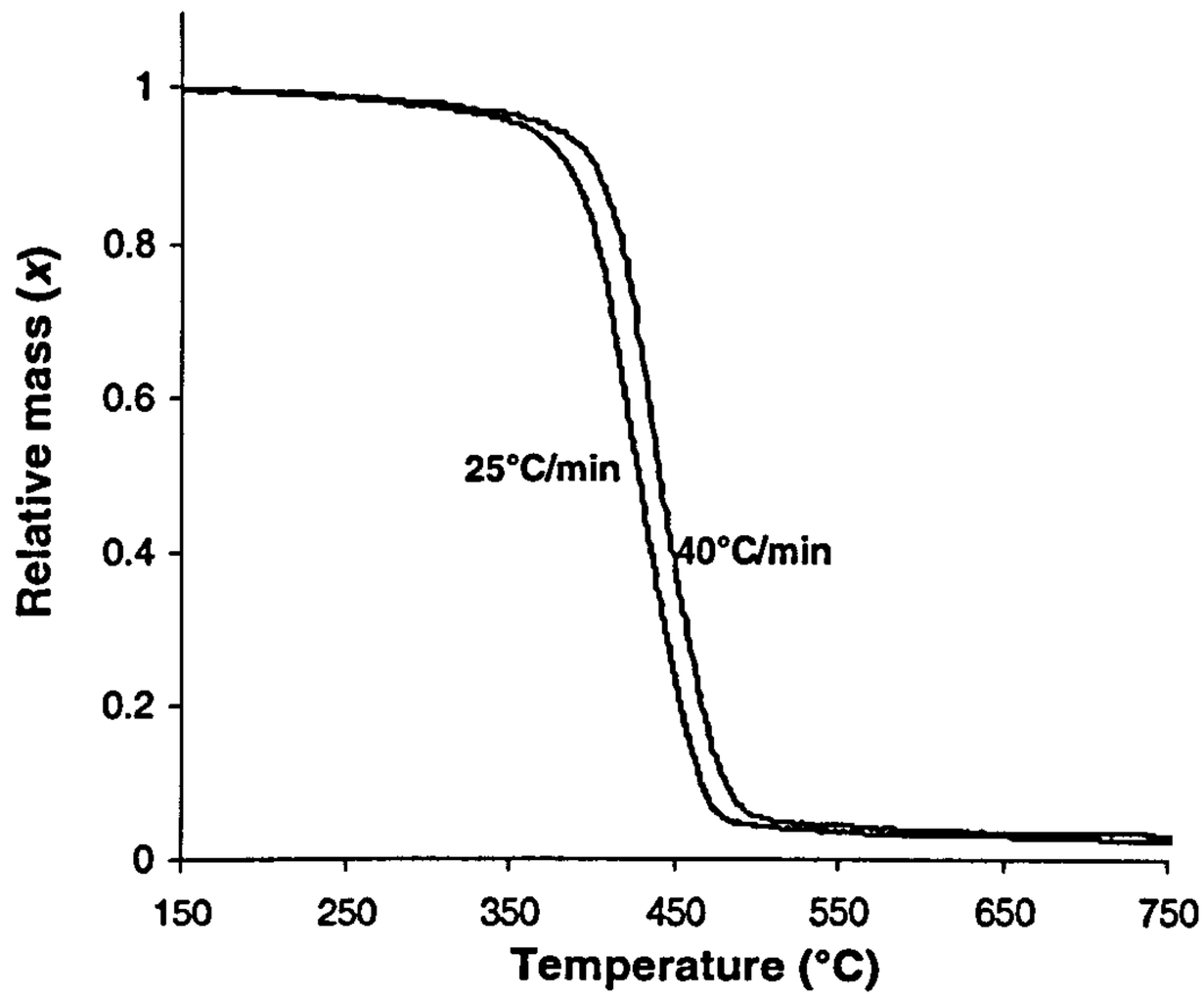

Figure 4.2 TGA test results for polyester resin. The mass loss curves are for two heating rates; 25°/min and 40°C/min.

Equation 4.1 can be rewritten as:

$$\frac{d\left(m/m_o\right)}{dt} = -A \cdot e^{\frac{B}{T}} \left(\frac{m - m_f}{m_o}\right)^n$$

If: $$\left(\frac{m - m_f}{m_o}\right)^n = f(x) \tag{4.2}$$

Then $$\dot{x} = A \cdot e^{\frac{B}{T}} \cdot f(x) \tag{4.3}$$

$$\therefore f(x) = \frac{\dot{x}}{A \cdot e^{\frac{B}{T}}} \tag{4.4}$$

where: $\dot{x}$ is the rate of change of relative mass and $B = E/R$.

f(x) was plotted against x for each heating rate. The relative mass *(x)* varied from a value of 1 to 0.02; when $x = 1$ decomposition had not yet taken place, and when $x = 0.02$, full decomposition had occurred leaving a small amount of residual resin.

By assuming initial values for A and B (E/R) the resulting curves looked similar to Figure 4.3(i). Equation 4.2 shows that as x varies from 1 to 0.02, *f(x)* must vary from 0.98 to 0. By altering the values of A and B, the two curves would either converge or diverge. The values of A and E which would cause the two heating rate curves to become superimposed on one another would be the values which best described the decomposition process. These values would then be valid for any given heating rate. The least squares method was adopted to find these values. Figure 4.3(ii) shows the two superimposed curves converging from an *f(x)* value of 0.98 to a value of 0.

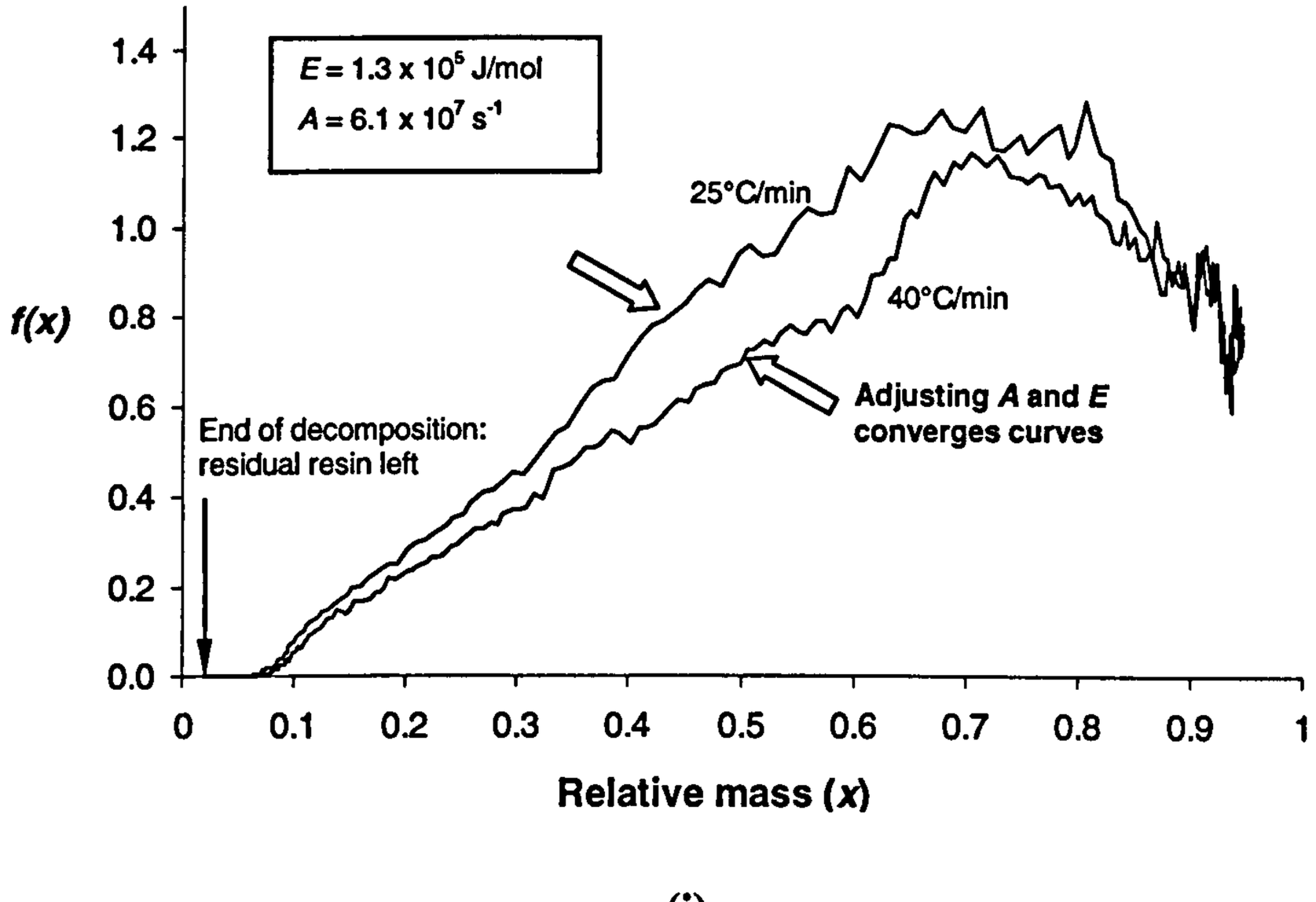

(i)

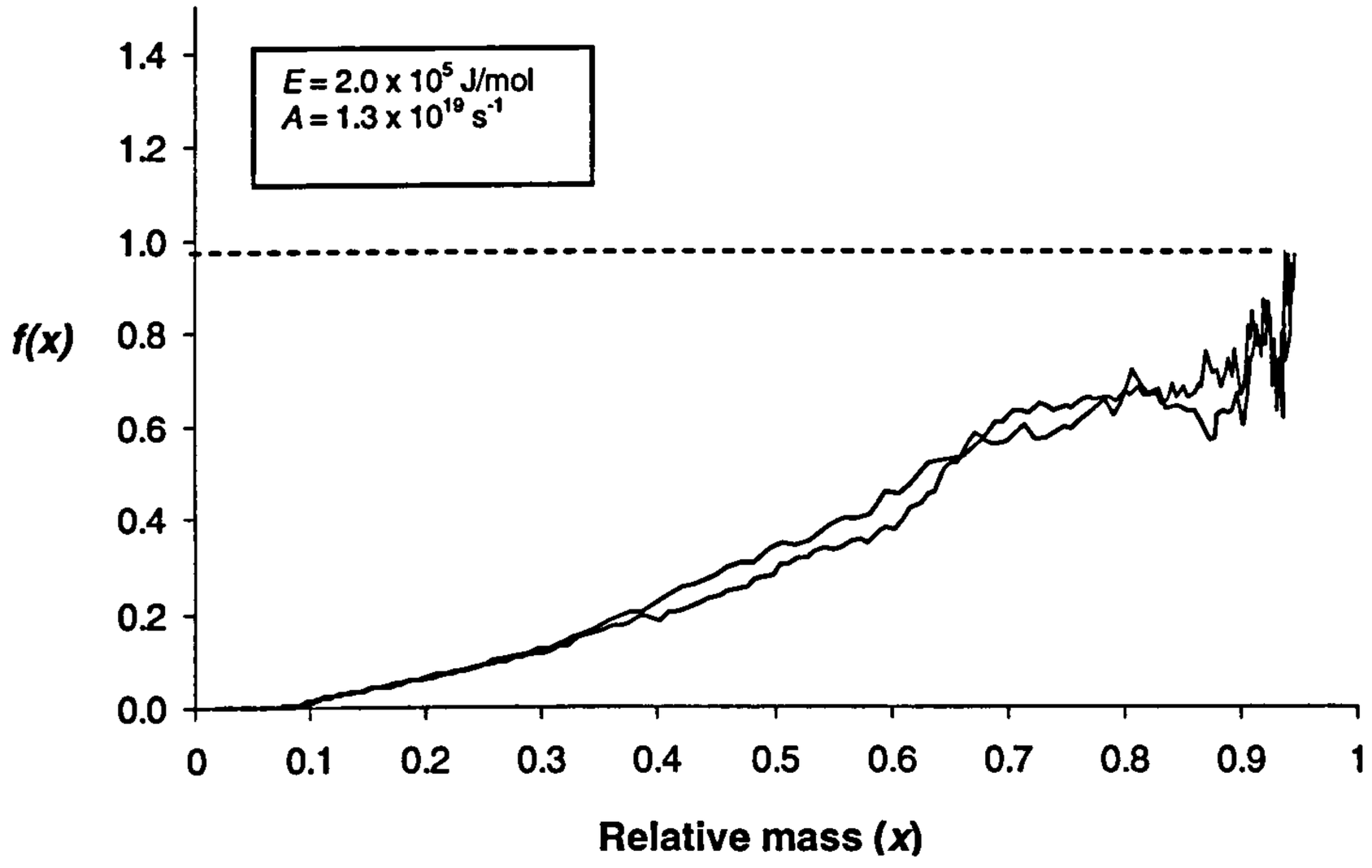

(ii)

Figure 4.3 Mass loss curve analysis. $f(x)$ was plotted against x and values for A and E adjusted until the curves converged at $f(x)$ =1.

In addition to the resin degradation parameters, the heat of combustion and order of reaction, n, were required for each material. The heat of combustion was assumed to be 226400 kJ and n was assumed to be 1 for all polymeric materials, based on the work of Friedman [97] and Henderson [55, 98]. A summary of the results is shown below.

Table 4.3 A summary of the resin decomposition rate constants for the three resin systems.

Resin	A (1/s)	E (J/mol)	n	H (kJ)
Polyester	6.31×10^{11}	1.83×10^{5}	1	226400
Vinyl ester	3.16×10^{12}	2.00×10^{5}	1	226400
Polypropylene	8.71×10^{18}	2.99×10^{5}	1	226400

Modelled mass loss curves were constructed using the measured mass loss rate and the derived decomposition rate parameters. Figure 4.4 shows comparisons between the measured and modelled mass loss curves for the three laminate systems. The modelled

curves described the decomposition region for both heating rates reasonably well in all cases. Hence it was concluded that the decomposition parameters were of sufficient accuracy to be used in the thermal model.

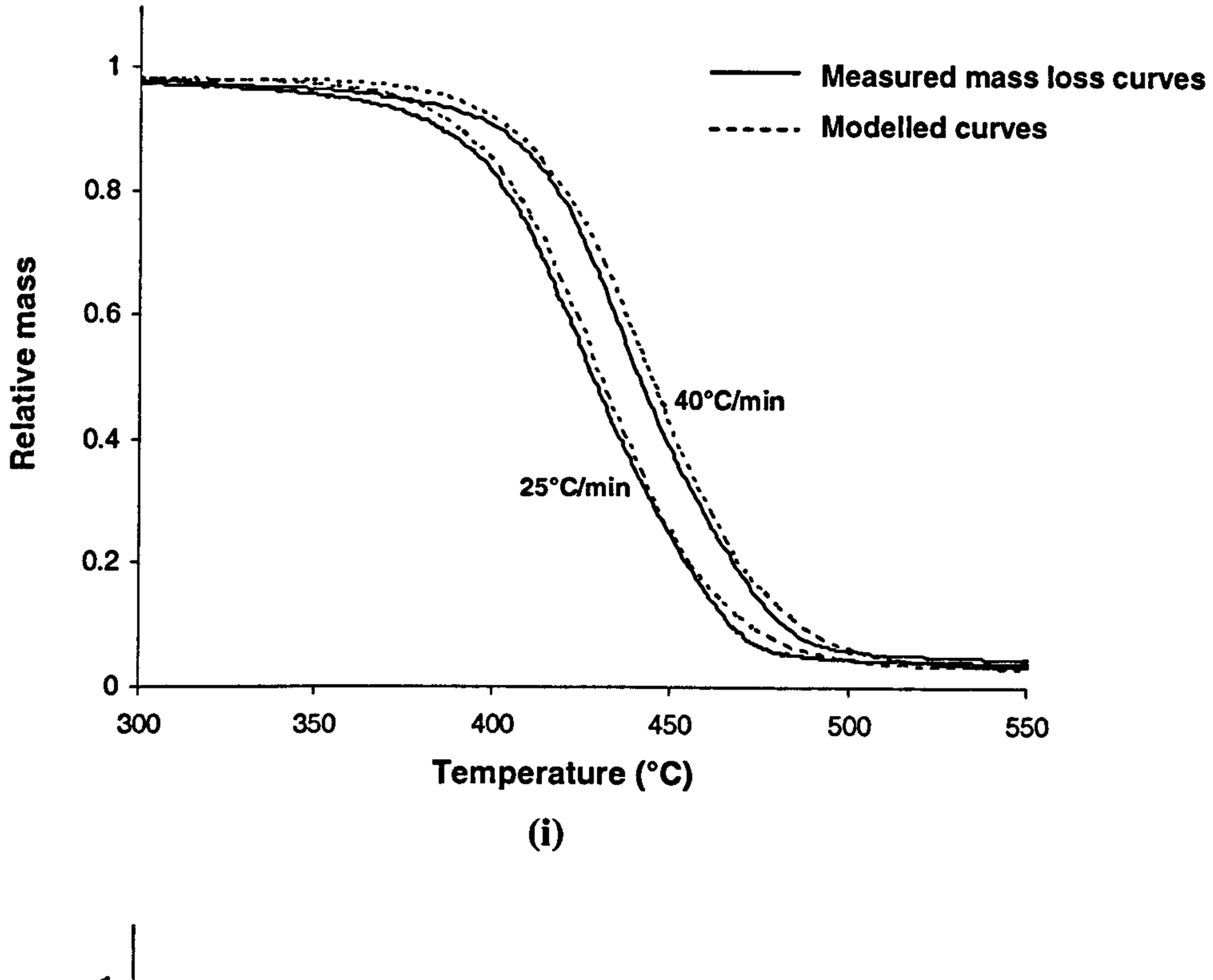

(i)

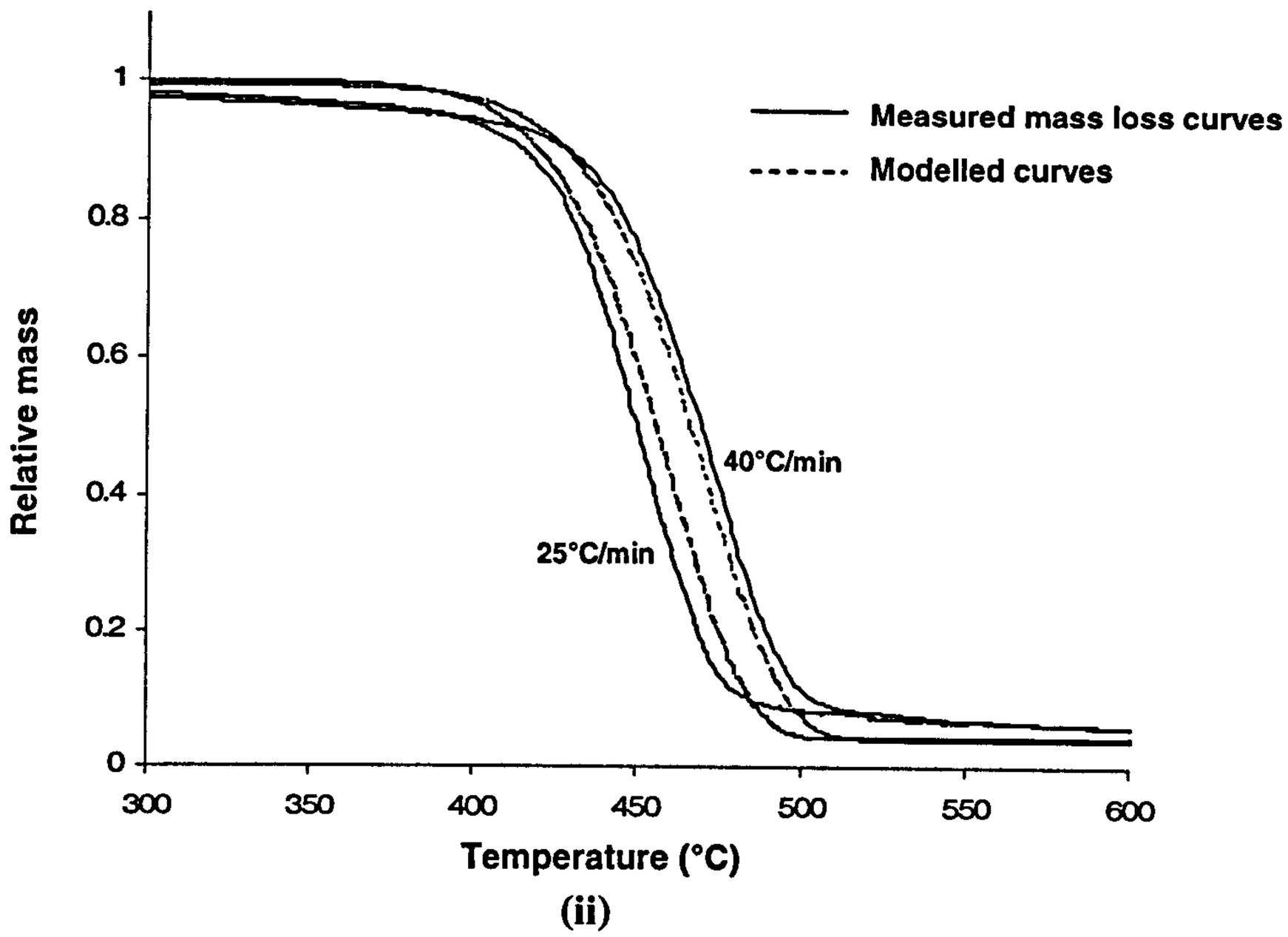

(ii)

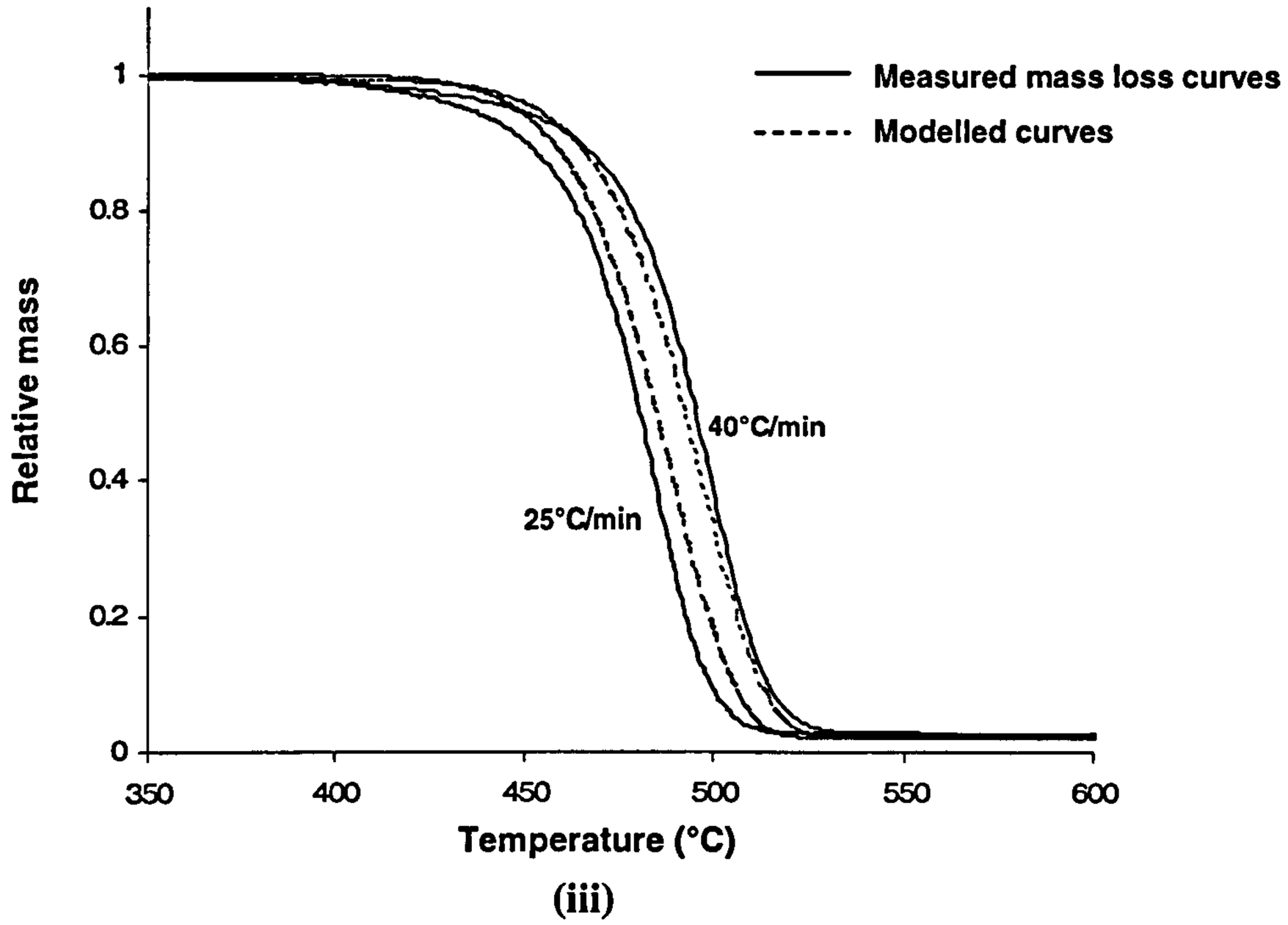

Figure 4.4 Measured and modelled mass loss curves for (i) a polyester laminate, (ii) a vinyl ester laminate, and (iii) a polypropylene laminate. Small samples were exposed to a 25°C/min heating rate and a 40°C/min heating rate. The main decomposition regions are shown (around 300-600°C).

4.3 Temperature dependent material properties

Tests were conducted on the variation of flexural modulus, tensile strength and compressive strength with temperature for each laminate system. A number of test rigs were designed in order to determine these properties at temperatures up to 400°C.

4.3.1 Flexural Modulus

Rectangular beam samples were placed under a three-point bend test within a controlled temperature cell, shown in Figure 4.5, to measure the variation of flexural modulus with temperature. The specially designed apparatus consisted of a set of rollers fixed to a test platform, and a temperature cell constructed using calcium silicate board and kaowool. The test was based on ISO 14125 "Fibre reinforced plastic composites – Determination of flexural properties" [99].

A load of 1N was applied to the centre of the beam and the deflection measured using a linear voltage displacement transducer (LVDT). The increase in deflection was measured over a period of 1000 seconds so that creep behaviour could also be investigated. A heat gun was used to increase the temperature slowly within the test cell; temperature controllers monitored and stabilised the cell temperature. This method was repeated for a range of temperatures from ambient to 160°C. It was not necessary to exceed 160°C as an adequate results trend was observed up to this temperature. The flexural modulus was calculated for a given temperature using Equation 4.5 [100]:

$$E = \frac{FL^3}{48\,\delta I} \tag{4.5}$$

where: E is the flexural modulus (Pa),

F is the applied load (N),

L is the sample span (m),

δ is the vertical deflection at the centre of the sample (m),

I is the second moment of area (m^4).

The effect of thermal expansion could significantly change a sample's dimensions. This in turn would affect the calculated flexural modulus value considerably. Before loading, the LVDT response was monitored whilst the sample was heated to a desired temperature. This response gave an indication as to the extent of the thermal expansion and was then used to derive the sample thickness for that given temperature. Hence a more accurate value of flexural modulus could be calculated.

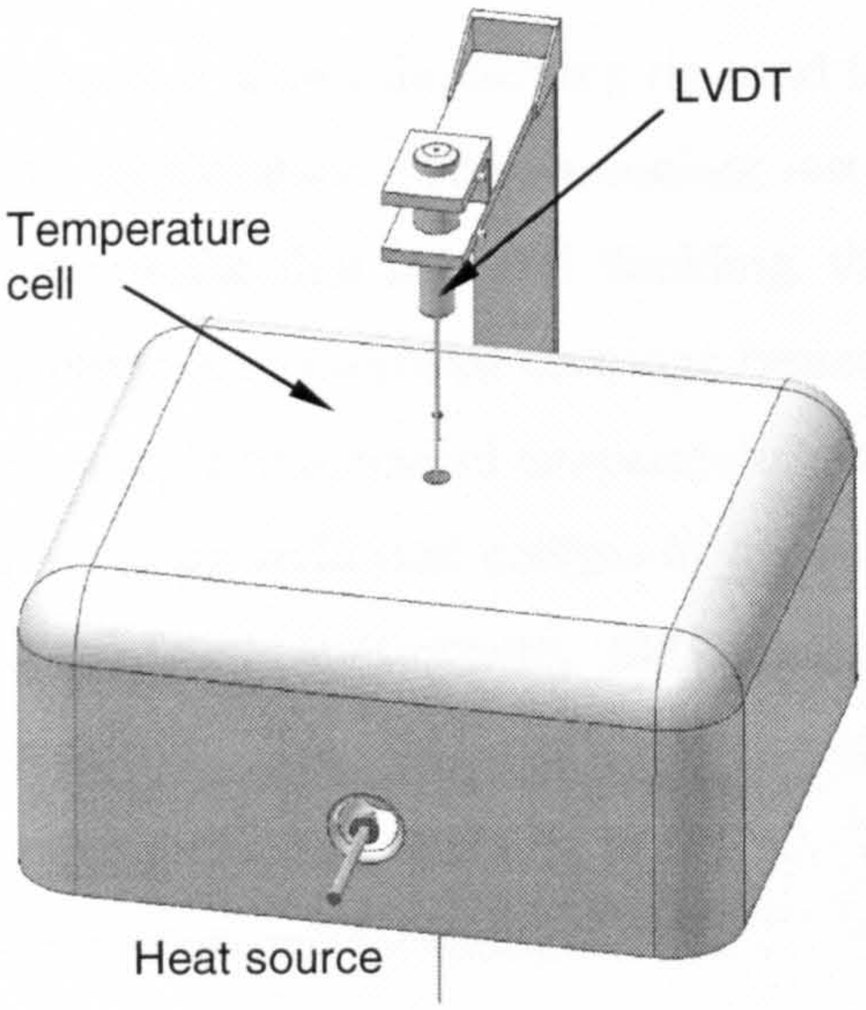

(i)

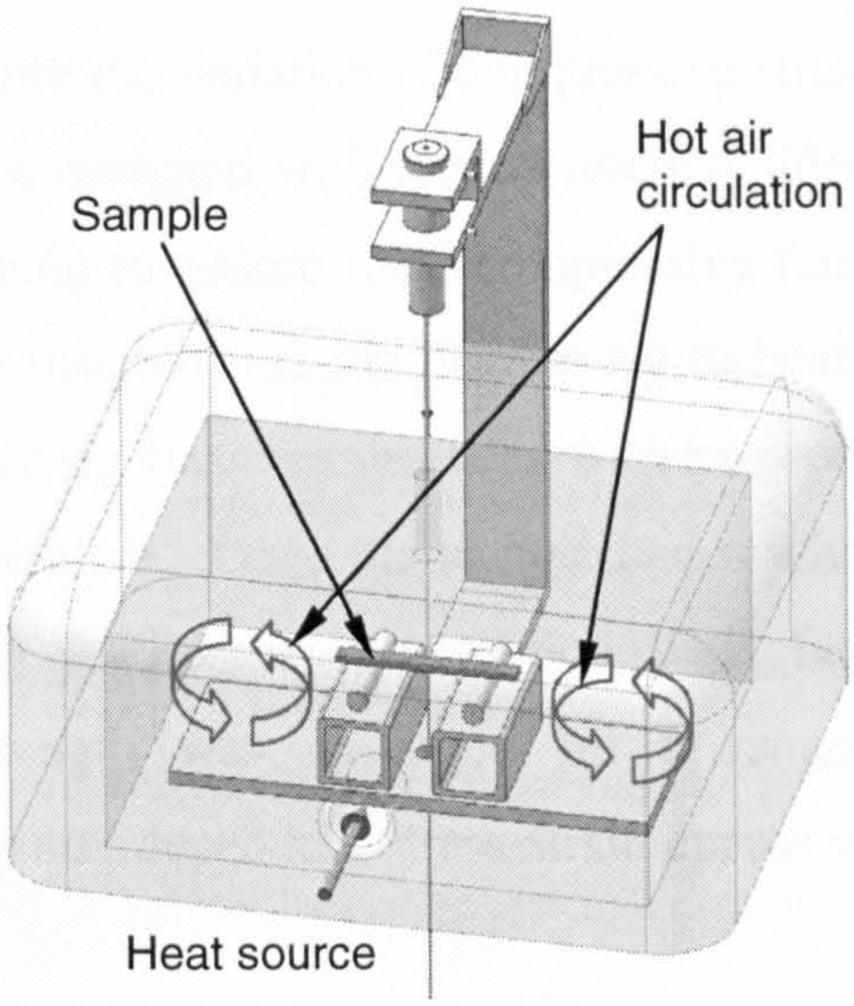

(ii)

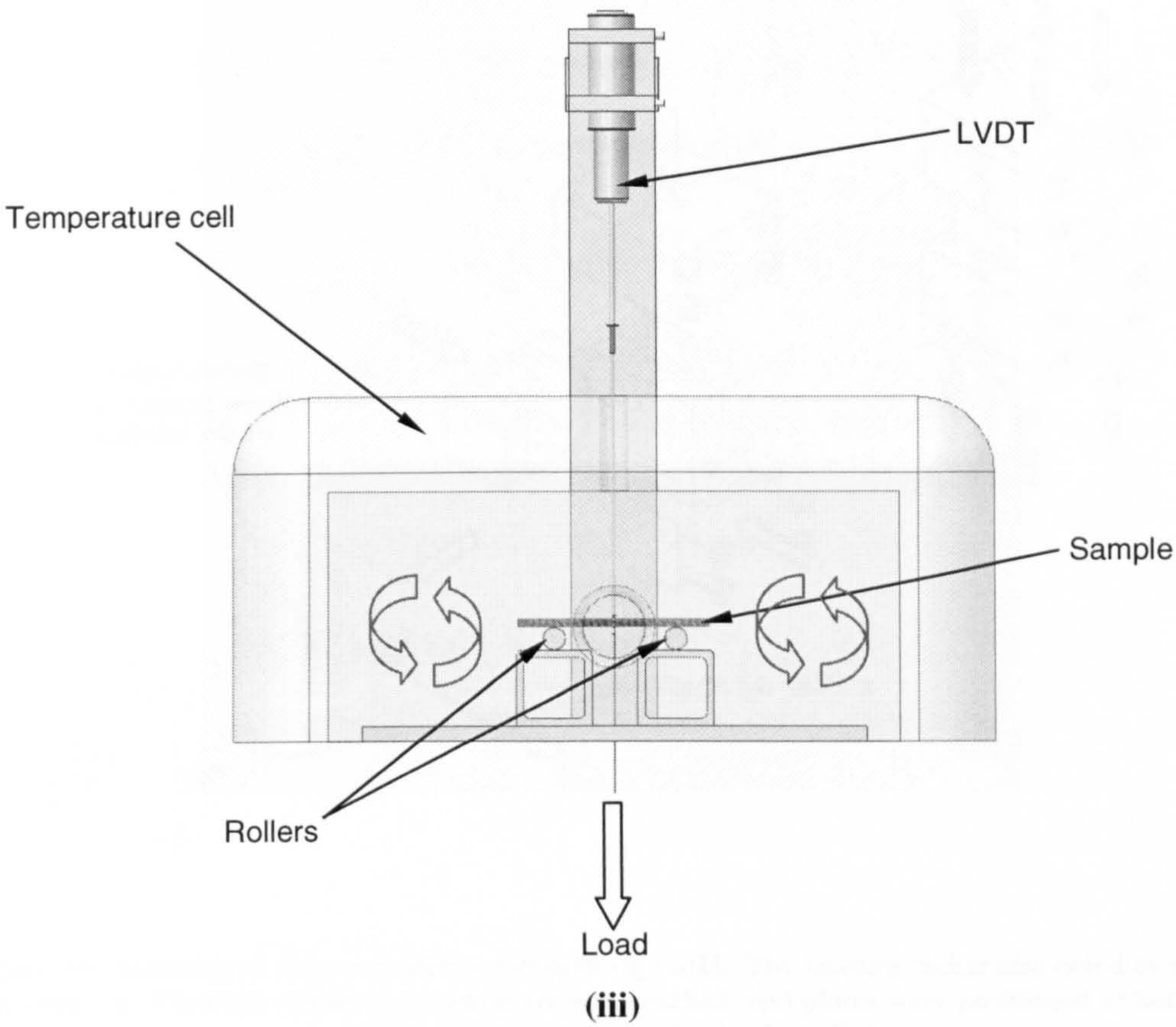

(iii)

Figure 4.5 The temperature cell used to measure flexural modulus over a range of temperatures. A static load was applied to the centre of the sample and the vertical deflection measured using an LVDT. Orthographic views are shown in (i) and (ii); (iii) illustrates the front view.

4.3.2 Compressive Strength

Figure 4.6 shows the heating rig used to measure the variation of compressive strength with temperature. The aluminium test rig was designed with sloped internal sides to suppress the first mode of buckling, thus helping to ensure local compressive failure. Temperature controlled cartridge heaters were inserted into the heating rig to heat the test sample to a desired temperature. The whole rig was then insulated with kaowool to allow more stabilised control of the test temperature. Once the sample had reached a consolidated temperature, the assembly was loaded in compression until failure occurred. The laminate's compressive strength was measured for a range of temperatures from ambient to 200°C. Temperature dependent stress-strain curves were also constructed for each material.

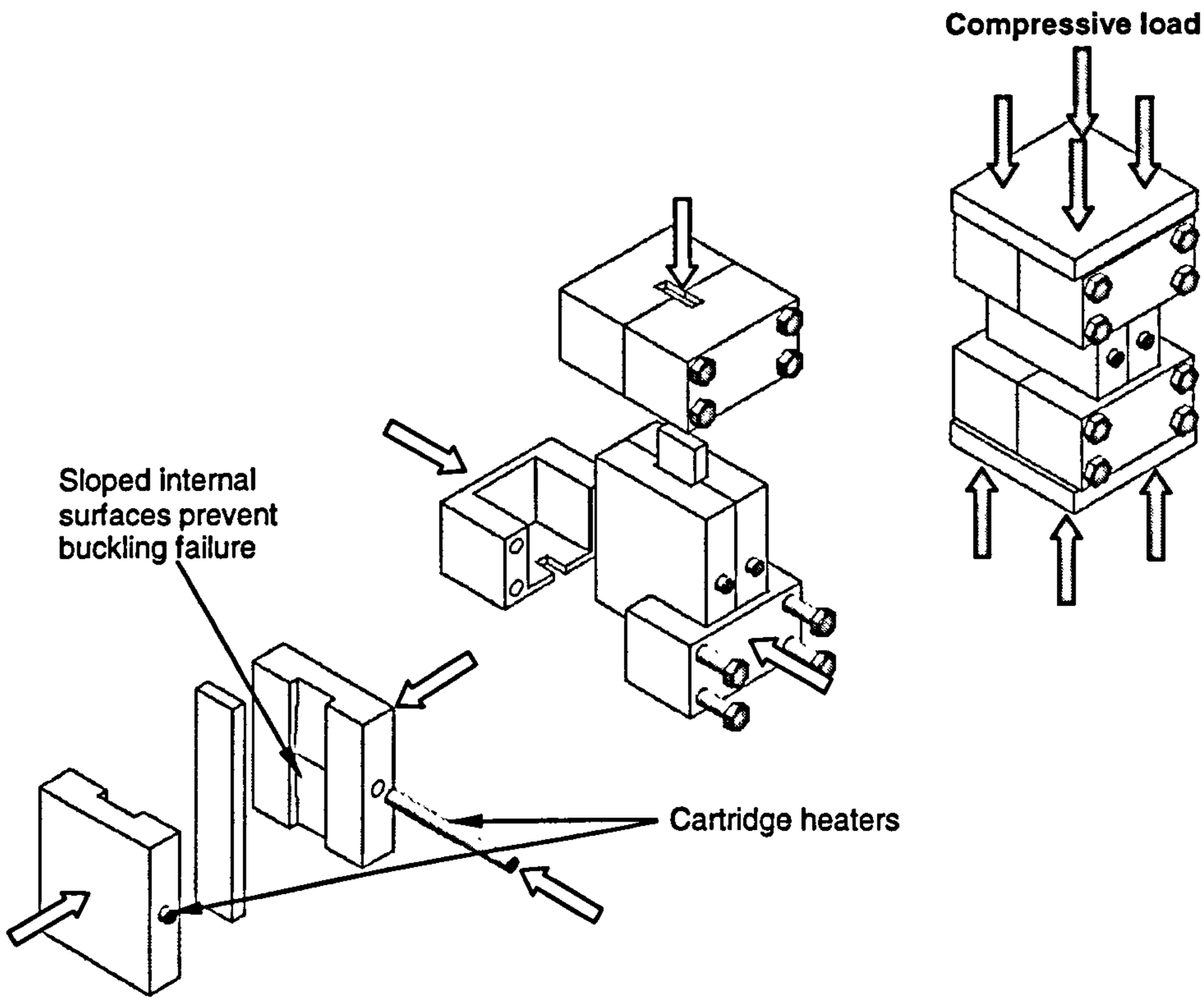

Figure 4.6 Assembly of the compressive strength rig [101]. The heating jacket also acted as an anti-buckling rig. Once the required temperature was reached, end plates were positioned at both ends of the rig and a compressive load applied.

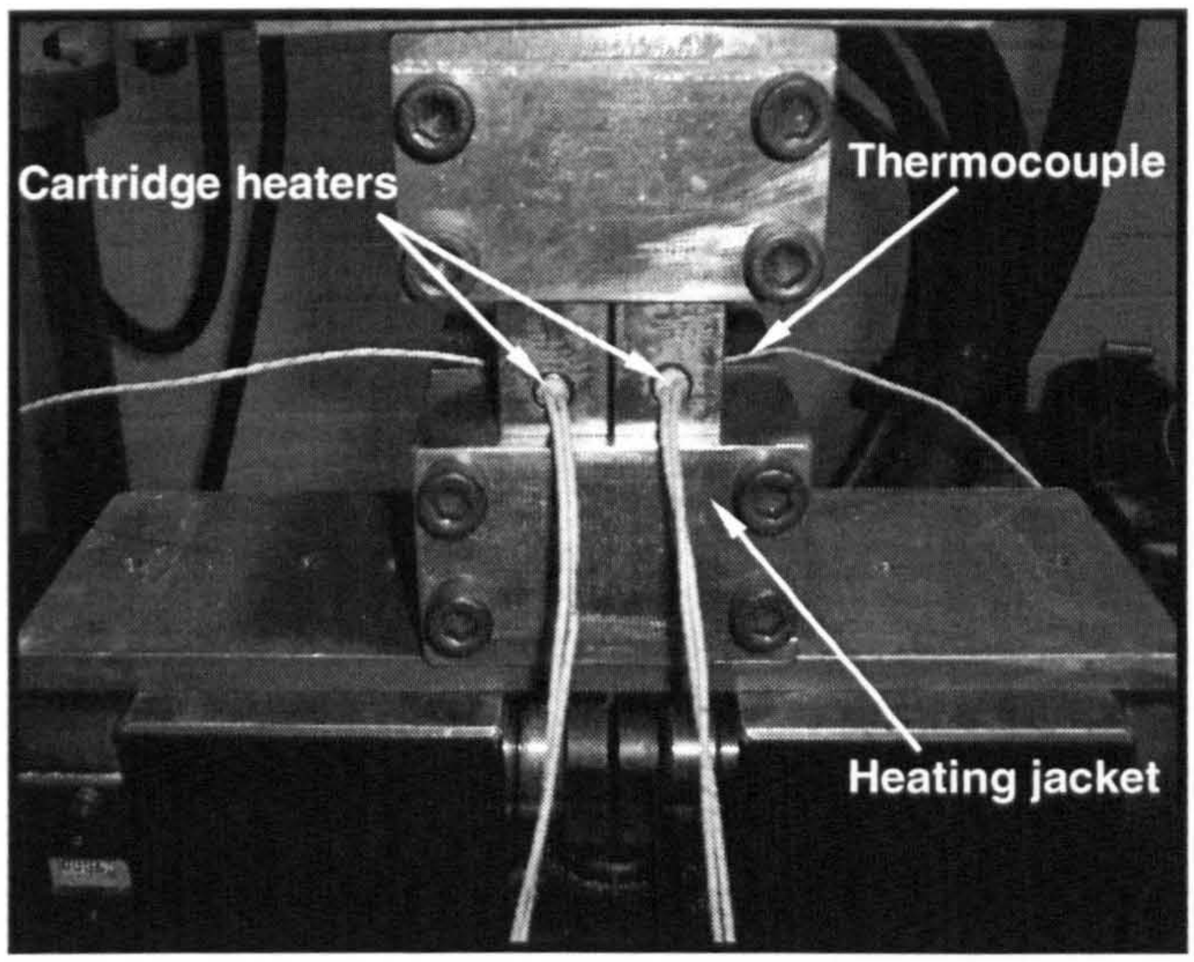

Figure 4.7 Photograph showing the compressive strength rig. Two thermocouples were used to monitor and control the rig temperature.

4.3.3 Tensile Strength

The variation of tensile strength with temperature was measured using conventional waisted samples. Samples were held in the grips of a test frame and heated using an aluminium heating jacket shown in Figure 4.8. The main advantage of this rig was that it only heated the sample gauge length. The test frame grips remained cool, and grip slippage or deformation was therefore avoided.

Cartridge heaters were inserted into the heating jacket and the whole apparatus insulated with kaowool. Temperature controllers allowed a desired temperature to be sustained during the test. Once the sample reached this consolidated temperature, the test frame applied a tensile load and the tensile strength of the material was measured. The aluminium heating jacket was designed to reach temperatures up to 400°C, allowing the strength of the residual glass to be determined at higher temperatures. These tests again provided useful stress-strain data for the materials at a range of temperatures.

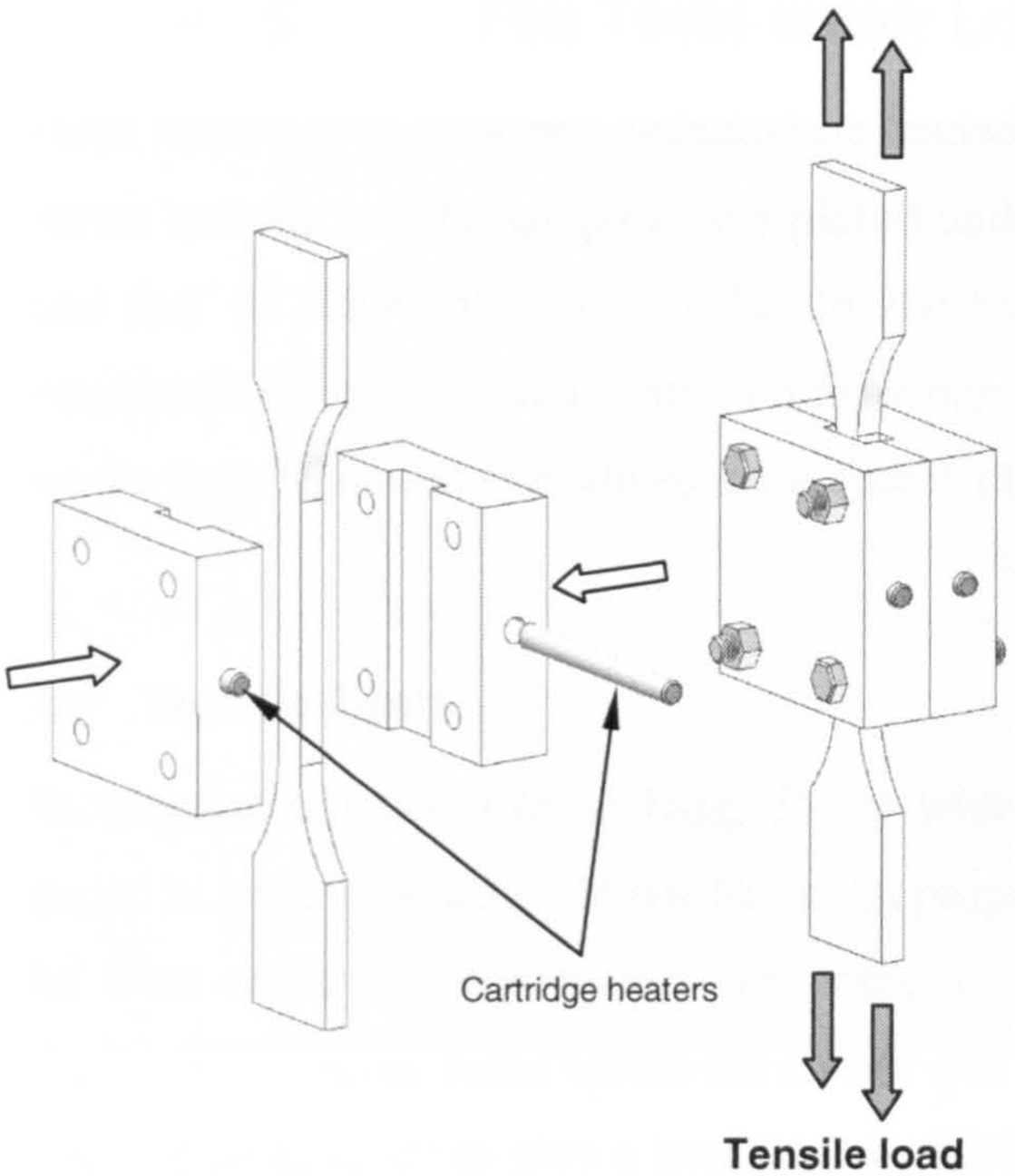

(i)

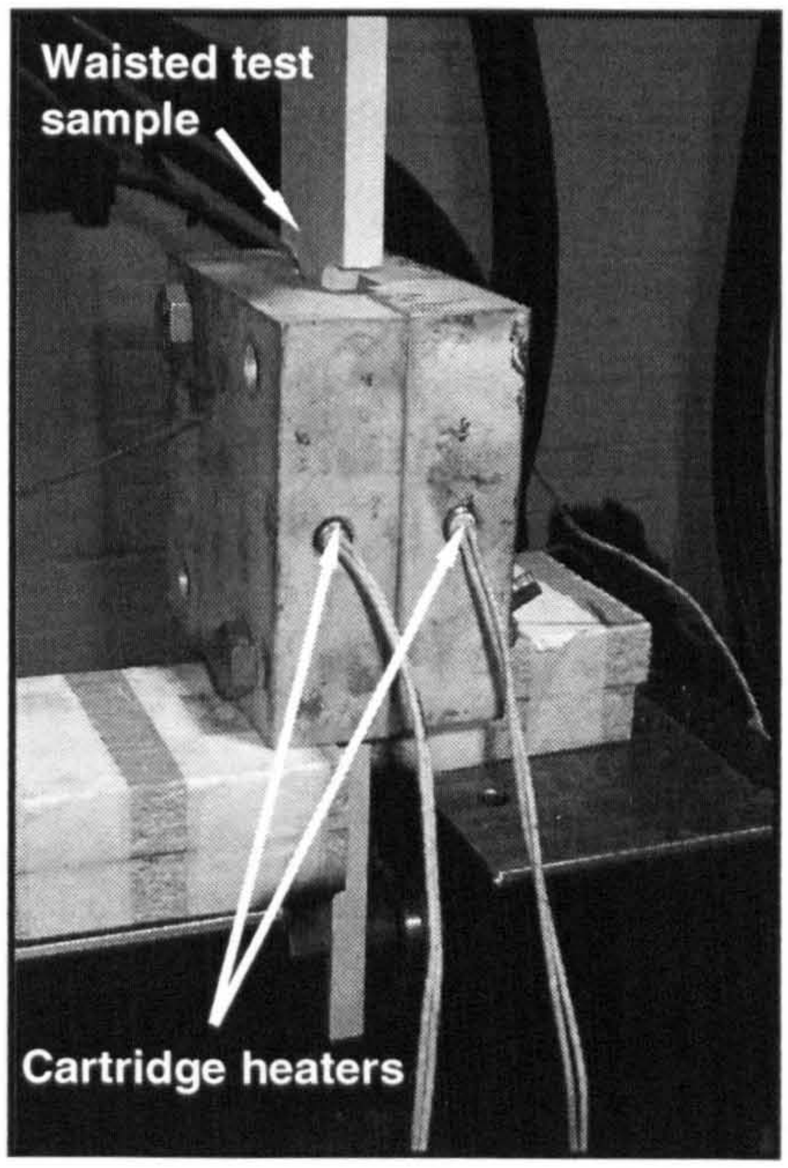

(ii)

Figure 4.8 (i) Assembly of the tensile strength heating jacket [101]. (ii) Photograph of a waisted sample held in the test rig.

Chapter 5 Fire Tests under Load

Small scale fire tests were conducted on loaded laminate samples using the calibrated burner technique. The samples were placed under tensile or compressive loading and a heat flux of 50kW/m^2 was provided by the burner. The time to failure (TTF) was measured for a given load and stress rupture curves constructed for each material. These results were then used to evaluate the accuracy of the laminate model.

5.1 Tensile Tests

Rectangular samples 500mm long, 75mm wide and approximately 12mm thick were loaded in tension on a 500kN test frame. A propane burner was positioned 350mm from the front surface of the loaded specimen, as shown in Figure 5.1. The load was increased to a given value before the burner was ignited. Once ignited, the gas pressure was immediately set to give a heat flux of 50kW/m^2. The load was kept at a constant value throughout the test by varying the applied strain rate accordingly, and the time to failure recorded.

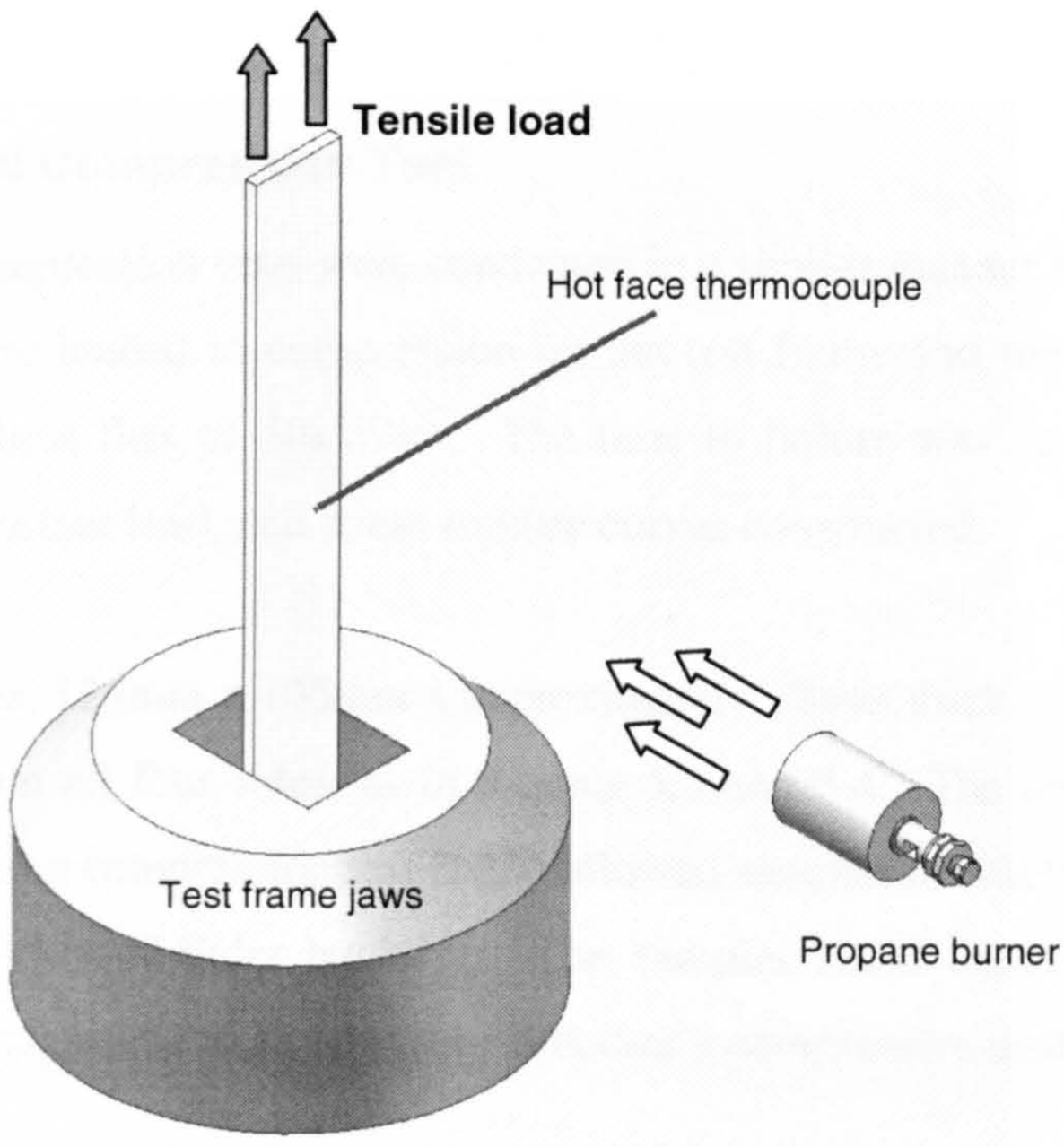

Figure 5.1 Schematic diagram of the tensile fire test. Samples were loaded on a test frame and then subjected to a one-sided heat flux of 50kW/m^2.

The test apparatus was insulated with kaowool to prevent the sample slipping in the grips and also to prevent the equipment from fire damage or overheating. Figure 5.2 shows front and rear views of a tensile fire test.

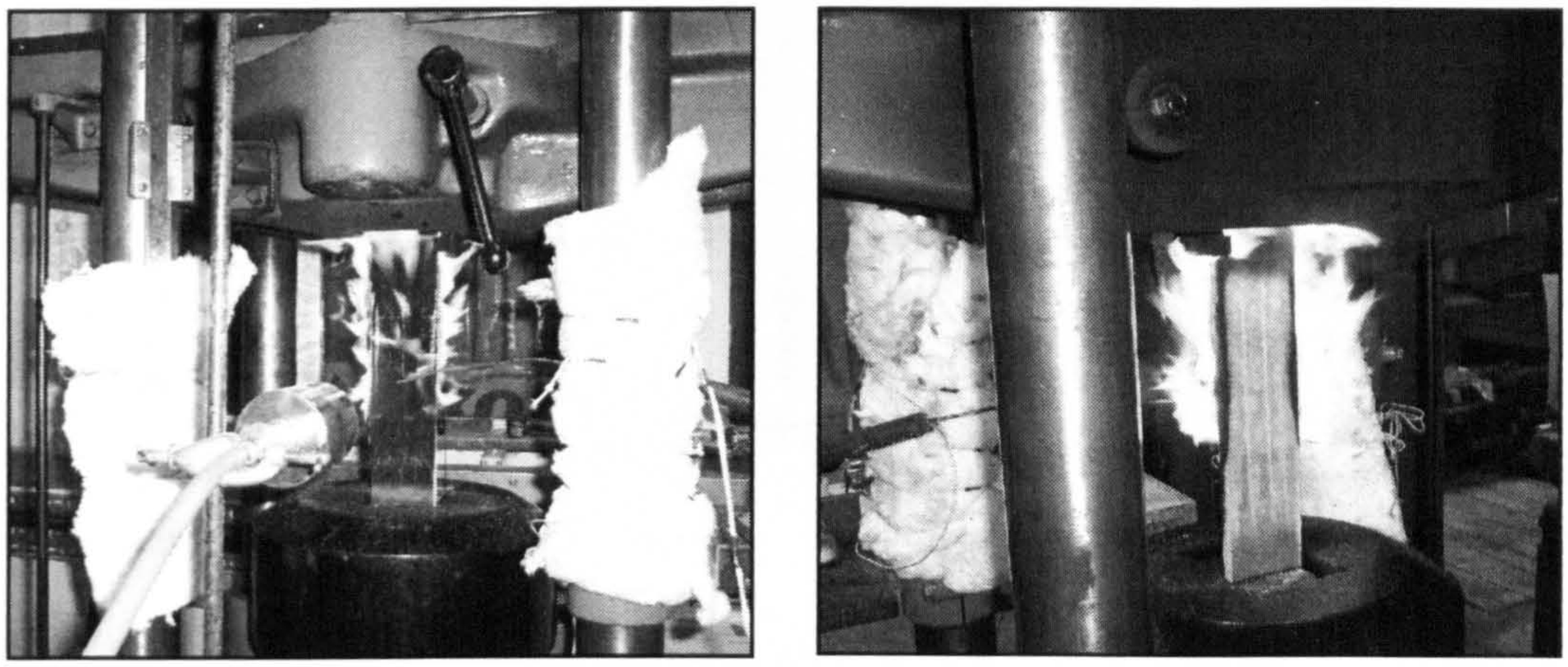

(i) **(ii)**

Figure 5.2 (i) Front and (ii) rear views of a polyester sample exposed to a 50kW/m^2 fire whilst subjected to a constant load of 100kN.

5.2 Constrained Compression Test

The constrained compression tests were conducted in a similar manner to the tensile fire tests. Samples were loaded in compression on the test frame and the propane burner used to provide a heat flux of 50kW/m^2. The time to failure was again recorded for samples under a constant load, and stress rupture curves constructed.

Rectangular samples, 125mm x 105mm x approximately 12mm thick, were held in a rig designed to constrain all four sides, as in Figures 5.3 and 5.4. The test rig, similar in principle to the Boeing compression test [102], allowed samples to reach higher loads by reducing the possibility of Euler buckling. The samples could therefore be tested at stresses similar in magnitude to a composite structure's compressive design stress.

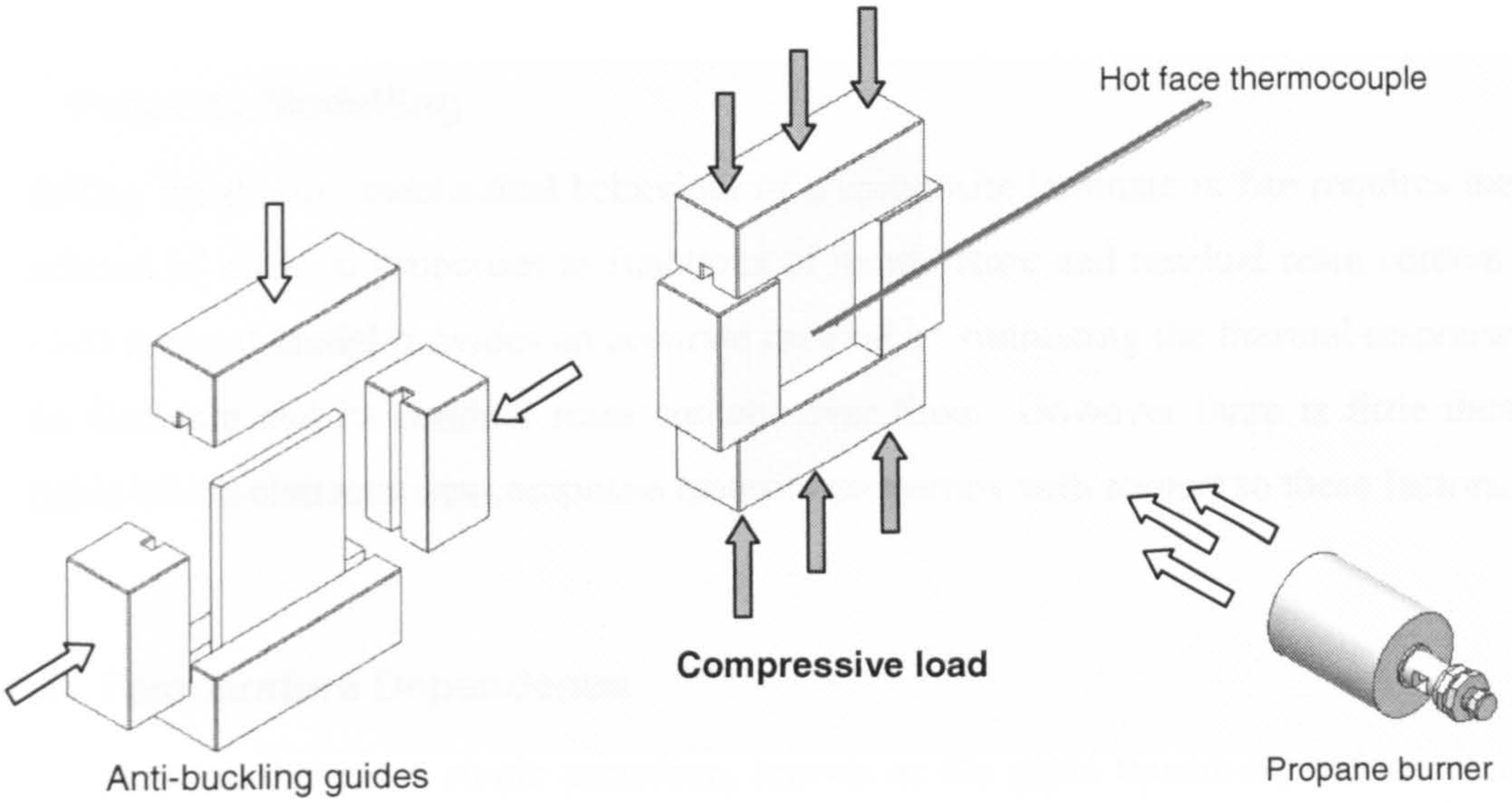

Figure 5.3 The constrained compression test. The edges of the test sample are constrained by four steel blocks to suppress Euler buckling.

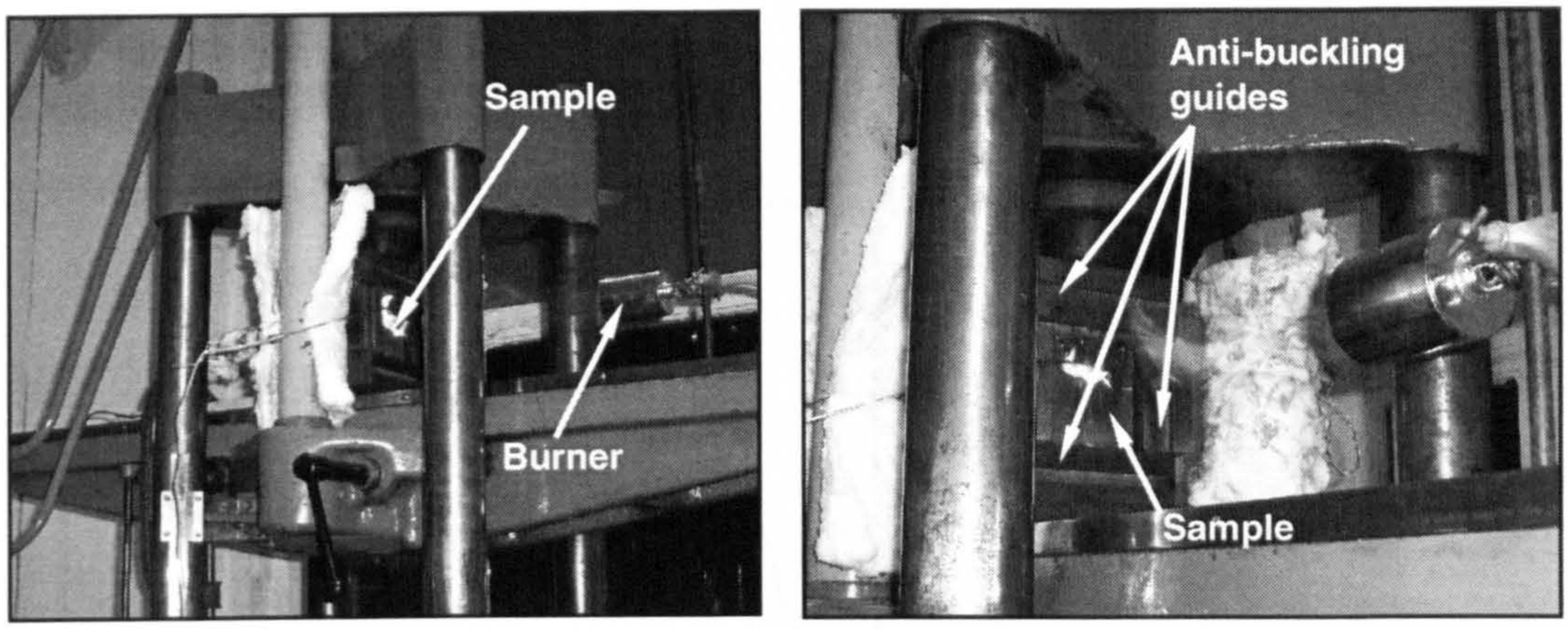

(i) **(ii)**

Figure 5.4 Photograph showing (i) a polyester sample under a compressive load of 50kN in a 50kW/m^2 fire, and (ii) a close-up picture showing the anti-buckling guides used to suppress Euler buckling.

Chapter 6 Results

6.1 Property Modelling

Modelling the thermo-mechanical behaviour of a composite laminate in fire requires the calculation of material properties as functions of temperature and residual resin content. The 1-D thermal model provides an accurate method of simulating the thermal response of the laminate and its residual resin content over time. However there is little data available which characterises composite material properties with respect to these factors.

6.1.1 Temperature Dependence

For thermosets, there is a single transition, known as the glass transition, before resin decomposition begins. Properties, such as flexural modulus, shear modulus, tensile strength and compressive strength, decrease rapidly through this region from an un-relaxed value (P_U) to a relaxed value (P_R), illustrated in Figure 6.1. This reduction is due to thermal softening of the polymer matrix from a glassy condition to a rubbery state. The glass transition temperature (T_g) is the temperature around which this transition normally occurs, although the drop in properties actually occurs over a wide temperature range.

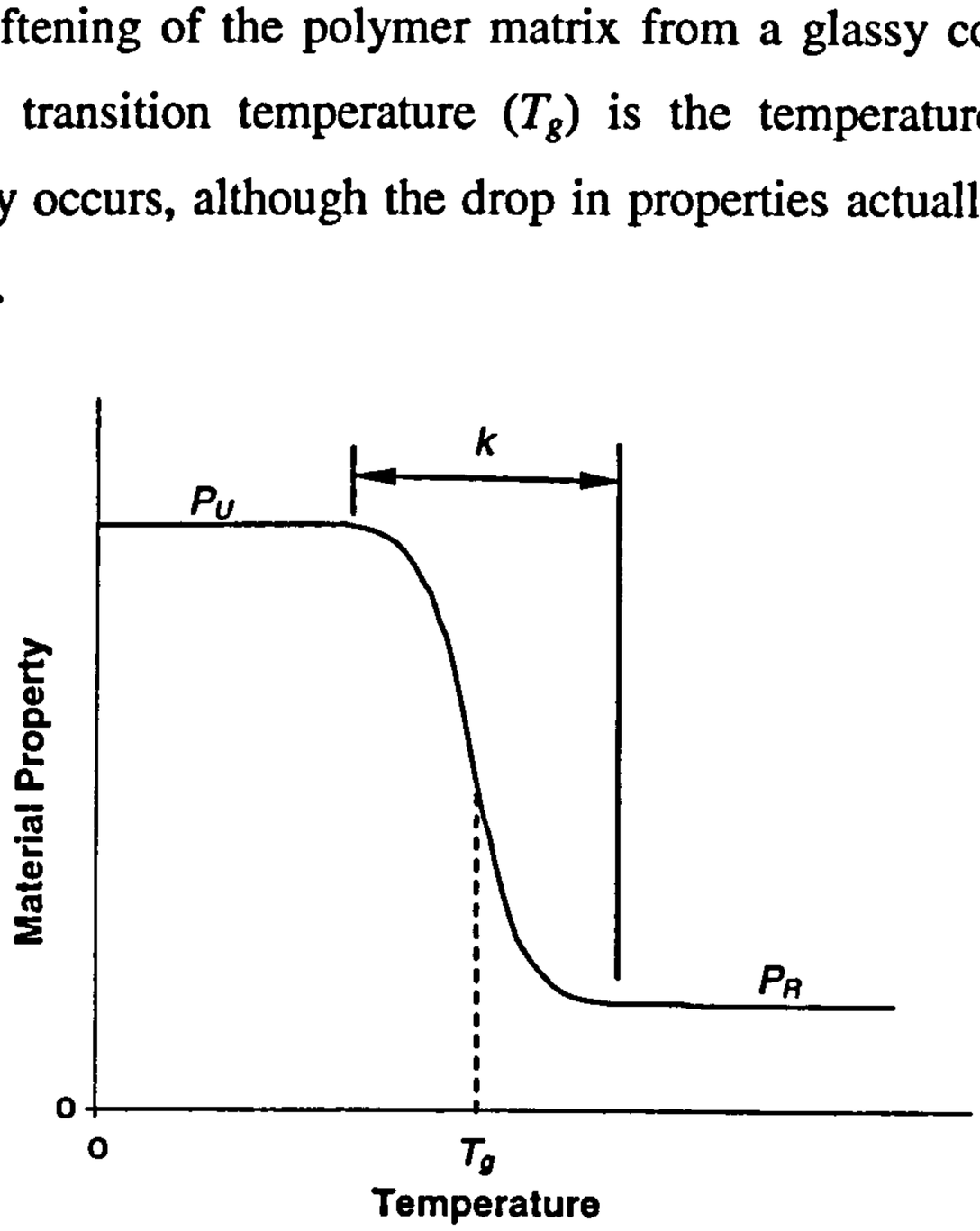

Figure 6.1 The glass transition region showing the reduction in mechanical properties with increasing temperature. (The parameter *k* is a measure of the breadth of the transition.)

A polynomial in temperature would appear to be an ideal method of describing a property such as flexural modulus in this transition region [85, 103]. However, in order to achieve sufficient accuracy, a polynomial of order five or six would be required, and the relationship would only be reliable within the range of fitted data as demonstrated in Figure 6.2.

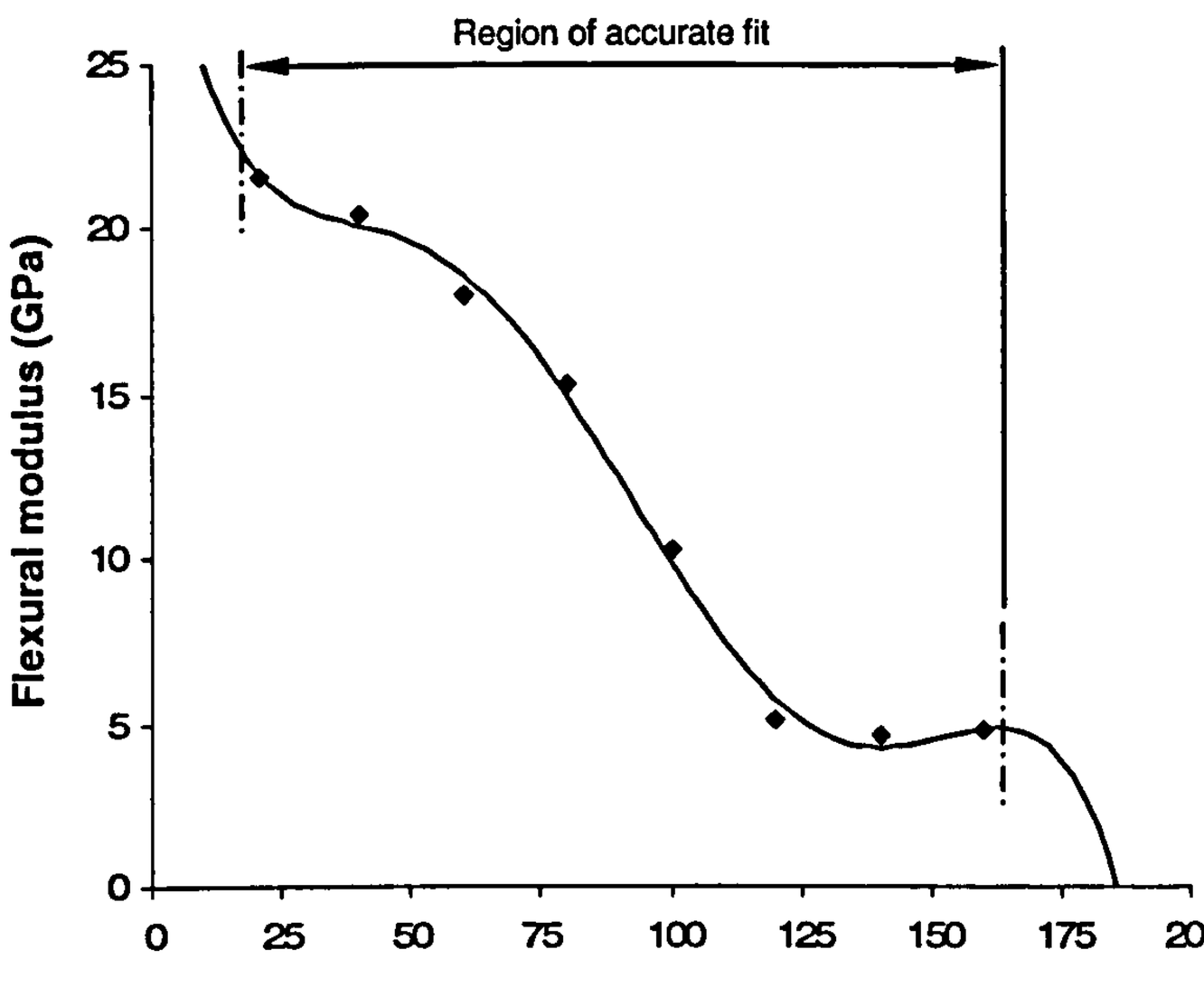

Figure 6.2 Flexural modulus results over a range of temperatures for a glass/polyester laminate. The fitted curve is a 5th order polynomial in temperature. Note that outside the measured data range, the polynomial fit loses accuracy.

An alternative empirical relationship was found to give an excellent fit to the test data. Using the hyperbolic tanh function, the transition from P_U to P_R was successfully modelled by the following relationship:

$$P(T) = P_R + \left(\frac{P_U - P_R}{2}\right) \cdot \{1 - \tanh[k \cdot (T - T')]\} \qquad (6.1)$$

where: $P(T)$ is a particular material property,

P_U and P_R are the un-relaxed and the relaxed property values respectively,

k is a constant relating to the breadth of the transition,

T' is a modelled transition temperature (°C) around which the fall in properties occurs (often similar in value to the material's glass transition temperature T_g)

The addition of two further constants would allow the calculation of the temperature variation of P_U and P_R, but it was concluded that this provision was not required, leaving the relationship with just four independent constants.

6.1.2 The Effect of Residual Resin Content

The effect of residual resin content on a particular property value was also modelled. Each mechanical property was modified by a power law factor:

$$P(T) = P_R + \left(\frac{P_U - P_R}{2}\right) \cdot \{1 - \tanh[k \cdot (T - T')]\} \cdot R^n \qquad (6.2)$$

where R^n is the power law factor for resin decomposition effect.

Not all of the material properties were as dependent on resin content as others. For example, the tensile strength of the laminate, which depends to a great extent on the strength of reinforcement, was not significantly influenced by resin content. Work conducted on the residual properties of glass/polyester laminates after fire by Gardiner et al. [82, 104] was used to fit the resin dependence value n. The results, shown in Figure 6.3, were normalised by dividing the residual property value by the undamaged laminate property value.

Figure 6.3(i) shows results for the residual compressive strength and flexural stiffness of a laminate after exposure to a 50kW/m^2 heat flux. The model curve shown has been fitted using a value of $n = 1$. The tensile strength, Figure 6.3(ii), was fitted with $n = 0$.

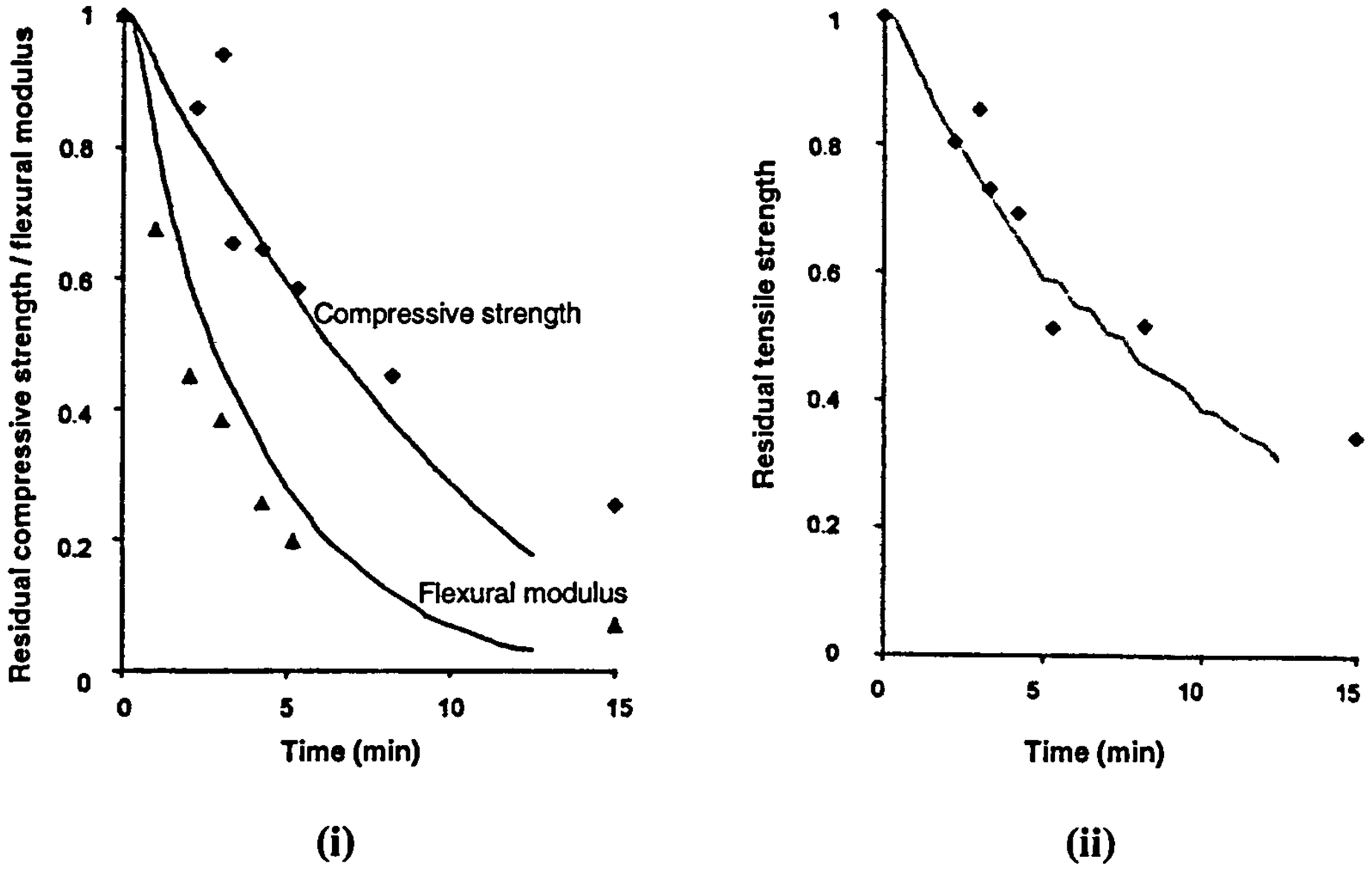

Figure 6.3 Normalised residual properties after exposure to a heat flux of 50kW/m^2[104]. Experimental points are the results of Gardiner et al. [82]. (i) Continuous curves are model predictions using n =1. (ii) The continuous curve is the model prediction using n = 0.

A value of $n = 0$ was therefore applied for tensile properties, reducing Equation 6.2 to Equation 6.1. Resin dependent properties however, such as flexural modulus, shear modulus and compressive strength, were described well using a value of $n = 1$.

6.2 Temperature Dependent Property Results

6.2.1 Flexural Modulus

The relationship described by Equation 6.1 provided an excellent fit for the variation in flexural modulus with temperature for polyester samples. A number of deflection readings were taken after 1, 10, 100 and 1000 seconds of loading. These deflection values were used to calculate the flexural modulus. The difference between modulus values at various time intervals corresponded to an effective 'shift' in the sample T_g value. It was possible to fit curves to these data points by varying the T' values in Equation 6.1, as can be seen from Figure 6.4.

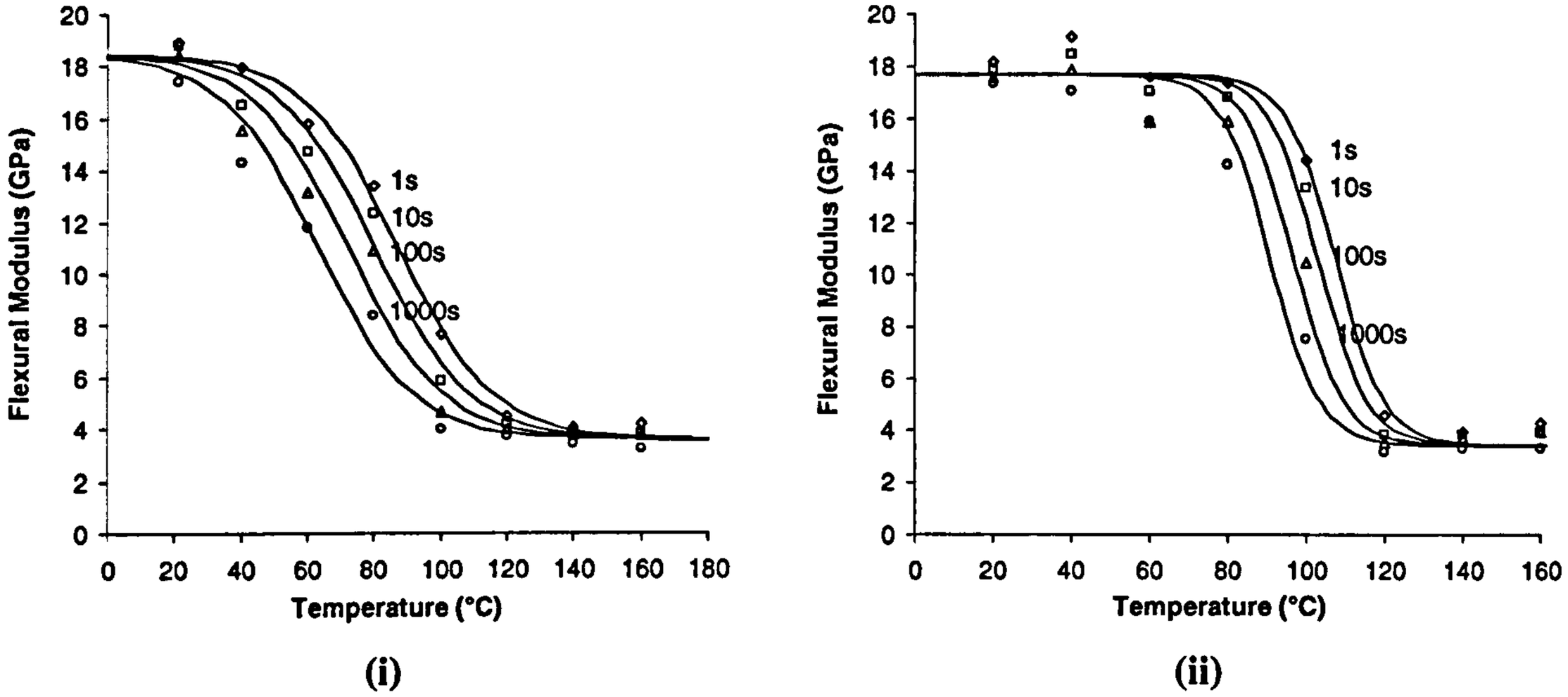

Figure 6.4 Variation of flexural modulus with temperature. Data points [1 (◊), 10 (□), 100 (Δ) and 1000 (○) seconds] are included to show the creep characteristics of each material. (i) Glass/polyester (ii) Glass/vinyl ester.

The effective "T_g shift" was not modelled as effectively for vinyl ester as for polyester. However, the general behaviour was considered to be satisfactory for the purposes of structural modelling. The flexural modulus test also demonstrated remarkable reproducibility. When the tests were repeated, the percentage error was estimated to be within 4% for polyester, and 6% for vinyl ester.

Polypropylene has two relaxation stages; a T' value of around 0°C [7, 11], and a high temperature crystalline relaxation which occurs prior to melting. This low value of T' effectively meant that the material had already passed the glass transition stage at the range of measured temperatures. The proposed relationship for temperature dependence (Equation 6.1) was therefore inappropriate in this case, and was modified to account for the two relaxation stages:

$$P(T) = P_R + \left(\frac{P_U - P_I}{2}\right)\cdot\{1-\tanh[k_1\cdot(T-T_1')]\} + \left(\frac{P_I - P_R}{2}\right)\cdot\{1-\tanh[k_2(T-T_2')]\} \quad (6.3)$$

where: P_U, P_I and P_R are the high (un-relaxed), intermediate and low (relaxed) temperature property values respectively,

T'_1 and T'_2 are the high and low temperatures around which each transition occurs.

k_1 and k_2 are the breadth of the high and low transition regions respectively.

Figure 6.5(i) shows the modelled flexural modulus curves for glass/polypropylene. Again, the creep effects were modelled by a T' shift but, in this case, the shift was applied at the two transition regions; around 0°C and 148°C. The percentage error calculated for the polypropylene tests was 2%.

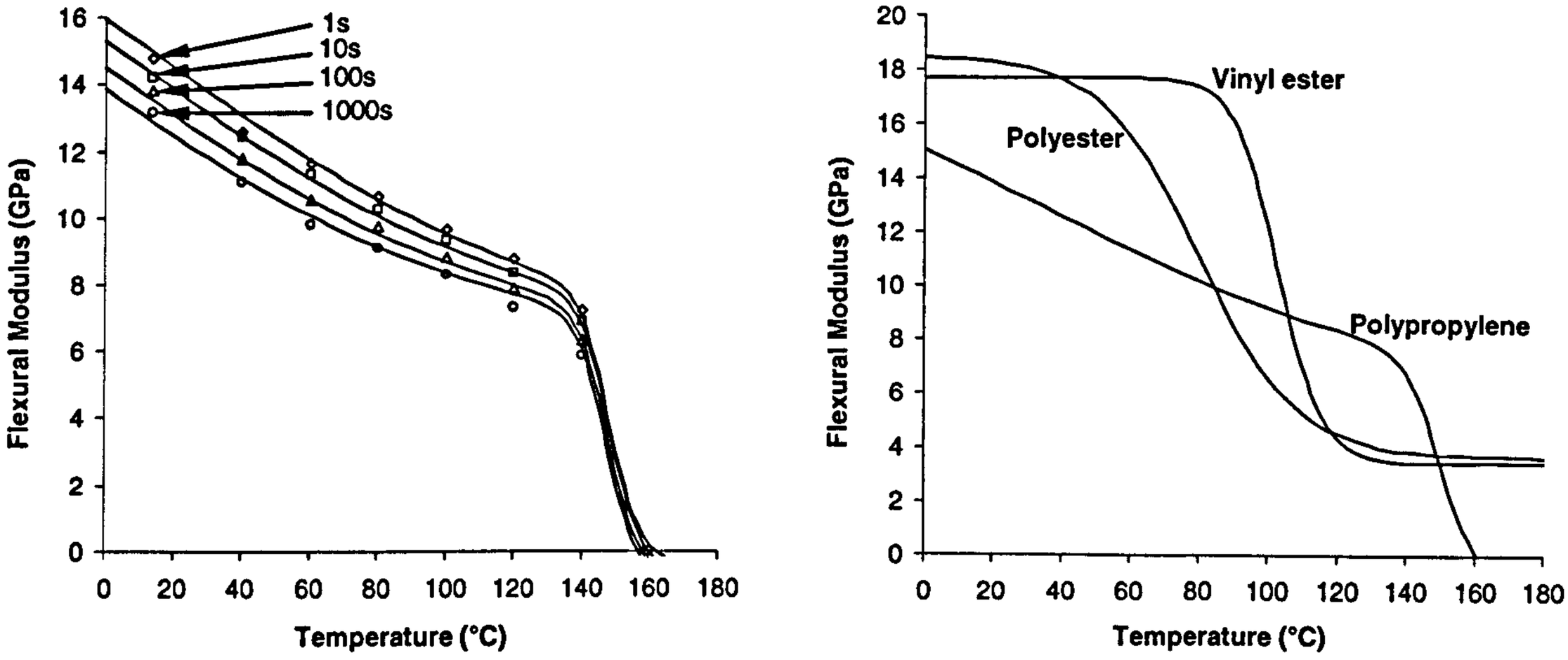

Figure 6.5 (i) The variation of flexural modulus with temperature for glass/polypropylene. 1 second (◊), 10 second (□), 100 second (Δ) and 1000 second (○) data points are included to show creep characteristics. (ii) A comparison of the variation of flexural modulus with temperature for all three laminate systems. 10 second curves are shown.

A comparison of all three systems is shown in Figure 6.5 (ii). The polyester laminate has similar stiffness to vinyl ester at room temperature and at high temperatures. The slightly superior properties of the vinyl ester laminate reflect its higher T_g value. Polypropylene, a crystalline thermoplastic, demonstrates the typical sharp drop in

properties for this type of material, as it approaches its melting point (around 140-160°C). The curves fitted for 10 second data points were used in the laminate model.

6.2.2 Compressive Strength Results

Figure 6.6 shows temperature dependent compressive strength results for the three laminate systems. Equation 6.1 provided an excellent fit for the polyester and vinyl ester laminates. Equation 6.3 was once again required to model the polypropylene system.

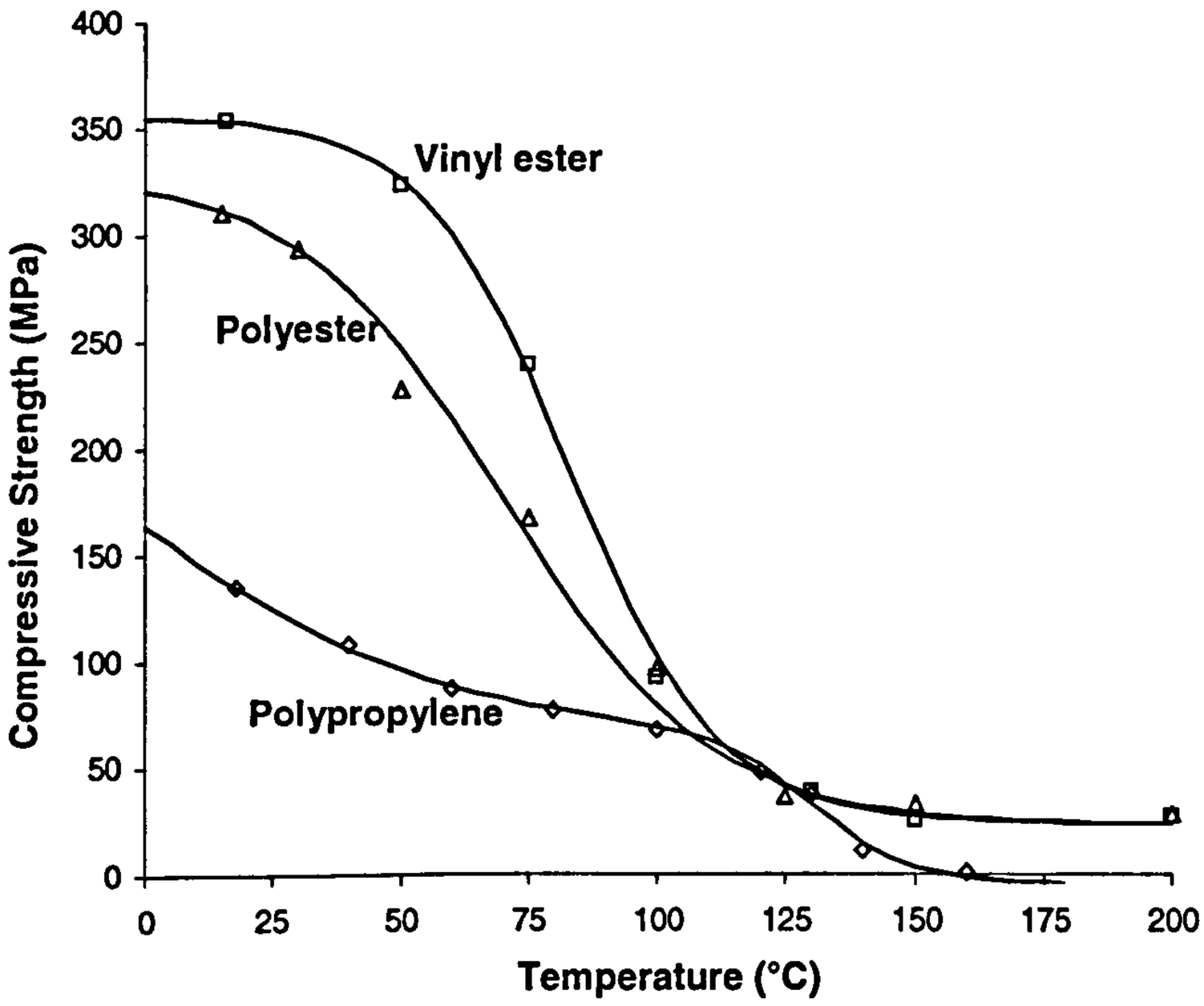

Figure 6.6 Variation of compressive strength with temperature for all three laminate systems. [Vinyl ester (□), polyester (Δ) and polypropylene (○).]

The polypropylene laminates exhibited lower levels of compressive strength even at low temperatures. The low intra-laminar shear strength of the polypropylene matrix and the woven architecture of the fibres would account for this. Woven laminates, having

inherent waviness and weave undulation, suffer from the fibre misalignment which leads to local shear deformation.

The polypropylene laminates show similar compressive strength to the thermoset systems between 100°C and 130°C. At higher temperatures however, the resin melts and there is effectively zero compressive strength. In contrast, the thermoset resins demonstrate greater residual high temperature structural capacity.

6.2.3 Compressive Stress-strain curves

Stress-strain curves were recorded for each material at a range of temperatures. Figures 6.7, 6.8 and 6.9 show compressive stress-strain curves for polyester, vinyl ester and polypropylene laminates respectively. Not only did these curves provide data on material response at elevated temperatures, but they were also used to model the structural response of composite laminates in fire, detailed in Chapter 7.

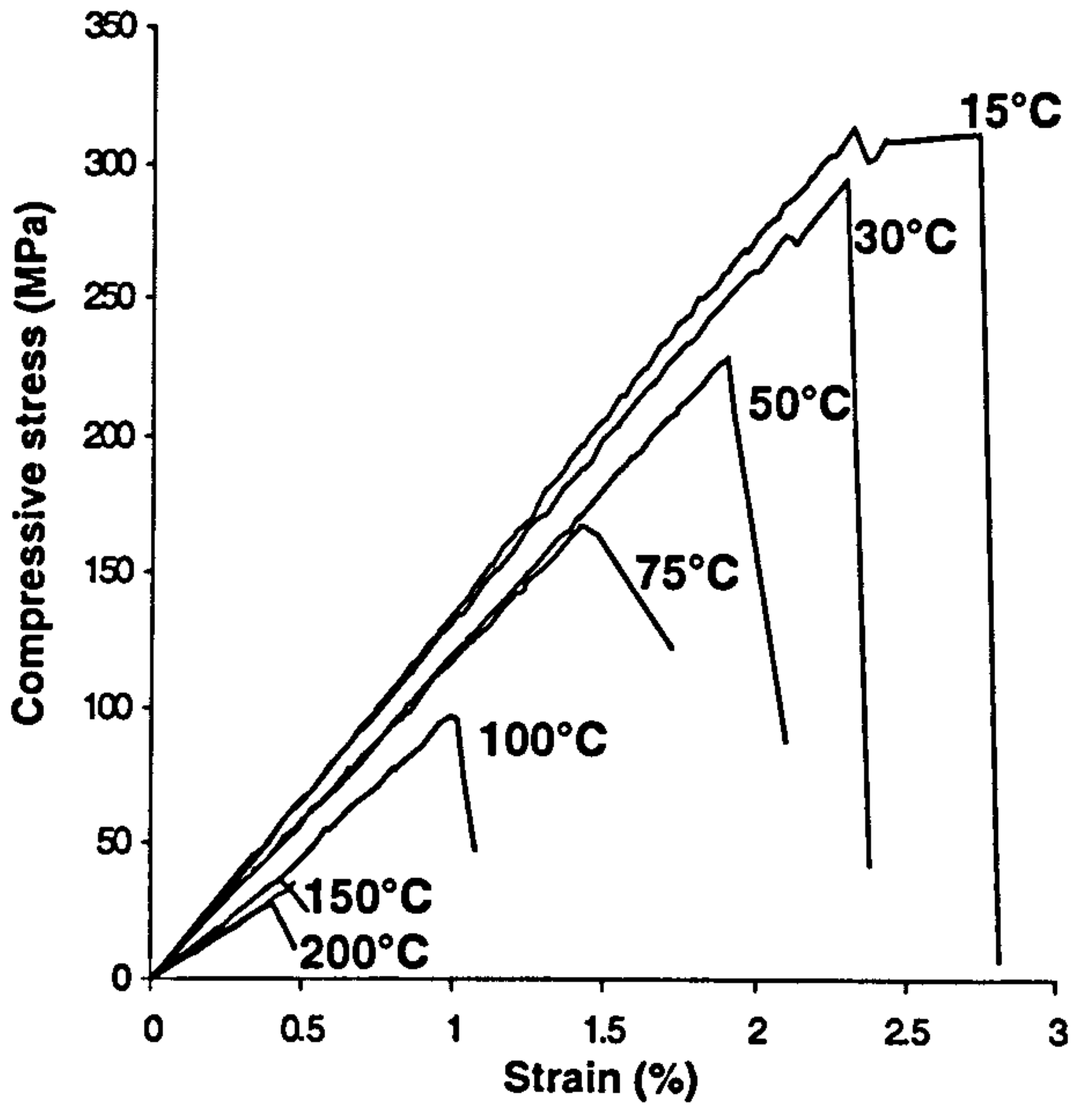

Figure 6.7 Compression stress-strain curves for glass/polyester at a range of temperatures.

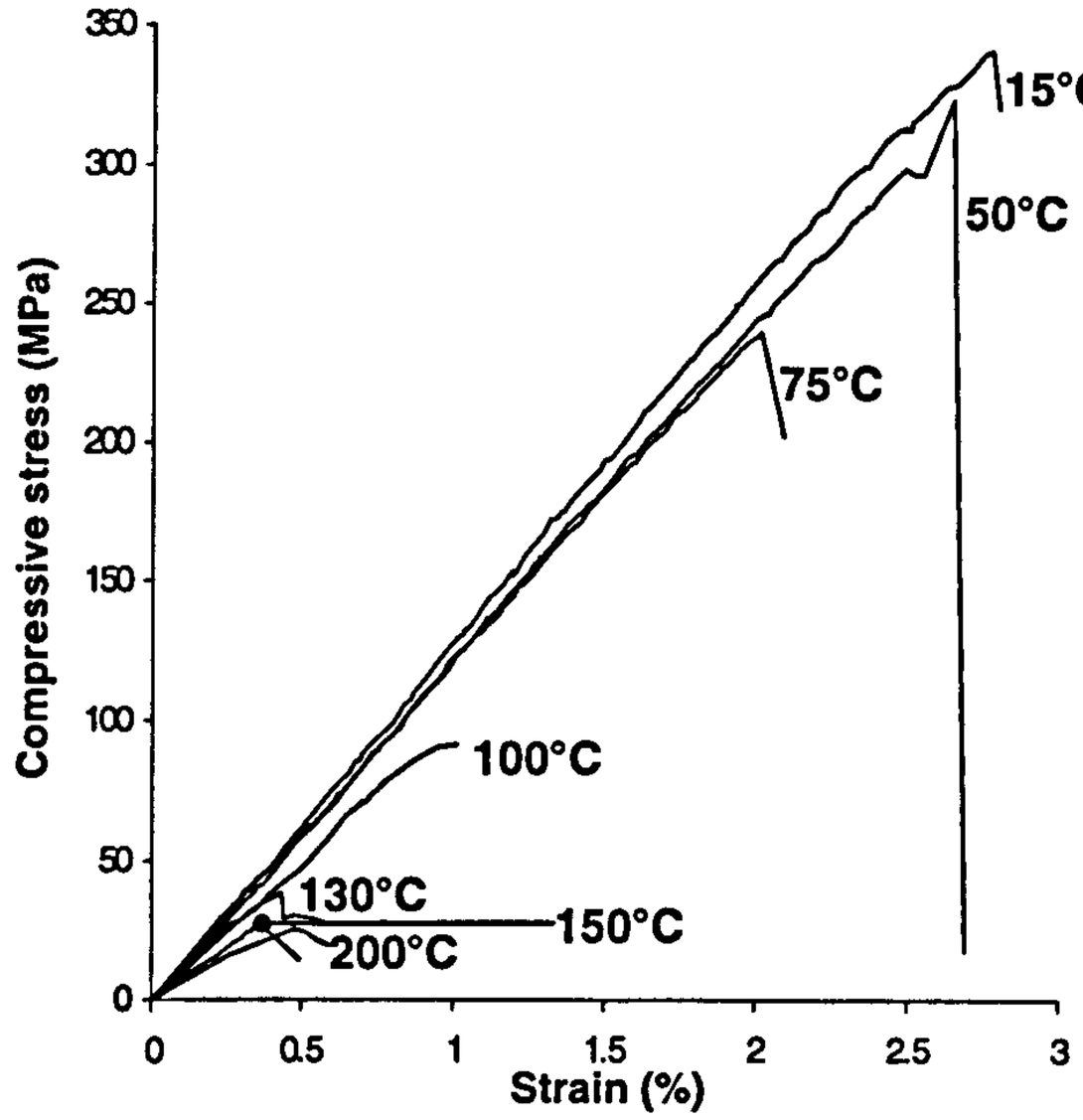

Figure 6.8 Compression stress-strain curves for glass/vinyl ester at a range of temperatures.

Figure 6.9 Compression stress-strain curves for glass/polypropylene at a range of temperatures.

6.2.4 Tensile Strength Results

Figure 6.10 shows the results of tensile strength measurements up to 400°C on the three laminate systems. Equations 6.1 and 6.3 were again used to model the reduction in properties in this temperature region. The initial drop in strength (which is apparent at around 70°C for polyester, 100°C for vinyl ester and 40°C for polypropylene) is due to initial resin softening, occurring as the materials are heated beyond their respective glass transition temperatures.

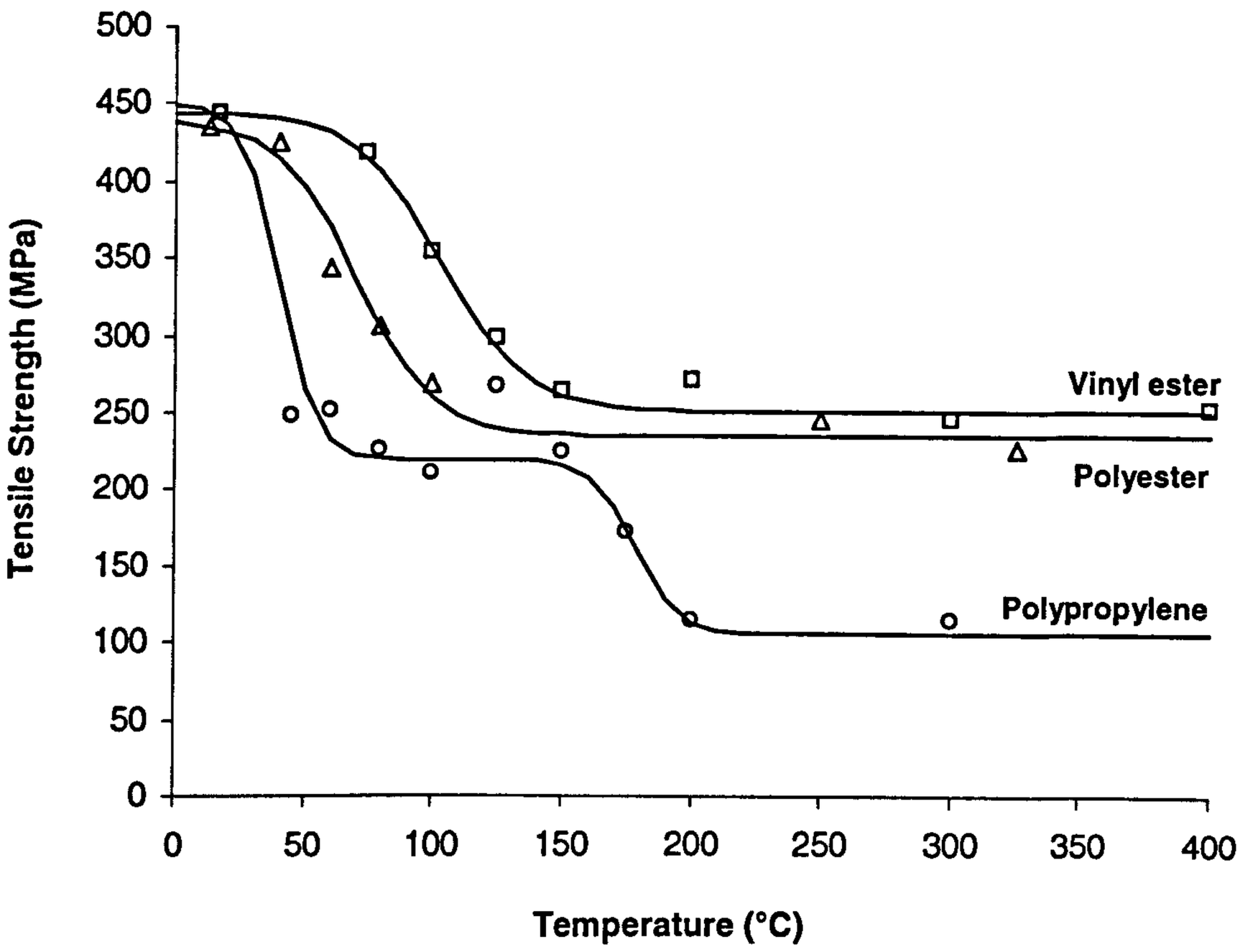

Figure 6.10 Tensile strength results for vinyl ester (□), polyester (Δ) and polypropylene (○) laminates.

The extent of this strength loss seems greater than would have been expected if resin softening were the only phenomenon taking place. Equation 6.4 shows the rule of mixtures calculation for the failure strength of a composite.

$$\sigma^* = \sigma_f^* \cdot V_f + \sigma_m^{'} \cdot \left(1 - V_f\right) \tag{6.4}$$

where: σ^* is the failure strength of the composite,

σ_f^* is the failure strength of the fibres,

V_f is the fibre volume fraction,

σ_m' is the stress in the matrix at the failure strain of the fibres.

Figure 6.11(i) shows the reduction in tensile strength with temperature for vinyl ester resin and for glass; the data was taken from literature [105, 106]. The theoretical composite strength, shown in Figure 6.11(ii), was estimated using Equation 6.4. Measured tensile strength results (Δ) for a glass/vinyl ester laminate (taken from Figure 6.10) are included for comparison. The test results experience a significant drop in strength around the glass transition temperature which is not described by the theoretical composite strength curve.

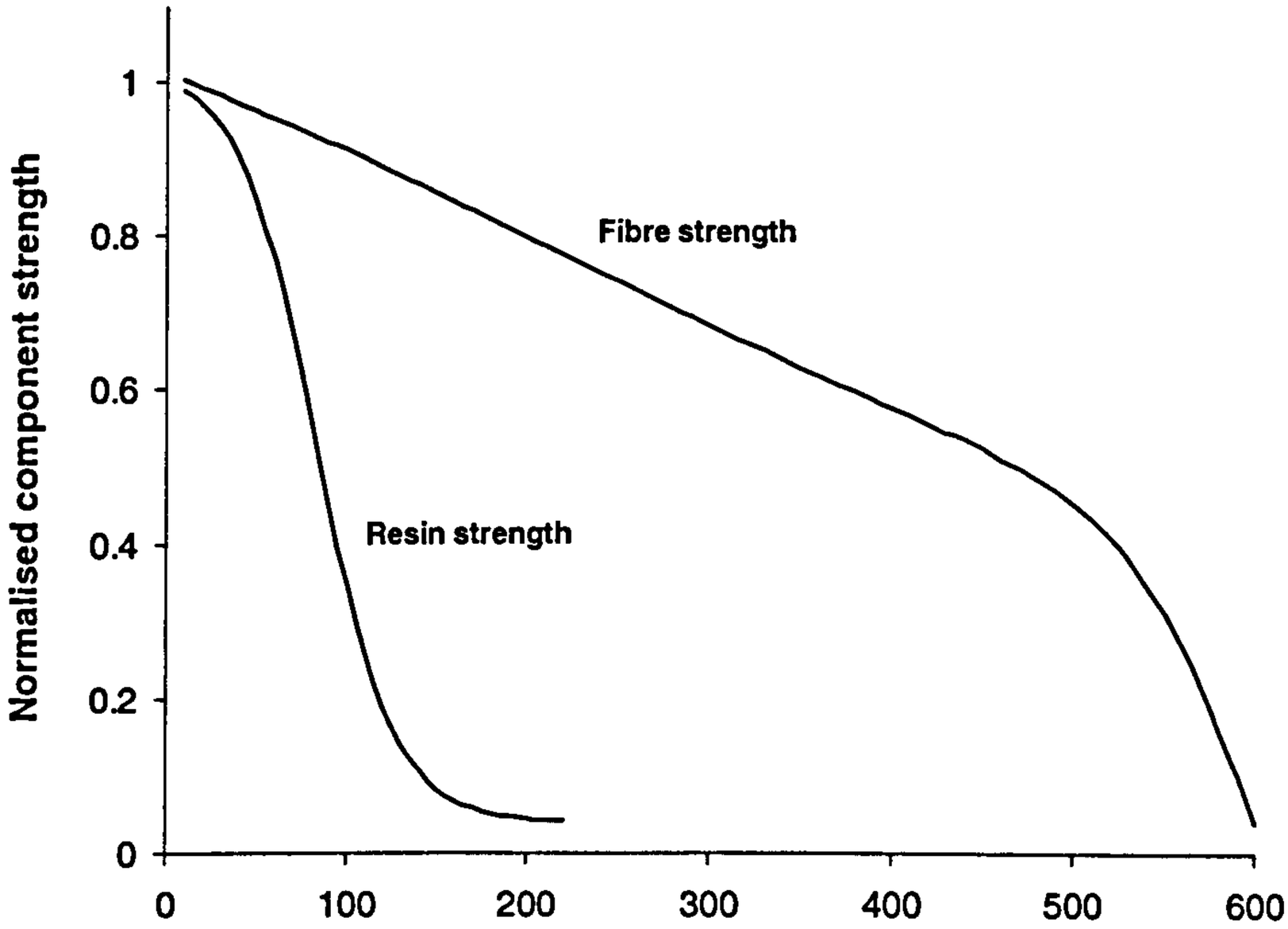

(i)

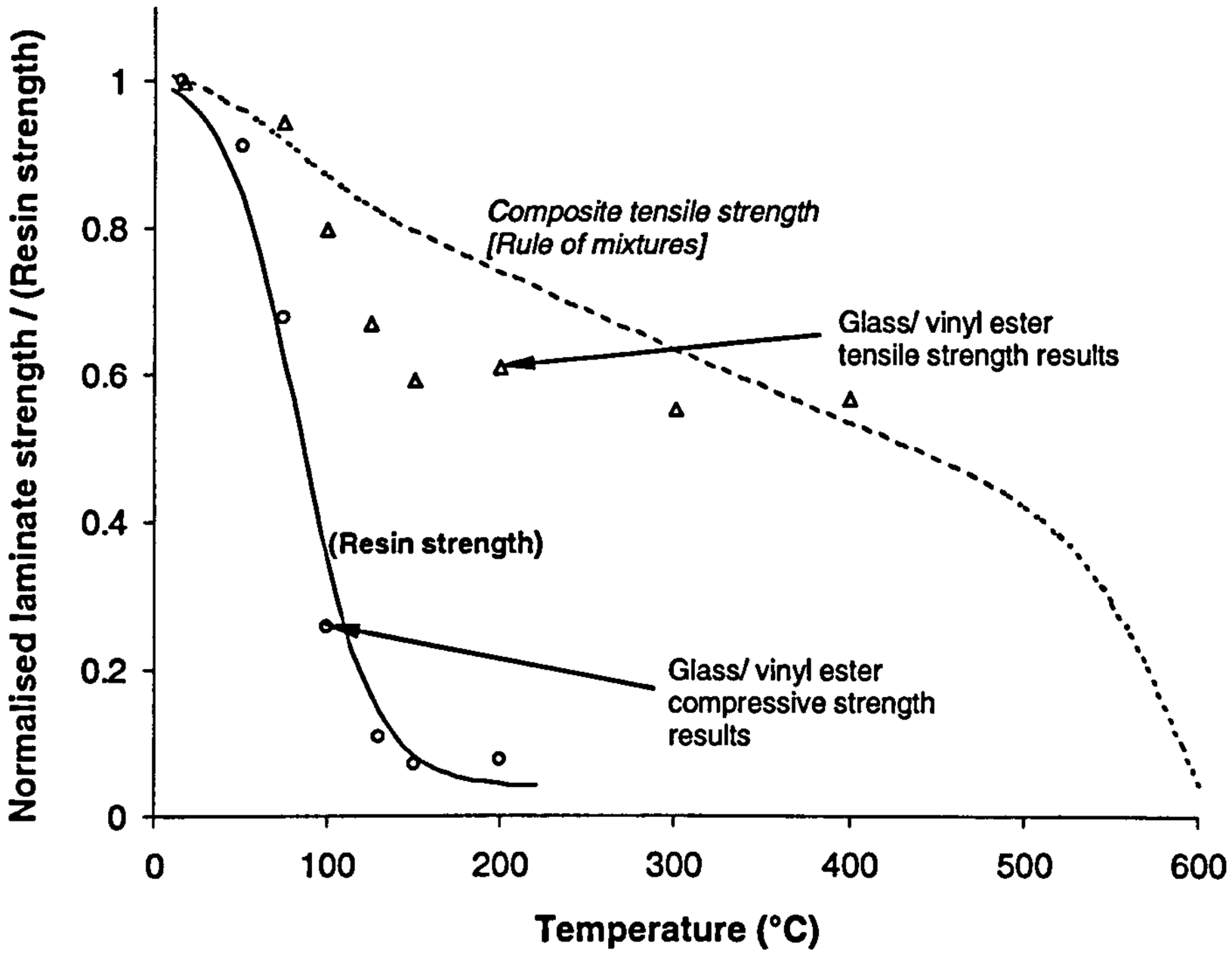

(ii)

Figure 6.11 (i) Variation of tensile strength with temperature for vinyl ester resin and glass fibres. (ii) Theoretical tensile strength of a glass/vinyl ester composite with increasing temperature. Measured tensile(Δ) and compressive(○) strength data points are included for comparison. Strength values have been normalised to their room temperature value.

The large drop in strength may be attributed to the loss of the "composite action" in the test sample. In a composite below T_g, the fibres all tend to fail at around the same strain regardless of manufacturing imperfections, such as fibre misalignment or waviness. Once the composite is heated beyond T_g, the matrix ceases to make a contribution to the composite action and these fibre path differences may cause fibres to fail at different strain values, with a consequent greater loss in predicted laminate strength.

Furthermore, when laminate compressive strength values (taken from Figure 6.6) were added to Figure 6.11(ii), they overlapped the resin strength values, further reinforcing the concept that a composite's compressive strength is heavily resin dependent.

The laminate samples retained significant strength, even at high temperatures, due to the residual strength of the fibres. Beyond these temperatures there may be some further degradation in glass strength. Equation 6.1 provided an excellent fit for the vinyl ester and polyester results up to 400°C. For the purposes of modelling, the relaxed property value (P_R) was assumed to be this value beyond 400°C.

Equation 6.3 was again used to model the polypropylene results. The high temperature residual strength of the polypropylene samples was much less than that of the polyester and vinyl ester samples. The difference in reinforcement architecture and glass content would explain this characteristic. The polypropylene samples were made from woven twill fabric and would therefore be more susceptible than the cross-ply laminates to fibre crimp and waviness problems.

6.2.5 Tensile Stress-strain Curves

Figures 6.12, 6.13 and 6.14 show tensile stress-strain curves for polyester, vinyl ester and polypropylene laminates respectively. These curves were also used to model the structural response of composite laminates in fire, detailed in Chapter 7.

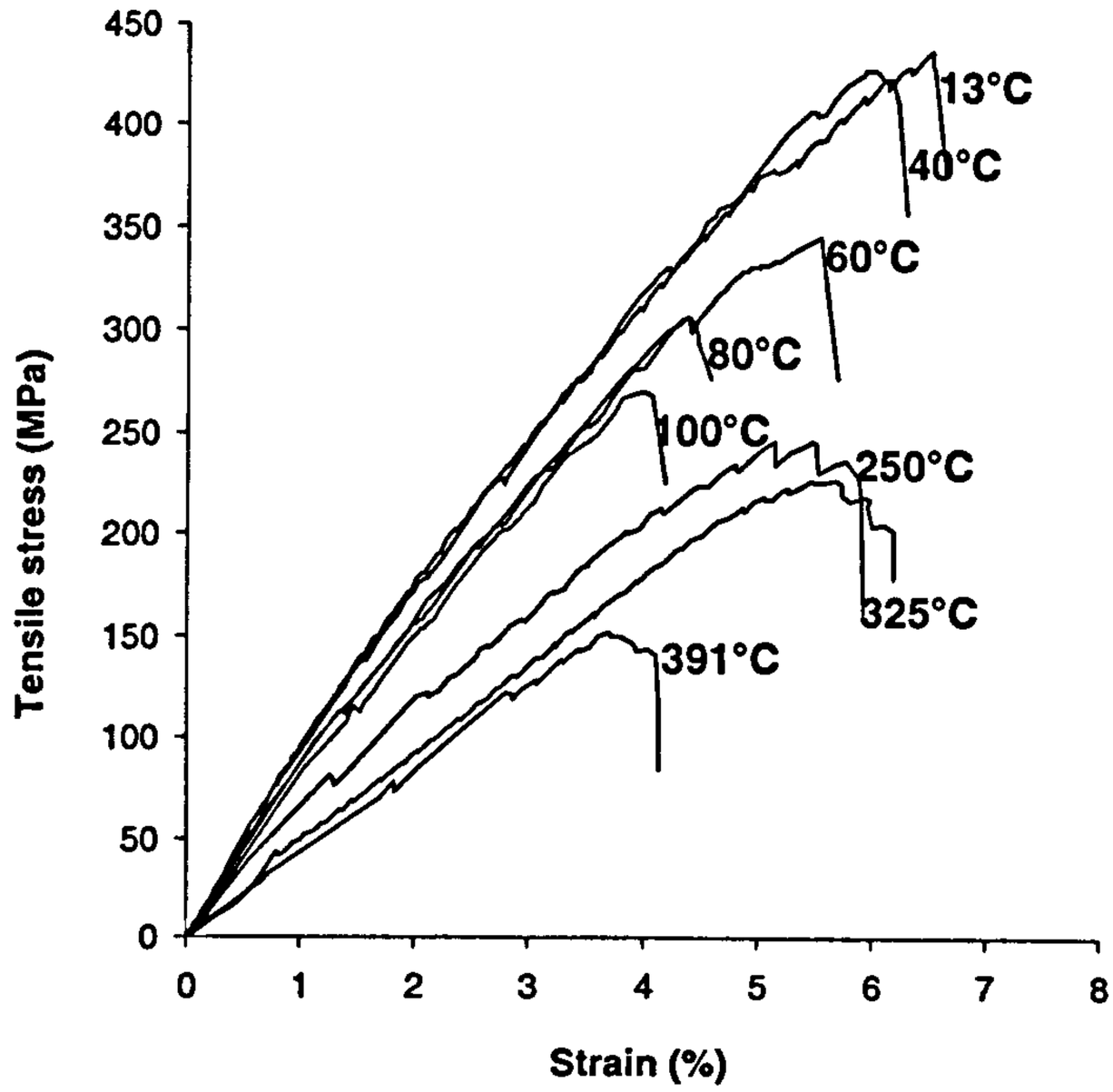

Figure 6.12 Tension stress-strain curves for glass/polyester at a range of temperatures.

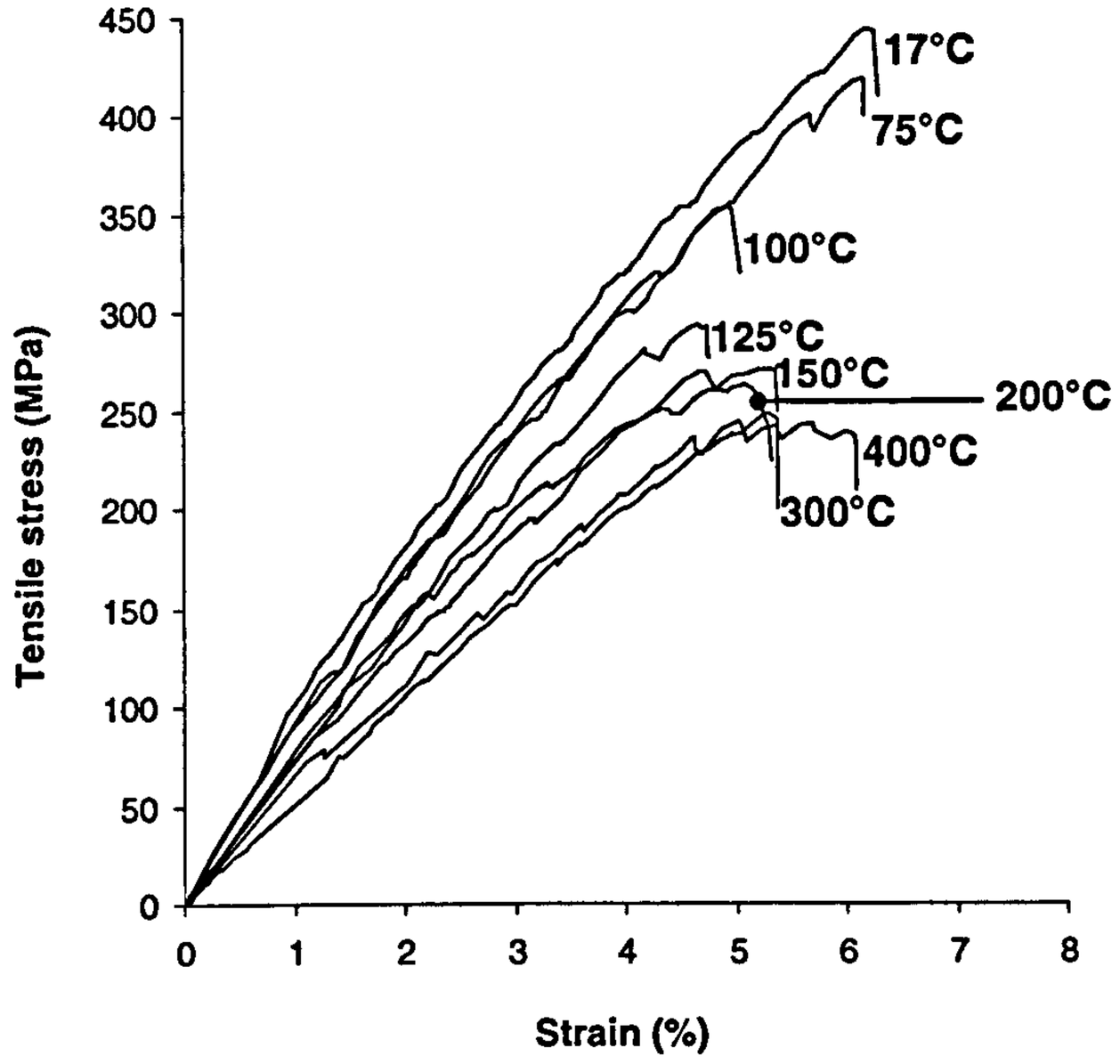

Figure 6.13 Tension stress-strain curves for glass/vinyl ester at a range of temperatures.

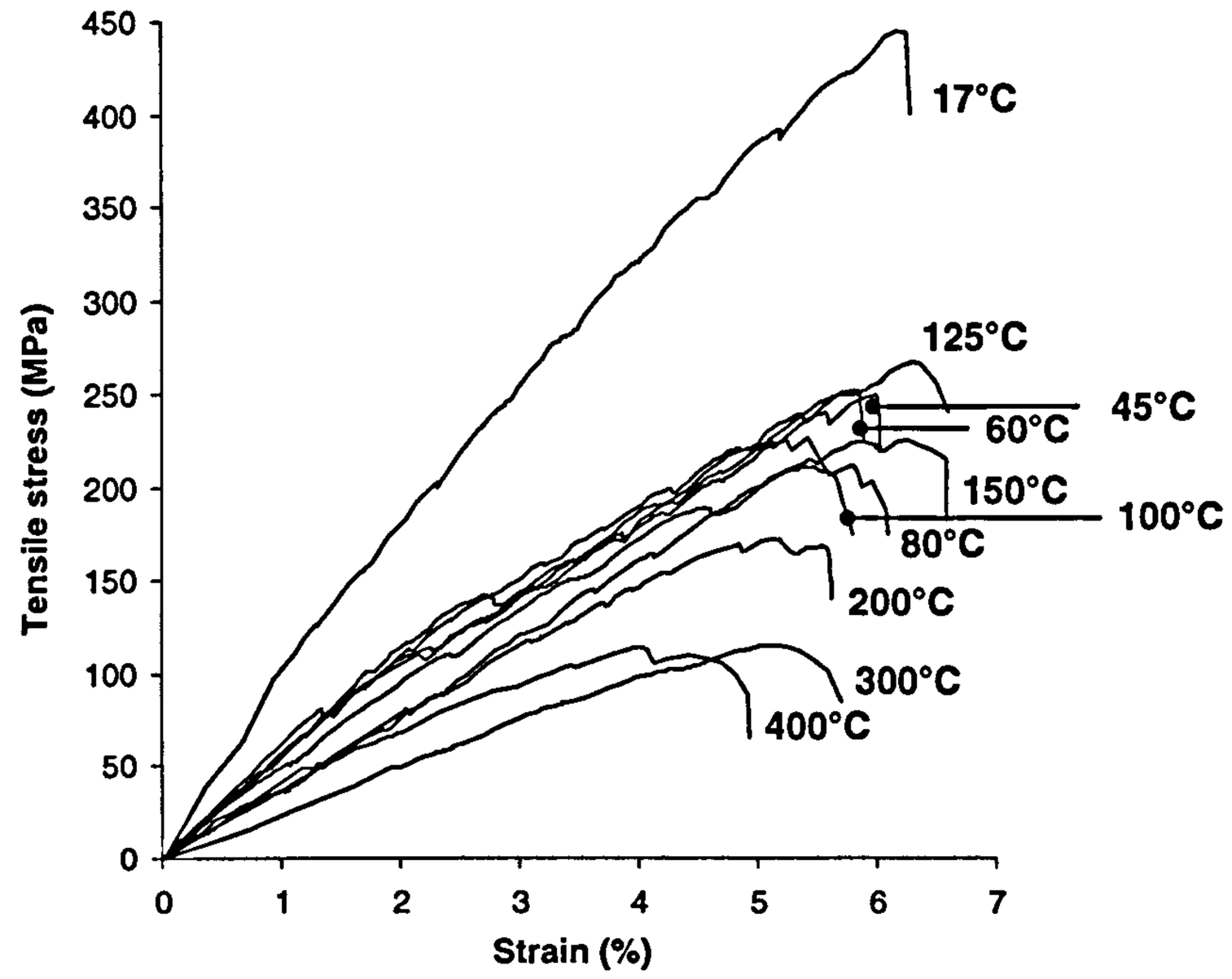

Figure 6.14 Tension stress-strain curves for glass/polypropylene at a range of temperatures.

6.2.6 Summary of Material Property Results

Tables 6.1, 6.2 and 6.3 below provide a summary of the main property values that were used in the failure model for each material. The flexural modulus (E_1 / E_2) values quoted are the parameters for the 10 second data point curves, σ_C refers to the modelled compressive strength curves and σ_T refers to tensile strength. It is interesting to note that the modelled T' values are fairly consistent for each material.

Table 6.1 Polyester parameters: A summary of the relevant parameters required for modelling the temperature dependent properties of glass/polyester laminates.

	P_U	P_R	k	T'
E_1 / E_2	18.5 GPa	3.6 GPa	0.035	80°C
σ_c	330 MPa	23 MPa	0.025	70°C
σ_T	440 MPa	235 MPa	0.033	70°C

Table 6.2 Vinyl ester parameters: A summary of the relevant parameters required for modelling the temperature dependent properties of glass/vinyl ester laminates.

	P_U	P_R	k	T'
E_1 / E_2	17.7 GPa	3.4 GPa	0.08	103°C
σ_c	356 MPa	24 MPa	0.035	83°C
σ_T	445 MPa	250 MPa	0.03	103°C

Table 6.3 Polypropylene parameters: A summary of the relevant parameters required for modelling the temperature dependent properties of glass/polypropylene laminates.

	P_U	P_I	P_R	k_1	k_2	T'_1	T'_2
E_1 / E_2	25 GPa	5.6 GPa	-2 GPa	0.0075	0.12	0°C	148°C
σ_c	260 MPa	68 MPa	-5 MPa	0.018	0.048	0°C	130°C
σ_T	450 MPa	220 MPa	105 MPa	0.07	0.06	40°C	178°C

6.3 Fire under Load Results

Stress rupture curves were created for analysis of the structural performance of each laminate system in a 50kW/m^2 fire. These curves show the time-to-failure of a laminate sample which has been placed under a constant load in fire. These results were not only useful for comparing the materials' fire resistance, but also provided data for verification of the laminate model.

6.3.1 Constrained Compression Fire Test Results

Figures 6.15, 6.16 and 6.17 show the compressive results for the laminate systems in fire. The 0 second points are the failure strength of the sample not exposed to fire. Although it is conceded that these samples would actually take a few seconds to fail, the stress rupture curves presented here refer to fire exposure time-to-failure. Hence, those samples not exposed to fire have a "failure time" of 0 seconds.

The compressive stress values were calculated as the initial compressive stress within a loaded sample before the fire was started. These stress values are plotted against the sample times to failure.

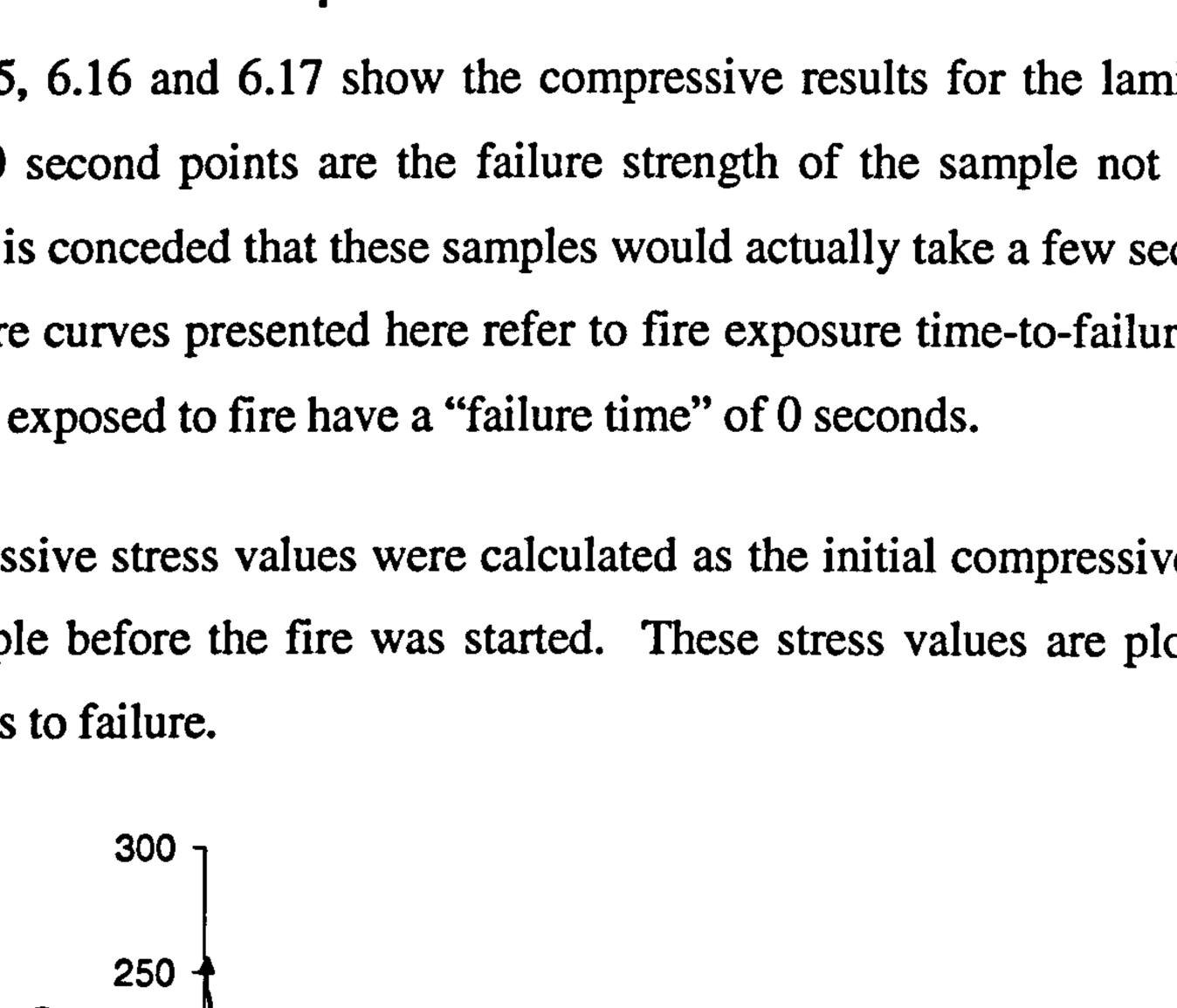

Figure 6.15 Constrained compression test results for a glass/polyester laminate exposed to a 50kW/m^2 heat flux. The stress values are an initially applied stress before the fire was started.

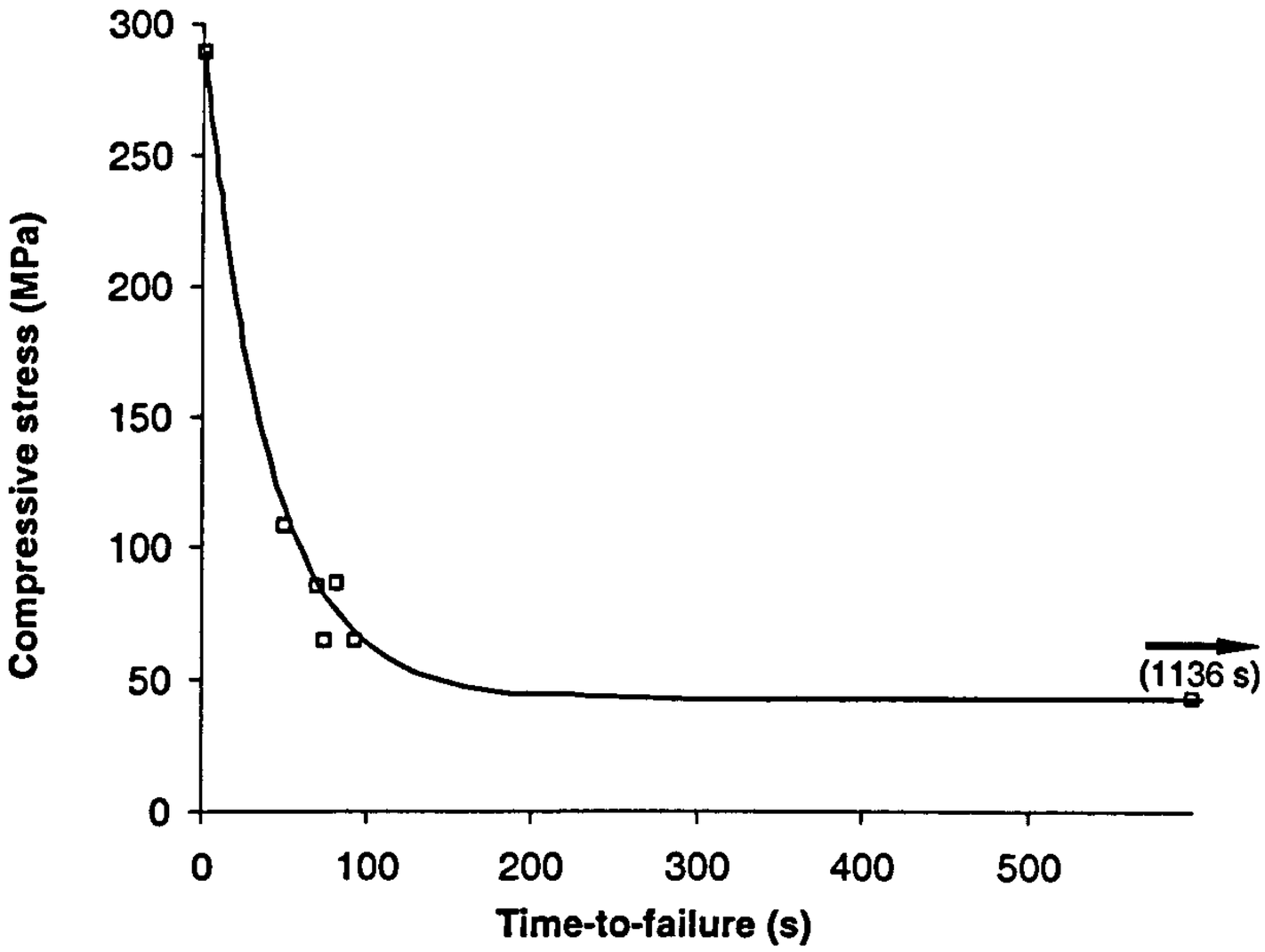

Figure 6.16 Constrained compression test results for a glass/vinyl ester laminate exposed to a 50kW/m^2 heat flux.

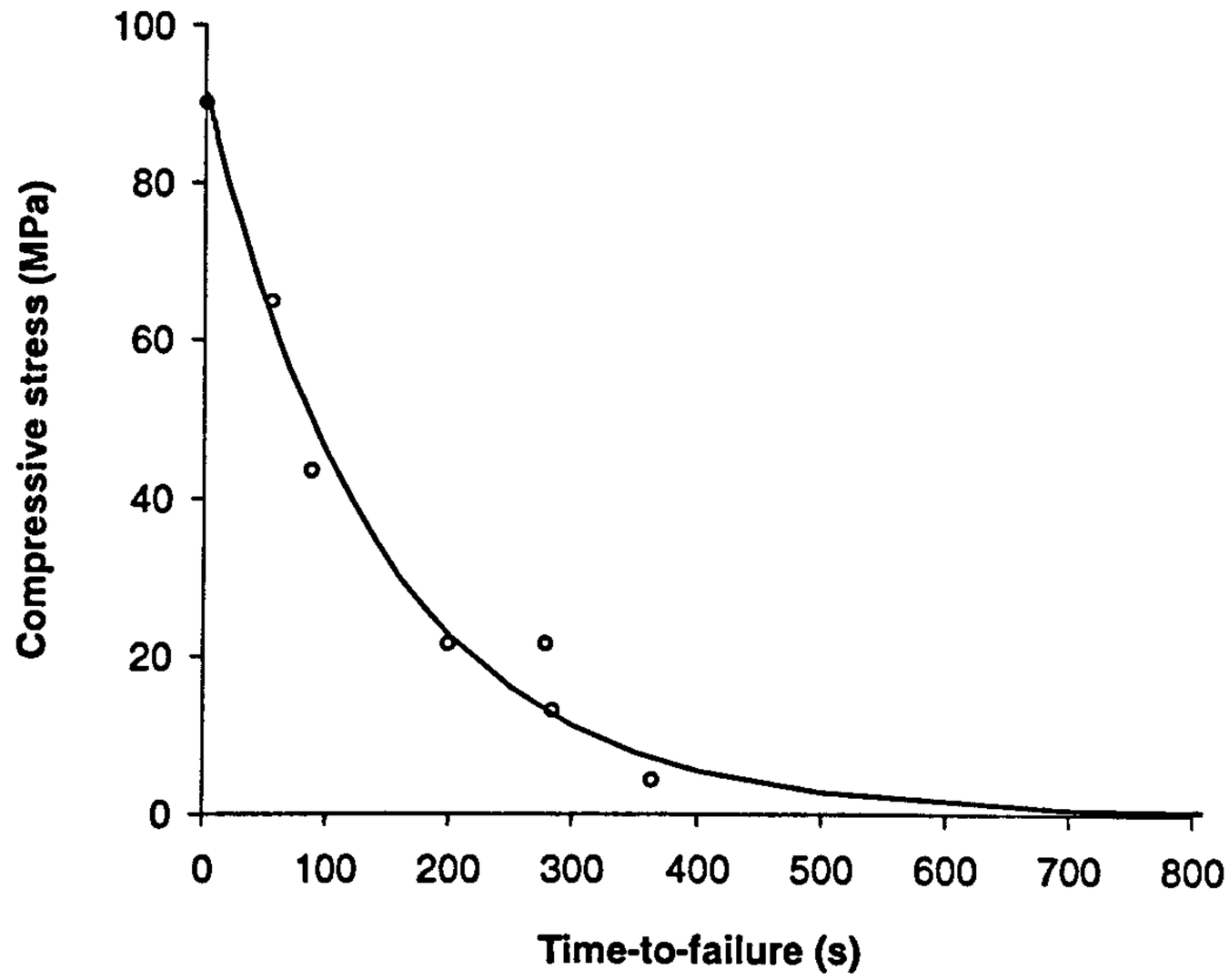

Figure 6.17 Constrained compression test results for a glass/polypropylene laminate exposed to a 50kW/m^2 heat flux.

The residual load bearing capability of all three materials was very low for exposure times in excess of 100 seconds. This highlights compressive behaviour as the main limitation in the use of fibre reinforced plastics for structural fire-risk applications.

From Figures 6.15 and 6.16, it may be discerned that the glass/vinyl ester laminates had marginally better compressive load resistance in fire than glass/polyester. This can be explained by glass/vinyl ester's slightly higher value of T', noticeable in Figure 6.6. Glass/polypropylene, although showing low compressive strength when not exposed to fire, performed considerably well for failure times up to 100 seconds. At these load levels (around 50MPa) the polypropylene laminates have compressive load resistance comparable to vinyl ester and polyester. However, when longer exposure times are experienced at very low load levels, the polypropylene laminates eventually melt and there is no run out of residual strength past 600 seconds.

6.3.2 Compressive Failure

Compressive failure usually initiates in an area where fibres are not perfectly aligned in the plane of loading [107]. The failure mechanism involves the formation of a band of kinked material in this region. Fibre misalignment causes high levels of shear loading between the fibres, which lead to local shear deformation.

In the case of a laminate in fire which has been restrained against global buckling, delamination cracks form between plies near the hot surface. The delaminated plies have little or no load bearing capability and hence the load is redistributed over the rest of the laminate. When the delamination free region reaches the material compressive strength, the laminate fails by plastic tow kinking [72].

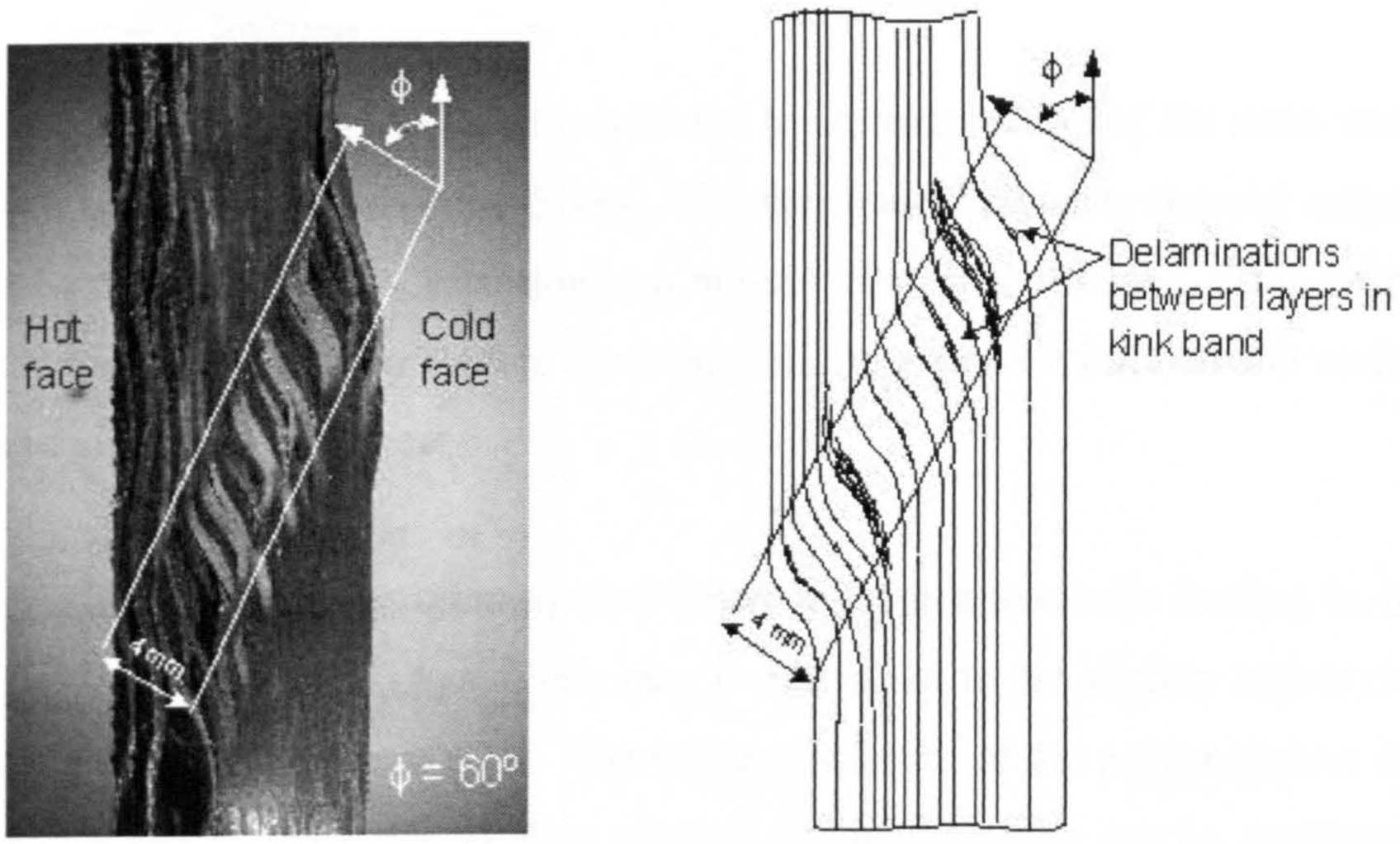

Figure 6.18 Local shear deformation in a glass/vinyl ester laminate which was placed under compressive loading in fire [72].

Figure 6.18 shows a photograph and schematic diagram of typical compressive failure within a laminate exposed to a one-sided heat flux. The low shear stiffness of the hot matrix allows the fibre tows to rotate through a large angle (Φ), causing plastic kinking of the tows away from the heat source.

6.3.3 Tension Fire Test Results

Tensile load bearing capability also falls rapidly under the effect of fire, as can be seen in Figures 6.19, 6.20 and 6.21. Again, the 0 second data points are the failure strength of the sample not exposed to fire. For the tests which were not conducted in fire, it would be expected that all three materials would reach the same stress (replicating the tensile strength vs. temperature results). However due to the rectangular shape of the plates tested, the samples failed in the grips and hence ultimate tensile strength (UTS) values were not reached.

6.3.4 Tensile Failure

Tensile failure of laminates in fire is initiated by decomposition of the resin matrix and followed by creep rupture of the fibres. The thermoset laminates showed considerable residual strength in tension, resulting in a run-out of around 160MPa. This observation is not surprising, as both materials are made from the same reinforcement architecture and have similar glass content.

Glass/vinyl ester laminates seem to have better resistance to tensile loading in fire than glass polyester laminates. Again, this may be attributed to the slightly higher modelled value of T' shown in Figure 6.10. The residual strength of the polypropylene laminate is around 60MPa; again, this smaller value of residual strength can be attributed to the woven style of reinforcement and the material's slightly lower glass content. Figure 6.10 further supports the lower residual strength value observed for polypropylene during the material property tests.

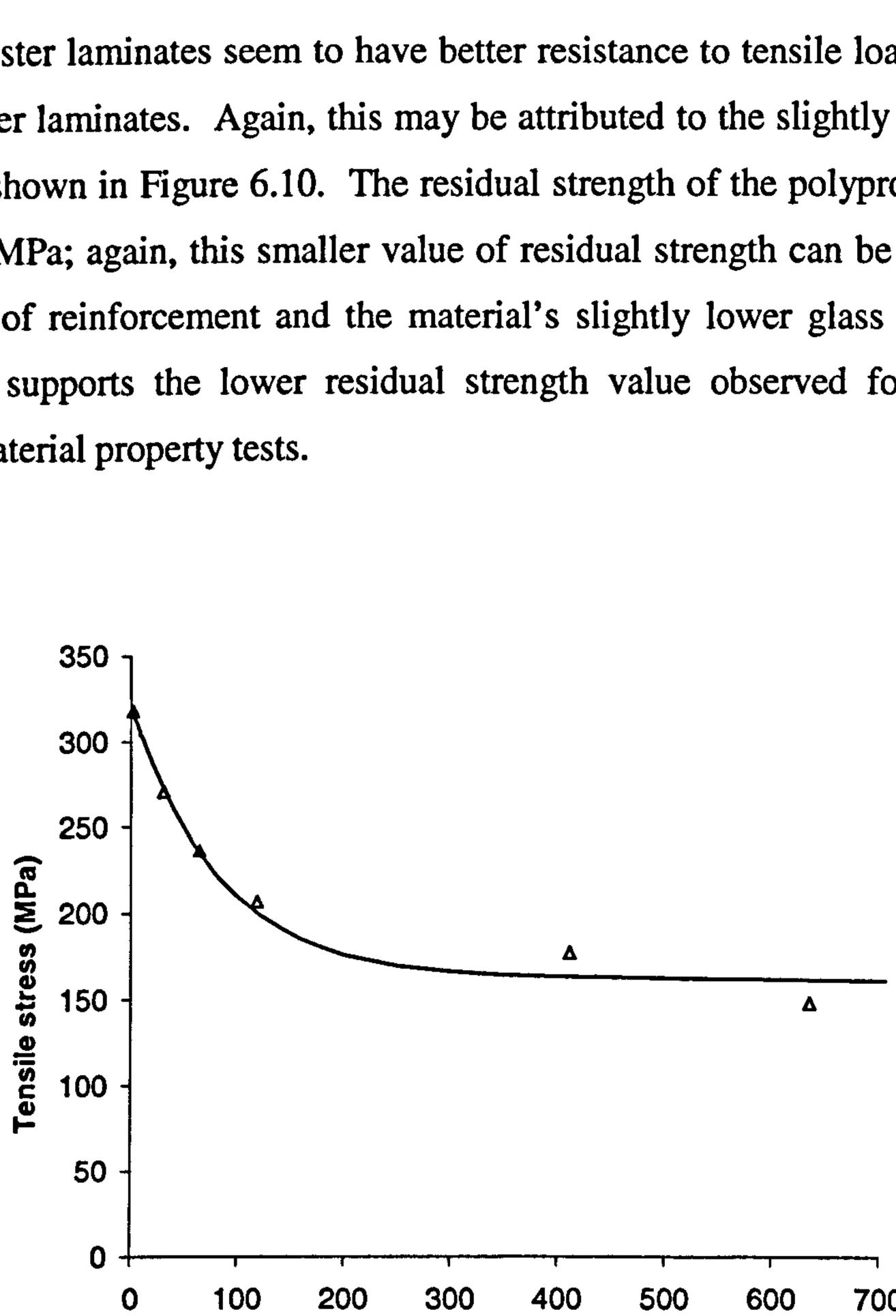

Figure 6.19 Tensile fire test results for a glass/polyester laminate exposed to a 50kW/m^2 fire. The time-to-failure is shown for the initially applied stress.

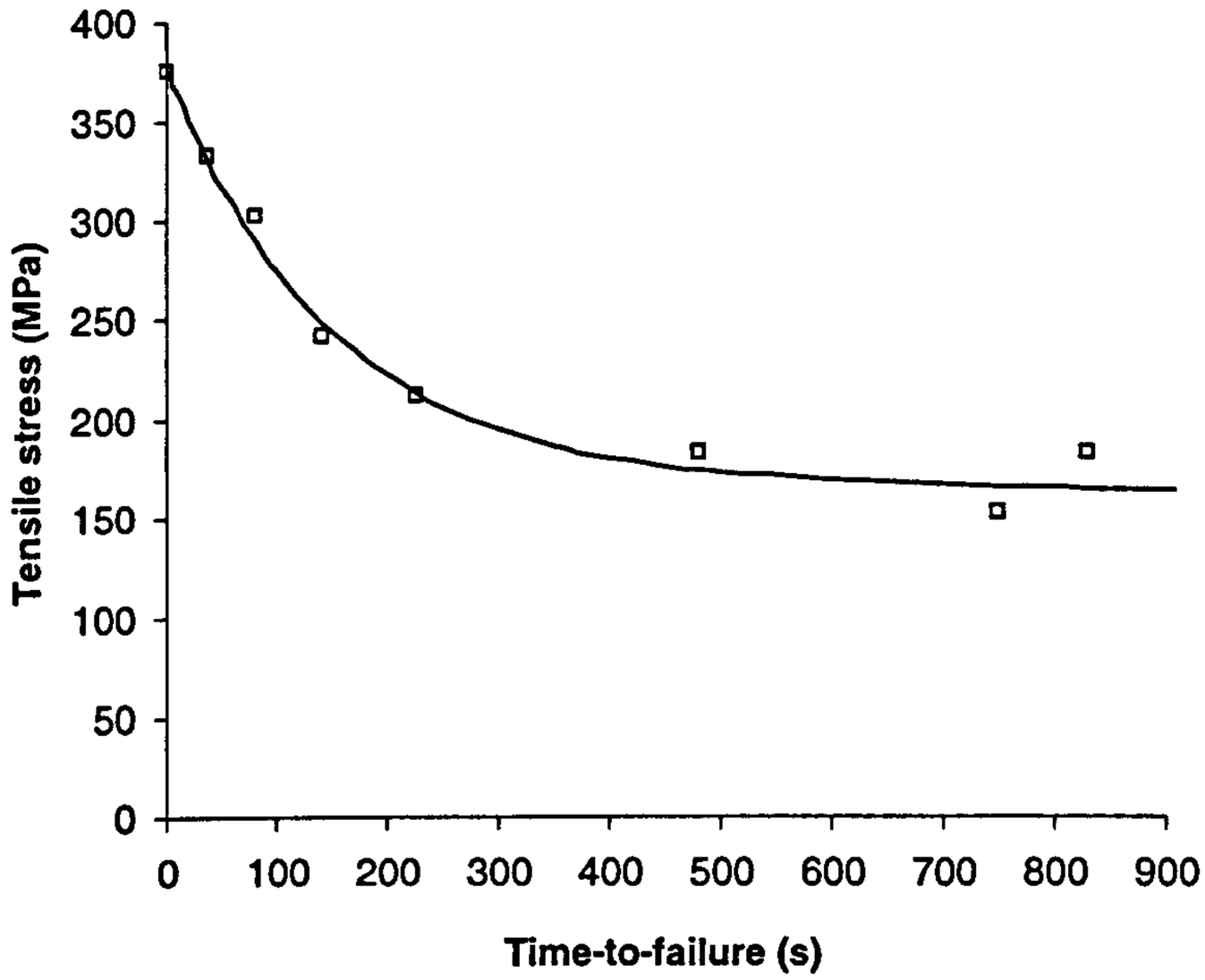

Figure 6.20 Tensile fire test results for a glass/vinyl ester laminate exposed to a 50kW/m^2 fire.

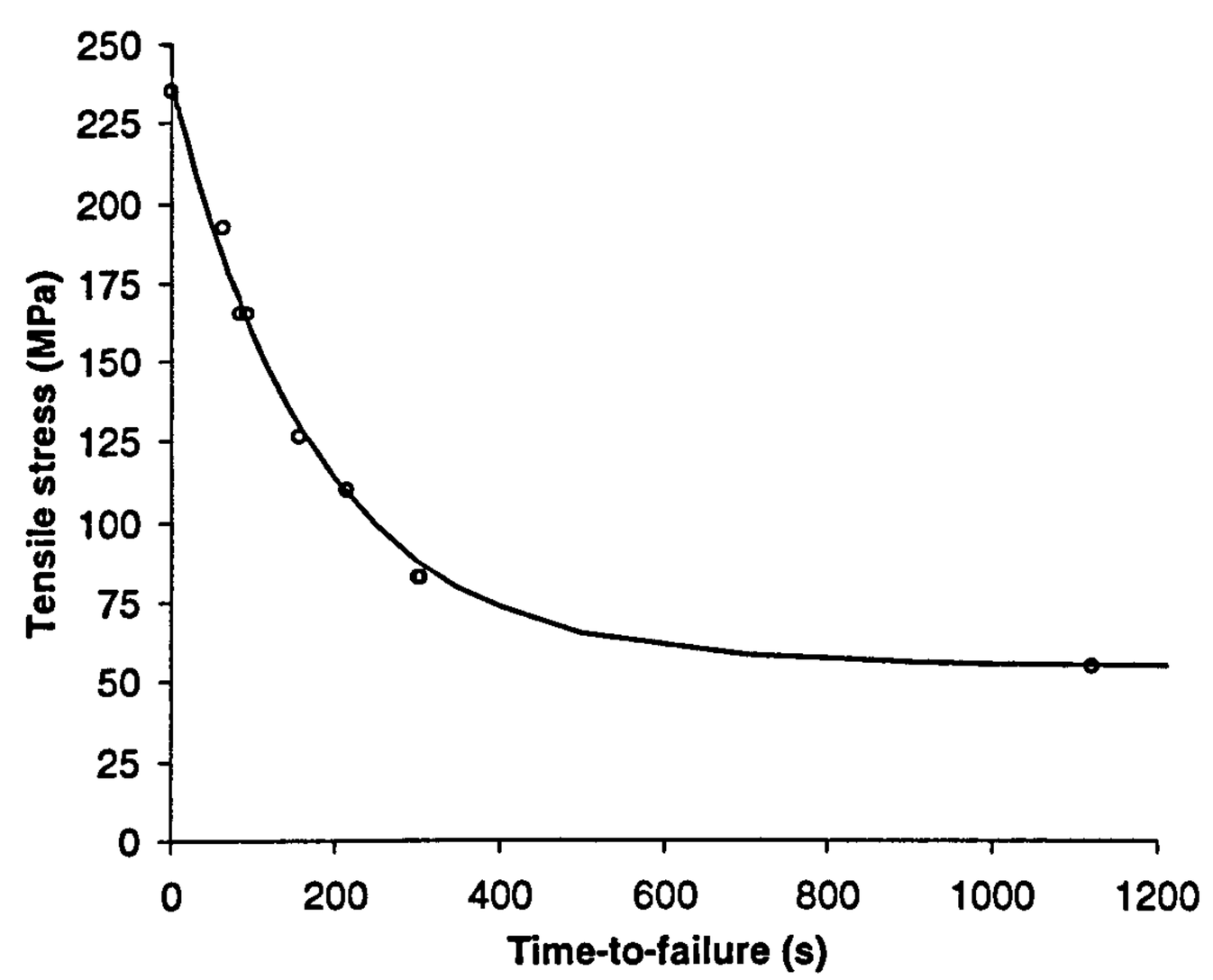

Figure 6.21 Tensile fire test results for a glass/polypropylene laminate exposed to a 50kW/m^2 fire.

Chapter 7 The Laminate Analysis Model

7.1 Introduction

Laminate analysis is a well established theory [1, 108, 109]. The failure model for composite laminates in fire was based on basic laminate theory and the 1-D thermal model. This chapter describes the laminate analysis model and presents some predictions and discussion on the structural response of glass reinforced laminates in fire.

The laminate model required several inputs for accurate fire resistance prediction, shown in Figure 7.1. First, the thermal model [49, 70], described in Chapter 2, was used to predict the thermal response of a particular laminate in a given fire scenario. The model provided predicted values for the temperature and residual resin content (RRC) at points through the thickness of the laminate. These predictions were validated using the burner technique detailed in Chapter 3. Relationships describing the relevant mechanical properties as functions of temperature and RRC (Chapter 6) were then used to construct ply constitutive equations. These equations provide input to the laminate analysis which allowed the prediction of mechanical response in fire.

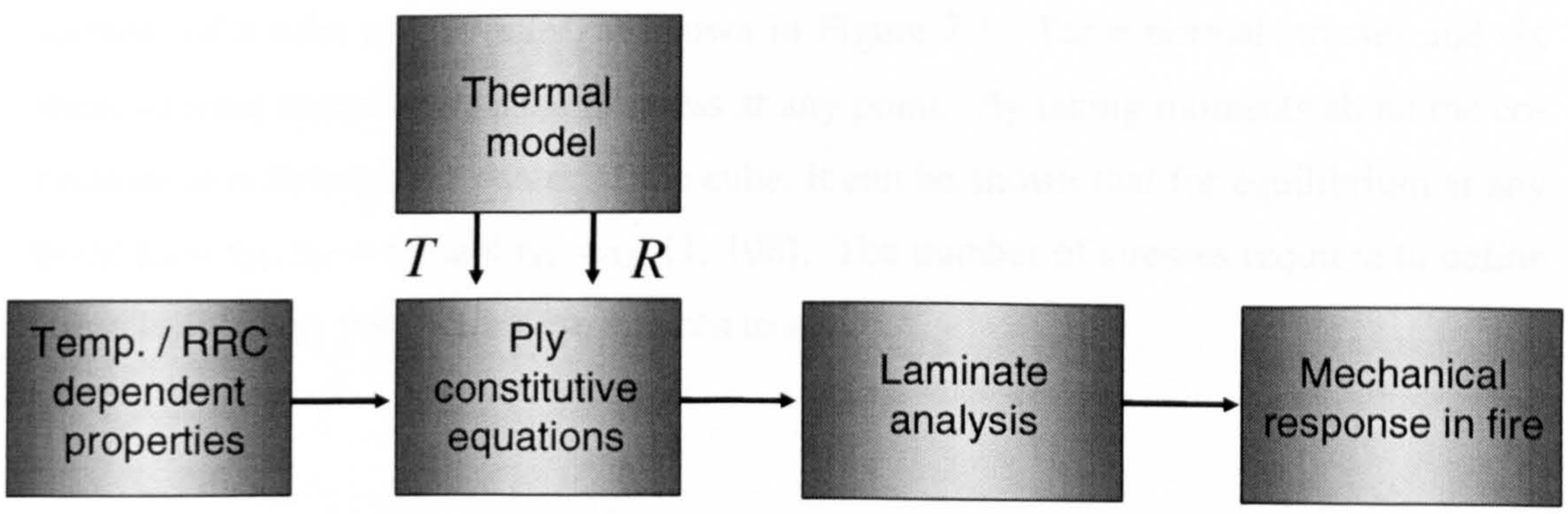

Figure 7.1 Steps involved in modelling the structural response of a loaded composite laminate in fire.

7.2 Ply Constitutive Equations

Simple laminate constructions consist of orthotropic laminae. These plies have three mutually perpendicular planes of material symmetry and the properties at any point are different in three mutually perpendicular directions [1]. Unidirectional, 0/90 cross ply and woven roving laminae are therefore all, orthotropic (Figure 7.2).

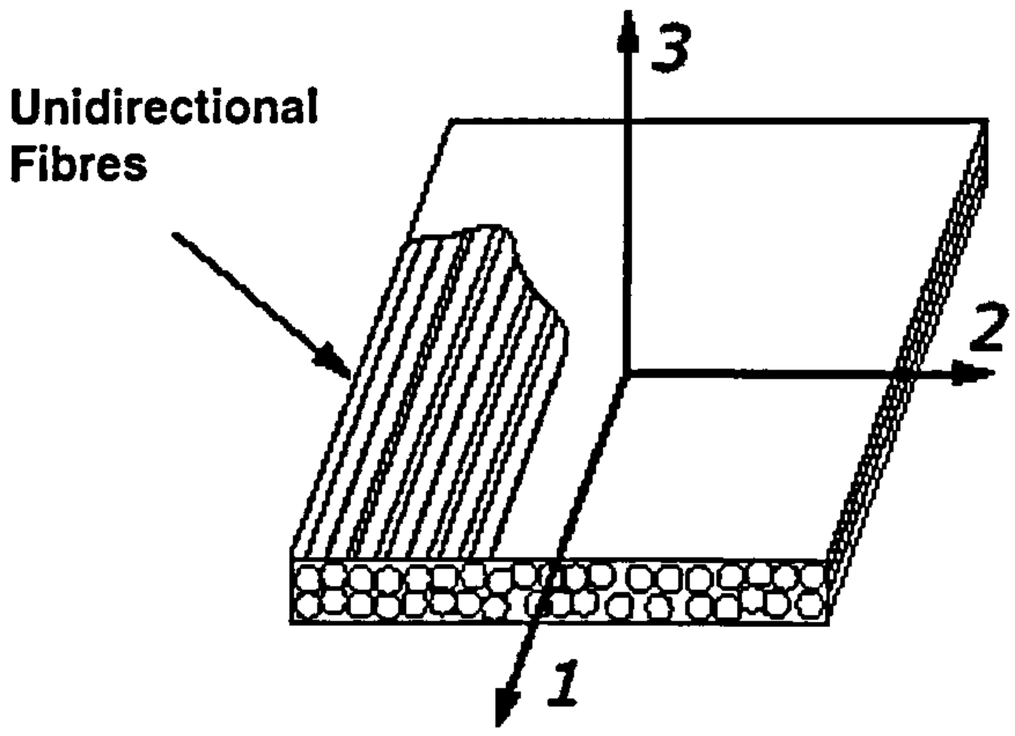

Figure 7.2 Three mutually perpendicular planes of material symmetry in a unidirectional laminate [110].

The stresses at a point within a lamina may be represented as the stresses acting on the surfaces of a cube at that point, as shown in Figure 7.3. Three normal stresses and six shear stresses describe the state of stress at any point. By taking moments about the co-ordinate axis through the centre of the cube, it can be shown that for equilibrium at any point $\tau_{23} = \tau_{32}$, $\tau_{31} = \tau_{13}$ and $\tau_{12} = \tau_{21}$ [1, 108]. The number of stresses required to define stress fully at any point therefore reduces to six.

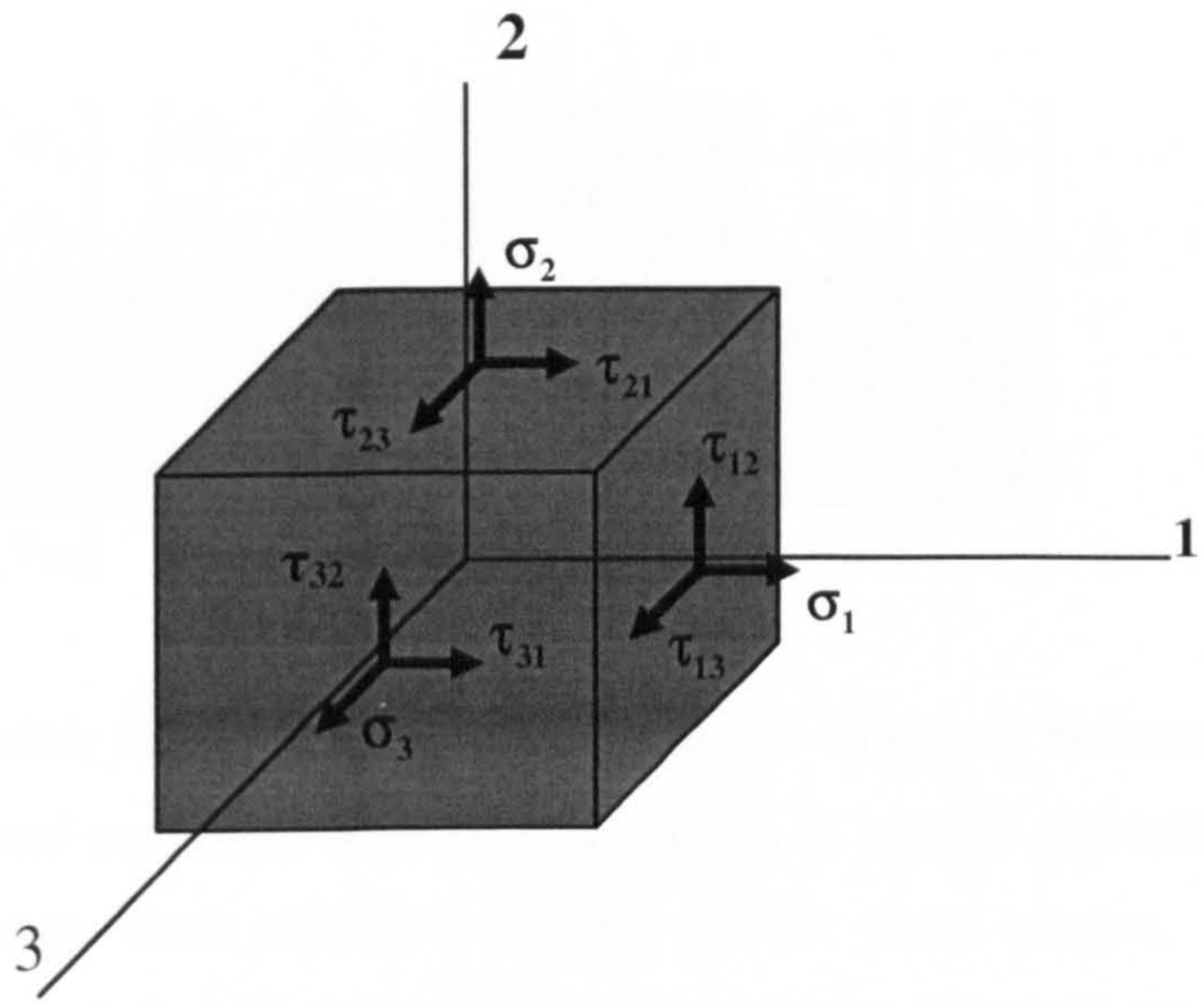

Figure 7.3 Components of stress acting on a small cube of material.

Hooke's law can be expressed in contracted notation to describe the relationship between the stresses and applied strains:

$$\sigma_i = \sum_{j=1}^{6} C_{ij} \cdot \varepsilon_j \qquad \textbf{(7.1)}$$

where: σ_i are the stress components,

ε_j are the strain components,

C_{ij} is the stiffness matrix,

$i,j = 1, 2,\ldots,6.$ ($\tau_{23} = \sigma_4$, $\tau_{31} = \sigma_5$, $\tau_{12} = \sigma_6$; $\gamma_{23} = \varepsilon_4$, $\gamma_{31} = \varepsilon_5$, $\gamma_{12} = \varepsilon_6$)

The stiffness matrix (C_{ij}) can be expanded to give the matrix notation for six equations relating stress to strain, shown as Equation 7.2. Laminae are considered to be sufficiently thin that all through thickness stresses are effectively zero (i.e. $\sigma_3 = \tau_{23} = \tau_{31} = 0$). The highlighted sections of Equation 7.2 can therefore be ignored.

$$\begin{bmatrix}\sigma_1\\ \sigma_2\\ \sigma_3\\ \tau_{23}\\ \tau_{31}\\ \tau_{12}\end{bmatrix} = \begin{bmatrix}C_{11} & C_{12} & C_{13} & C_{14} & C_{15} & C_{16}\\ C_{12} & C_{22} & C_{23} & C_{24} & C_{25} & C_{26}\\ C_{13} & C_{23} & C_{33} & C_{34} & C_{35} & C_{36}\\ C_{14} & C_{24} & C_{34} & C_{44} & C_{45} & C_{46}\\ C_{15} & C_{25} & C_{35} & C_{45} & C_{55} & C_{56}\\ C_{16} & C_{26} & C_{36} & C_{46} & C_{56} & C_{66}\end{bmatrix} \cdot \begin{bmatrix}\varepsilon_1\\ \varepsilon_2\\ \varepsilon_3\\ \gamma_{23}\\ \gamma_{31}\\ \gamma_{12}\end{bmatrix} \qquad \textbf{(7.2)}$$

Orthotropic materials further simplify the constitutive equations because of the absence of shear-extensional coupling. That is, when tested in tension and compression along their principal axes, these materials do not exhibit shear strains. Similarly, the application of shear strain will only produce a shear stress. The reduced stiffness matrix for the lamina's stress-strain relationship therefore becomes:

$$\begin{bmatrix}\sigma_1\\ \sigma_2\\ \tau_{12}\end{bmatrix} = \begin{bmatrix}Q_{11} & Q_{12} & Q_{16}\\ Q_{12} & Q_{22} & Q_{26}\\ Q_{16} & Q_{26} & Q_{66}\end{bmatrix} \cdot \begin{bmatrix}\varepsilon_1\\ \varepsilon_2\\ \gamma_{12}\end{bmatrix} \qquad \textbf{(7.3)}$$

$$Q_{11} = C_{11} = \frac{E_1}{1-\upsilon_{12}\upsilon_{21}} \qquad Q_{22} = C_{22} = \frac{E_2}{1-\upsilon_{12}\upsilon_{21}}$$

$$Q_{12} = C_{12} = \frac{\upsilon_{12}E_2}{1-\upsilon_{12}\upsilon_{21}} = \frac{\upsilon_{21}E_1}{1-\upsilon_{12}\upsilon_{21}} \qquad Q_{16} = Q_{26} = 0$$

$$Q_{66} = G_{12}$$

where: E_1 is the modulus of the material in the 1-direction [longitudinal] (GPa),

E_2 is the modulus of the material in the 2-direction [transverse] (GPa),

υ_{12} is Poisson's ratio (referring to the strains produced in the 2-direction when the lamina is stressed in the 1-direction),

υ_{21} is Poisson's ratio (referring to the strains produced in the 1-direction when the lamina is stressed in the 2-direction),

G_{12} is the shear modulus of the material (GPa).

The transformed stiffness matrix ($\overline{Q}$) of a ply describes the relationship between stresses and applied strains when the lamina is tested at arbitrary axes to the principal material directions (Figure 7.4).

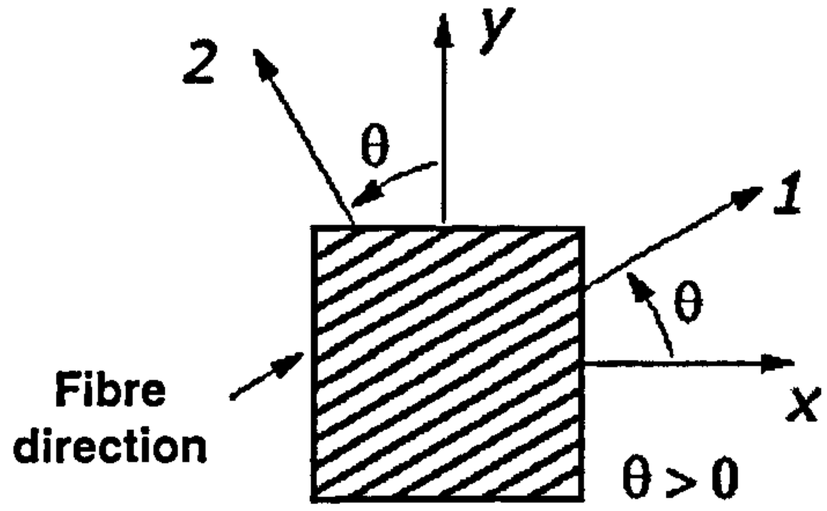

Figure 7.4 The rotation of axes from co-ordinate system 1-2 to x-y [110].

This allows the calculation of material properties for a ply subjected to any loading direction within the *x-y* plane. The stress-strain relationship becomes:

$$\begin{bmatrix}\sigma_x\\ \sigma_y\\ \tau_{xy}\end{bmatrix}=\begin{bmatrix}\overline{Q}_{11} & \overline{Q}_{12} & \overline{Q}_{16}\\ \overline{Q}_{12} & \overline{Q}_{22} & \overline{Q}_{26}\\ \overline{Q}_{16} & \overline{Q}_{26} & \overline{Q}_{66}\end{bmatrix}\cdot\begin{bmatrix}\varepsilon_x\\ \varepsilon_y\\ \gamma_{xy}\end{bmatrix} \qquad (7.4)$$

where: $\overline{Q}_{11} = Q_{11}c^4 + 2(Q_{12} + 2Q_{66})s^2c^2 + Q_{22}s^4$

$$\overline{Q}_{12} = (Q_{11} + Q_{22} - 4Q_{66})s^2c^2 + Q_{12}(s^4 + c^4)$$

$$\overline{Q}_{22} = Q_{11}s^4 + 2(Q_{12} + 2Q_{66})s^2c^2 + Q_{22}c^4$$

$$\overline{Q}_{16} = (Q_{11} - Q_{12} - 2Q_{66})sc^3 + (Q_{12} - Q_{22} + 2Q_{66})s^3c$$

$$\overline{Q}_{26} = (Q_{11} - Q_{12} - 2Q_{66})s^3c + (Q_{12} - Q_{22} + 2Q_{66})sc^3$$

$$\overline{Q}_{66} = (Q_{11} + Q_{22} - 2Q_{12} - 2Q_{66})s^2c^2 + Q_{66}(s^4 + c^4)$$

(*s* and *c* denote $sin\theta$ and $cos\theta$ respectively.)

The work presented here involved the fire testing and prediction of orthotropic laminates which are loaded in their principal directions only. In these cases, the $\overline{Q}$ values reduce back to the simpler form shown in Equation 7.3, as $\theta = 0°$. For each time step, stiffness matrices were calculated for each ply using the temperature and resin dependent equations (Tables 6.1, 6.2 and 6.3). Laminate theory was then applied to analyse the variation of stress across the laminate thickness.

7.3 Laminate Analysis

Lamina strains ε_x, ε_y and γ_{xy} can be rewritten in terms of mid-plane strains (ε^0) and plate curvatures (k) as follows [108]:

$$\begin{bmatrix} \varepsilon_x \\ \varepsilon_y \\ \gamma_{xy} \end{bmatrix} = \begin{bmatrix} \varepsilon_x^0 \\ \varepsilon_y^0 \\ \gamma_{xy}^0 \end{bmatrix} + z \begin{bmatrix} k_x \\ k_y \\ k_{xy} \end{bmatrix} \tag{7.5}$$

where: z is the distance from the laminate mid-plane to the lamina mid-plane, defined in Figure 7.5.

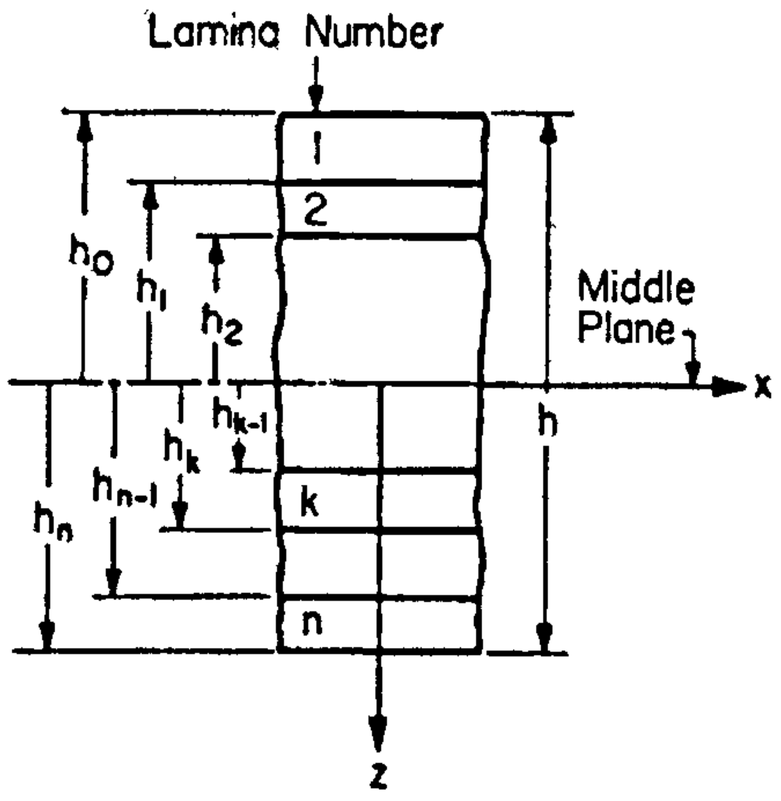

Figure 7.5 Geometry of a multi-layered laminate consisting of n orthotropic laminae. h is the laminate thickness [108].

Equation 7.5 can be substituted into the stress-strain relationship for a lamina:

$$\begin{bmatrix}\sigma_x\\ \sigma_y\\ \tau_{xy}\end{bmatrix}=\begin{bmatrix}\overline{Q}_{11} & \overline{Q}_{12} & \overline{Q}_{16}\\ \overline{Q}_{12} & \overline{Q}_{22} & \overline{Q}_{26}\\ \overline{Q}_{16} & \overline{Q}_{26} & \overline{Q}_{66}\end{bmatrix}\cdot\begin{bmatrix}\varepsilon_x^0\\ \varepsilon_y^0\\ \gamma_{xy}^0\end{bmatrix}+z\begin{bmatrix}\overline{Q}_{11} & \overline{Q}_{12} & \overline{Q}_{16}\\ \overline{Q}_{12} & \overline{Q}_{22} & \overline{Q}_{26}\\ \overline{Q}_{16} & \overline{Q}_{26} & \overline{Q}_{66}\end{bmatrix}\cdot\begin{bmatrix}k_x\\ k_y\\ k_{xy}\end{bmatrix} \qquad (7.6)$$

The variation in stress through the laminate thickness can be determined by using Equation 7.6 to calculate the stress in each lamina. In this case, the stress through the laminate will vary substantially from layer to layer. A more convenient method of analysis involves the use of equivalent forces and moments acting on the laminate's cross section. The resultant forces (N) are calculated by integrating the corresponding stresses through the laminate thickness h, and the resultant moments (M) are determined by integration of the corresponding moments with respect to the mid-plane:

$$N_x=\int_{-h/2}^{h/2}\sigma_x\cdot dz \qquad M_x=\int_{-h/2}^{h/2}\sigma_x z\cdot dz$$

$$N_y=\int_{-h/2}^{h/2}\sigma_y\cdot dz \qquad M_y=\int_{-h/2}^{h/2}\sigma_y z\cdot dz \qquad (7.7)$$

$$N_{xy}=\int_{-h/2}^{h/2}\tau_{xy}\cdot dz \qquad M_{xy}=\int_{-h/2}^{h/2}\tau_{xy} z\cdot dz$$

Laminate A, B, and D matrices were calculated using the $\overline{Q}$ matrix (Equation 7.6) to give a representation of overall laminate response. The conventional summation procedure was adapted by using numerical integration to allow for temperature and property variation through each ply.

$$A=\sum_{k=1}^{n}\int_{h_{k-1}}^{h_k}\overline{Q}\,dz \qquad B=\sum_{k=1}^{n}\int_{h_{k-1}}^{h_k}\overline{Q}z\,dz \qquad D=\sum_{k=1}^{n}\int_{h_{k-1}}^{h_k}\overline{Q}z^2\,dz \qquad (7.8)$$

The A, B and D matrices are used to relate the resulting in-plane loads or bending moments, defined in Figure 7.6, to the mid-plane strains and curvatures with the relationship:

$$\begin{bmatrix} N \\ M \end{bmatrix} = \begin{bmatrix} A & B \\ B & D \end{bmatrix} \begin{bmatrix} \varepsilon_o \\ k \end{bmatrix} \tag{7.9}$$

where: N and M are the matrices of applied loads and bending moments respectively,

ε_o and k are the mid-plane strains and curvatures respectively.

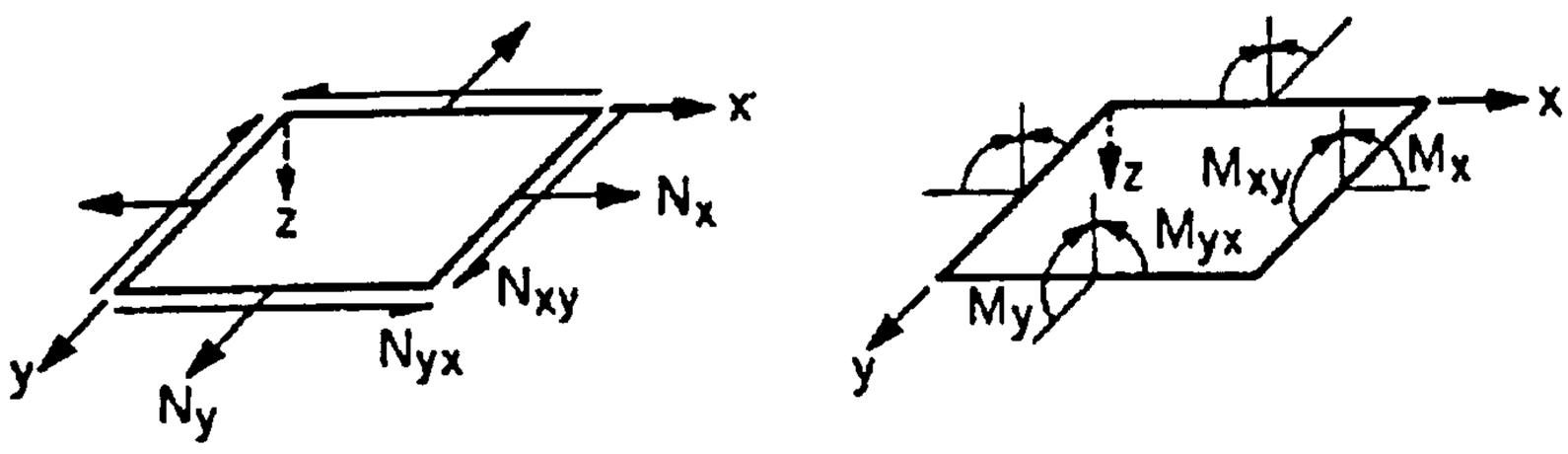

Figure 7.6 Positive sense of resultant forces (N) and moments (M) [108].

An inverted version of Equation 7.9 was also used for the model predictions presented here. First, the matrices were partially inverted:

$$\begin{bmatrix} \varepsilon_o \\ k \end{bmatrix} = \begin{bmatrix} A^* & B^* \\ C^* & D^* \end{bmatrix} \cdot \begin{bmatrix} N \\ M \end{bmatrix} \tag{7.10}$$

where:

$$[A^*] = [A^{-1}]$$

$$[B^*] = -[A^{-1}][B]$$

$$[C^*] = [B][A^{-1}] = [B^*]^T$$

$$[D^*] = [D] - [B][A^{-1}][B]$$

Then, the fully inverted matrices were calculated by applying the following operations:

$$[A'] = [A^*] - [B^*]\,[D^{*-1}]\,[C^*] = [A^*] + [B^*][D^{*-1}][B^*]^T$$

$$[B'] = [B^*][D^{*-1}]$$

$$[C'] = -\,[D^{*-1}]\,[C^*] = [B^*]^T = [B']$$

$$[D'] = [D^{*-1}]$$

The inverted form of the A, B, and D matrices allow analysis of laminate structures when the input parameters are the loads:

$$\begin{bmatrix} \varepsilon_o \\ k \end{bmatrix} = \begin{bmatrix} A' & B' \\ B' & D' \end{bmatrix} \cdot \begin{bmatrix} N \\ M \end{bmatrix} \tag{7.11}$$

7.4 Model Matrix Predictions

7.4.1 The *A*, *B* and *D* matrices

Predictions of the variation of A, B and D with time for all three laminate systems are shown in Figures 7.7 and 7.8. Figure 7.7 shows the main matrix components for a 12mm polyester laminate. Figure 7.8 details A_{11}, B_{11} and D_{11} for the vinyl ester and polypropylene laminates. The predictions are based on a 50kW/m^2 fire scenario.

The A matrix, which describes the laminate in-plane stiffness, falls continuously due to the general deterioration of the elastic properties with increasing temperature and resin degradation.

The laminate interaction term, B, describes the interaction between in-plane loads and out of plane bending. B initially starts at zero because of the symmetry of the laminate about its centreline. The imbalance of moduli in regions on either side of the laminate centreline causes B to rise rapidly when a heat flux is initially applied. B then falls as the general deterioration of elastic properties within the laminate progresses. B seems to fall more slowly in the polypropylene laminate when compared to the polyester and vinyl ester systems. This can be explained by the dramatic loss in mechanical properties

which occurs when polypropylene is heated to within 20°C of its melting temperature (T_m). This sudden loss in stiffness prolongs the asymmetric behaviour of the laminate until, ultimately, the entire cross section of the laminate melts at around 700 seconds.

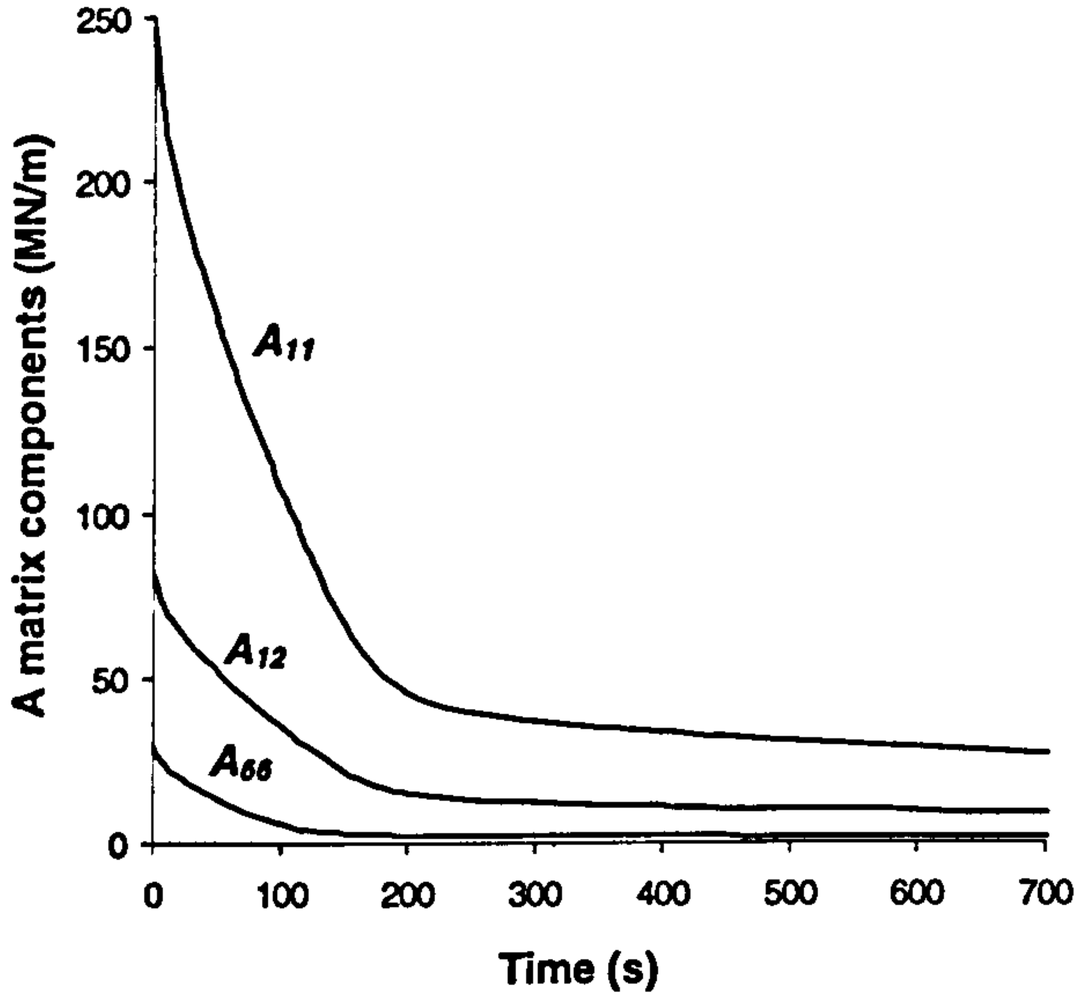

(i)

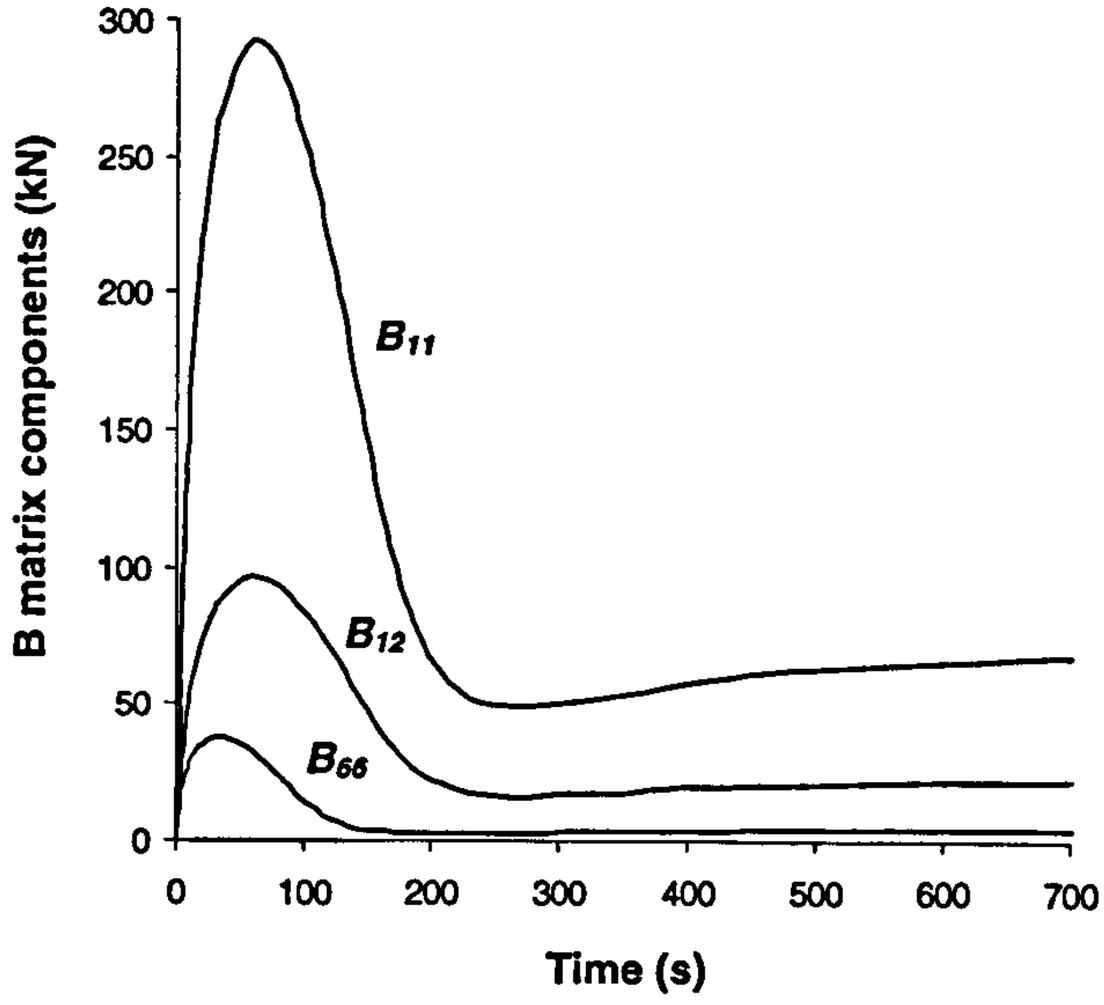

(ii)

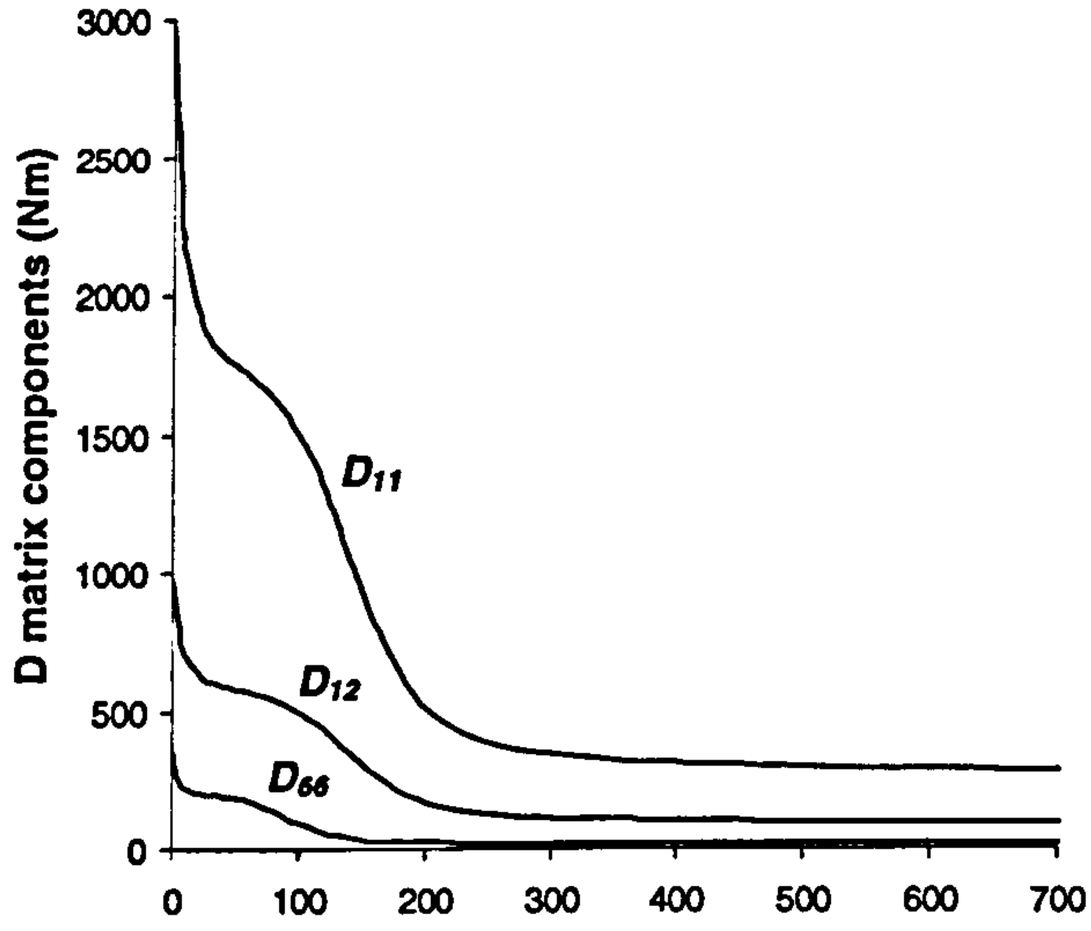

(iii)

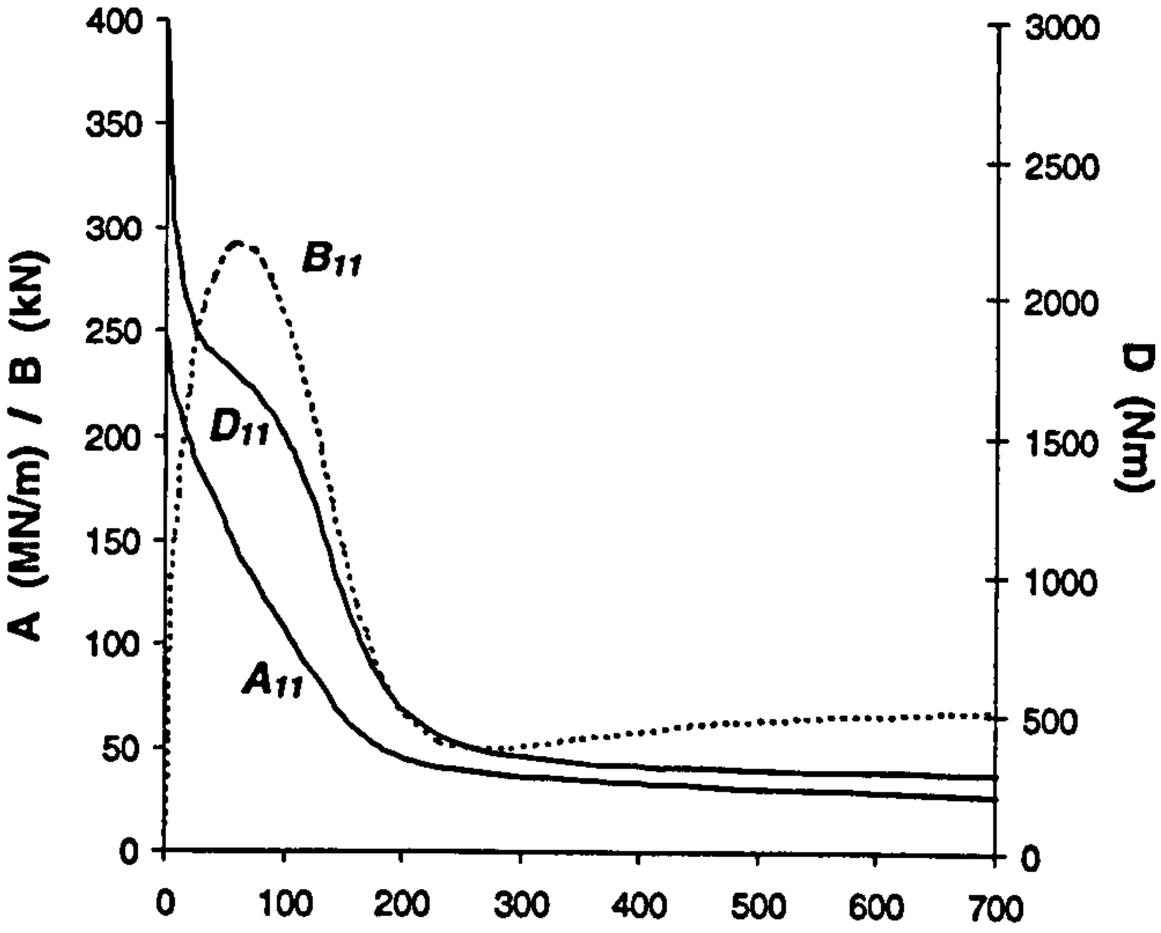

(iv)

Figure 7.7 The main (i) *A*, (ii) *B* and (iii) *D* matrix components for a 12mm polyester laminate exposed to a one-sided 50kW/m^2 heat flux. (iv) A comparison of the leading *A*, *B* and *D* matrix components.

The D matrix describes the laminate's resistance to bending. As expected, D declines rapidly with time. The development of laminate asymmetry, shown by the B matrix, is also reflected in the D matrix.

As the B matrix is the laminate interaction term, any variations in B's form are reflected in A and D. Figures 7.7(iv) and 7.8(i) show the relationships between A_{11}, B_{11} and D_{11} for a glass/polyester laminate, and a glass/vinyl ester laminate in a 50kW/m^2 fire.

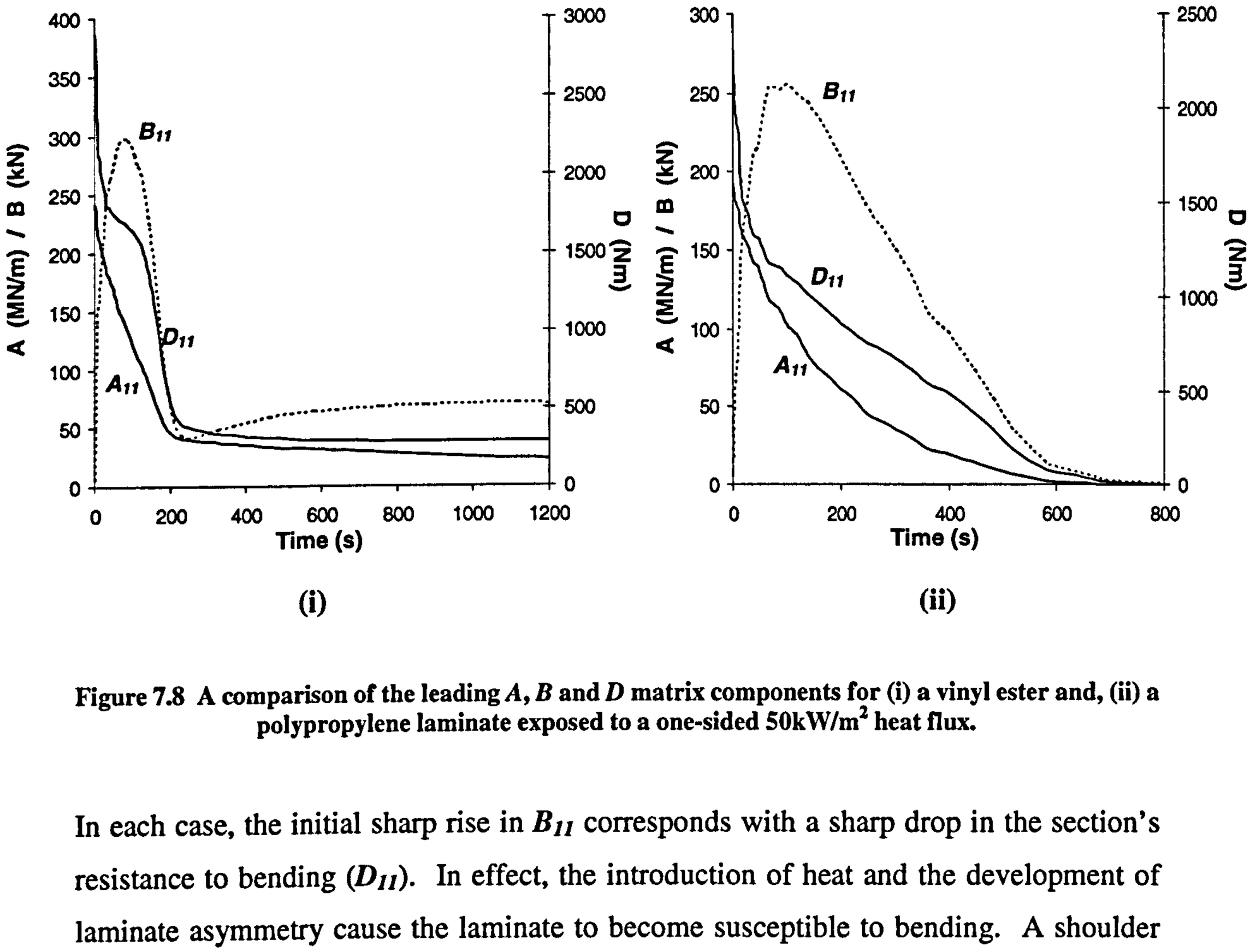

Figure 7.8 A comparison of the leading A, B and D matrix components for (i) a vinyl ester and, (ii) a polypropylene laminate exposed to a one-sided 50kW/m^2 heat flux.

In each case, the initial sharp rise in B_{11} corresponds with a sharp drop in the section's resistance to bending (D_{11}). In effect, the introduction of heat and the development of laminate asymmetry cause the laminate to become susceptible to bending. A shoulder on the D matrix curve coincides exactly in time with the peak values of the B matrix. As the rate of change of B reduces, the progression of asymmetrical behaviour slows momentarily creating the "shoulder" in the curve. B then falls rapidly, causing the laminate to bend once more as it attempts to return to its original configuration. When B

finally becomes more stable, at around 220 seconds, the laminates resistance to bending (*D*) also becomes stable.

The *A* matrix controls the laminate's in plane stiffness. In this case, as *B* is associated with the mid-plane curvatures, any variation in curvature causes the in-plane stiffness to reduce significantly. When *B* stabilises at around 220 seconds, the *A* matrix also stabilises under more symmetrical conditions.

Figure 7.8(ii) shows the leading terms of the *A*, *B* and *D* matrices for a glass/polypropylene laminate. Variations in A_{11}, B_{11} and D_{11}, although not as obvious, follow a very similar pattern to the polyester and vinyl ester systems. Because the laminate progressively melts during a fire test, *B* takes much longer to regain symmetrical behaviour and reduce back towards zero. The shoulder in D_{11} can therefore be assumed to carry from the initial peak in *B* right through to the point at which almost the entire cross section of the laminate has melted (at around 600 seconds).

Figure 7.9 shows the elastic resistance of the section $1/D'_{11}$, which is equivalent to the '*EI*' value, for each of the three laminates. The bending stiffness response declines rapidly with time. Not only was this parameter an interesting characteristic of the laminate's fire response, but it also served as a check to validate the accuracy of the model. *EI* was calculated for the laminate for each time step and the results compared to $1/D'_{11}$.

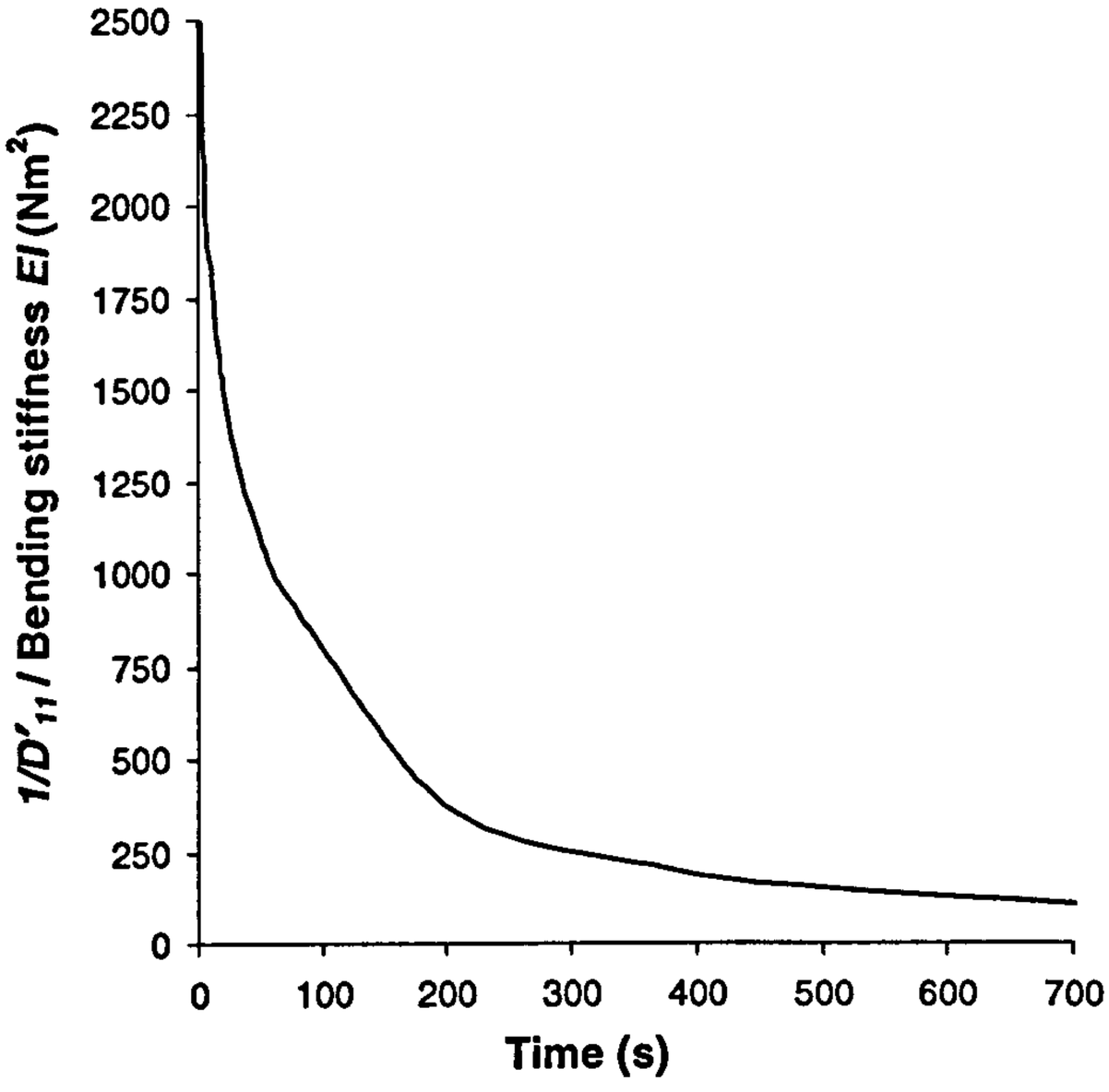
2500
2250
2000
1750
1500
1250
1000
750
500
250
0
1/D'11 / Bending stiffness EI (Nm2)
0
100
200
300
400
500
600
700
Time (s)

(i)

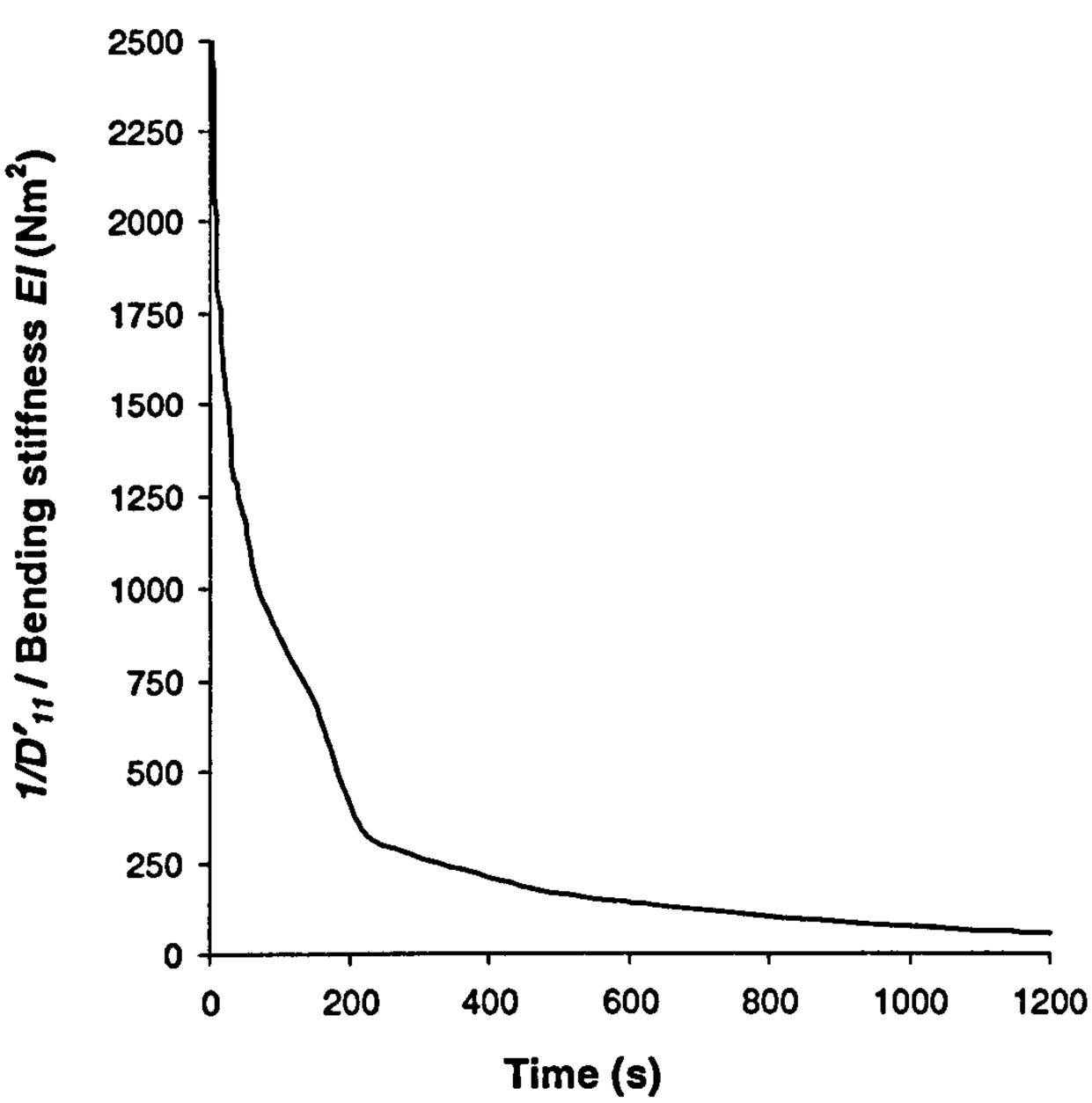
2500
2250
2000
1750
1500
1250
1000
750
500
250
0
1/D'11 / Bending stiffness EI (Nm2)
0
200
400
600
800
1000
1200
Time (s)

(ii)

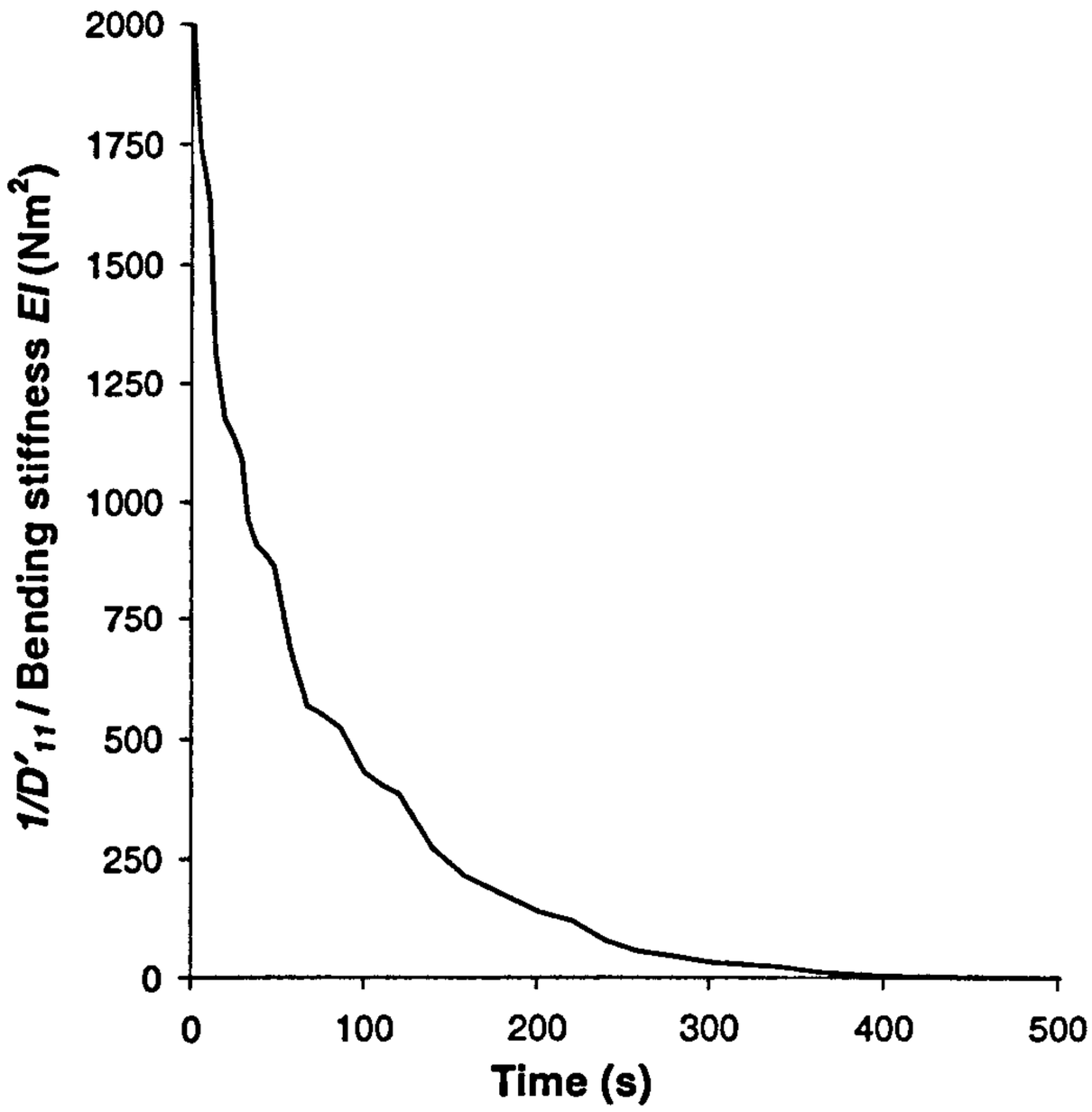

(iii)

Figure 7.9 Model predictions of the variation of bending stiffness for (i) a glass/polyester laminate, (ii) a glass/vinyl ester laminate, and (iii) a glass/polypropylene laminate exposed to a one-sided 50kW/m^2 heat flux.

7.5 Strength Prediction

The compressive and tensile strength of the three laminate systems were also modelled. This was achieved using two methods. The first method regarded ply failure as a sudden, catastrophic event, and hence the modelled laminate stress-strain curves would take a "saw-tooth" form. The second method involved modelling the measured stress-strain curves (Chapter 6) individually for each material.

7.5.1 "Saw Tooth" Curve Model

Laminate stress-strain curves were constructed for each time step by increasing an applied strain in small increments. The 12mm thick laminate was considered to have 13 nodes, one for each millimetre in the through thickness direction. Stresses at each node were calculated using the temperature and RRC dependent values of Young's modulus (E_l) for every given strain value. Once any stress had reached the calculated

compressive or tensile strength value, the ply in question was considered to have failed and the strength value reset to zero. These assumptions led to the saw-tooth stress-strain curve form. The laminate stress at any given strain value was found by averaging the stress at each node through the laminate. The laminate strength for each time step was then taken to be the maximum averaged stress value observed from the stress-strain curves, as in Figures 7.10 and 7.11.

The applied strain values, used to calculate the laminate strength, were increased to 7% strain for tensile and 3% strain for compressive loading. These strain limits were based on the maximum strain values reached by the materials in the material properties tests.

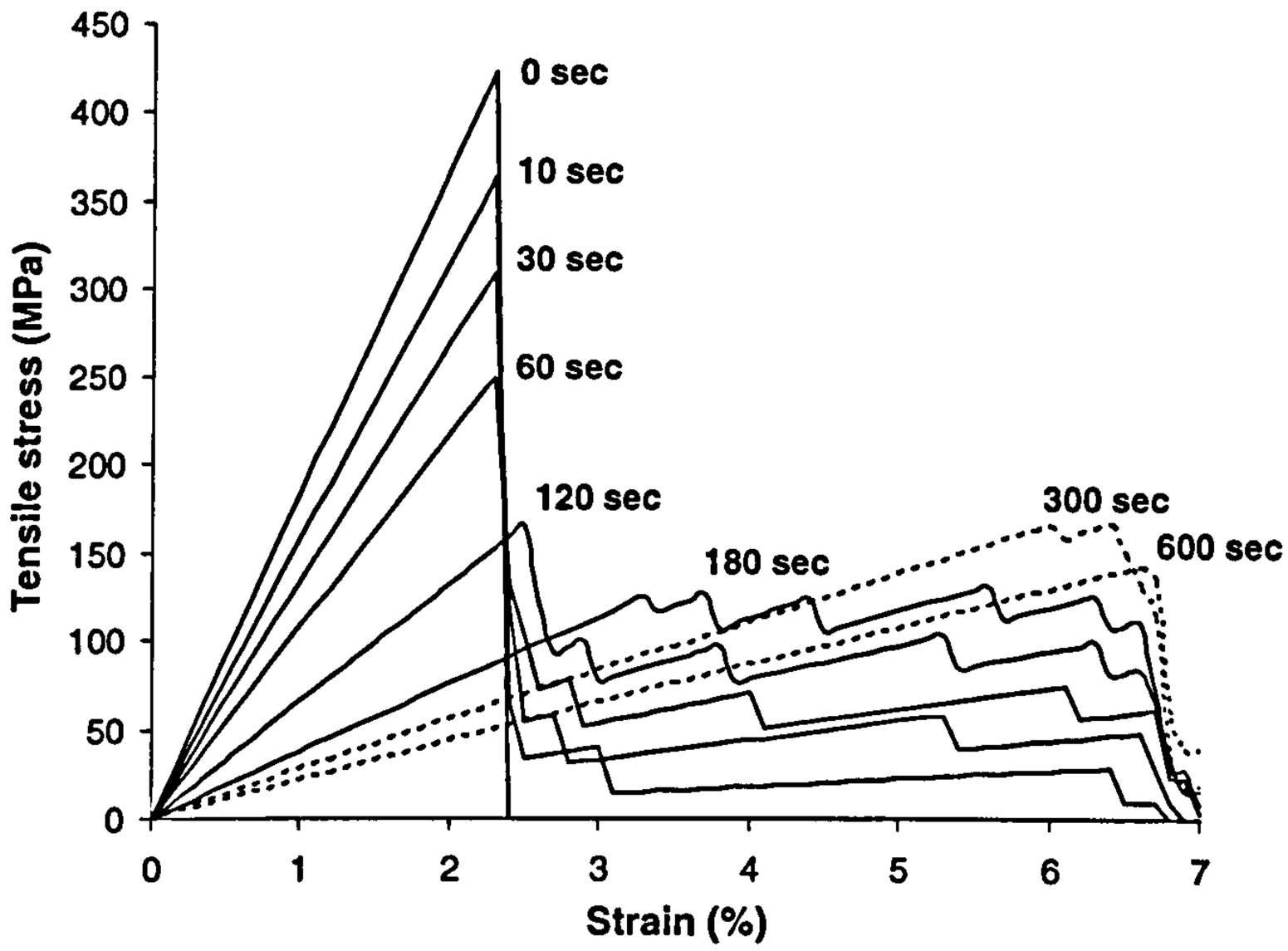

Figure 7.10 Modelled tensile stress-strain curves (using the "Saw tooth" model) for polyester laminate under tensile load in a 50kW/m^2 fire. The maximum stress value for each time step was used to create a laminate strength curve.

Figure 7.10 shows the modelled laminate tensile stress-strain curves for a polyester laminate. The peak stress values for each time-step were taken to be the laminate strength at that particular time. At the start of the fire, the laminate shows catastrophic failure when loaded to its tensile strength; at these low temperatures, the laminate is very stiff. Later, when the fire is more developed, the full cross section of the laminate has

softened and, although failure occurs at a much lower stress, the laminate experiences much larger strain levels.

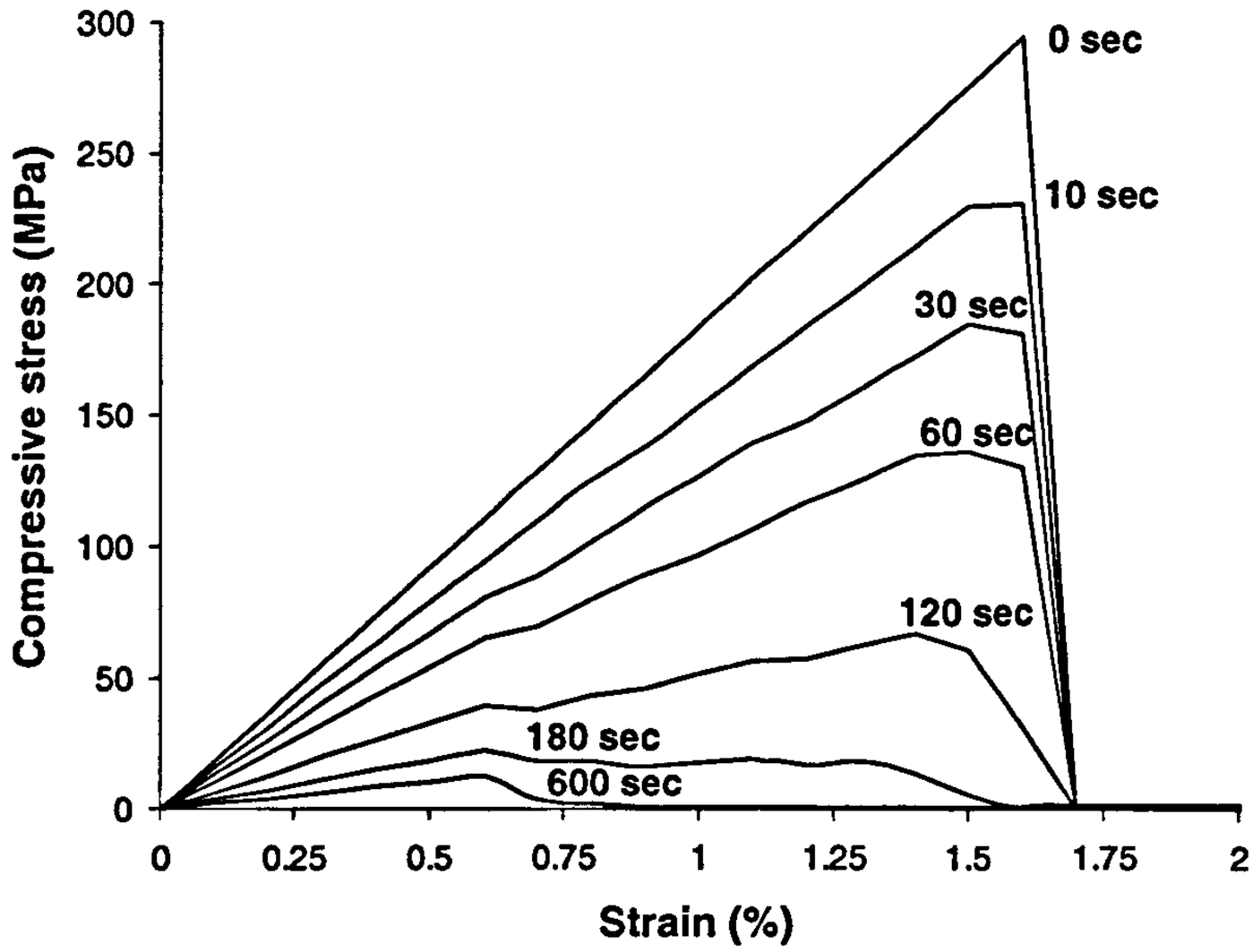

Figure 7.11 Modelled compressive stress-strain curves (using the "Saw tooth" model) for a polyester laminate under compressive load in a 50kW/m^2 fire.

Modelled laminate compressive stress-strain curves are shown in Figure 7.11. The discontinuities observed in the curves correspond to individual ply failure. Again, the peak stress values were used to create laminate strength curves. These are shown in Figures 7.16, 7.17 and 7.18.

7.5.2 Temperature Dependent Stress-Strain Curve Model

Compressive and tensile stress-strain curves were measured for each material and detailed in Chapter 6. For more accurate laminate strength predictions, each set of curves was modelled using the following empirical relationship:

$$\sigma = \sigma_{max} \cdot \left(1 - e^{\left(\frac{-E \cdot \varepsilon}{\sigma_{max}} \right)} \right)$$

Figure 7.12 explains the theory behind the modelled temperature dependent stress-strain curves. By increasing an applied strain (ε), the modelled stress (σ) approaches, although never reaches, an imaginary maximum stress value (σ_{max}). The Young's modulus (E) for a given temperature describes the initial slope of the model curve.

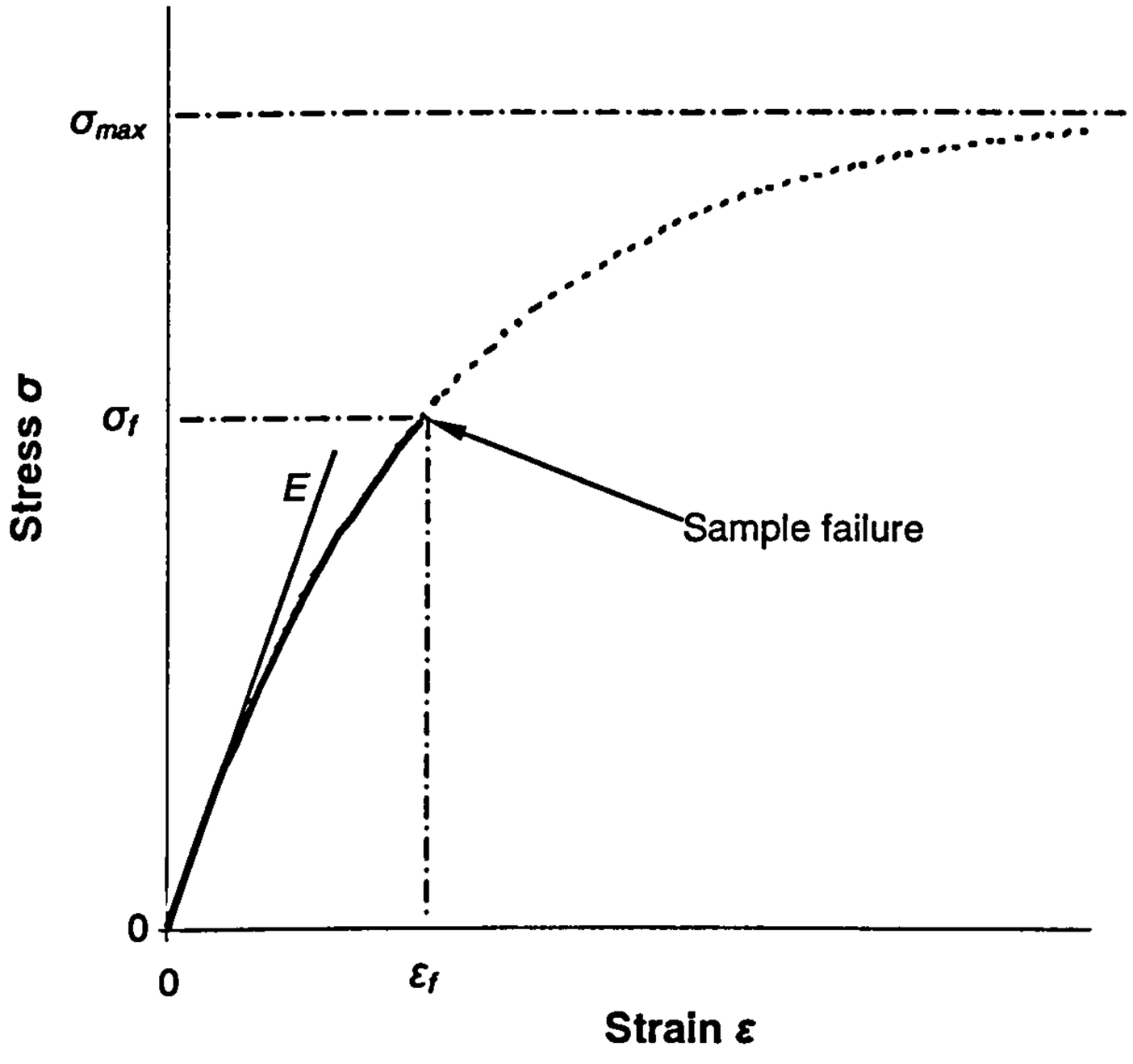

Figure 7.12 The parameters involved in modelling a stress-strain curve. σ_f and ε_f denote the stress and strain at which the sample has failed.

Each stress-strain curve, measured at a particular temperature, was modelled in this way by adjusting the two parameters E and σ_{max}. Hence, the stress within a particular ply, at a given temperature, could be accurately determined using the modelled stress-strain curve for that temperature. Figure 7.13 shows a comparison of measured and modelled curves for glass/vinyl ester. The modelled curves for glass/polyester and glass/polypropylene are shown in Figures 7.14 and 7.15 respectively (the corresponding measured curves are shown in Figures 6.7 - 6.9 and 6.12 - 6.14.)

The modelled tensile stress-strain curves were used to make laminate strength predictions, shown in Figures 7.16, 7.17 and 7.18. The modelled compression curves however have the "saw-tooth" form expected from catastrophic compressive failure. Hence, it was not necessary to use the modelled curves for laminate compressive strength prediction.

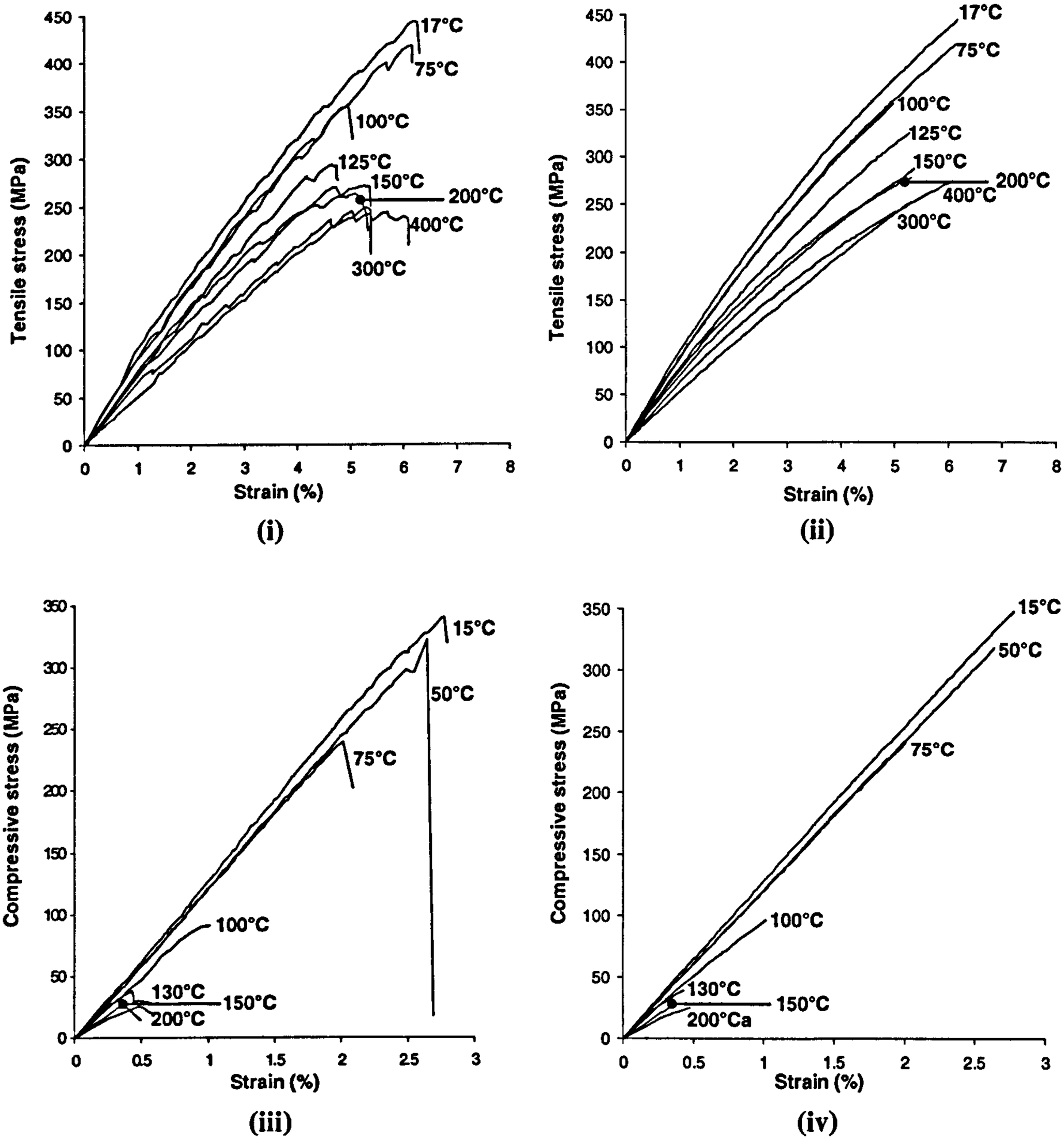

Figure 7.13 Temperature dependent stress-strain curves for a vinyl ester laminate. (i) Tensile stress-strain curves. (ii) Modelled tensile stress-strain curves. (iii) Compressive stress-strain curves. (iv) Modelled compressive stress-strain curves.

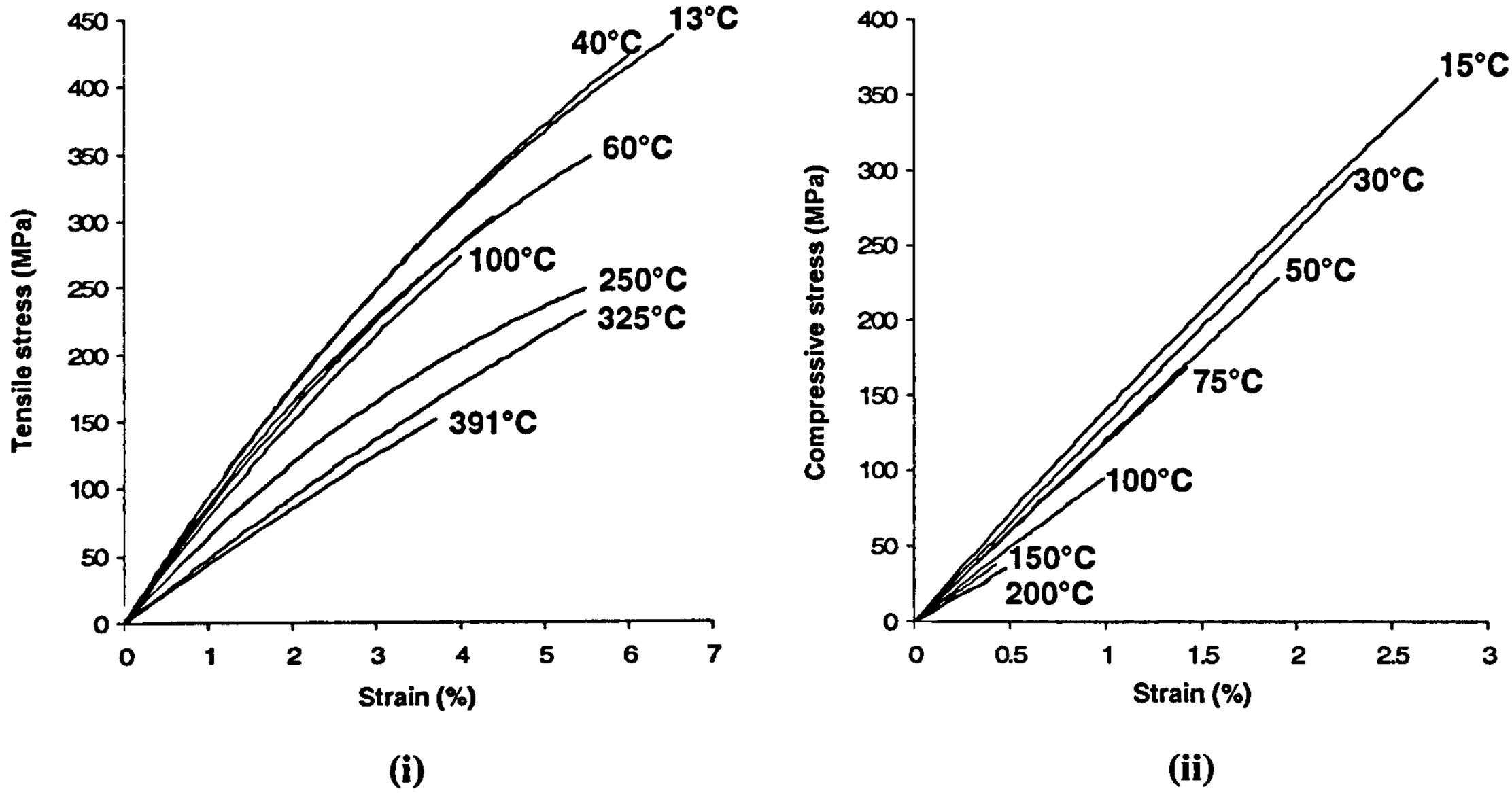

Figure 7.14 Temperature dependent stress-strain curves for a polyester laminate. (i) Modelled tensile stress-strain curves. (ii) Modelled compressive stress-strain curves.

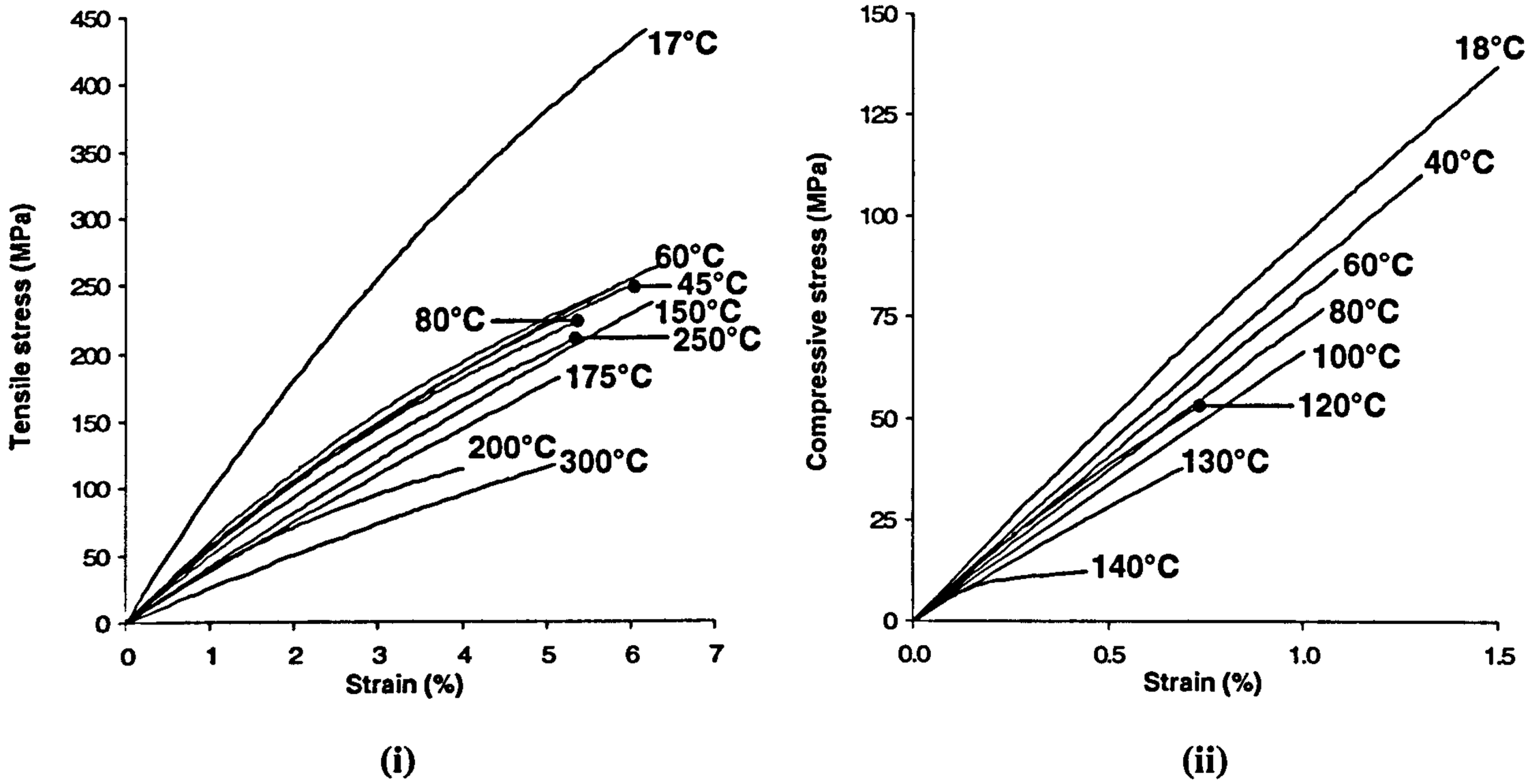

Figure 7.15 Temperature dependent stress-strain curves for a polypropylene laminate. (i) Modelled tensile stress-strain curves. (ii) Modelled compressive stress-strain curves.

7.5.3 Laminate Model Strength Prediction

Figures 7.16, 7.17 and 7.18 show model strength predictions for the three laminate systems in a 50kW/m^2 fire. Model curves are shown for the "Saw tooth" model and the modelled temperature dependent stress-strain (TDSS) curve method.

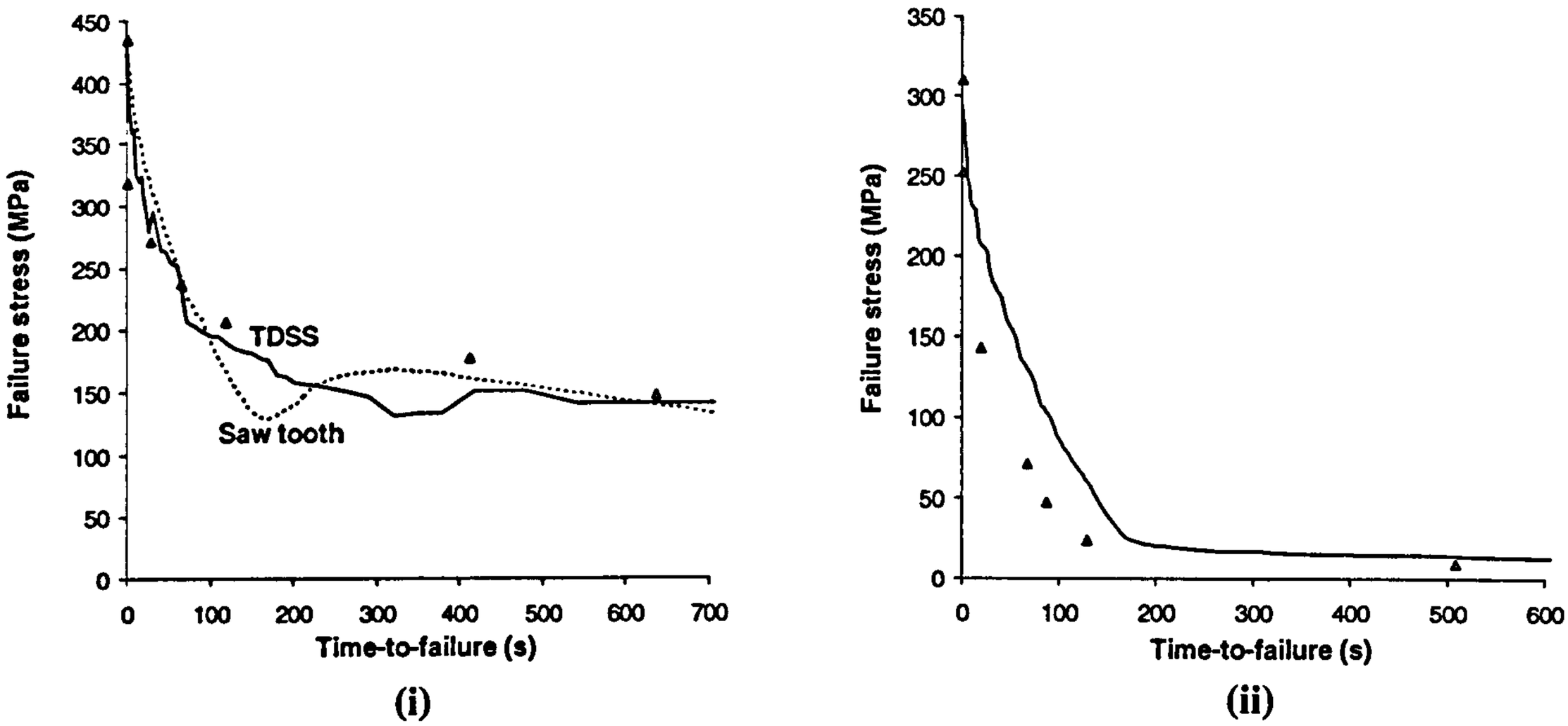

Figure 7.16 Laminate model strength predictions for a 12mm polyester laminate in a 50kW/m^2 fire. Fire under load test results are included to show the accuracy of the model predictions. (i) Tensile strength predictions; (ii) compressive strength predictions.

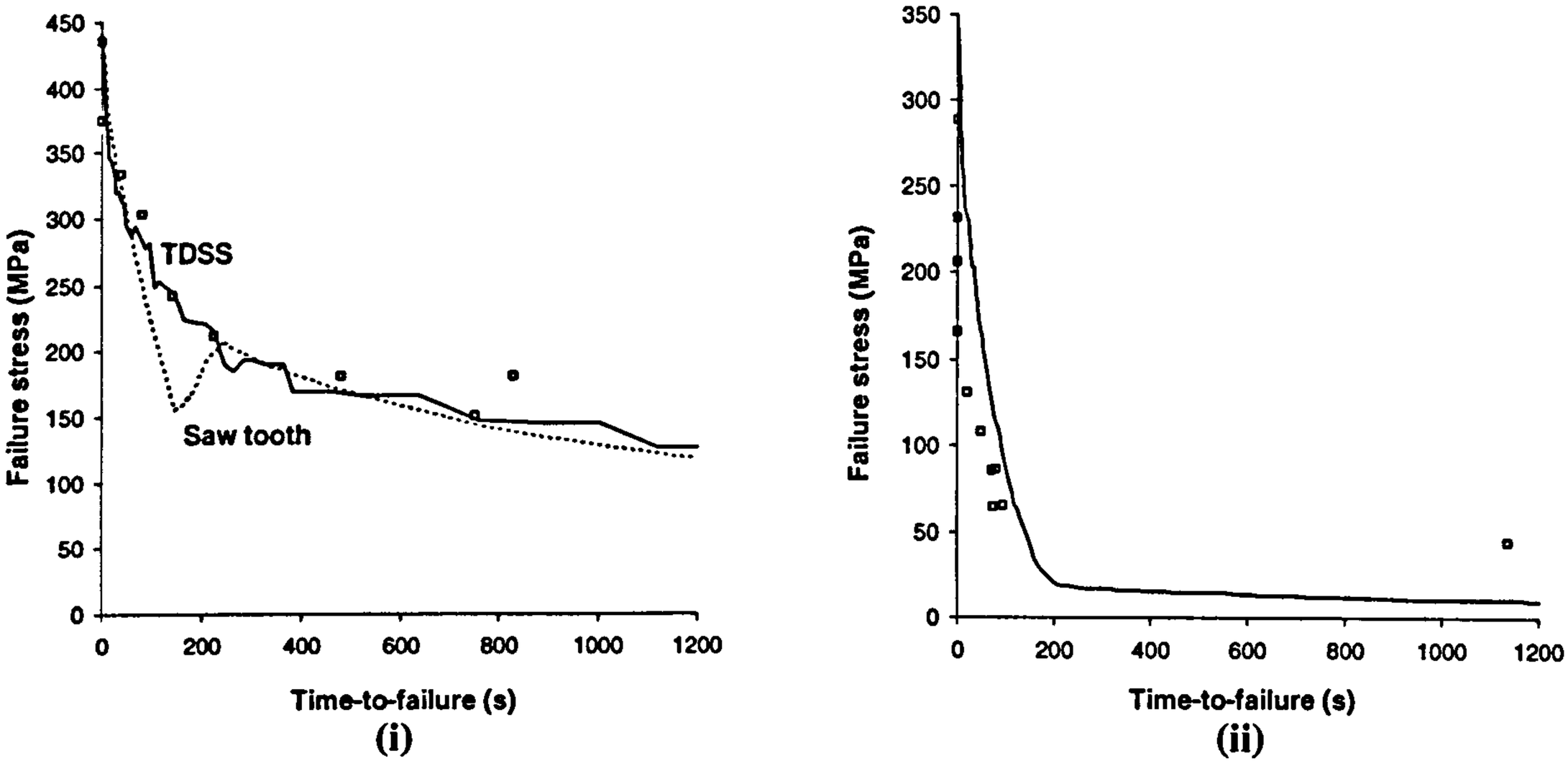

Figure 7.17 Laminate model strength predictions for a 12mm vinyl ester laminate in a 50kW/m^2 fire. (i) Tensile strength predictions; (ii) compressive strength predictions.

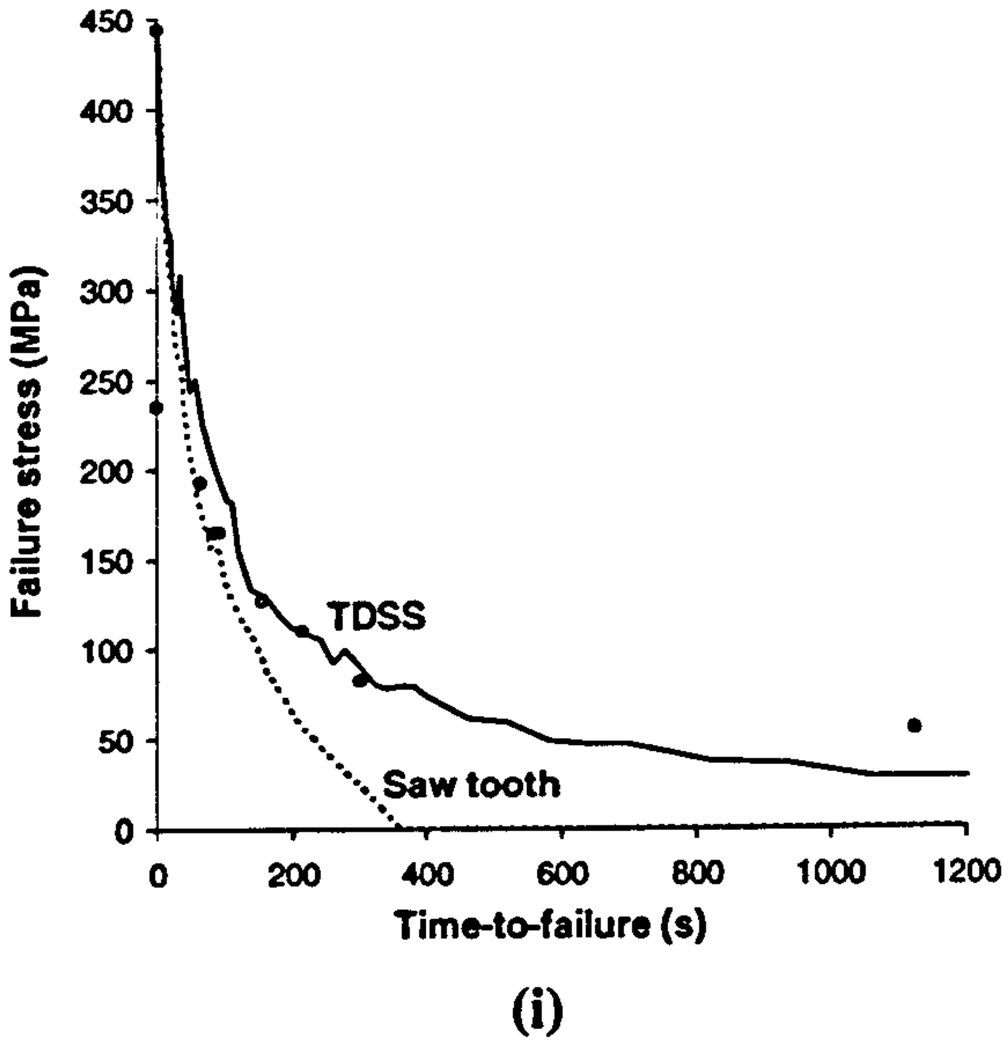

Figure 7.18 Laminate model strength predictions for a 12mm polypropylene laminate in a 50kW/m^2 fire. (i) Tensile strength predictions; (ii) compressive strength predictions.

The strength model produced some very accurate predictions. Both the saw tooth model and the TDSS model produced very accurate predictions for the tensile strength of polyester and vinyl ester laminates in fire. The accuracy of the TDSS method was further supported by the polypropylene tensile strength prediction. The Saw Tooth model produced very poor results for polypropylene's tensile strength. Saw Tooth model predictions were based on the flexural modulus property results. At temperatures over 160°C, the polypropylene resin had melted and the flexural modulus was effectively zero. Hence tensile strength results, calculated using a value of zero modulus were also equal to zero. This method of strength estimation neglected the strength of the residual glass and therefore produced very inaccurate results.

Both the polyester and vinyl ester saw tooth predictions have regions where the failure stress is under-estimated at failure times of around 180 seconds. This may be explained by the laminate stress-strain curves at failure times just over 180 seconds (highlighted as the dashed curves in Figure 7.10).

For failure times up to 180 seconds, much of the laminate is still reasonably cold towards the rear face. An increase in strain causes stress concentrations at the cold face and ply failure occurs in these stiffer regions, creating the dip in the laminate failure curve. At longer exposure times however, for example 300-600 seconds, the laminate cross section is generally hotter and softer and can therefore withstand much larger levels of strain. The plies share the load more efficiently in this case and hence longer failure times are predicted by the model for a given applied stress (for example, at 300 seconds or 400 seconds). In reality however, these failure times would not be reached by the laminate as it would have already failed.

The model also produced some reasonably accurate compressive failure results. The model gave an excellent compression prediction for the polypropylene laminate, but slightly over-estimated the failure strength of the polyester and vinyl ester samples. This may have been because these test samples did not fail by local compressive failure. The constrained compression test, although limiting Euler buckling, might allow a degree of local buckling to occur. This would account for the slightly lower compressive failure stresses measured during testing.

Chapter 8 Conclusions

8.1 The Propane Burner Test

- The propane burner test is a low cost, small scale test method capable of producing a constant heat flux which can be reproduced in any laboratory.
- The burner heat flux can be calibrated using a simple capacitance-type calorimeter. However, the process requires the use of a calibrated cone calorimeter.
- The thermal model produces reasonably accurate predictions of the thermal response and residual resin content of composite laminates in fire.

8.2 Material Property Classification

- The proposed tanh relationship provides an excellent representation of the variation of flexural modulus, tensile strength and compressive strength of thermoset laminates with temperature.
- The polypropylene laminates displayed two transitions in the range of measured temperatures. The first was around the glass transition temperature (T_g) and the second was prior to the resin melting point (T_m).
- Flexural modulus creep behaviour was characterised by an effective shift in the material T' value.
- Under-estimation of the tensile strength of the laminate systems at higher temperatures was explained by the loss of composite action. Once the composite was heated beyond T_g, the matrix ceased to make a contribution to the composite action. Fibre imperfections cause fibres to fail at different strain values, with a consequent greater loss in predicted laminate strength.

8.3 Fire under Load Tests

- All three laminate systems displayed considerable residual tensile strength at high temperatures.

- Compressive behaviour is the main limitation to the use of composites in fire risk applications. Most of the samples tested under compression in fire failed within 100 seconds, even at relatively low load levels.
- Tensile failure is initiated by the decomposition of the resin matrix and followed by creep rupture of the fibres.
- Observations presented here on compressive failure mechanisms in a loaded composite laminate in fire further support the work of Feih et al [105]. Compressive failure is initiated by delamination cracks forming between plies near the hot surface. The delaminated plies have little or no load bearing capability and hence the load is redistributed over the rest of the laminate. When the delamination free region reaches the material compressive strength, the laminate fails by plastic tow kinking.

8.4 The Laminate Model

- The *A* matrix, which describes the laminate in-plane stiffness, falls continuously due to the general deterioration of elastic properties with increasing temperature and resin degradation.
- The laminate interaction term, *B*, initially starts at zero because of the symmetry of the laminate about its centreline. The imbalance of moduli in regions on either side of the laminate centreline causes *B* to rise rapidly when a heat flux is applied. *B* then falls as the general deterioration of elastic properties within the laminate progresses.
- The *D* matrix describes the laminate's resistance to bending. *D* declines rapidly with time in fire. $1/D'_{11}$, is equivalent to the plate '*EI*' value. This bending stiffness response also declines rapidly with time.
- The model produced very accurate tensile strength predictions.
- Compressive behaviour was generally over-estimated for all the thermoset laminate systems. It was suggested that some of the failure modes may have included local buckling and hence the samples tended to fail within slightly shorter failure times.

Chapter 9 Further Work

Although the laminate model has demonstrated excellent prediction for the structural response of laminates in fire, there are several ways in which the model can be improved. The model may also be extended for use in other applications.

9.1 Extensions to the Laminate Model

9.1.1 Properties Library

A comprehensive library of thermal and temperature-dependent mechanical properties is required for the application of the model to any composite material. Although the variation of shear modulus (G_{12}) with temperature was taken from the literature for the research presented here, it may also be derived from other known mechanical properties [108]:

$$\frac{1}{E_x} = \frac{\cos^4\theta}{E_1} + \frac{\sin^4\theta}{E_2} + \frac{1}{4}\left(\frac{1}{G_{12}} - \frac{2\nu_{12}}{E_1}\right)\sin^2 2\theta \qquad (9.1)$$

where: E_1 is the longitudinal flexural modulus (GPa),

E_2 is the transverse flexural modulus (GPa),

$E_x = E_{45}$ (GPa), measured in the same way as E_1,

ν_{12} = Poisson's ratio.

Shear predictions would be more accurate if this property estimation were incorporated into the model.

9.1.2 Fire Protection Techniques

There are numerous fire protection methods available ranging from paints and intumescent material to sacrificial protection layers. Implementing these systems into the thermal model would be a fairly straight forward process once the heat transfer

processes and thermal properties are characterised. However, the application of many of these products to the laminate failure model may be problematic. When applied to loaded structures, fire protection systems tend to fracture easily revealing the substrate beneath.

9.1.3 The Effect of Thermal Expansion

The laminate model presented here does not consider the effects of thermal expansion. Prediction of the thermal expansion of a composite material with temperature can be complex [56-58, 111, 112]. At low temperatures, the composite expands at a slow linear rate with temperature because of the natural expansion of the fibres and matrix. Once the resin starts to decompose at around 300°C, the composite expands more dramatically due to the formation and build-up of volatiles. However, the formation of char at temperatures in excess of 500°C causes the material to contract again.

The laminate model should be adapted to consider thermal expansion by the inclusion of thermally induced deformations in Equation 7.9:

$$\begin{bmatrix} N \\ M \end{bmatrix} = \begin{bmatrix} A & B \\ B & D \end{bmatrix} \begin{bmatrix} \varepsilon_o - \varepsilon_o^T \\ k - k^T \end{bmatrix} \tag{9.2}$$

where: ε_o^T and k_o^T are the thermally induced strains and curvatures which occur in a zero load condition.

9.1.4 Buckling Behaviour

It was highlighted that the constrained compression test, although limiting Euler buckling, might allow a degree of local buckling to occur (Chapter 7.5.3). One of two methods could overcome this test limitation. One option would be to design a compressive fire test that could completely ensure true compressive failure. However, the design of such a test would be difficult in practice. The test sample would be

constrained in such a way that exposing a surface area for the incident heat flux would be almost impossible.

The other possibility is to calculate a theoretical buckling failure stress using the laminate failure model. Eckhold suggests a formula for the buckling stress of a square plate, constrained at each of its four edges [109]:

$$\sigma_{Buckling} = \frac{C'}{b^2 t} \cdot \sqrt{D_{11} D_{22}} \qquad (9.3)$$

where: $\sigma_{Buckling}$ is the sample buckling failure stress (MPa),

C' is a constant (between 1 and 7) which defines the nature of constraint the plate is under (1 being simply supported and 7 being fully clamped),

b is the breadth of the plate (m),

t is the thickness of the plate (m).

Predicted values of D_{11} and D_{22} could be used to calculate a model buckling failure curve. However, the constant C' would have to be determined experimentally. This could be achieved by testing mock plates without fire exposure.

Recesses, cut from the area normally exposed to fire, would simulate the progression of resin degradation in a typical fire scenario and give the sample an "effective sample thickness" (t'). The buckling failure stress for a given effective thickness could be measured by loading the sample in the constrained compression test rig. A value for C' could then be calculated by repeating the test for a number of samples with various effective thicknesses.

9.2 Other Applications for the Laminate Model

9.2.1 Sandwich Panels

The laminate model could be developed for the analysis of sandwich structures. The thermal model could be run for each layer of material with special consideration paid to the boundary conditions at each layer interface. Further information on the thermal and mechanical properties of various core materials would also be required.

Problems might be encountered when predicting the laminate-core bond strength. When a loaded sandwich panel is exposed to a one-sided heat flux, the hot face laminate would experience a large increase in bending and twisting as the B matrix increases. The cold face panel however would remain largely unaffected due to the insulating core. This exaggerated asymmetric behaviour could lead to large shear forces at the hot-face panel / core interface and premature failure would occur.

The application of laminate theory to sandwich panels may also cause problems. Laminate theory is most effective when applied to thin plates. The limitations of laminate theory to thick sandwich sections should be thoroughly investigated.

9.2.2 Finite Element Analysis

More detailed structural analysis would be possible if the laminate model were linked to a finite element package. Graphical presentation of stress variations and temperature profiles would assist the understanding of the failure mechanisms under various loading conditions.

References

1. Hull, D., *An Introduction to Composite Materials*. 1st ed. Cambridge Solid State Science Series. 1981, Cambridge, England: Cambridge University Press.

2. *Composite Materials in Maritime Structures*. 1st ed. Cambridge Ocean Technology Series 4, ed. R.A. Shenoi and J.F. Wellicome. Vol. 1. 1993, Cambridge: Cambridge University Press.

3. *Pictures courtesy of The British Glass Confederation (http://www.britglass.org.uk).*

4. *Pictures courtesy of JYTT International Pte Ltd (http://www.jytt-intl.com).*

5. *Pictures courtesy of Opti-x (http:\\www.opti-x.dk).*

6. *Glass reinforced plastics*. 1st ed, ed. B. Parkyn. 1970, London: Butterworth & Co. Ltd.

7. Murphy, J., *The Reinforced Plastics Handbook*. 1994, Oxford: Elsevier Advanced Technology.

8. *Pictures courtesy of Netcomposites (http:\\www.netcomposites.com).*

9. *Pictures courtesy of Vectorply (http:\\vectorply.com).*

10. Bedouin, N., *Setting sail with recyclables*, in *High Vision for Composites magazine (No. 15): Saint-Gobain Reinforcements*. 2006. p. 14.

11. Rosato, D. and D. Rosato, *Reinforced Plastics Handbook*. 3rd ed. 2004, Oxford: Elsevier Advanced Technology.

12. Dodds, N., et al., *Fire behaviour of composite laminates*. Composites: Part A, 2000. **31**(7): p. 689 - 702.

13. Kirby, B.R., *Recent Developments and Applications in Structural Fire Engineering Design - A Review.* Fire Safety Journal, 1986. **11**(3): p. 141-179.

14. Kirby, B.R., *The Application of BS5950: Part 8 on Fire Limit State Design to the Performance of 'Old' Structural Mild Steel.* Fire Safety Journal, 1993. **20**(4): p. 353-376.

15. EN45545: "*Fire protection on railway vehicles.*" 2004: p. 1-17.

16. Briggs, P. *Fire performance of composites in European construction applications.* in *Proceedings of Composites in Fire 3: 3rd International Conference on the Response of Composites in Fire.* 2003. Newcastle upon Tyne.

17. Murrell, J. and P. Briggs. *Developments in European and international fire test methods for composites used in building and transport applications.* in *Composites in Fire 2: 2nd International Conference on the Response of Composite Materials to Fire.* 2001. Newcastle upon Tyne.

18. *International Code for Application of Fire Test Procedures (FTP Code).* Resolution MSC.61(67). 1997, International Maritime Organisation, London.

19. *International Code for High Speed Craft (HSC Code).* Resolution MSC.36(63). 1995, International Maritime Organisation, London.

20. Høyning, B. and J. Taby. *Fire performance of composite marine structures in relation to the IMO high speed craft code.* in *Composites in Fire 2: 2nd International Conference on the Response of Composite Materials to Fire.* 2001. Newcastle upon Tyne.

21. Gibson, A.G. *Basic Mechanisms of Fire Damage in Organic Matrix Composites.* in *Composites in Fire 3: 3rd International Conference on the Response of Composite Materials to Fire.* 2003. Newcastle upon Tyne, England.

22. *ISO 5660-1: "Reaction-to-fire tests - Heat release, smoke production and mass loss rate - Part 1: (cone calorimeter method)".* International Organization for Standardization, Second Edition, 2002.

23. *Pictures courtesy of SpecialChem (http://www.specialchem4polymers.com).*

24. *ISO 4589: "Plastics - Determination of burning behaviour by oxygen index".* International Organization for Standardization, First edition, 1996.

25. *Pictures courtesy of Qualitest (http://www.qualitest-inc.com).*

26. *Pictures courtesy of the Bolton Fire Materials Laboratory, University of Bolton, (http://www.bolton.ac.uk/fire).*

27. *ISO 5659-2: "Plastics - Smoke generation - Part 2: Determination of optical density by a single-chamber test".* International Organization for Standardization, First edition, 1998.

28. *Pictures courtesy of the Tin Technology website (http://www.tintechnology.com).*

29. *ASTM E 162-02a: "Standard test method for surface flammability of materials using a radiant heat energy source".* ASTM International, 2002.

30. *Pictures courtesy of Govmark Fire Laboratories (http:\\www.govmark.com).*

31. *ISO 9705: "Fire Tests - Full-scale room test for surface products".* International Organization for Standardization, First edition, 1993.

32. *BS EN 13823: "Reaction to fire for building products. Building products excluding floorings exposed to the thermal attack by a single burning item".* British Standards Institution, First edition, 2002.

33. *Pictures courtesy of the Swedish National Testing and Research Institute, (http://www.sp.se).*

34. Kirby, B.R., et al., *Natural Fires in Large Scale Compartments.* International Journal on Engineering Performance-Based Fire Codes, 1999. **1**(2): p. 43-58.

35. *BS 476-20/21: "Fire tests on building materials and structures. Method for determination of the fire resistance of elements of construction ".* British Standards Institution, First edition, 1987.

36. *International convention for the safety of life at sea (SOLAS) 1974.* Consolidated Edition, International Maritime Organisation, London, 1992.

37. *ISO 834-3: "Fire resistance tests - Elements of building construction - Part 3: Commentary on test method and test data application".* International Organization for Standardization, First edition, 1999.

38. Gibson, A.G., et al. *A Low Cost Burner Technique for the Development and Modelling of Laminates in Fire.* in *Composites in Fire 3: 3rd International Conference on the Response of Composite Materials to Fire.* 2003. Newcastle upon Tyne, England.

39. Sultan, M.A., *The effect of furnace parameters on fire severity in standard fire resistance tests.* Fire & Materials, 1996. **20**: p. 245-252.

40. *Pictures courtesy of SINTEF, the Norwegian Fire Resource Centre (http://www.sintef.no).*

41. *The Institute for Combustion and Energy Studies, University of Utah (http:\\www.ices.utah.edu).*

42. *Pictures courtesy of the IEEE Computer Society (http://www.computer.org).*

43. *Pictures courtesy of the Advantica Ltd. website (http://www.spadeadam.biz).*

44. Folkers, J. *Fire testing and performance of fiber glass pipe.* in *Proceedings of Composites in Fire.* 1999. Newcastle upon Tyne.

45. Gibson, A.G., et al. *A low cost burner technique for the development and modelling of laminates in fire.* in *Composites in Fire 3: 3rd International Conference on the Response of Composite Materials to Fire.* 2003. Newcastle upon Tyne, England.

46. Hill, P.S. and G.C. White. *Jet fire testing and performance of composite materials.* in *Proceedings of Composites in Fire.* 1999. Newcastle upon Tyne.

47. DeMarco, R.A. *Composite applications at sea: fire related issues.* in *36th International SAMPE Symposium.* 1991. Anaheim, CA.

48. Looyeh, M.R.E., P. Bettess, and A.G. Gibson, *A one-dimensional finite element simulation for the fire-performance of GRP panels for offshore structures.* International Journal of Numerical Methods for Heat & Fluid Flow, 1997. 7(6): p. 609-625.

49. Gibson, A.G., et al., *A model for the thermal performance of thick composite laminates in hydrocarbon fires.* Revue de l'Institut Français du Pétrole, 1995. 50(1): p. 69-74 (special issue).

50. Fredlund, B., *Modelling of heat and mass transfer in wood structures during fire.* Fire Safety Journal, 1993. 20: p. 39-69.

51. Kansa, E.J., H.E. Perlee, and R.F. Chaiken, *Mathematical model of wood pyrolysis inlcuding internal forced convection.* Combustion and Flame, 1977. 29: p. 311-324.

52. Kung, H.C., *A mathematical model of wood pyrolysis.* Combustion & Flame, 1972. 18: p. 185-195.

53. Munson, T.R. and R.J. Spindler, *Transient thermal behaviour of decomposing materials: Part 1 General theory and application to convective heating*, in *RAD-TR-61-10.* 1961, AVCO Corporation.

54. Bamford, C.H. and D.H. Malan, *The combustion of wood, Part 1.* Proceedings of the Cambridge Philosophical Society, 1946. **42**: p. 166-182.

55. Henderson, J.B., J.A. Wiebelt, and M.R. Tant, *A Model for the thermal response of polymer composite materials with experimental verification.* Journal of Composite Materials, 1985. **19**: p. 579-594.

56. Tant, M.R., J.B. Henderson, and C.T. Boyer, *Measurement and modelling of the thermochemical expansion of polymer composites.* Composites, 1985. **16**: p. 121-126.

57. Henderson, J.B. and M.R. Tant, *Measurement of thermal and kinetic properties of a glass-filled polymer composite to high temperatures.* High Temperatures-High Pressures, 1996. **18**: p. 17-28.

58. Henderson, J.B. and M.P. Doherty, *Measurement of selected properties of a glass-filled polymer composite.* High Temperatures-High Pressures, 1987. **19**: p. 95-102.

59. Henderson, J.B. and T.E. Wiecek, *A mathematical model to predict the thermal response of decomposing, expanding polymer composites.* Journal of Composite Materials, 1987. **21**: p. 373-393.

60. Florio, J., J.B. Henderson, and F.L. Test, *Measurement of the thermochemical expansion of porous composite materials.* High Temperatures-High Pressures, 1989. **21**: p. 157-165.

61. Florio, J., et al., *A study of the effects of the assumption of local-thermal equilibrium on the overall thermally-induced response of a decomposition, glass-filled polymer composite.* International Journal of Heat & Mass Transfer, 1991. **34**: p. 135-147.

62. Sullivan, R.M. and N.J. Salamon, *A finite element method for the thermochemical decomposition of polymeric materials - I. Theory.* International Journal of Engineering Science, 1992. **30**: p. 431-441.

63. Sullivan, R.M. and N.J. Salamon, *A finite element method for the thermochemical decomposition of polymeric materials - II. Carbon phenolic composites.* International Journal of Engineering Science, 1992. **30**: p. 939-951.

64. Sullivan, R.M., *A coupled solution method for predicting the thermostructural response of decomposing, expanding polymeric composites.* Journal of Composite Materials, 1993. **27**: p. 408-434.

65. Pering, G.A., P.V. Farrell, and G.S. Springer, *Degradation of tensile and shear properties of composites exposed to fire or high temperature.* Journal of Composite Materials, 1980. **14**: p. 54-66.

66. McManus, H.L. and G.S. Springer, *High temperature behaviour and thermomechanical behaviour of carbon-phenolic and carbon-carbon composites, I. Analysis.* Journal of Composite Materials, 1992. **26**: p. 206-229.

67. McManus, H.L. and G.S. Springer, *High temperature behaviour of thermomechanical behaviour of carbon-phenolic and carbon-carbon composites, II. Results.* Journal of Composite Materials, 1992. **26**: p. 230-255.

68. Dimitrienko, Y.I., *Thermal stresses and heat-mass-transfer in ablating composite materials.* Journal of Heat and Mass Transfer, 1995. **38**: p. 139-146.

69. Dimitrienko, Y.I., *Thermomechanical behaviour of composite materials and structures under high temperatures: 1. Materials.* Composites: Part A, 1997. **28**: p. 453-461.

70. Dodds, N., et al., *Fire behaviour of composite laminates.* Composites: Part A, 2000. **31(7)**: p. 689-702.

71. Chang, C.I., *Thermal effects on polymer composite structures.* Theoretical & Applied Fracture Mechanics, 1986. **6**: p. 113-120.

72. Mouritz, A.P. and A.G. Gibson, *Fire Properties of Polymer Composite Materials*. Solid Mechanics and its Applications, ed. G.M.L. Gladwell. 2006 (In press): Springer.

73. Asaro, R.J., M. Dao, and N. Schultz, *Fire protection techniques for commerical vessels: structural fire protection modelling*. Flame Retardant Polymers, 1998: p. 113-127.

74. Charles, J.A. and D.W. Wilson, *A model for passive thermal non-destructive evaluation of composite laminates*. Polymer Composites, 1981. **2**: p. 105-111.

75. Milke, J. and A.J. Vizzini, *Thermal response of fire-exposed composites*. Journal of Composites Technology & Research, 1991. **13**: p. 145-151.

76. Griffis, C.A., et al., *Degradation in strength of laminated composites subjected to intense heating and mechanical loading*. Journal of Composite Materials, 1986. **20**: p. 216-235.

77. Looyeh, M.R.E. and P. Bettess, *A finite element model for the fire performance of GRP panels including variable thermal properties*. Finite Elements in Analysis & Design, 1998. **30**: p. 313-324.

78. Lui, L., et al. *Compressive response of composites under combined fire and compressive loading*. in *Composites in Fire 4*. 2005. University of Newcastle upon Tyne.

79. Lua, J. and J. O'Brien. *Fire simulation for woven fabric composites with temperature and mass dependent thermal mechanical properties*. in *Composites in Fire 3*. 2003. Newcastle upon Tyne, England.

80. Mouritz, A.P. and Z. Mathys, *Post-fire mechanical properties of marine polymer composites*. Composite Structures, 1999. **47**(1-4): p. 643-653.

81. Mouritz, A.P. and Z. Mathys, *Post-fire mechanical properties of glass-reinforced polyester composites.* Composites Science and Technology, 2001. **61**(4): p. 475-490.

82. Gardiner, C.P., Z. Mathys, and A.P. Mouritz, *Tensile and compressive properties of FRP composites with localised fire damage.* Applied Composite Materials, 2002. **9**(6): p. 353-367.

83. Anilturk, D. and W.S. Chan, *Structural stability of composite laminated column exposed to high temperature or fire.* Journal of Composite Materials, 2003. **37**(8): p. 687-700.

84. Bausano, J., et al. *Composite life under sustained compression and one sided simulated fire exposure: characterisation and prediction.* in *Composites in Fire 3.* 2003. Newcastle upon Tyne, England.

85. Gibson, A.G., et al., *Modelling residual mechanical properties of polymer composites after fire.* Plastics, Rubber and Composites, 2003. **32**(2): p. 81-90.

86. Gibson, A.G., et al., *The integrity of polymer composites during and after fire.* Journal of Composite Materials, 2004. **38**: p. 1283-1308.

87. Dao, M. and R.J. Asaro, *A study on failure prediction and design criteria for fibre composites under fire degradation.* Composites: Part A, 1999. **30**(2): p. 123-131.

88. Halverson, H., et al. *Simulation of structural response of composite structures under fire exposure.* in *Composites in Fire 3.* 2003. Newcastle upon Tyne, England.

89. Gibson, A.G., et al., *Laminate theory analysis of composites under load in fire.* Journal of Composite Materials, 2006. **40**(7): p. 639-658.

90. Seggewiß, P.G.B. *Properties of fire damaged polymer matrix composites.* in *Composites in Fire 3.* 2003. Newcastle upon Tyne, England.

91. Kidd, C.T. and C.G. Nelson. *How the Schmidt-Boelter gage really works*. in *41st International Instruments Symposium*. 1995. Denver, Colorado.

92. Incropera, F.P. and D.P. DeWitt, *Introduction to Heat Transfer*. Third ed. 1996, Chichester: John Wiley & Sons.

93. Kreith, F. and M.S. Bohn, *Principles of Heat Transfer*. Fifth ed. 1993, San Francisco: West Publishing Company.

94. Janna, W.S., *Engineering Heat Transfer*. Second ed. 2000, London: CRC Press.

95. *ASTM E 457-96(2002): "Standard test method for measuring heat transfer rate using a thermal capacitance (slug) calorimeter"*. ASTM International, 2002.

96. *ASTM D 792-00: "Standard test methods for density and specific gravity (relative density) of plastics by displacement. Method A - For testing solid plastics in water"*. ASTM International, 2000.

97. Friedman, H.L. *Kinetics of thermal degradation of char-forming plastics from thermogravimetry: Application to a phenolic plastic*. in *Proceedings of the 136th American Chemical Society meeting*. 1959. Atlantic City, NJ.

98. Henderson, J.B., et al., *A method for the determination of the specific heat and heat of decomposition of composite materials*. Thermochimica Acta, 1982. **57**(2): p. 161-171.

99. *ISO 14125: "Fibre-reinforced plastic composites - Determination of flexural properties"*. International Organization for Standardization, First edition, 1998.

100. Young, W.C. and R.G. Budynas, *Roark's Formulas for Stress and Strain*. 7th ed. General Engineering Series. 2002, London: McGraw-Hill.

101. Easby, R.C., *PhD Thesis: Fire behaviour of pultruded composites*, in *School of Mechanical and Systems Engineering*. 2006, University of Newcastle upon Tyne: Newcastle upon Tyne.

102. *Boeing specification support standard.* Advanced composite compression tests, BSS 7260, 1986.

103. Kulcami, A.P. and R.F. Gibson. *Non-destructive characterisation of effects of temperature and moisture on elastic moduli of vinyl ester resin and E-glass/vinyl ester resin composite.* in *Proceedings of the American Society of Composites, 18th Annual Technical Conference.* 19th-22nd October, 2003. Florida.

104. Gibson, A.G., et al. *Laminate theory analysis of composites under load in fire.* in *Composites in Fire 4: 4th International Conference on Composites in Fire.* 2005. Newcastle upon Tyne, UK: CompositeLink Consultants Limited.

105. Feih, S., et al. *Property degradation of fibreglass composites in fire.* in *Composites in Fire 4: 4th International Conference on Composites in Fire.* 2005. Newcastle upon Tyne, UK: CompositeLink Consultants Limited.

106. *A G Y Technical paper: "High strength glass fibres".* 2004, Pub no. LIT-2004-011 R1: USA.

107. Bubiansky, B. and N.A. Fleck, *Compressive failure of fiber composites.* Journal of the Mechanics and Physics of Solids, 1993. **41**: p. 183-211.

108. Agarwal, B.D. and L.J. Broutman, *Analysis and performance of fiber composites.* 2nd ed. 1990, Chichester: John Wiley & Sons, Inc.

109. Eckold, G., *Design snd Manufacture of Composite Structures.* 1994, Cambridge: Woodhead Publishing Ltd.

110. *Pictures courtesy of the efunda website (http://www.efunda.com).*

111. Goetzel, C.G., *High temperature properties of some reinforced phenolic composites.* High Temperatures-High Pressures, 1980. **12**: p. 131-146.

112. Buch, J.D. *Thermal expansion behaviour of a thermally degrading organic matrix composite.* in *Thermomechanical Behaviour of High-Temperature Composites.* 1982. ASME Publication AD-04: ASME, New York.

List of Publications

- A.G. Gibson, Y-S Wu, T.N.A. Browne and A.P. Mouritz. *Laminate analysis model for the failure of composite structures in fire,* in: *4th International Conference of Composite Materials in Offshore Operations (CMOO-4)* 2005, Houston, Texas, USA: CEAC

- A.G. Gibson, Y-S Wu, T.N.A. Browne, R.C. Easby, Z. Mathys and A.P. Mouritz. *Laminate theory analysis of composites under load in fire,* in: *Proceedings of Composites in Fire 4: Fourth International Conference on Composites in Fire.* 2005. Newcastle upon Tyne.

- T.N.A. Browne, R.C. Easby, A. Elmughrabi, A.G. Gibson and A. P. Mouritz. *Composite structures under load in fire*, in: *Characterisation and Modelling Procedures of DURACOSYS (Durability of Composite Systems)*, 2006, Virginia Tech., Blacksburg VA, USA.

Appendix

I. Laminate Analysis Model / Saw Tooth Model Code

An example of the Visual Basic code for the laminate analysis model / Saw Tooth strength model is detailed below. The code applies to a loaded glass/polyester laminate in a 50kW/m^2 fire.

```
Sub ABCDvsTIME()

Rem Perform Calculations for all time intervals
For j = 1 To 42

Dim Time(50)

Worksheets("Temp profile").Activate
Time(j) = ActiveSheet.Cells(j + 7, 1).Value

Worksheets("A'B'C'D' Matrix").Activate
ActiveSheet.Cells(j + 29, 2).Value = Time(j)

Rem Calculate Q-matrix per node

For i = 1 To 13


Rem Read Temperature Profile Values

Dim tem(20)
Worksheets("Temp profile").Activate
tem(i) = ActiveSheet.Cells(j + 7, i + 1).Value


Rem Read RRC Values

Dim rc(20)
Worksheets("RRC").Activate
rc(i) = ActiveSheet.Cells(j + 7, i + 1).Value


Rem Calculate E1, E2, G12 and u21

Dim E1(20)
Dim E2(20)
Dim G12(20)
Dim u12(20)
Dim u21(20)
```

```
Dim cE1(20)
Dim cE2(20)
Dim cG12(20)
Dim TanhE1(20)
Dim TanhE2(20)
Dim TanhG12(20)

Worksheets("Model").Activate

TgE1 = ActiveSheet.Cells(4, 2)
TgE2 = ActiveSheet.Cells(5, 2)
TgG12 = ActiveSheet.Cells(6, 2)

kE1 = ActiveSheet.Cells(4, 3)
kE2 = ActiveSheet.Cells(5, 3)
kG12 = ActiveSheet.Cells(6, 3)

MuE1 = ActiveSheet.Cells(4, 4)
MuE2 = ActiveSheet.Cells(5, 4)
MuG12 = ActiveSheet.Cells(6, 4)

MrE1 = ActiveSheet.Cells(4, 5)
MrE2 = ActiveSheet.Cells(5, 5)
MrG12 = ActiveSheet.Cells(6, 5)

cE1(i) = kE1 * (tem(i) - TgE1)
TanhE1(i) = (Exp(cE1(i)) - Exp(-cE1(i))) / (Exp(cE1(i)) + Exp(-cE1(i)))
E1(i) = (((1 - TanhE1(i)) * (MuE1 - MrE1)) / 2 + MrE1) * (rc(i) / 100)
^ 1

cE2(i) = kE2 * (tem(i) - TgE2)
TanhE2(i) = (Exp(cE2(i)) - Exp(-cE2(i))) / (Exp(cE2(i)) + Exp(-cE2(i)))
E2(i) = (((1 - TanhE2(i)) * (MuE2 - MrE2)) / 2 + MrE2) * (rc(i) / 100)
^ 1

cG12(i) = kG12 * (tem(i) - TgG12)
TanhG12(i) = (Exp(cG12(i)) - Exp(-cG12(i))) / (Exp(cG12(i)) + Exp(-
cG12(i)))
G12(i) = (((1 - TanhG12(i)) * (MuG12 - MrG12)) / 2 + MrG12) * (rc(i) /
100) ^ 1

u12(i) = ActiveSheet.Cells(3, 8).Value
u21(i) = u12(i) * E2(i) / E1(i)


Rem Calculate Q Matrix

Dim Q11(20)
Dim Q12(20)
Dim Q22(20)
Dim Q66(20)

uxy = 1 - u12(i) * u21(i)
Q11(i) = E1(i) / uxy
Q12(i) = u12(i) * E2(i) / uxy
Q22(i) = E2(i) / uxy
Q13 = 0
```

```
Q21 = Q12
Q31 = 0
Q23 = 0
Q66(i) = G12(i)

Next i


Rem Calculate EI

Dim EItotal(50)
Yna = 0
Ey = 0
Esum = 0
Ealpha = 0

For i = 1 To 12

y = i - 0.5
Ey = Ey + (E1(i) * y)
Esum = Esum + E1(i)

Next i


Yna = Ey / Esum

For i = 1 To 12
y = i - 0.5
Ealpha = Ealpha + (E1(i) * 1000000 * (Yna * 0.001 - y * 0.001) ^ 2)

Next i


EItotal(j) = (Esum / 12) + Ealpha

Worksheets("A'B'C'D' Matrix").Activate
ActiveSheet.Cells(j + 29, 3).Value = Yna
ActiveSheet.Cells(j + 29, 4).Value = EItotal(j)


Rem Calculate Laminate A, B, D Matrix

A11 = 1 / 3 * ((Q11(1) + Q11(13)) + 4 * (Q11(2) + Q11(4) + Q11(6) +
Q11(8) + Q11(10) + Q11(12)) + 2 * (Q11(3) + Q11(5) + Q11(7) + Q11(9) +
Q11(11)))

A12 = 1 / 3 * ((Q12(1) + Q12(13)) + 4 * (Q12(2) + Q12(4) + Q12(6) +
Q12(8) + Q12(10) + Q12(12)) + 2 * (Q12(3) + Q12(5) + Q12(7) + Q12(9) +
Q12(11)))

A16 = 0

A22 = 1 / 3 * ((Q22(1) + Q22(13)) + 4 * (Q22(2) + Q22(4) + Q22(6) +
Q22(8) + Q22(10) + Q22(12)) + 2 * (Q22(3) + Q22(5) + Q22(7) + Q22(9) +
Q22(11)))
```

```
A26 = 0

A66 = 1 / 3 * ((Q66(1) + Q66(13)) + 4 * (Q66(2) + Q66(4) + Q66(6) +
Q66(8) + Q66(10) + Q66(12)) + 2 * (Q66(3) + Q66(5) + Q66(7) + Q66(9) +
Q66(11)))


B11 = 1 / 3 * ((Q11(1) * -6 + Q11(13) * 6 + 4 * (Q11(2) * -5 + Q11(4) *
-3 - Q11(6) + Q11(8) + Q11(10) * 3 + Q11(12) * 5) + 2 * (Q11(3) * -4 +
Q11(5) * -2 + Q11(9) * 2 + Q11(11) * 4)))

B12 = 1 / 3 * ((Q12(1) * -6 + Q12(13) * 6 + 4 * (Q12(2) * -5 + Q12(4) *
-3 - Q12(6) + Q12(8) + Q12(10) * 3 + Q12(12) * 5) + 2 * (Q12(3) * -4 +
Q12(5) * -2 + Q12(9) * 2 + Q12(11) * 4)))

B16 = 0

B22 = 1 / 3 * ((Q22(1) * -6 + Q22(13) * 6 + 4 * (Q22(2) * -5 + Q22(4) *
-3 - Q22(6) + Q22(8) + Q22(10) * 3 + Q22(12) * 5) + 2 * (Q22(3) * -4 +
Q22(5) * -2 + Q22(9) * 2 + Q22(11) * 4)))

B26 = 0

B66 = 1 / 3 * ((Q66(1) * -6 + Q66(13) * 6 + 4 * (Q66(2) * -5 + Q66(4) *
-3 - Q66(6) + Q66(8) + Q66(10) * 3 + Q66(12) * 5) + 2 * (Q66(3) * -4 +
Q66(5) * -2 + Q66(9) * 2 + Q66(11) * 4)))


D11 = 1 / 3 * ((Q11(1) * 36 + Q11(13) * 36 + 4 * (Q11(2) * 25 + Q11(4)
* 9 + Q11(6) + Q11(8) + Q11(10) * 9 + Q11(12) * 25) + 2 * (Q11(3) * 16
+ Q11(5) * 4 + Q11(9) * 4 + Q11(11) * 16)))

D12 = 1 / 3 * ((Q12(1) * 36 + Q12(13) * 36 + 4 * (Q12(2) * 25 + Q12(4)
* 9 + Q12(6) + Q12(8) + Q12(10) * 9 + Q12(12) * 25) + 2 * (Q12(3) * 16
+ Q12(5) * 4 + Q12(9) * 4 + Q12(11) * 16)))

D16 = 0

D22 = 1 / 3 * ((Q22(1) * 36 + Q22(13) * 36 + 4 * (Q22(2) * 25 + Q22(4)
* 9 + Q22(6) + Q22(8) + Q22(10) * 9 + Q22(12) * 25) + 2 * (Q22(3) * 16
+ Q22(5) * 4 + Q22(9) * 4 + Q22(11) * 16)))

D26 = 0

D66 = 1 / 3 * ((Q66(1) * 36 + Q66(13) * 36 + 4 * (Q66(2) * 25 + Q66(4)
* 9 + Q66(6) + Q66(8) + Q66(10) * 9 + Q66(12) * 25) + 2 * (Q66(3) * 16
+ Q66(5) * 4 + Q66(9) * 4 + Q66(11) * 16)))


Worksheets("Model").Activate

ActiveSheet.Cells(31, 2).Value = A11
ActiveSheet.Cells(31, 3).Value = A12
ActiveSheet.Cells(32, 2).Value = A12
ActiveSheet.Cells(31, 4).Value = A16
ActiveSheet.Cells(33, 2).Value = A16
ActiveSheet.Cells(32, 3).Value = A22
```

```
ActiveSheet.Cells(33, 3).Value = A26
ActiveSheet.Cells(32, 4).Value = A26
ActiveSheet.Cells(33, 4).Value = A66

ActiveSheet.Cells(31, 7).Value = B11
ActiveSheet.Cells(31, 8).Value = B12
ActiveSheet.Cells(32, 7).Value = B12
ActiveSheet.Cells(31, 9).Value = B16
ActiveSheet.Cells(33, 7).Value = B16
ActiveSheet.Cells(32, 8).Value = B22
ActiveSheet.Cells(33, 8).Value = B26
ActiveSheet.Cells(32, 9).Value = B26
ActiveSheet.Cells(33, 9).Value = B66

ActiveSheet.Cells(31, 12).Value = D11
ActiveSheet.Cells(31, 13).Value = D12
ActiveSheet.Cells(32, 12).Value = D12
ActiveSheet.Cells(31, 14).Value = D16
ActiveSheet.Cells(33, 12).Value = D16
ActiveSheet.Cells(32, 13).Value = D22
ActiveSheet.Cells(33, 13).Value = D26
ActiveSheet.Cells(32, 14).Value = D26
ActiveSheet.Cells(33, 14).Value = D66

Rem Calculate EI for current time step and print in A'B'C'D' Worksheet


Rem Read A',B',C',D' and Print in A'B'C'D' Matrix Worksheet

Dim A1dash(20)
Dim A2dash(20)
Dim A6dash(20)
Dim B1dash(20)
Dim B2dash(20)
Dim B6dash(20)
Dim D1dash(20)
Dim D2dash(20)
Dim D6dash(20)
Dim DOne(20)
Dim DTwo(20)
Dim A1(20)
Dim B1(20)


For i = 1 To 3

Worksheets("Model").Activate
A1dash(i) = ActiveSheet.Cells(41, i + 1).Value
A2dash(i) = ActiveSheet.Cells(42, i + 1).Value
A6dash(i) = ActiveSheet.Cells(43, i + 1).Value

B1dash(i) = ActiveSheet.Cells(41, i + 6).Value
B2dash(i) = ActiveSheet.Cells(42, i + 6).Value
B6dash(i) = ActiveSheet.Cells(43, i + 6).Value

D1dash(i) = ActiveSheet.Cells(41, i + 16).Value
D2dash(i) = ActiveSheet.Cells(42, i + 16).Value
```

```
D6dash(i) = ActiveSheet.Cells(43, i + 16).Value

DOne(i) = ActiveSheet.Cells(31, 12).Value
DTwo(i) = ActiveSheet.Cells(31, 13).Value
A1(i) = ActiveSheet.Cells(31, i + 1).Value
A6 = ActiveSheet.Cells(33, 4).Value
B1(i) = ActiveSheet.Cells(31, i + 6).Value
B6 = ActiveSheet.Cells(33, 9).Value
D6 = ActiveSheet.Cells(33, 14).Value

Worksheets("A'B'C'D' Matrix").Activate

ActiveSheet.Cells(j + 29, i + 4).Value = A1dash(i)
ActiveSheet.Cells(j + 29, i + 7).Value = A2dash(i)
ActiveSheet.Cells(j + 29, i + 10).Value = A6dash(i)

ActiveSheet.Cells(j + 29, i + 13).Value = B1dash(i)
ActiveSheet.Cells(j + 29, i + 16).Value = B2dash(i)
ActiveSheet.Cells(j + 29, i + 19).Value = B6dash(i)

ActiveSheet.Cells(j + 29, i + 22).Value = D1dash(i)
ActiveSheet.Cells(j + 29, i + 25).Value = D2dash(i)
ActiveSheet.Cells(j + 29, i + 28).Value = D6dash(i)

ActiveSheet.Cells(j + 29, 33).Value = DOne(i)
ActiveSheet.Cells(j + 29, 34).Value = DTwo(i)
ActiveSheet.Cells(j + 29, i + 38).Value = A1(i)
ActiveSheet.Cells(j + 29, i + 41).Value = B1(i)
ActiveSheet.Cells(j + 29, 45).Value = A6
ActiveSheet.Cells(j + 29, 46).Value = B6
ActiveSheet.Cells(j + 29, 47).Value = D6


Next i


Next j


End Sub
```

II. TDSS Strength Model Code

An example of the Visual Basic code for the TDSS strength model is detailed below. The code applies to a glass/polyester laminate under tensile loading in a 50kW/m^2 fire.

```
Private Sub CommandButton1_Click()

Rem Perform stress calculation based on ply temperature

For j = 1 To 42

Dim Time(50)

Worksheets("Temp profile").Activate
Time(j) = ActiveSheet.Cells(j + 7, 1).Value

Worksheets("Output").Activate
ActiveSheet.Cells(j + 7, 1).Value = Time(j)


Rem Read temperature values for each node

Dim tem(20)
Dim TStress(20)
Dim TStren(200)

For k = 0 To 100

For i = 1 To 13

Worksheets("Temp profile").Activate
tem(i) = ActiveSheet.Cells(j + 7, i + 1).Value


Rem Calculate stress for ply temperature

If 0 < tem(i) And tem(i) <= 26.5 Then E = 10
If 0 < tem(i) And tem(i) <= 26.5 Then sigma = 755.35

If 26.5 < tem(i) And tem(i) <= 50 Then E = 9.8
If 26.5 < tem(i) And tem(i) <= 50 Then sigma = 836

If 50 < tem(i) And tem(i) <= 70 Then E = 9.64
If 50 < tem(i) And tem(i) <= 70 Then sigma = 573.51

If 70 < tem(i) And tem(i) <= 90 Then E = 8.99
If 70 < tem(i) And tem(i) <= 90 Then sigma = 704.14

If 90 < tem(i) And tem(i) <= 175 Then E = 8.25
If 90 < tem(i) And tem(i) <= 175 Then sigma = 818.6

If 175 < tem(i) And tem(i) <= 287.5 Then E = 7.02
```

```
If 175 < tem(i) And tem(i) <= 287.5 Then sigma = 405.25

If 287.5 < tem(i) And tem(i) <= 358 Then E = 4.93
If 287.5 < tem(i) And tem(i) <= 358 Then sigma = 855.49

If 358 < tem(i) Then E = 1000000
If 358 < tem(i) Then sigma = 1000000

strain = k / 1000

TStress(i) = sigma * (1 - Exp((-(1000 * E) * strain) / sigma))

Rem Calculate failure stress

Dim sT(20)

TgsT = 68

ksT = 0.035

MusT = 440

MrsT = 235

csT = ksT * (tem(i) - TgsT)
TanhsT = (Exp(csT) - Exp(-csT)) / (Exp(csT) + Exp(-csT))
sT(i) = (((1 - TanhsT) * (MusT - MrsT)) / 2 + MrsT)

Rem Is calculated stress larger than failure stress?

If TStress(i) >= sT(i) Then TStress(i) = 0


Next i


Rem Calculate laminate strength

TStren(k) = (1 / 2 * ((TStress(1) + TStress(13)) + 2 * (TStress(2) +
TStress(3) + TStress(4) + TStress(5) + TStress(6) + TStress(7) +
TStress(8) + TStress(9) + TStress(10) + TStress(11) + TStress(12)))) /
12

Worksheets("Output").Activate
ActiveSheet.Cells(j + 7, k + 2).Value = TStren(k)

Next k

Next j

End Sub
```